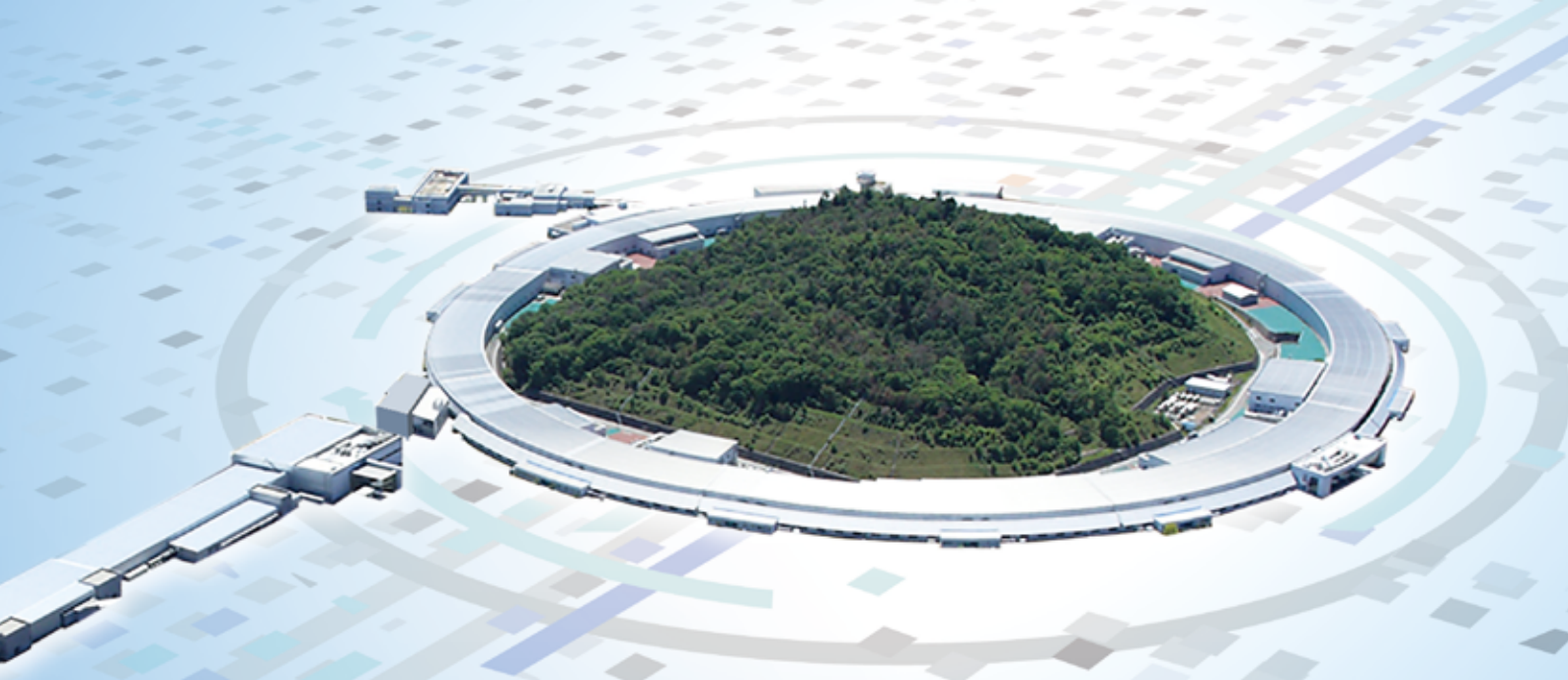

Research Frontiers 2017

SPring-8
SACLA

ISSN 2433-5126
SPring-8 Document D2018-007

SPring-8/SACLA Research Frontiers 2017

CONTENTS

Physical Science

Chemical Science

Earth & Planetary Science

Archaeology

Industrial Applications

Accelerators & Beamlines Frontiers 96

SPring-8

New Apparatus, Upgrades & Methodology

SACLA

Facility Frontiers 103

Note: The principal publication(s) concerning each article is indicated with all author's names in italics in the list of references.

Preface

Today, the SPring-8 campus operates two world-leading accelerator based light sources of SPring-8 and SACLA and offers a unique environment where the two facilities can be used synergistically.

SPring-8 (Super Photon ring 8 GeV), one of the world's largest synchrotron facilities, welcomed over 17,000 users in 2017. In 2017, 10,720 users conducted 1,575 experiments at the public beamlines, and 6,887 users performed 681 experiments at the contract beamlines. The operation time of the storage ring in 2017 was 5,282 h and the user time was 4,479 h. Currently, SPring-8 users are publishing over 1,000 research papers per year, and the ratio of papers in the top 1% of the citation index was as high as 1.9% for the papers published in 2016.

SACLA (SPring-8 Angstrom Compact free electron LAser) is the second operating hard X-ray Free Electron Laser (XFEL) in the world and the first compact XFEL, which was opened to users in March 2012. In 2017, 1,219 users conducted 94 experiments at 3 beamlines, and SACLA users published over 80 research papers. The ratio of papers in the top 1% of the citation index was as high as 4.1% for the papers published by SACLA users in 2016.

A number of SPring-8 and SACLA users were awarded prizes in 2017 and 2018 for their achievements in science and technology. Prof. Chikashi Toyoshima (The University of Tokyo) was awarded the Imperial Prize and Japan Academy Prize in 2018 for his achievement in the elucidation of the molecular mechanism of the ATP-driven ion-transport across the membranes. Prof. Takeshi Aida (RIKEN) was awarded the Japan Academy Prize in 2018 for his achievement in studies on precision hierarchical design on innovative soft materials. Prof. Yuuichi Komizo (JASRI) and Prof. Maki Kawai (Institute of Molecular Science) were respectively awarded the Medal with Purple Ribbon in Fall 2017. Prof. Osamu Nureki (The University of Tokyo) and Prof. Yukihiro Ozaki (Kwansei Gakuin University) were awarded respectively the Medal with Purple Ribbon in Spring 2018. In 2018, eight active users from academia and industry were awarded Prizes for Science and Technology by the Minister of Education, Culture, Sports, Science and Technology, and twelve young users were awarded Young Scientists Prizes by the Minister.

In this volume, two comprehensive reviews are reported by Prof. Jian-Ren Shen (Okayama University) and Prof. Makoto Seto (Kyoto University). Active users of SPring-8 have also contributed the essence of their results as review articles in this volume. In addition, four articles are provided by active users of SACLA.

I am very grateful to the many authors and experts who contributed their papers to this volume. Special thanks are due to Dr. Naoto Yagi and the members of the editorial board for their continuous efforts.

土肥義治

Yoshiharu Doi
President
Japan Synchrotron Radiation Research Institute (JASRI)

Editor's Note

This is the 2017 issue of SPring-8/SACLA Research Frontiers that covers outstanding scientific outcomes of SPring-8 and SACLA in 2016 and 2017. The cream of the scientific achievements is collected here.

Reviews in this issue were contributed by Prof. Jian-Ren Shen of Okayama University and Prof. Makoto Seto of Kyoto University. Prof. Shen has been working on mechanism of photosynthesis in plants, in which oxygen molecule and sugar are produced from carbon dioxide and water with the energy of light. This process is important for mankind for prevention of global warming and solving energy and food crises. The protein Prof. Shen is working on is photosystem II (PSII) which is a huge membrane-protein complex with a total molecular weight of 700 kDa. This protein performs the initial water-splitting reaction of photosynthesis. After getting its high-resolution crystal structure in 2011, Prof. Shen's group proceeded to clarify detailed mechanism of the reaction by making use of SACLA. The damage-free structure of the Mn cluster at the catalytic center of the protein was revealed with pulse X-rays of SACLA. Further, structure of an intermediate state of the reaction was clarified in a pump-probe experiment. This research is still under progress for complete understanding of the reaction, and the current situation is summarized in the review.

Prof. Seto has been working on nuclear resonant scattering at BL09XU since SPring-8 started operation 20 years ago. This is fundamental physics research requiring very sophisticated experimental techniques. His group has been publishing many top-class physics papers over the years. Initially, the experiment looked formidable for non-specialists, but thanks to the very bright and stable X-ray beam of SPring-8 and high skills of the Prof. Seto's group, applications of the technique are increasing. NRVS (Nuclear Resonance Vibrational Spectroscopy) is extensively used to study catalytic centers of metalloproteins. Since the experiment can be now possible under high pressure, Mössbauer radiation was used in earth science to measure thermal conductivity of silicate melts. The narrow energy bandwidth (neV) allows studies on slow dynamics of liquid by quasi-elastic scattering measurements. These experiments emerged from the long-time efforts of Prof. Seto, to which SPring-8 owes much.

SPring-8/SACLA Research Frontiers is made of two parts. The first is the scientific results (Scientific Frontiers) and the second is additional information on hard and soft infrastructures that support scientific research. Although some important numbers such as the operation time are given in the second part, other information and more complete statistical numbers on the operation of SPring-8 and SACLA are available on the website so that more updated information can be accessed (http://www.spring8.or.jp/en/about_us/spring8data/).

The full text of SPring-8/SACLA Research Frontiers is also available on the SPring-8 website (http://www.spring8.or.jp/). For the list of publications produced by SPring-8 users and staff, please visit the publication database at http://www.spring8.or.jp/en/science/publication_database/.

On behalf of all the editors, I would like to thank those who helped us by recommending excellent research results suitable for publication in this issue, and the users and staff of SPring-8 who contributed their reports to this issue.

Naoto Yagi
- Editor in Chief -
Japan Synchrotron Radiation Research Institute (JASRI)

Editorial Board

Scientific Frontiers

Review Article

The Engine of Life Driven by Light – Structure of Photosystem II and the Mechanism of Water-splitting

Oxygenic photosynthesis is a process by which cyanobacteria, various algae and higher plants utilize light energy from the sun to split water and to convert carbon dioxide into carbohydrates using the reducing equivalents derived from water-splitting. Two products generated from this process are molecular oxygen and sugar; the former is the source of oxygen in the atmosphere and indispensable for aerobic life on the earth, whereas the latter provides the energy sustaining almost all life forms on the earth. Thus, photosynthesis is an important process for sustaining life activities on the earth.

The first reaction in photosynthesis is light-induced water-oxidation as depicted below:

$$2H_2O \xrightarrow{\text{Light}} 4e^- + 4H^+ + O_2$$

This reaction is catalyzed by an oxygen-evolving center (OEC) in photosystem II (PSII), a huge membrane-protein complex consisting of 17 trans-membrane subunits and 3 peripheral, hydrophilic subunits with a total molecular mass of 350 kDa for a monomer. PSII functions as a dimer located in the thylakoid membranes of oxygenic organisms, so its total molecular mass is 700 kDa.

The water-splitting reaction proceeds through the so-called S-state cycle [1,2], in which the catalyst adopts 5 different states denoted as S_i (where i= 0–4) (Fig. 1). The S_1-state is dark-stable; upon absorption of one photon, it advances to S_2 and subsequently to S_3, S_0 upon further absorption of photons. These transitions are accompanied by the release of electrons and protons. The S_4-state is a transient one, and molecular oxygen is formed and released during the transition from S_4 to S_0.

In order to unravel the mechanism of water-oxidation by PSII, it is essential to solve the crystal structure of PSII and its reaction intermediates. We purified the PSII dimer from a thermophilic cyanobacterium *Thermosynechococcus (T.) vulcanus*, and succeeded in its crystallization [3]. By optimizing the purification and crystallization conditions, we obtained high-quality crystals of PSII and solved its crystal structure at 1.9 Å using the synchrotron radiation (SR) X-rays at SPring-8 beamlines BL41XU and BL44XU [4]. This structure provided the first detailed picture of OEC, which is a Mn_4CaO_5-cluster organized in a distorted chair form. However, due to the strong, continuous synchrotron X-rays used, the structure has been suggested to suffer partially from X-ray radiation damage, which may cause partial reduction of the Mn ions and thus slightly longer distances in some of the Mn-Mn distances within the cluster. In order to obtain the radiation-damage free structure of OEC, we used the femtosecond X-ray free electron lasers (XFEL) provided by SACLA and a "fixed-target serial femtosecond crystallography" approach with large PSII crystals, and analyzed its structure at 1.95 Å resolution [5]. Furthermore, we employed a pump-probe approach in which, 2 laser flashes were used to "pump" the OEC to the S_3-state, and the serial femtosecond crystallography (SFX) method using PSII micro-crystals was used as the "probe" to detect structural changes occurred during the S-state transition from S_1-to-S_3 [6]. The results obtained from these studies allowed us to propose the mechanism for photosynthetic water-oxidation catalyzed by the Mn_4CaO_5-cluster.

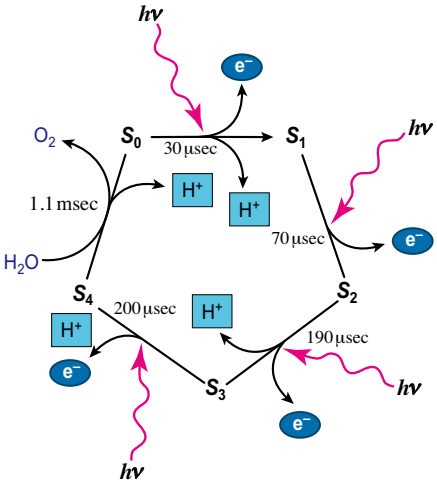

Fig. 1. S-state transition of the water-splitting reaction catalyzed by PSII.

The overall structure of PSII and the OEC

The overall structure of PSII analyzed at 1.9 Å resolution is depicted in Fig. 2(a). In this structure, 40 protein subunits were assigned, together with more than 150 cofactors. In addition, around 2,800 water molecules are found, which are mostly distributed in the two

membrane surfaces at the stromal and lumenal sides, demonstrating the typical feature of PSII as a membrane protein complex. The catalytic center for water oxidation was found to be a Mn_4CaO_5-cluster located at the lumenal surface. The Mn_4CaO_5-cluster is organized in a distorted chair form, with 3 Mn ions and 1 Ca ion connected by 4 oxygen atoms (oxo-bridges) forming the distorted chair base (cubane), and the 4th Mn connected to the outside of cubane (Fig. 2(b)). The metal ions are coordinated by 7 amino acid residues, among them, 6 are carboxyl ligands whereas 1 is a His ligand (Fig. 2(c)). Most of the carboxyl ligands are bidentate, and only 1 carboxyl ligand (D1-Glu189) and the His ligand are monodentate. In addition to the amino acid ligands, 4 water molecules were found to serve as terminal ligands; 2 of them are bonded to the Ca ion and 2 to the 4th Mn ion (Mn4). These ligands together make a saturated coordination environment for the metal ions; namely, all of the 4 Mn ions are 6-coordinated whereas the Ca ion is 7-coordinated. A number of additional water molecules were found around the cluster, suggesting that the metal cluster is located in a rather hydrophilic environment in the interior of the protein matrix. These water molecules are not coordinated directly to the metal ions but form extended hydrogen bonds (HBs) which are important for the release of protons [4,7].

The distortion found in the Mn_4CaO_5-cluster is caused by two main factors. One is the difference between the distances of Mn-O and Ca-O. The typical distances found between Mn-O are in the range of 1.8-2.1 Å, whereas that of Ca-O is in the range of 2.3-2.6 Å. The other factor is the differences between Mn-O. Among the 5 oxygen atoms found within the Mn_4CaO_5-cluster, O1-O4 have bond distances typical for manganese oxides (1.8-2.1 Å), whereas the O5 atom has unusually longer distance to its nearby Mn ions. Especially, the distance between O5-Mn1 and O5-Mn4 were found to be 2.6 Å and 2.5 Å, respectively. These results suggest that the binding of O5 to its nearby Mn ions are weak than the typical Mn-O bonds found for the other oxy-bridges, and thus the O5 atom may be cut out during the reaction cycle to provide one of the substrate oxygen for the O=O bond formation.

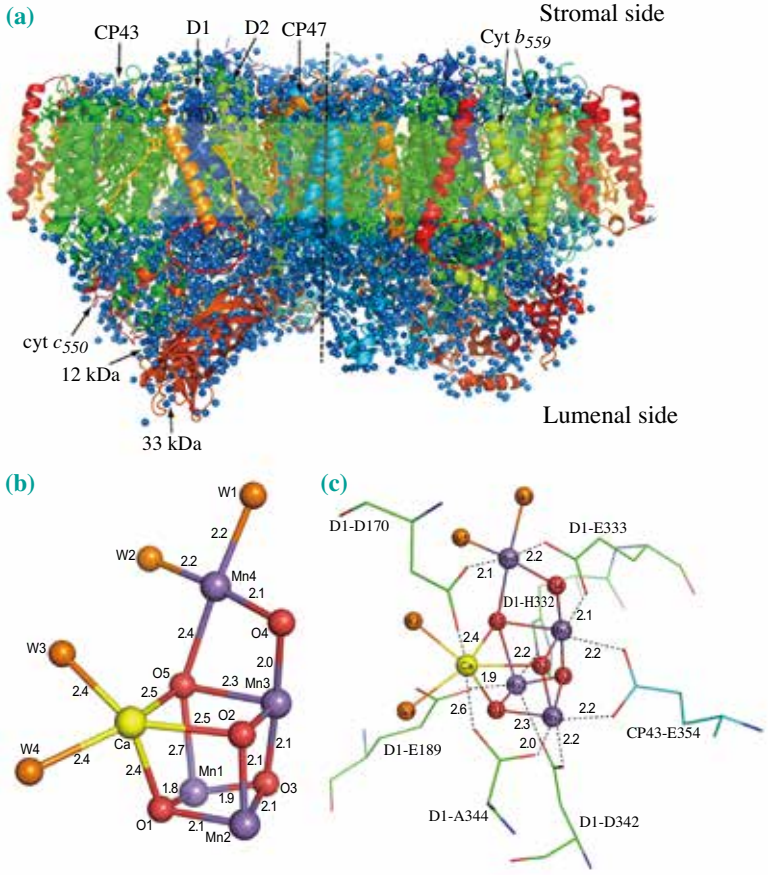

Fig. 2. Overall structure of the PSII dimer and that of OEC. **(a)** Overall structure of PSII dimer, with a view parallel to the membrane plane. The region painted in weak yellow represents the trans-membrane region, and blue balls represent water molecules. The areas circled by red dotted lines represent the site where OEC is located. **(b)** The structure of OEC, the Mn_4CaO_5-cluster. Numbers represent inter-atomic distances in Å. **(c)** Amino acid ligands of the Mn_4CaO_5-cluster.

The distorted shape of the Mn_4CaO_5-cluster suggests that it is rather instable, a distinct feature important for the catalytic activity. During the S-state cycle, the catalyst is believed to undergo subtle structural changes to advance to the higher S-states. This has been proven by various spectroscopic studies including X-ray absorption, electron paramagnetic resonance, infrared spectroscopy, etc. [8] The instable, or flexible nature of the Mn_4CaO_5-cluster implies that it can easily undergo structural changes to advance the catalyst to the intermediate states, enabling it to catalyze the water-splitting reaction efficiently.

The structural features discussed above were based on the structure solved using SR X-rays at SPring-8, and questions arose that it has suffered from some radiation damage, resulting in the reduction of some Mn ions and thus an elongation in some of the Mn-Mn pairs as well as the Mn-O distances. In fact, X-ray spectroscopic measurements [8] and theoretical calculations [9-11] based on the crystal structure we solved have suggested some slightly shorter Mn-Mn distances than that were observed in the crystal structure.

Radiation damage-free structure of the Mn_4CaO_5-cluster

In order to remove the possible radiation damage and obtain the structure of the Mn_4CaO_5-cluster in its native state, we employed the femtosecond XFEL from SACLA to collect the diffraction data. To solve the radiation damage-free structure of PSII at a sufficiently high resolution, we used large PSII crystals (1.0 mm × 0.4 mm × 0.15 mm) at a cryogenic temperature, and adopted a fixed-target serial femtosecond crystallography method [12]. This was done by illuminating one point of the crystal with a pulse of XFEL, and then move the crystal by 50 μm with a rotation of 0.2° to obtain a continuous, fresh diffraction image. By using more than 100 large PSII crystals, we were able to obtain one full diffraction data set. In order to ensure the reproducibility, we collected two independent data sets to obtain average inter-atomic distances. The results showed that most of the Mn-Mn distances are shorter by 0.1–0.3 Å compared with the structure obtained by SR X-rays (Fig. 3(a)). Some of the Mn-O and Mn-ligand distances also changed slightly. However, the feature of the unusually longer distances between O5 and its nearby Mn ions was retained, although the Mn1-O5, Mn4-O5 distances were changed to 2.7 Å, 2.3 Å respectively (Fig. 3(b)) [5]. This suggests that O5 may participate in the O=O bond formation, and its binding to Mn1 at the S_1-state is very weak.

Light-induced structural changes and the site of O=O bond formation

The structure solved above corresponds to the catalyst at the S_1-state before the water-splitting reaction starts. In order to unravel the mechanism of water-splitting and O=O bond formation, it is essential to solve the structures of the Mn_4CaO_5-cluster at the reaction intermediate states (S-states other than S_1). To this purpose, we employed a "pump-probe" approach in which, 2 laser-flashes separated by 10 msec were used to "pump" the Mn_4CaO_5-cluster to the S_3-state, which is a state immediately before the O_2 release, and XFEL pulses were used as the probe to detect the structural changes at room temperature [6]. To obtain a high efficiency of excitation by the 2 flashes, PSII micro-crystals were used, for which the SFX method is the most suitable approach to collect the X-ray diffraction data. The data obtained was used to calculate the Fourier difference map between the S_3 and S_1-states, which showed structural changes at both the electron donor and acceptor sides (Fig. 4).

At the electron acceptor side, the secondary electron acceptor Q_B was found to rotate slightly, along with some small changes in its vicinity (Fig. 4(a)). This causes a slight shortening of the H-bond between the head of Q_B and D1-

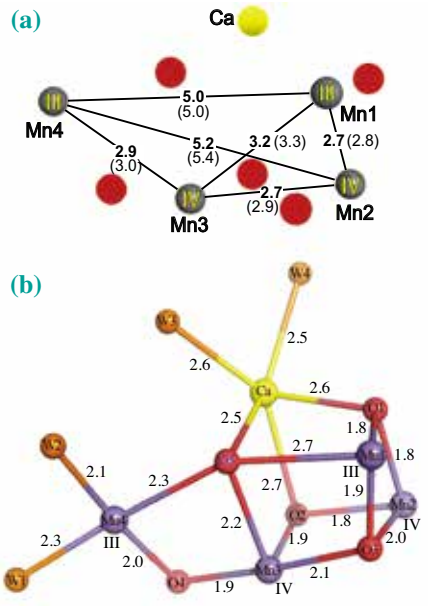

Fig. 3. Radiation damage-free structure of the Mn_4CaO_5-cluster. **(a)** Mn-Mn distances (numbers in parentheses are the distances determined by SR previously [4]). **(b)** Mn-O and Ca-O distances.

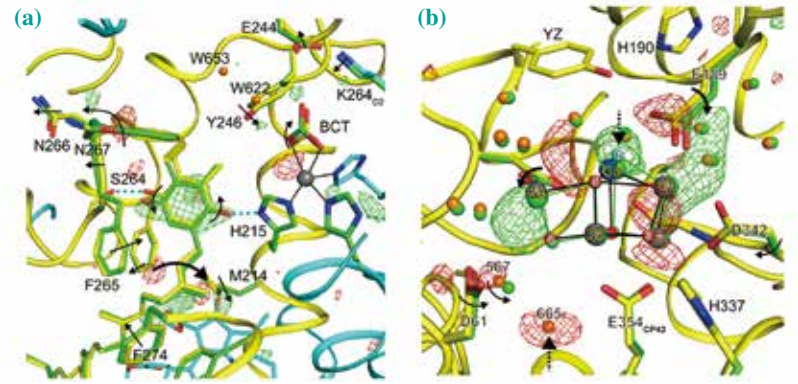

Fig. 4. Fourier difference electron density maps between the 2-flashes illuminated S_3-state and the S_1-state, and their corresponding structural changes. **(a)** The region of the acceptor (reducing) side. **(b)** The region of the donor (oxidizing) side. In both panels, green represents positive and red represents negative Fourier difference maps contoured at ±5.0 σ.

Ser264. This is explained to reflect that, upon 2-flashes illumination, a part of Q_B remains reduced due to the short time interval between the flash illumination and the XFEL pulses as well as the crystal environment that may limit the efficiency of electron transfer from Q_A to Q_B, which enhances the H-bond between Q_B and D1-Ser264, resulting in the shortening of their distance [6]. This in turn suggests that the 2 flashes illumination employed was successful in advancing the S-states.

At the donor (oxidizing) side, two major changes were found. One is the appearance of a strong negative density at the position of water-665 (W665), suggesting that this water molecule becomes mobile upon 2-flashes illumination (Fig. 4(b)) [6]. This water is H-bonded with O4 through another water molecule W567, and this H-bond was broken after 2-flashes illumination. This is considered to reflect a proton transfer occurring through the O4-W567-W665 H-bond network that extends to the bulk solution at the lumenal side, during the S_1-S_3 transition [7,13].

The second large change observed at the donor side is the appearance of a strong positive density at a position close to O5. This positive density could be modeled as a new water molecule (O6), which has a distance of 1.5 Å and coordinated to Mn1 directly [6]. This suggests that a new water molecule is inserted during the transition from S_1 to S_3 (mostly from S_2 to S_3), which is able to form the O=O bond with O5 (Fig. 5). Thus, the O5 atom provides one of the substrate oxygen atoms; upon its release in the following S-state transition, a new water molecule is expected to come in to occupy the vacant position and returns the catalyst to the S_0-state.

In conclusion, a combination of high-resolution structural analysis using SR of SPring-8 and time-resolved "pump-probe" structural analysis using XFEL of SACLA allowed us to solve the structure and reaction mechanism of the catalytic center for photosynthetic water oxidation, the Mn_4CaO_5-cluster, coordinated within the huge membrane protein complex PSII. These results provide important clues for the development of artificial catalysts for water-splitting using visible light, an important step toward acquisition of clean, renewable energy from the sun, which will greatly contribute to the realization of a sustainable society.

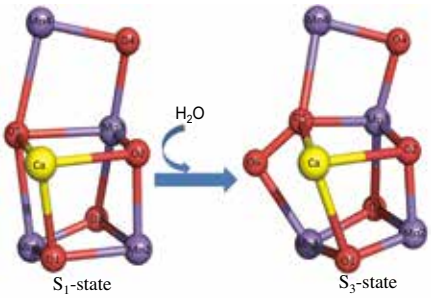

Fig. 5. Structural changes of the Mn_4CaO_5-cluster upon transition from the S_1-state to the S_3-state induced by 2-flashes illumination.

Jian-Ren Shen

Research Institute for Interdisciplinary Science, Okayama University

Email: shen@cc.okayama-u.ac.jp

References

[1] P. Joliot *et al.*: Photochem. Photobiol. **10** (1969) 309.
[2] B. Kok *et al.*: Photochem. Photobiol. **11** (1970) 457.
[3] J.-R. Shen, N. Kamiya: Biochemistry **39** (2000) 14739.
[4] Y. Umena *et al.*: Nature **473** (2011) 55.
[5] M. Suga *et al.*: Nature **517** (2015) 99.
[6] M. Suga *et al.*: Nature **543** (2017) 131.
[7] J.-R. Shen: Annu. Rev. Plant Biol. **66** (2015) 23.
[8] J. Yano and V. Yachandra: Chem. Rev. **114** (2014) 4175.
[9] K. Kanda *et al.*: Chem. Phys. Lett. **506** (2011) 98.
[10] S. Yamanaka *et al.*: Chem. Phys. Lett. **511** (2011) 138.
[11] M.R. Blomberg *et al.*: Chem. Rev. **114** (2014) 3601.
[12] K. Hirata *et al.*: Nat. Methods **11** (2014) 734.
[13] K. Saito *et al.*: Nat. Commun. **6** (2015) 8488.

Review Article

Evolution of Nuclear Resonant Scattering Research at SPring-8

Spectroscopy using the nuclear resonant scattering of synchrotron radiation has been used effectively in a wide range of research areas, taking advantage of its excellent features. Since only one nuclide (isotope) is resonantly excited with the undulator radiation, it enables the measurement of element (isotope)-specific electronic states through hyperfine interactions between the nucleus and the surrounding electrons. Moreover, the measurement of element (isotope)-specific phonons (lattice vibrations) is possible using nuclear resonant inelastic scattering. In addition, by using the ultranarrow width of the nuclear excited states (for example, the width of the first nuclear excited state of ^{57}Fe is 4.7 neV), quasi-elastic scattering measurement is possible, allowing the study of the slow dynamics of macromolecules and glass transitions. Since the nuclear resonant scattering method enables a wide range of measurements from the electronic state to quasi-elastic and inelastic scattering with an element (isotope)-specific feature, the range of areas of application is very wide such as materials science, earth science, physics, chemistry, and biology. Measurement methods employing these unique features of nuclear resonant scattering have progressively been advanced at SPring-8. Here, recent nuclear resonant scattering studies using these features are reviewed.

1. Nuclear Resonant Elastic Scattering of Synchrotron Radiation (Mössbauer Spectroscopy)

Mössbauer spectroscopy, which uses the recoilless nuclear resonant absorption effect known as the Mössbauer effect, is a powerful and well-established method used in a wide variety of research areas. One of the most important tasks of Mössbauer spectroscopy is to elucidate the electronic states of a specific element, and this can be achieved via the measurement of nuclear energy levels. This is because nuclear energy levels are affected by the surrounding electrons; if a resonant atom has a magnetic moment and/or an anisotropic electronic structure, the nuclear energy levels are split. A schematic of the nuclear energy levels of ^{57}Fe with (and without) magnetic field splitting and corresponding typical Mössbauer spectra are shown in Fig. 1. The density of electrons at the nucleus affects the nuclear energy levels and induces an energy shift, which is directly due to *s*-electrons and indirectly due to other electrons. Therefore, the measurement of the nuclear energy levels provides information on the electronic states. To determine the electronic state, this method seems to be indirect, but the identification of the observed element is obvious and the disturbance for the electronic states usually can be ignored. Table 1 shows the elements for which the Mössbauer effect has been observed.

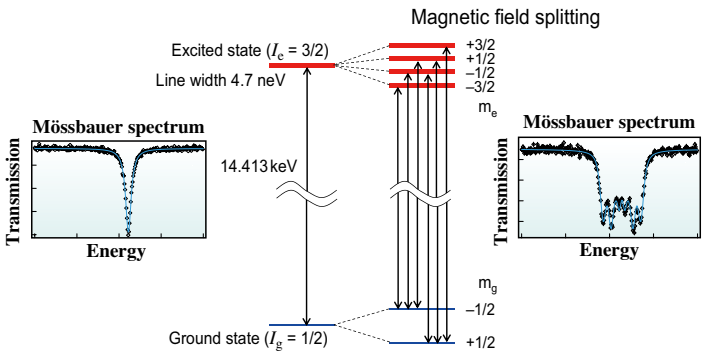

Fig. 1. Nuclear energy levels of ^{57}Fe with (right) and without (left) magnetic field splitting and corresponding typical Mössbauer spectra.

Synchrotron Mössbauer Sources

The ability to measure element (isotope)-specific electronic states is one of the unique features of nuclear resonant scattering; by combining this feature and high brilliance synchrotron radiation as an excitation source, novel studies that are difficult with radioactive isotope (RI) sources such as measurement under extreme conditions are possible. Synchrotron radiation, however, cannot be used as a simple alternative Mössbauer γ-ray source because the bandwidth of the incident synchrotron radiation is much broader than the line width of the nuclear levels usually used and even hyperfine splitting (typically below μeV). One method of generation an ultranarrow-width X-ray is to use electronically forbidden but nuclear-allowed Bragg reflections called synchrotron Mössbauer source (SMS). In this method, the obtained Mössbauer radiation is collimated, polarized, and 100% recoilless, and the spectrum obtained using an SMS is essentially identical to that obtained using conventional RI sources, although an SMS has only been realized for ^{57}Fe using iron borate ($FeBO_3$) single crystals set under diffraction conditions at the Néel temperature (75.3°C). The measurement of iron-enriched dense silicate glasses, as laboratory analogues for dense magmas, up to a pressure of 85 GPa was performed using an SMS at SPring-8 BL11XU [1]. Although the

possible presence of dense magmas at Earth's core-mantle boundary is expected to substantially affect the dynamics and thermal evolution of Earth's interior, the thermal transport properties of silicate melts under relevant high-pressure conditions are not understood fully. Combined with the result of *in situ* high-pressure optical absorption measurement, it was suggested that the radiative thermal conductivity of dense silicate melts may decrease with increasing pressure and, therefore, may be significantly smaller than previously expected under core-mantle boundary conditions.

1 H																	2 He
3 Li	4 Be											5 B	6 C	7 N	8 O	9 F	10 Ne
11 Na	12 Mg											13 Al	14 Si	15 P	16 S	17 Cl	18 Ar
19 K	20 Ca	21 Sc	22 Ti	23 V	24 Cr	25 Mn	26 Fe	27 Co	28 Ni	29 Cu	30 Zn	31 Ga	32 Ge	33 As	34 Se	35 Br	36 Kr
37 Rb	38 Sr	39 Y	40 Zr	41 Nb	42 Mo	43 Tc	44 Ru	45 Rh	46 Pd	47 Ag	48 Cd	49 In	50 Sn	51 Sb	52 Te	53 I	54 Xe
55 Cs	56 Ba		72 Hf	73 Ta	74 W	75 Re	76 Os	77 Ir	78 Pt	79 Au	80 Hg	81 Tl	82 Pb	83 Bi	84 Po	85 At	86 Rn
87 Fr	88 Ra		104 Rf	105 Db	106 Sg	107 Bh	108 Hs	109 Mt	110 Ds	111 Rg	112 Cn	113 Nh	114 Fl	115 Mc	116 Lv	117 Ts	118 Og
			57 La	58 Ce	59 Pr	60 Nd	61 Pm	62 Sm	63 Eu	64 Gd	65 Tb	66 Dy	67 Ho	68 Er	69 Tm	70 Yb	71 Lu
			89 Ac	90 Th	91 Pa	92 U	93 Np	94 Pu	95 Am	96 Cm	97 Bk	98 Cf	99 Es	100 Fm	101 Md	102 No	103 Lr

Table I. Periodic table of the elements for which the Mössbauer effect has been observed (elements on blue backgrounds).

Synchrotron-radiation-based Mössbauer absorption spectroscopy

To utilize the element (isotope)-specific feature, we should use other methods. Previously, nuclear resonant forward scattering (NFS) measurement in the time domain has been used. Recently synchrotron-radiation-based Mössbauer spectroscopy in the energy domain was developed at BL09XU and BL11XU; this method yields absorption spectra that are similar to Mössbauer spectra measured with radioactive sources [2]. The high brilliance of the radiation enables the measurement of tiny samples, such as samples held in diamond anvil cells. In fact, a ^{151}Eu Mössbauer study has already been performed under high pressure with this method [3]. It, however, took a long time for the measurement and, therefore, a detection system using a windowless avalanche photodiode (APD) X-ray detector in a cryostat chamber was developed to enhance the measurement efficiency [4]. In the previous measurement, γ-rays and/or fluorescent X-rays accompanied with internal conversion (IC) electron emissions from the resonantly excited nuclei were detected, but the IC electrons themselves were not detected because the electrons were shielded by the X-ray windows of the cryostat and the detector used. A schematic drawing of the experimental setup and a photograph of the detection system are shown in Fig. 2. The developed system was applied to SR-based Mössbauer spectroscopy for the 76.5 keV-excited state of ^{174}Yb. Moreover, although the natural abundance of ^{61}Ni is only 1.14%, it made the measurement of Ni samples without isotope enrichment possible. This method has been applied to studies on the electronic state of Ni nanoparticles [5], Ni-substituted proteins [6], and so forth.

2. Nuclear Resonant Inelastic Scattering

Nuclear resonant inelastic scattering spectroscopy is a method for investigating the vibrational states in substances. This method utilizes the nuclear resonance excitation accompanied by the creation and/or annihilation of phonons. The recoilless excitation of atomic nuclei is known as the Mössbauer effect, while resonance excitation of the nuclei and phonon generation can occur when the energy of the incident synchrotron radiation is larger than the resonant excitation energy and the difference is equal to the energy of a phonon. Also, when the incident energy is lower than the resonant excitation energy and the difference is equal to the energy of a phonon, annihilation of the phonon and resonant excitation occur. These are nuclear resonance inelastic excitations. In this method, phonon energy spectra are measured by counting the scattering from the excited nuclei as a function of the incident photon energy as shown in Fig. 3. The typical resolution of the spectra is around 1 meV for ^{57}Fe measurement.

Nuclear resonant inelastic scattering has many interesting features and, owing to the high brilliance of the synchrotron radiation, samples under extreme conditions such as high pressures can be measured. One of the most important features is that it is possible to excite specific isotopes as in electronic state measurement. Therefore, for compounds composed of many elements, phonon information concerning only the excited nuclide is obtained; more precisely, partial phonon densities of states (PDOSs) are obtained. This feature is very advantageous when there is interest

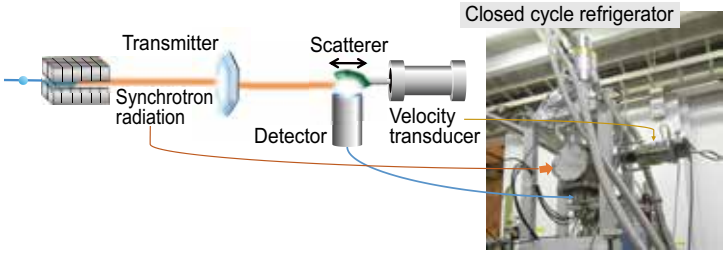

Fig. 2. Schematic drawing of the experimental setup and photograph of the detection system using a windowless avalanche photodiode (APD) X-ray detector in a cryostat chamber.

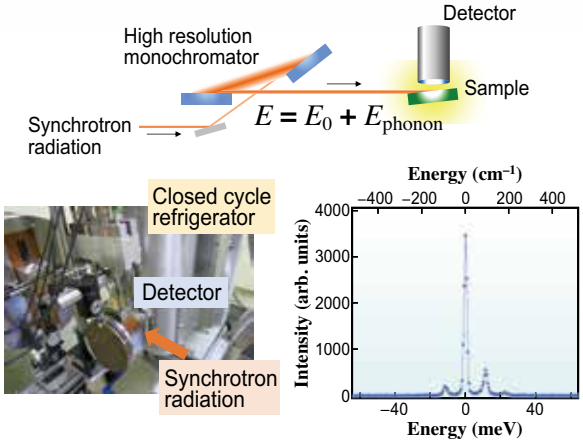

Fig. 3. Schematic for the measurement of nuclear resonant excitation accompanied by phonon creation (upper). Photograph of the detector and the cryostat with a closed-cycle refrigerator (lower left) and typical phonon energy spectrum (lower right).

in the function and/or local structure of a specific element (isotope) in a complex compound. From a spectroscopic viewpoint, this method is similar to resonant Raman spectroscopy, which provides valuable information on the vibrational properties of samples such as metalloprotein samples. Resonant Raman spectroscopy is very useful and has been used effectively. However, the selection rule sometimes hampers the observation of vibrational modes of interest while the nuclear resonant inelastic scattering method gives all modes that involve the motion of resonant nuclides.

Recently, this method has been actively performed in studies on the specific sites in large molecules such as metalloprotein samples involving thousands of other atoms. In these studies, the structure around a specific site of interest is investigated by comparing the obtained phonon energy spectrum with the vibrational spectrum obtained from density functional theory (DFT) calculations under the assumption of a feasible structural model. Using this methodology, which is sometimes called nuclear resonance vibrational spectroscopy (NRVS), many interesting studies have been performed at SPring-8 [e.g., 7-12]. This method is particularly effective for samples that cannot be crystallized, such as the intermediates in the catalytic cycles of enzymes, and a study on the structural characterization of the reactive Fe(IV)=O intermediate in the catalytic cycles of a mononuclear non-haem iron (NHFe) enzyme (the halogenase SyrB2 from the bacterium *Pseudomonas syringae* pv. *syringae*) has been performed [7]. This intermediate reacts through an initial hydrogen-atom abstraction step and performs subsequent halogenation of the native substrate or hydroxylation of non-native substrates and, therefore, it is essential and important to reveal the local structure and the mechanism. In this study, it was found that the orientation of the Fe(IV)=O intermediate depends on the substrate, presenting specific frontier molecular orbitals responsible for hydrogen-atom abstraction that can selectively lead to halogenation or hydroxylation.

Moreover, NRVS was applied to study the catalytic mechanism of hydrogenases, which catalyze the reversible conversion of molecular hydrogen to protons and electrons. Understanding the mechanism is significant because it is expected to lead to the development of clean energy sources producing hydrogen. NRVS was applied to an [FeFe]-hydrogenase variant lacking the amine proton shuttle, which stabilizes a putative hydride state [11]; [FeFe]-hydrogenases are metalloenzymes that reversibly reduce protons to molecular hydrogen with extremely high efficiency. NRVS spectra clearly showed the bending modes of the terminal Fe–H species, which were consistent with widely accepted models of the catalytic cycle.

3. Quasi-elastic Scattering Measurement Using Nuclear Resonant Scattering

The topics discussed thus far take full advantage of the properties of nuclear resonance excitation and, therefore, they are isotope-specific. Another important property is the ultranarrow bandwidth of the excited states (for example, a width of 4.7 neV for the first excited state of ^{57}Fe with an excited state energy of 14.4 keV). This unique property sheds light on the small energy shift of the microscopic region induced by quasi-elastic scattering measurement. Studies on the slow dynamics of glass-forming molecular liquids, alloys, ionic liquids, liquid crystal polymers, and biological molecules are possible using the property, and experimental studies have been performed at SPring-8 [e.g., 13,14].

In this method, the small energy broadening of a scattered γ-ray due to the motion of the atoms (molecules) is analyzed using reference absorbers containing the resonant nuclide. This method is known as the Rayleigh scattering of Mössbauer radiation (RSMR) method. Note that, in contrast to the previously discussed method, this method does not require a sample containing the resonant nuclide. A time-domain interferometry (TDI) method that uses the nuclear resonant scattering of synchrotron radiation is the time-domain analogue of the RSMR method. In the TDI method, the quasi-elastic broadening of nuclear resonant scattering in the energy domain can be observed as a relaxation in the time domain. A schematic of the experimental method of TDI measurement is shown in Fig. 4. To observe the relaxation, an interference pattern in the time domain is used; the pattern is formed by the interference between the nuclear resonant scattering of pulsed synchrotron radiation from the upstream nuclear absorber and that from the downstream nuclear absorber with resonance energy different from that of the upstream one. As shown in Fig. 5, if a suitable sample is placed between the absorbers, the interference pattern is perturbed by the energy broadening of the radiation from the upstream nuclear absorber caused by the

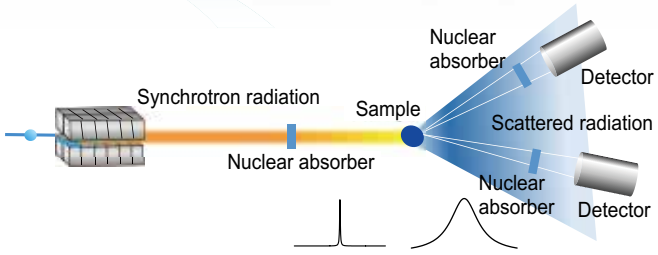

Fig. 4. Schematic of the TDI method. A sample is illuminated by synchrotron radiation transmitted through an upstream nuclear absorber, and the scattered radiation from the sample is transmitted through a downstream nuclear absorber. The nuclear absorbers contain the resonant nuclide such as ^{57}Fe. The time evolution of the transmitted radiation, reflecting the relaxation of molecules (ions) in the sample, is measured by a detector.

motion of the atoms in the sample. To analyze the change in the pattern from the non-perturbed one, we can obtain the relaxation of the atoms in the sample. The resolution of this method is typically on the order of neV; however, the line width of synchrotron radiation is on the order of eV and, therefore, most of the synchrotron radiation is not used even considering the energy broadening of μeV order. Although the efficiency of this method using synchrotron radiation is considerably higher than that with RI sources, it is not sufficient for measurement under special conditions such as at small angles. Recently, a multi-line TDI system was developed to improve the efficiency by increasing the number of nuclear absorbers with different resonance energies in order to use the unused part of the synchrotron radiation [15]. The developed multi-line TDI method allows us to obtain microscopic relaxation pictures much more rapidly and accurately than conventional single-line TDI.

Recently, using this method, a study on the slow dynamics of liquids with a mesoscopic structure and its relation to the shear viscosity was performed [13]. In this work, quasi-elastic scattering measurements were performed on a liquid higher alcohol, 3,7-dimethyl-1-octanol; the properties of liquids with mesoscopic structures have been attracting many researchers. The intermolecular correlation in simple liquids appears at the wavenumber corresponding to the contact distance as a peak of the static structure factor called the "main peak" and, in some liquids, an additional peak, called a "prepeak", is observed at a wavenumber lower than that of the main peak. The prepeak exhibits the presence of a characteristic mesoscopic structure with a spatial dimension much larger than the intermolecular contact distance. Using the developed method, the structural relaxation at the two wavenumbers of the prepeak and the main peak of the static structure factor was determined. This result indicates that the dynamics of a mesoscopic structure represented as the prepeak contributes to the shear viscosity through the slowest mode of the viscoelastic relaxation by comparison with the viscoelastic spectrum exhibiting bimodal relaxation.

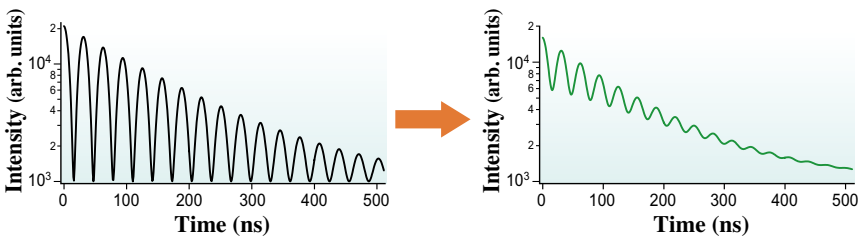

Fig. 5. The interference pattern without a sample (left) is perturbed by the energy broadening of the radiation from the upstream nuclear absorber caused by the motion of the atoms in the sample. A typical perturbed spectrum is shown on the right.

Summary

Recent nuclear resonant scattering studies at SPring-8 using advanced features such as element (isotope)-specific electronic states and an ultranarrow width were reviewed. The efficiency of the methods has been improved and will be further improved as a result of development. Moreover, more advanced methods such as depth-selective Mössbauer spectroscopy are expected to be realized. In addition to the reviewed work, many interesting studies have been performed and, in particular, important studies on fundamental physics have been performed [16,17]. The range of areas in which nuclear resonant scattering methods can be used is very wide, as discussed, and further important results are expected.

Makoto Seto

Institute for Integrated Radiation and Nuclear Science, Kyoto University

Email: seto@rri.kyoto-u.ac.jp

References

[1] M. Murakami *et al.*: Nat. Commun. **5** (2014) 5428.
[2] M. Seto *et al.*: Phys. Rev. Lett. **102** (2009) 217602.
[3] T. Matsuoka *et al.*: Phys. Rev. Lett. **107** (2011) 025501.
[4] R. Masuda *et al.*: Appl. Phys. Lett. **104** (2014) 082411.
[5] R. Masuda *et al.*: Sci. Rep. **6** (2016) 20861.
[6] L.B. Gee *et al.*: Inorg. Chem. **55** (2016) 6866.
[7] S. D. Wong *et al.*: Nature **499** (2013) 320.
[8] K. Park *et al.*: Proc. Natl. Acad. Sci. USA, **110** (2013) 6275.
[9] H. Ogata *et al.*: Nat. Commun. **6** (2015) 7890.
[10] K. Sutherlin *et al.*: J. Am. Chem. Soc. **138** (2016) 14294.
[11] E. J. Reijerse *et al.*: J. Am. Chem. Soc. **139** (2017) 4306.
[12] V. Pelmenschikov *et al.*: J. Am. Chem. Soc. **139** (2017) 16894.
[13] T. Yamaguchi *et al.*: J. Phys. Chem. Lett. **9** (2018) 298.
[14] T. Kanaya *et al.*: J. Chem. Phys. **140** (2014) 144906.
[15] M. Saito *et al.*: Sci. Rep. **7** (2017) 12558.
[16] A.I. Chumakov *et al.*: Nat. Phys. **14** (2017) 261.
[17] A. Yoshimi *et al.*: Phys. Rev. C **97** (2018) 024607.

A molecular movie of structural changes in the light-driven proton pump bacteriorhodopsin

Bacteriorhodopsin (bR) is a light-driven proton pump derived from *Halobacterium salinarum*. The protein harvests the energy content of light to drive conformational changes leading to unidirectional proton transport (Fig. 1(a)). The resulting proton concentration gradient is converted by adenosine triphosphate (ATP) synthase into ATP or is coupled to other transport processes.

bR comprises a seven-transmembrane helix and contains a buried all-*trans* retinal chromophore that is covalently bound to Lys216 (Fig. 1). The all-*trans* retinal undergoes isomerization to the 13-*cis* configuration by the absorption of light, which initiates a photocycle, accompanying a sequence of spectral and structural changes.

The primary proton transfer occurs between a protonated Schiff base and Asp85. In the resting-state bR structure, the protonated Schiff base and Asp85 form hydrogen-bond interactions with three water molecules and two amino acid residues as shown in Fig. 2(a). The hydrogen-bond network results in a difference of 11 orders of magnitude between the proton affinities of the primary donor and acceptor, which prevents the leakage of protons from the extracellular medium to the cytoplasm. After light excitation, these proton affinities approach each other to facilitate spontaneous proton exchange, but this raises the question of what brings the change of the proton affinities. It is also puzzling why it takes microseconds for the primary proton transfer to occur when the Schiff base and Asp85 are initially separated by only 4 Å and a water-mediated proton exchange pathway between the proton donor and acceptor is seen in the resting state. Moreover, protons are pumped from the cytoplasm to the extracellular side, yet retinal isomerization redirects the Schiff base proton away from the extracellular side and toward the cytoplasm.

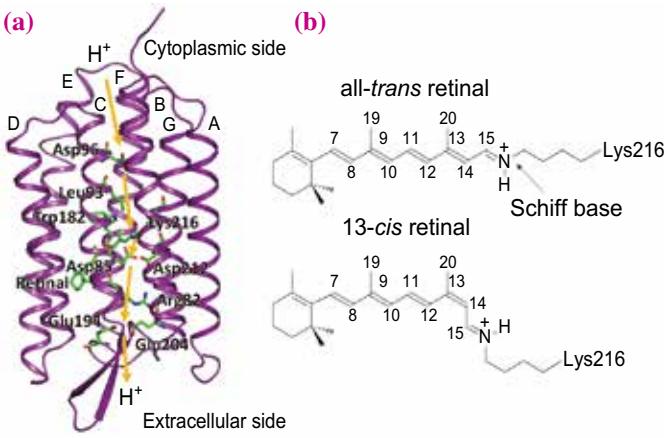

Fig. 1. Structure and function of bacteriorhodopsin (bR). **(a)** Proton-exchange steps (arrows) achieving proton pumping by bR. **(b)** Schematic illustrating retinal covalently bound to Lys216 through a protonated Schiff base in the retinal.

Considerable effort has been made to understand how structural changes in bR transport a proton uphill against a transmembrane potential. Many research groups have performed cryo-trapping experiments on bR using synchrotron radiation sources, providing information about structural changes during the photocycle. Despite these successes, there were certainly weaknesses in these experiments. Intermediate trapping studies were performed at a low temperature and thus were not truly time-dependent. Furthermore, conventional crystallography is subject to radiation damage and early results have been criticized for this reason.

We circumvent these concerns by recording a three-dimensional movie of structural changes in bR at room temperature with 2.1 Å resolution using time-resolved (TR) serial femtosecond crystallography (SFX) at SACLA **BL3**. The recent advent of intense femtosecond X-ray pulses from an X-ray free electron laser (XFEL) has enabled to acquire diffraction patterns from protein microcrystals before the onset of radiation damage. In SFX, microcrystals are continuously delivered with a solvent or a carrier media by an injector, allowing the observation of a damage-free structure at physiological temperature [1]. We used an optical-fiber-based setup for nanosecond pump-probe TR-SFX to visualize conformational changes in bR [2]. In TR-SFX, a continuous stream of microcrystals is injected across a focused XFEL beam, and the delay between sample photoactivation and the arrival of an XFEL pulse is controlled electronically.

TR-SFX data were collected from light-adapted bR microcrystals after photoactivation by a nanosecond laser pulse for $\Delta t = 16$ ns, 40 ns, 110 ns, 290 ns, 760 ns, 2 μs, 5.25 μs, 13.8 μs, 36.2 μs, 95.2 μs, 250 μs, 657 μs, and 1.725 ms. Our data revealed that the retinal is initially tilted in response to photoisomerization at $\Delta t = 16$ ns, and a water molecule (W402) is rapidly disordered by retinal isomerization (Fig. 2(b)). Low-temperature trapping studies have suggested that W402 disorders upon retinal photoisomerization [3], but this conclusion was challenged in light of similar

observations due to X-ray-induced radiation damage. Because no effects of radiation damage are visible when using <10 fs XFEL pulses at an X-ray dose of 12 MGy [4], these TR-SFX data bring closure to this debate.

Retinal isomerization reorients the Schiff base proton into a hydrophobic cavity while breaking its hydrogen bond to W402, both of which lower the proton affinity of the Schiff base. An initially twisted retinal becomes planar within 290 ns, causing Trp182 and Leu93 to be displaced toward the cytoplasm. These displacements allow a water molecule (W452) to order between Leu93, Thr89, and the Schiff base, which is observed for 40 ns ≤ Δt ≤ 13.8 μs but W452 disappears after a proton is transferred to Asp85 (Fig. 3(a)). Hydrogen-bond interactions from the protonated Schiff base to W452 or Thr89 create a pathway for proton transfer to Asp85 and explain how the Schiff base comes in contact with Asp85 despite having been turned toward the cytoplasmic side by photoisomerization.

On the extracellular side of the retinal, the disordering of W402 triggers the disordering of W400 and W401 and the ordering of a new water molecule, Wat451, between Asp85 and Asp212 from Δt≥13.8 μs (Fig. 3(b)). These water rearrangements allow that the extracellular portions of helix C bend toward helix G approximately 10 μs after photoactivation, which raises the p*Ka* of Asp85 to the point where it may spontaneously accept a proton from the Schiff base. Consequently, the time required for bR to evolve to a conformation with helix C bent toward helix G is the rate-limiting step that controls the primary proton transfer and explains why it takes microseconds for the Schiff base to be deprotonated.

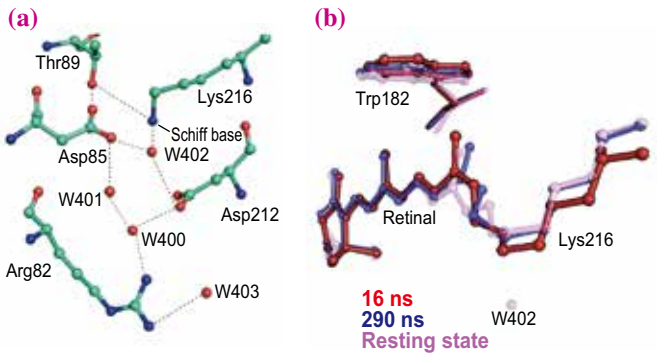

Fig. 2. Early structural changes in the bR photocycle. **(a)** Key amino acid residues and water molecules for the proton transfer in the resting conformation. **(b)** Crystallography models derived from partial-occupancy refinement for Δt = 16 ns (blue) and Δt = 290 ns (red) superimposed on the resting bR structure (purple, partially transparent).

Furthermore, we found that once a proton is transferred, the hydrogen-bond interaction between Asp85 and Thr89 is lost, which breaks the connectivity to the extracellular side of the protein, enabling unidirectional proton transport (Fig. 3(b)). The resulting cascade of structural changes throughout the protein provides an unprecedented insight into how structural changes in bR conspire to achieve unidirectional proton transport.

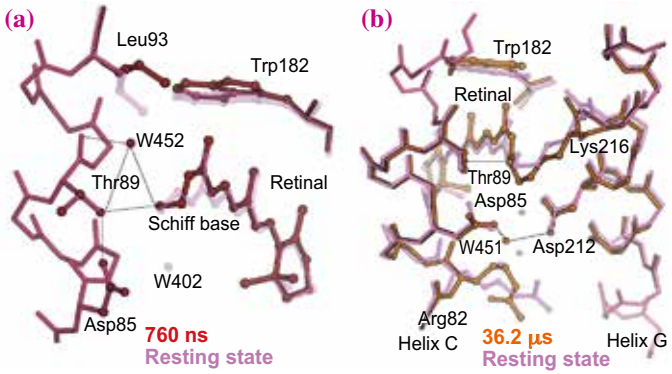

Fig. 3. Structural changes for Δt = 760 ns and Δt = 36.2 μs in the bR active site. **(a)** Crystallographic model for the time point Δt = 760 ns (red) superimposed upon the resting-state model (purple, partially transparent). **(b)** Crystallographic structural models derived from partial-occupancy refinement superimposed on the resting bR structure (purple, partially transparent) for Δt = 36.2 μs (orange).

Eriko Nango[a,b] and So Iwata[a,b,*]

[a] Department of Medical Chemistry and Cell Biology, Kyoto University Graduate School of Medicine
[b] RIKEN SPring-8 Center

*Email: s.iwata@mfour.med.kyoto-u.ac.jp

References

[1] H. Chapman *et al.*: Nature **470** (2011) 73.
[2] K. Minoru *et al.*: J. Synchrotron Rad. **24** (2017) 1086.
[3] K. Edman *et al.*: Nature **401** (1999) 822.
[4] K. Hirata *et al.*: Nat. Methods **11** (2014) 734.
[5] *E. Nango, A. Royant, M. Kubo, T. Nakane, C. Wickstrand, T. Kimura, T. Tanaka, K. Tono, C. Song, R. Tanaka, T. Arima, A. Yamashita, J. Kobayashi, T. Hosaka, E. Mizohata, P. Nogly, M. Sugahara, D. Nam, T. Nomura, T. Shimamura, D. Im, T. Fujiwara, Y. Yamanaka, B. Jeon, T. Nishizawa, K. Oda, M. Fukuda, R. Andersson, P. Bath, R. Dods, J. Davidsson, S. Matsuoka, S. Kawatake, M. Murata, O. Nureki, S. Owada, T. Kameshima, T. Hatsui, Y. Joti, G. Schertler, M. Yabashi, A. N. Bondar, J. Standfuss, R. Neutze and S. Iwata: Science **354** (2016) 1552.*

Nanosecond time-resolved XFEL structure analyses of bovine cytochrome c oxidase reveals the timing of proton-pump channel closure

Mitochondria occupy a substantial portion of the cytoplasmic volume of animal cells, and produce ATP used in a wide range of cellular processes. The mitochondrial ATPase synthesizes ATP using a transmembrane proton motive force, which is generated by respiratory enzymes. Cytochrome c oxidase (CcO), the terminal enzyme of cellular respiration, reduces O_2 to H_2O; this reaction is coupled to proton pumping across the mitochondrial inner membrane (Fig. 1(a)). Bovine CcO is a large transmembrane protein that exists as a 420-kDa dimer in the crystalline state. Each monomer includes four redox active metal sites (Fe_a, Fe_{a3}, Cu_B, and Cu_A). The O_2 reduction site contains Cu_B and Fe_{a3} (Fig. 1(b)). O_2 is transiently trapped at Cu_B before binding to Fe_{a3} [1-2]. Via Fe_a, four electrons are sequentially transferred from cytochrome c at the P-side to O_2 at Fe_{a3} (but not to O_2 at Cu_B), while four protons are actively transferred from the N-side (the P- and N-sides designate the outside and inside of the mitochondrial inner membrane, which are positively and negatively charged, respectively). The protons are transferred through the H-pathway, which consists of a water channel (light-blue arrows in Fig. 1) and a hydrogen bond network (red arrows in Fig. 1) operating in tandem. The water channel in the H-pathway includes water cavities.

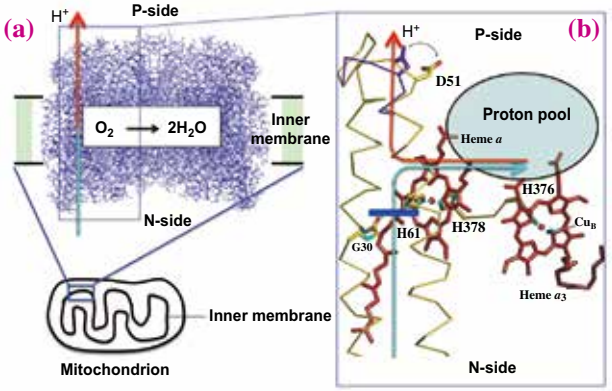

Fig. 1. Cytochrome c oxidase in the mitochondrial inner membrane. (Bottom **a**) Schematic drawing of a mitochondrion. (Top **a**) Structure of bovine CcO with dimeric structure. The enzyme reduces O_2 to H_2O using electrons from cytochrome c and pumps protons through the H-pathway (indicated by a light blue line and a red arrow from the N-side to P-side). (**b**) A close-up view of the H-pathway, proton pool, heme a, and O_2 reduction site consisting of heme a_3 and Cu_B. The H-pathway consists of a water channel (light-blue arrow) and a hydrogen bond network (red arrow). The blue line in the water channel is a gate operated by a conformational change in helix X. When the gate is opened, four protons accumulate in the proton pool. Pumping of each proton to the P-side is coupled with transfer of an electron from cytochrome c to heme a_3 via heme a.

The proton-pumping step is divided into two stages. First, four protons accumulate in the proton pool through the water channel of the H-pathway. As each electron is transferred from heme a to heme a_3, a proton is transferred from the proton pool to the P-side through the hydrogen bond network of the H-pathway, driven by electrostatic repulsion between the proton and the net positive charge of Fe_a. The water channel must be closed during electron transfer from heme a to heme a_3; if it were to remain open, spontaneous backflow of the collected protons would occur. To elucidate the channel closure mechanism, the opening of the channel, which occurs upon release of CO from CcO, has been investigated by newly developed time-resolved X-ray free-electron laser and infrared techniques with nanosecond time resolution [3]. CO has been widely used to probe the active sites of heme proteins.

In this project, we used a newly developed serial femtosecond rotational crystallography (SF-ROX) method [4] based on analysis of many large single crystals. Furthermore, we used time-resolved IR to monitor CO movements in CcO crystals.

Time-resolved infrared spectral changes occurring during CO migration in the single crystalline state of CcO were traced at 4°C from 20 ns to 500 ms after flash photolysis of the fully reduced CO-bound state. The spectral changes suggested that 100% of CO molecules moved from the Fe_{a3} site to the Cu_B site at 20 ns; about 76% of CO disappeared from the O_2 reduction center, and about 24% of CO remained at Cu_B at 100 μs, and 100% of CO returned to the Fe_{a3} site at 100 μs after photolysis.

The XFEL diffraction data obtained without pump laser irradiation (dark) and at 20 ns and 100 μs after pump laser irradiation were collected from 40, 24, and 43 crystals, respectively, all at 4°C. The experimental setup at SACLA EH4c/**BL3** was as described for a previous XFEL experiment for damage-free crystallography [4]. The structures of three states were determined: at 2.2 Å resolution for the dark and 100-μs crystals, and at 2.4 Å resolution for the 20-ns crystal. Refinements converged well to R_{work} = 0.173, 0.185, and 0.173, and R_{free} = 0.202, 0.229, and 0.208, for dark, 20-ns, and 100-μs crystals, respectively.

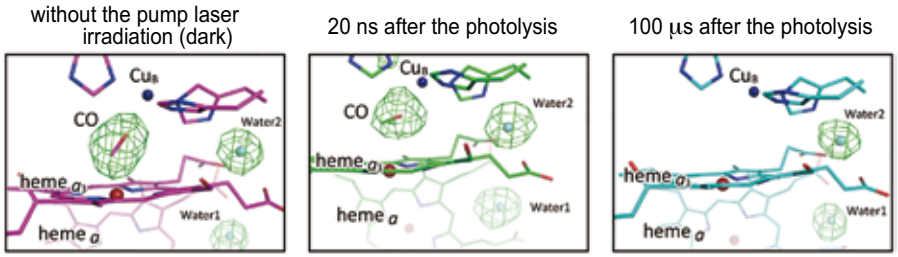

Fig. 2. Structures of the O_2 reduction sites of the CO-bound fully reduced state of the dark, 20-ns, and 100-μs structures. F_o-F_c difference electron density maps at 3.5σ and structural models. Purple spheres indicate iron ions, blue spheres copper ions, and light blue spheres the oxygen atoms of water molecules. Blue and red sticks indicate nitrogen and oxygen atoms, respectively. Purple, green, and light blue sticks indicate other atoms of dark, 20-ns, and 100-μs structures, respectively. CO, water 1, and water 2 were not included in the structural refinement. No significant electron density assignable to the CO molecule between Fe_{a3} and Cu_B is detectable in the 100-μs structure at the σ level depicted in the figure.

The CO molecules in the three states were located in the F_o-F_c difference maps (Fig. 2), and the structural changes of helix X are shown in the F_o-F_c difference map for two types of models (Fig. 3). These structural analyses indicated that the CO molecule moved from the Fe_{a3} site to the Cu_B site 20 ns after photolysis and disappeared from the O_2 reduction center 100 μs after photolysis. Moreover, the structures of helix X in the dark and 20-ns crystals were in a closed form that blocked proton transfer, whereas in the 100-μs crystal, helix X changed to an open conformation at a rate of 45% that opened a proton transfer gate of the water channel in the H-pathway. Thus, CO release from Cu_B to the outside of the O_2 reduction center drives the transition of the closed structure to the open structure.

Based on our inspection of structural features of hemes and helix X for all three states, we propose a mechanism for closure of the water channel. When the O_2 reduction site is in the fully reduced state, the water channel is opened, and protons are transferred from the N-side to the proton pool. Once O_2 is trapped at Cu_B, closure of the water channel is induced as follows: (i) The plane of Fe_{a3} migrates; (ii) van der Waals interactions are altered between the vinyl group of Fe_{a3} and L381 of the helix X; and (iii) a bulge forms at S382 when L381 moves to close the water channel. This process is followed by O_2 transfer to Fe_{a3} (1-2), yielding Fe_{a3}^{3+}-O_2^-, which readily extracts electrons from Fe_a when it is reduced. Oxidation of Fe_a induces electrostatic repulsion against protons in the storage site. The closure of the water channel after O_2 migration to Cu_B, before formation of the Fe_{a3}-O_2 bond, causes obligatory pumping of protons to the P-side because the water channel has been closed.

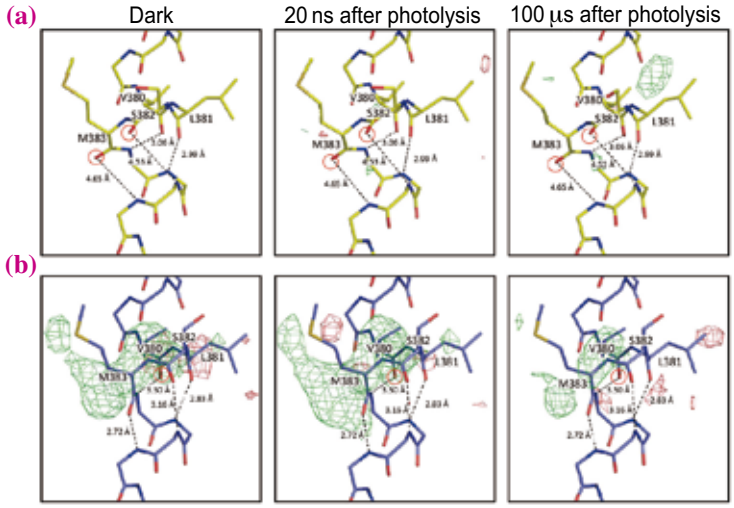

Fig. 3. F_o-F_c difference electron density maps of the dark, 20-ns, and 100-μs structures. The structural factors of Fc were calculated from the closed and open structures of helix X, with two bulges at S382 and M383 **(a)** and with one bulge at V380 **(b)**, and F_o-F_c difference electron density maps were drawn at 3.5σ along with the closed and open structures of helix X, respectively. Red circles mark the locations of the bulges.

Tomitake Tsukihara[a,b,*], Hideo Ago[c] and Shinya Yoshikawa[a]

[a] Graduate School of Life Science, University of Hyogo
[b] Institute for Protein Research, Osaka University
[c] RIKEN SPring-8 Center

*Email: tsuki@protein.osaka-u.ac.jp

References

[1] S. Yoshikawa *et al.*: Chem. Rev. **115** (2015) 1936.
[2] P.R. Rich and A. Maréchal: J. R. Soc. Interface **10** (2013) 20130183.
[3] *A. Shimada, M. Kubo, S. Baba, K. Yamashita, K. Hirata, G. Ueno, T. Nomura, T. Kimura, K. Shinzawa-Itoh, J. Baba, K. Hatano, Y. Eto, A. Miyamoto, H. Murakami, T. Kumasaka, S. Owada, K. Tono, M. Yabashi, Y. Yamaguchi, S. Yanagisawa, M. Sakaguchi T. Ogura, R. Komiya, J. Yan, E. Yamashita, M. Yamamoto, H. Ago, S. Yoshikawa, T. Tsukihara: Sci. Adv.* ***3*** *(2017) e1603042.*
[4] K. Hirata *et al.*: Nat. Methods **11** (2014) 734.

Protein-phospholipid interplay in a Ca^{2+}-pump revealed by X-ray solvent contrast modulation

It is well established that transmembrane helices of a membrane transport protein may rearrange substantially during the reaction cycle. In fact, some transmembrane helices in the Ca^{2+}-pump (Ca^{2+}-ATPase or SERCA1a) undergo large scale rearrangements [1], involving apparently perpendicular movements of 10 Å to the bilayer plane during the reaction cycle. If that occurs without bringing residues in/out of the bilayer, the bilayer has to be extremely flexible. Yet, in the other part of the reaction cycle, that is, in releasing bound Ca^{2+} to the lumen of the sarcoplasmic reticulum, a 100° rotation of the A domain is converted to the downward movement of the M4 helix, which requires that the bilayer does not largely deform [1]. Thus, the bilayer exhibits an apparently contradictory nature at different stages of the reaction cycle [2]. To resolve this problem we ought to visualize the lipid bilayer in the crystals of the Ca^{2+}-pump.

Our knowledge on the protein-phospholipid interaction (Fig. 1) was severely limited [3] because conventional X-ray crystallography failed to resolve phospholipids unless they are immobilized between protein molecules in the crystal lattice. This is because phospholipids are extremely mobile and contribute to only low resolution structure factors discarded in conventional crystallography, although the actual contribution of the bilayer exceeds that of protein at lower than 15 Å resolution [2]. This means that the phases obtained from protein atomic model cannot be correct and we ought to develop an experimental method for obtaining phases for such low resolution reflections.

By developing X-ray solvent contrast modulation and collecting diffraction data for all reflections from 170 to 3.2 Å resolution at SPring-8 **BL41XU** [2], we have succeeded in visualizing the entire first layer phospholipids (*ca.* 45 molecules) that surround the transmembrane region of the Ca^{2+}-pump crystallized in four different states and in refining the atomic models (Fig. 2 and Fig. 3). The atomic models were further examined by molecular dynamics simulations (Fig. 3(b)). Several key findings in this study are: (i) The bilayers are far from flat (Fig. 2(a)) and change their thickness (30.9–33.4 Å; Fig. 3), the number of the first layer phospholipids (44–48) and, accordingly, the cross-section of the transmembrane region of the protein during the reaction cycle. These differences will cause substantial changes in free energy and may work as driving forces to proceed the reaction. (ii) Phospholipids are anchored primarily by Arg/Lys-phosphate salt bridges (Fig. 1) and follow the movements of transmembrane helices, but they are less than half of the first layer phospholipids. There are apparently two classes in anchoring basic residues. The first one consists of those “snorkelling” from within the bilayer (Fig. 1 left). They cause local distortion of the bilayer when the transmembrane helices move (e.g. R63 and K262; Fig. 2(a)). Such distortion will act as a counter force to bring the transmembrane helices back to the most stable positions but may even be used as an energy source for rearranging them. (iii) The second class of basic residues (Fig. 1 right) extend their side chains through the cytoplasm to exploit phospholipids as “anchors” for conformational switching (e.g. R324

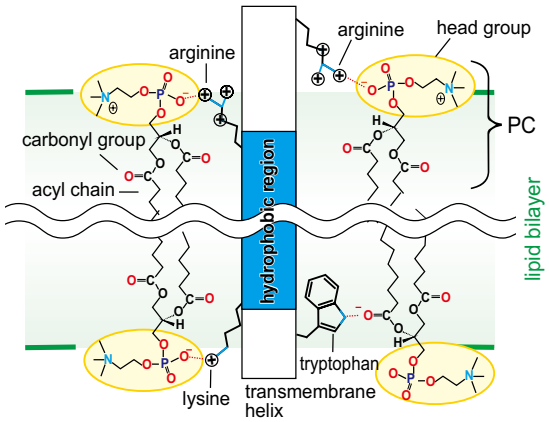

Fig. 1. Schematic illustration to show polar interactions between protein residues and phospholipids (phosphatidylcholine (PC) in this case) that constitute a lipid bilayer. The acyl chain of phospholipid varies between 14-20 carbon chain. The thickness of the bilayer can be affected by these residues, causing “protein-lipid mismatch” [3].

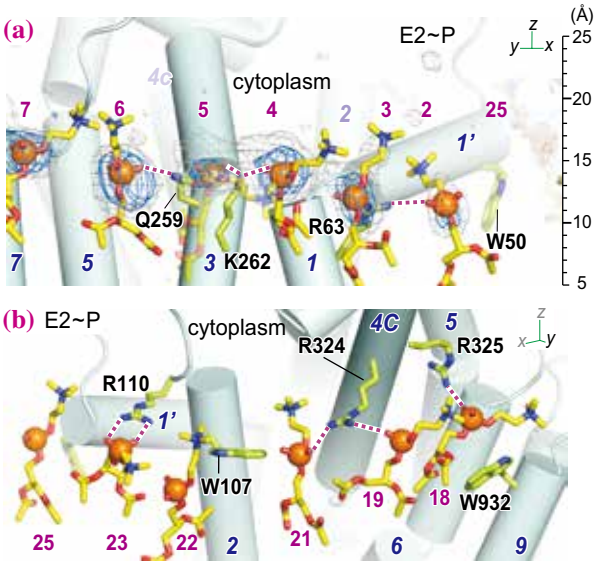

Fig. 2. First layer phospholipids that surround the transmembrane region of the Ca^{2+}-pump. Atomic models of phospholipids (from the head group to the carbonyl group of phosphatidylcholine; sticks with orange spheres for phosphorous atoms) are based on electron density maps derived from X-ray solvent contrast modulation. Blue and gray nets in **(a)** represent $2|Fo|-|Fc|$ electron density maps calculated at 3.2 Å resolution with combined phases and contoured at 0.7σ (gray) and 1.0σ (blue). Cylinders represent α-helices. Small numbers in purple identify phospholipids, and those in italics transmembrane helices (M1-M10). Purple broken lines represent likely hydrogen bonds. The ruler in the margin of **(a)** shows the distance from the bilayer center.

in Fig. 2(b)). (iv) The inclination of the entire protein changes during the reaction cycle (Fig. 3) governed primarily by a belt of Trp residues, acting as membrane "floats". Such change in inclination is a mechanism to allow large perpendicular movements of transmembrane helices.

Thus, we now see that phospholipids are a key component of calcium pump function and phospholipid-Arg/Lys and phospholipid-Trp interactions have distinct functional roles in the dynamics of ion pumps. We certainly expect similar protein-phospholipid interplay in other membrane proteins.

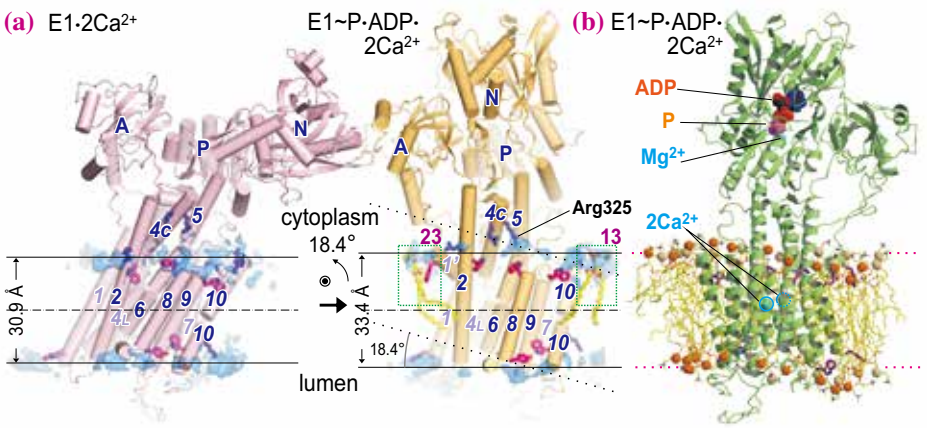

Fig. 3. **(a)** A change in orientation of the entire Ca^{2+}-pump molecule (18.4°) caused by the binding of ATP and transfer of the γ-phosphate to the pump protein. Placed so that the planes approximating the positions of the phosphorous atoms (horizontal solid lines) become horizontal in each crystal form. Inclined dotted lines show the corresponding planes in the conventional alignment with the M7-M10 helices, which do not undergo a rearrangement in the reaction cycle. Cyan surfaces show contrast modulation electron density maps for bilayers calculated at 4.5 Å resolution and contoured at 0.44 $e^{-}/Å^3$. Atomic models for a phospholipid molecule (PL23) around M1', an amphipathic helix, and that (PL13) near M10 in the cytoplasmic leaflet are shown in sticks (also boxed) in E1~P·ADP·$2Ca^{2+}$. **(b)** A full atomic model of the Ca^{2+}-pump and the first layer phospholipids after a 100 ns molecular dynamics simulation, viewed from the opposite direction to that in **(a)**. Orange spheres represent phosphorous atoms in the phospholipid head groups. The side chains of Arg/Lys and Trp/Tyr appear as dark blue and magenta sticks, respectively.

Chikashi Toyoshima* and Yoshiyuki Norimatsu

Institute of Molecular and Cellular Biosciences,
The University of Tokyo

*Email: ct@iam.u-tokyo.ac.jp

References

[1] C. Toyoshima: Biochim. Biophys. Acta **1793** (2009) 941.
[2] *Y. Norimatsu, K. Hasegawa, N. Shimizu and C. Toyoshima: Nature* ***545*** *(2017) 193.*
[3] J.A. Killian and G. von Heijne: Trends Biochem. Sci. **25** (2000) 429.

Structural biology study of human cannabinoid receptor CB1

Marijuana from *Cannabis sativa L.* has been used for both therapeutic and recreational purposes for many centuries. The active constituent Δ^9-tetrahydrocannabinol (THC) [1], exerts its psychotropic effects mainly through cannabinoid receptor 1 (CB1) [2], which is also the primary target of the endocannabinoids, anandamide (AEA) and 2-arachidonoyl glycerol (2-AG) [3] (Fig. 1). CB1 belongs to the class A G protein-coupled receptor (GPCR) family, signal through inhibitory $G\alpha_{i/o}$ heterotrimeric G proteins, and interact with β-arrestins (Fig. 1). Moreover, CB1 is the most highly expressed GPCR in the human brain and is expressed throughout the body, with the highest levels found in the central nervous system.

CB1-selective small-molecule agonists have shown therapeutic promise in a wide range of disorders, including pain and inflammation, multiple sclerosis, and neurodegenerative disorders. Antagonists of CB1 have been explored as potential therapeutics for obesity-related metabolic disorders, mental illness, liver fibrosis and nicotine addiction. The molecular details defining the binding modes of both endogenous and exogenous ligands are still unknown. In order to address this deficit in understanding, we have determined the crystal structures of CB1 in complex with antagonist [4] and agonist [5]. The structures provide very important molecular basis of how ligands engage to modulate the cannabinoid system and reveal important insights into the activation mechanism of CB1.

Crystallization of GPCRs, especially active (active-like) –state, has been challenging due to their inherent conformational flexibility and biochemical instability. To facilitate crystallization, Flavodoxin was identified as a stabilizing fusion partner and the receptor was truncated on both the N and C termini by 98 and 58 residues, respectively. In order to further improve the expression and thermostability, four computationally and rationally designed mutations were introduced to the CB1 sequence. Fortunately, the modified CB1 construct has comparable affinity for both antagonists and agonists as the wild-type receptor. Finally, we obtained the crystals of CB1 in complex with antagonist AM6538 and agonist AM11542, respectively (Fig. 2). The diffraction datasets were collected at the SPring-8 **BL41XU**, GM/CA-CAT beamline 23ID-B of APS and beamline X06SA of Swiss Light Source.

The overall CB1 contains seven transmembrane (7TM) α-helices (I to VII) connected by three extracellular loops (ECL1-3), three intracellular loops (ICL1-3), and an amphipathic helix VIII. The antagonist AM6538 binds quite deep in the binding pocket and adopts an extended conformation (Fig. 2). The agonist AM11542 adopts an L-shape conformation in the orthosteric-binding pocket, which is much smaller than the more expanded binding domain of AM6538 (Fig. 2 and Fig. 3(c)). Both the AM6538 and AM11542 are forming mainly hydrophobic interactions with the receptor.

Comparisons between the agonist- and antagonist-bound CB1 reveal significant structural rearrangements

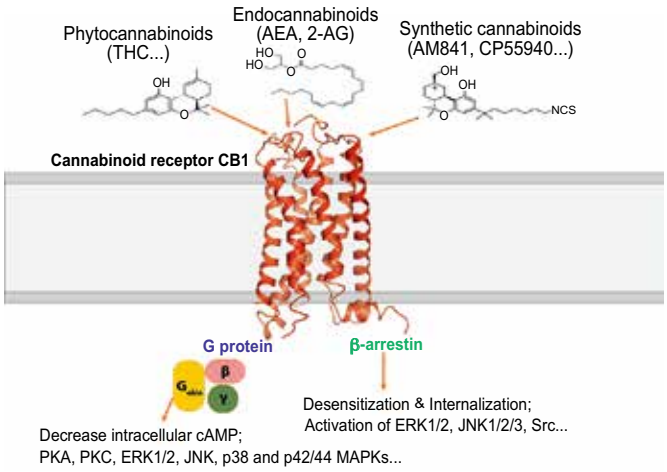

Fig. 1. Schematic representation of CB1-mediated signaling pathways. CB1 can be activated by phytocannabinoids, endocannabinoids and synthetic cannabinoids and induce the G protein or β-arrestin activation pathways.

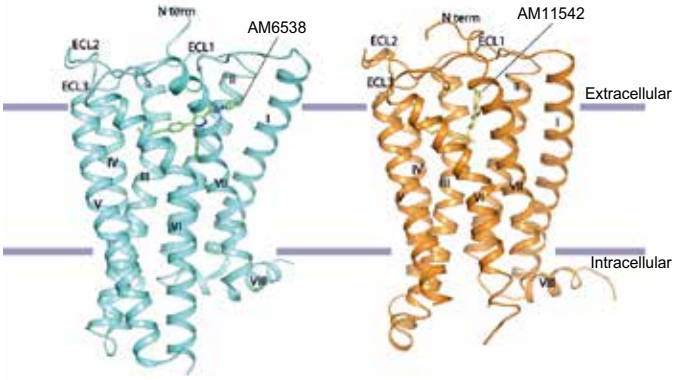

Fig. 2. The overall structures of antagonist- and agonist-bound CB1. The antagonist AM6538 (green sticks) bound CB1 structure and agonist AM11542 (yellow sticks) bound CB1 structure is shown in cyan and orange cartoon, respectively.

(C_α r.m.s.d. of the overall structure without fusion protein: 3.52 Å). The notable conformational change occurs in helices I and II. The extracellular part of helix I bends inwards by 6.6 Å and helix II rotates in by about 6.8 Å, respectively in the AM11542-bound structure (Fig. 3(a)). Similarly, conformational changes are also observed in the cytoplasmic part of the receptor, in which helix VI moves outwards by about 8 Å (Fig. 3(b)). This is the largest structural change, especially within the extracellular portion, observed in the solved agonist/antagonist-bound pairs of class A GPCRs.

The agonist-induced conformational changes probably trigger the activation and downstream signaling. CB1 seems to use an extended molecular toggle switch involving a synergistic conformational change between Phe200$^{3.36}$ and Trp356$^{6.38}$, which we refer to as the 'twin toggle switch' (Fig. 3(d)). Comparing previously proposed 'toggle switch' of Trp356$^{6.38}$, the synergistic movement of two residues during the activation of the receptor has never been observed before and we speculate that this 'twin toggle switch' is related to CB1 activation.

A notable feature of the CB1 agonist-bound structure is the large (53%) reduction in volume in the ligand-binding pocket. Such plasticity in the orthosteric binding pocket enables CB1 to respond to a diverse array of ligands with considerably different sizes, shapes and associated functions, consistent with the repertoire of CB1 to modulate such variety of physiological and psychological activities (Fig. 1).

In summary, the current study reported the first crystal structure of antagonist-bound CB1 and also the agonist-bound CB1, which reveal the inactive and active-like states of the receptor and provide important structural insights to the activation mechanism of the receptor. In most agonist- and antagonist-bound structural pairs of class A GPCRs, the extracellular half shows small changes while larger conformational changes in the intracellular half. As an exception, CB1 has the largest ligand-binding pocket volume change, contributed mainly by the movements of the extracellular half of helices I and II. The balloon-like flexibility of CB1 in the extracellular region may also occur in other GPCRs. Therefore, in designing GPCR agonists or antagonists using structure-based strategies, multiple, structurally varied receptor models should be considered.

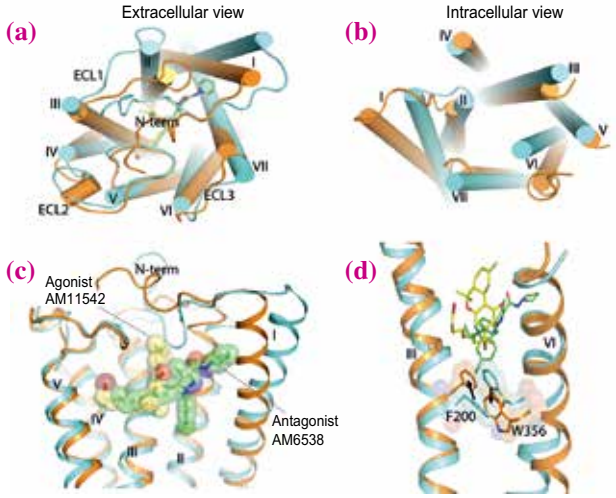

Fig. 3. Comparison of agonist- and antagonist-bound CB1 structures. The extracellular **(a)** and intracellular **(b)** views of the compared receptors. **(c)** Comparison of agonist-bound (orange cartoon) and antagonist-bound (cyan cartoon) CB1 ligand-binding pockets. AM11542 (yellow) and AM6538 (green) are shown in sticks and sphere representations. **(d)** The 'twin toggle switch', F200/W356, is shown in sticks and spheres.

Tian Hua and Zhijie Liu*

iHuman Institute, ShanghaiTech University

*Email: liuzhj@shanghaitech.edu.cn

References

[1] Y. Gaoni and R. Mechoulam: J. Am. Chem. Soc. **86** (1964) 1646.
[2] L.A. Matsuda *et al.*: Nature **346** (1990) 561.
[3] R. Mechoulam *et al.*: Endocannabinoids. Eur. J. Pharmacol. **359** (1998) 1.
[4] T. Hua *et al.*: Cell **167** (2016) 750.
[5] *T. Hua, K. Vemuri, S.P. Nikas, R.B. Laprairie, Y. Wu, L. Qu, M. Pu, A. Korde, S. Jiang, J.-H. Ho, G.W. Han, K. Ding, X. Li, H. Liu, M.A. Hanson, S. Zhao, L.M. Bohn, A. Makriyannis, R.C. Stevens & Z.-J. Liu: Nature* ***547*** *(2017) 468.*

Crystal structure of overlapping dinucleosome reconstituted with human histones

In eukaryotes, genomic DNA is folded into an ordered architecture called chromatin in the nucleus. Nucleosomes are the basic structure of chromatin, in which short linker DNA segments connect the nucleosomes giving a "beads-on-a-string" appearance [1]. The nucleosome formation suppresses genome functions, such as transcription, repair, recombination, and replication, by limiting the DNA binding of proteins. Therefore, the nucleosomes must be remodeled by sliding and repositioning along DNA when the genomic DNA functions. The nucleosome remodeling process is spontaneously or enzymatically promoted and, consequently, collision occurs between neighboring nucleosomes. Interestingly, the nucleosome collision promotes formation of an unusual nucleosome structure called overlapping dinucleosome [2,3], however, the structure of overlapping dinucleosome has not yet been determined.

To reveal the structure of overlapping dinucleosome, we reconstituted overlapping dinucleosome with a 250-base-pair DNA containing a tandem repeat of the Widom 601 sequence, which is known as a strong nucleosome positioning sequence [3]. The overlapping dinucleosome was then successfully reconstituted with human histones H2A, H2B, H3.1, and H4. The resulting overlapping dinucleosome was dialyzed against 10 mM Tris-HCl buffer (pH 7.5) containing 1 mM dithiothreitol, 1 mM EDTA, and 0.25 M KCl, and was heated at 55°C for 2 h to remove improperly reconstituted molecules. The remaining overlapping dinucleosome was purified by electrophoresis with a native polyacrylamide gel. The purified overlapping dinucleosome was dialyzed against potassium cacodylate buffer (pH 6.0) containing 1 mM EDTA, and was crystallized by the sitting-drop vapor diffusion method at 20°C. For crystallization, the purified overlapping dinucleosome (13.6 mg/ml) was mixed with an equal volume of reservoir solution containing 50 mM Tris-HCl buffer (pH 7.8), 100 mM potassium bromide, 100 mM potassium thiocyanate, 1.5% PGA-LM (Molecular Dimensions), and 12% PEG 400. The crystal was soaked in a cryoprotectant solution containing 50 mM Tris-HCl buffer (pH 7.8), 100 mM potassium bromide, 100 mM potassium thiocyanate, 1.5% PGA-LM, and 35% PEG 400, and flash-cooled in liquid nitrogen.

The crystal structure of the overlapping dinucleosome was determined at 3.14 Å resolution [4]. The overlapping dinucleosome crystal belonged to the space group *P*1 with unit cell dimensions a = 90.58 Å, b = 101.80 Å, c = 102.43 Å, α = 119.30°, β = 106.51°, γ = 91.36°. In the crystal, one overlapping dinucleosome was present in the asymmetric unit. Diffraction data were collected at SPring-8 **BL41XU** at a wavelength of 1.00 Å. The overlapping dinucleosome structure was solved by the molecular replacement method. To achieve this, the human nucleosome structure (PDB ID: 3AFA) and the hexasome model structure, in which one H2A-H2B dimer was removed from the nucleosome structure, were used as guides. According to Ramachandran plots of the final structure, 96.8% and 3.2% of the residues appear in the favored regions and in the allowed regions, respectively.

In the crystal structure of the overlapping dinucleosome, the 250-base-pair DNA is continuously wrapped three turns around the histone octamer and hexamer without an obvious linker DNA segment between them (Fig. 1). In the histone hexamer moiety, one H2A-H2B dimer is maintained at the surface opposite the hexasome-octasome interface (Fig. 2). In the canonical nucleosome, acidic patches are created by the H2A-H2B dimer on both nucleosomal

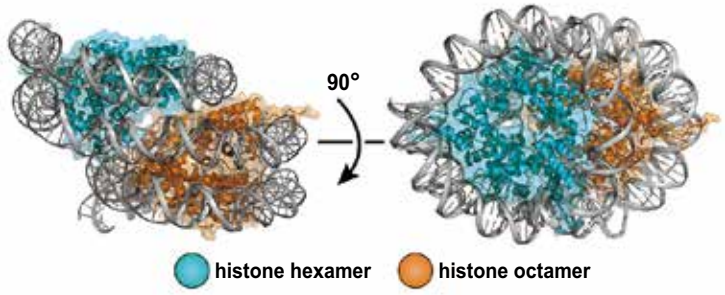

Fig. 1. Crystal structure of the overlapping dinucleosome. The histone hexamer and octamer moieties in the overlapping dinucleosome are colored in light blue and orange, respectively.

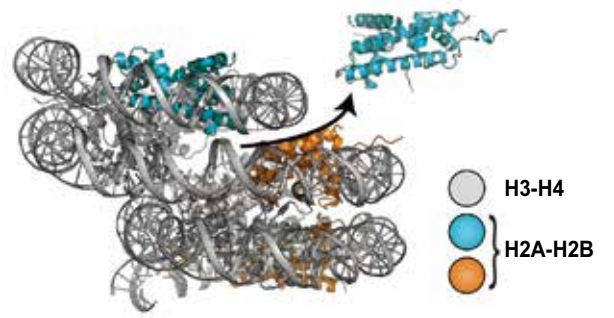

Fig. 2. Location of the region missing a H2A-H2B dimer. The missing H2A-H2B dimer and the H2A-H2B dimer in the hexasome moiety are shown in light blue, and the H2A-H2B dimers in the octasome moiety are shown in orange.

surfaces. In the overlapping dinucleosome, one of the acidic patches is missing in the hexasome moiety at the hexasome-octasome interface, and one of the octasome acidic patches is concealed by the interaction with the hexasome. Consistently, an acidic patch binding protein, such as RCC1, binds to the overlapping dinucleosome with a significantly reduced rate as compared with the canonical nucleosome [4]. Therefore, the overlapping dinucleosome formation may function to down-regulate the nucleosome binding proteins.

The missing H2A-H2B dimer also induces the shortening of the hexasomal H3 αN-helix located at the hexasome-octasome interface of the overlapping dinucleosome (Fig. 3). On the other hand, the other three H3 αN-helices of the overlapping dinucleosome are the same as those found in the canonical nucleosome. On the hexasome-octasome interface, the H3 Lys56 and H3 Thr80 residues of the hexasome may interact with the DNA backbone of the octasome. In addition, the H2A Asn68, H2A Arg71, H2B Lys108, H2B Ser112, and H2B Lys116 residues of the octasome may interact with the DNA backbone of the hexasome. These residues are not located near the DNA in the canonical nucleosome. Therefore, these residues may have roles in the formation and determination of the physical properties of the overlapping dinucleosome. In particular, the H3 Lys56 residue is intriguing because it is known to be an acetylation site within the canonical nucleosome.

In the present study, we revealed the first unusual nucleosome structure, the overlapping dinucleosome structure. In the overlapping dinucleosome structure, the 250-base-pair DNA was protected from micrococcal nuclease (MNase), which preferentially cleaves the histone-free DNA region. We then found that the MNase-resisting 250-base-pair DNA fragments could be mapped at the downstream (+1) regions of transcription start sites of the human genome [4]. This finding suggested that the overlapping dinucleosome may function to regulate gene expression in the human genome. Therefore, it will be interesting to see whether the overlapping dinucleosome formation correlates with transcription levels in the genome.

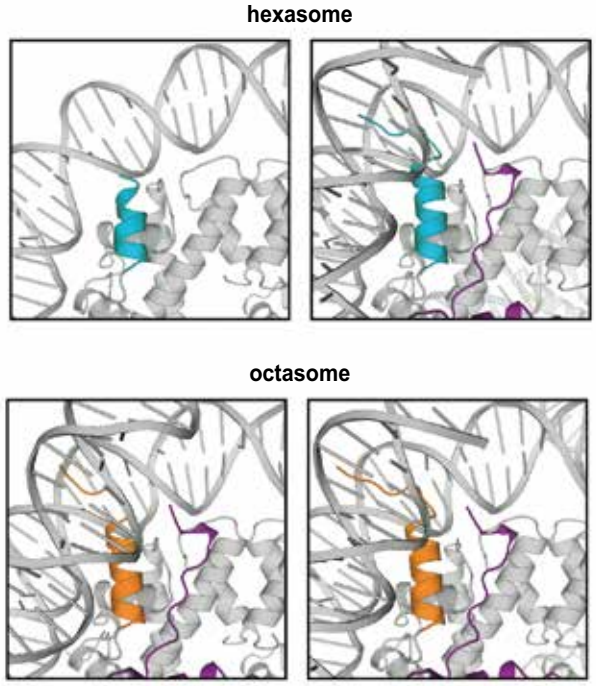

Fig. 3. Close-up view of the H3 αN-helices. The H3 αN-helices in the hexasome and octasome moieties are colored in light blue and orange, respectively. The H2A molecules are shown in purple.

Hitoshi Kurumizaka*, Daiki Kato and Akihisa Osakabe

Laboratory of Structural Biology, Waseda University

*Email: kurumizaka@waseda.jp

References

[1] A. Wolffe: Chromatin: Structure and Function. 3rd Ed., Academic Press, San Diego (1998).
[2] N.P. Ulyanova, G.R. Schnitzler: Mol. Cell. Biol. **25** (2005) 11156.
[3] M. Engeholm *et al.*: Nat. Struct. Mol. Biol. **16** (2009) 151.
[4] *D. Kato, A. Osakabe, Y. Arimura, Y. Mizukami, N. Horikoshi, K. Saikusa, S. Akashi, Y. Nishimura, S.-Y. Park, J. Nogami, K. Maehara, Y. Ohkawa, A. Matsumoto, H. Kono, R. Inoue, M. Sugiyama and H. Kurumizaka: Science* ***356*** *(2017) 205.*

Crystal structures of the NAD$^+$-reducing soluble [NiFe]-hydrogenase

Hydrogenases catalyze the synthesis and decomposition of molecular hydrogen ($2H^+ + 2e^- \leftrightarrow H_2$). The enzymes are classified into three types based on the metal composition of the active site: Ni–Fe, Fe–Fe, and Fe types. Of these, [NiFe]-hydrogenases comprise the widest variety of members regarding their physiological function, whereas the hydrogenase unit, consisting of large and small subunits, is highly conserved among the members, and the peripheral unit and cellular localization mainly determine their functions. It has been proposed that the physiological function of the NAD$^+$-reducing soluble [NiFe]-hydrogenase (SH), a member of the group III [NiFe]-hydrogenase, is the consumption of the excess amount of reducing equivalents by coupling the oxidation of NADH and the synthesis of H_2 (Fig. 1(a)) [1]. While SH from some organisms contains auxiliary subunit(s), the core of the enzyme complex is conserved as a heterotetrameric complex consisting of the diaphorase unit (HoxFU subcomplex) and hydrogenase unit (HoxYH subcomplex). Amino acid sequence analyses have indicated that the four subunits are evolutionally related to those of NADH:quinone oxidoreductase (complex I), which is responsible for the first step of the respiratory chain by coupling the oxidation of NADH and the reduction of quinone species (Fig. 1(b)) [2]. As with complex I, SH functions in organisms that grow under oxic environments. It has been widely accepted that the active sites of the hydrogenases are highly sensitive to O_2 and that some mechanism is required to protect SH from O_2 attack. In order to obtain insights into the O_2 protection mechanism and molecular evolutional relationship between SH and complex I, we have determined the X-ray crystal structures of SH [3].

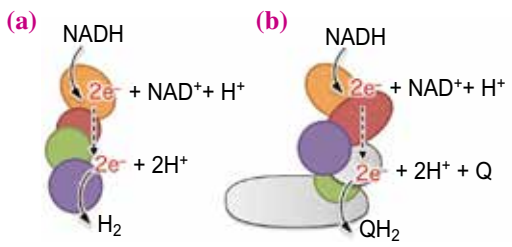

Fig. 1. Physiological reactions catalyzed by SH **(a)** and complex I **(b)**. "Q" represents quinone species. Homologous subunits are shown in the same color. It has been proposed that complex I mechanically couples the quinone reduction and proton pumping, which is omitted in (b).

SH was extracted and purified from *Hydrogenophilus thermoluteolus* TH-1, a thermophilic H_2-oxidizing bacterium, without any genetic manipulation [4]. The purification and crystallization were performed under aerobic conditions, and the crystals of the as-purified sample were termed the air-oxidized state and those soaked in a buffer containing 1 mM benzyl viologen (BV) and saturated H_2 at 0.1 MPa for 24 h at 293 K were termed the H_2-reduced state. During the soaking, the reduction of BV and the oxidation of H_2 by SH occurred, as indicated by the blue color of the reduced BV around the crystals. X-ray diffraction experiments were performed at SPring-8 beamlines **BL32XU**, **BL38B1**, **BL41XU**, and **BL44XU**. The final sets of data of the air-oxidized and H_2-reduced states were collected at BL44XU. The initial phases were calculated using single anomalous dispersion signals from the intrinsic iron and nickel atoms in SH, and the structure models for the air-oxidized and H_2-reduced states were refined to 2.58 and 2.70 Å resolution, respectively.

The overall structure shows a heterotetrameric architecture (Fig. 2(a)) consisting of the diaphorase HoxFU (~90 kDa) and hydrogenase HoxHY (~73 kDa) subcomplexes, sharing a shape-complementary interaction with an interface area of 2084 Å^2, which shares 4.4% of the total surface of the heterotetramer. As predicted from the amino acid sequence analyses [2], each subunit has a structural similarity to that of complex I. HoxF (residues 165–438), HoxU, HoxY, and HoxH are superposed on Nqo1, Nqo3, Nqo6, and Nqo4 of complex I from *Thermus thermophilus* HB8 (*Tt*-complex I) [5] with root mean square deviation (r.m.s.d.) values of 1.6, 2.1, 2.6, and 2.3 Å for 256, 174, 83, and 228 Cα atoms, respectively. In addition, the N-terminal part of HoxF (9–127) is superposed on Nqo2 with an r.m.s.d. of 1.8 Å for 115 Cα residues, revealing that HoxF has evolved as a fusion protein of Nqo1 and Nqo2. In contrast to the structural similarities between SH and complex I at the tertiary structure level, the superposition of the tetrameric SH complex on complex I requires a considerable rigid body movement of either subcomplex (Figs. 2(a) and 2(b)). Superposition of the Nqo1•2•3 subcomplex of *Tt*-complex I on the HoxFU subcomplex of SH revealed that the species of Fe–S clusters and their positions are highly conserved except for N1a [2Fe–2S] and N7 [4Fe–4S] clusters, which are inherently absent in SH and located at off-line positions of the electron-transfer pathway in *Tt*-complex I, implying

that SH has a minimum set of Fe–S clusters for the electron transfer. The different orientations of subcomplexes supports the hypothesis that the hydrogenase and Nqo4•6 subcomplexes diverged at some point of the molecular evolutional process and independently acquired the diaphorase subcomplex, which was assembled into each energy metabolism machinery.

One of the most prominent structural differences between air-oxidized and H_2-reduced states was observed at the Ni–Fe active site. The coordination geometry of the Ni–Fe cluster of the air-oxidized state with no precedent in nature showed that the carboxy group of Glu32 binds six-coordinate Ni as a bidentate ligand (Fig. 3), which is in contrast to the previously reported Ni–Fe clusters consisting of five-coordinate Ni without binding of the carboxy group. On the other hand, the Ni–Fe active site of the H_2-reduced state has a regular coordination geometry (Fig. 3). Electron paramagnetic resonance spectroscopic analyses detected signals of the oxidized state attributable to Ni(III) that do not match those identified for the oxidized states of [NiFe]-hydrogenases, implying that the distinct configuration of the Ni–Fe active site of the oxidized SH is not an artifact caused by the crystallization or X-ray exposure during the diffraction data collection. On the basis of the structure comparison between the air-oxidized and H_2-reduced states, we assume that the redox-dependent conformational change is induced by the reduction and oxidation of the proximal Y1 [4Fe–4S] cluster. When the Y1 cluster maintains the oxidized $[4Fe–4S]^{2+}$ state for a certain time period, the guanidinium group of Arg58 moves away from the Fe–S cluster owing to electrostatic repulsion. The displacement of Arg58 is transferred to Glu32 via the hydrogen-bond network, resulting in the coordination of Glu32 to Ni (Fig. 3). The Ni–Fe active site in the air-oxidized form appears to be highly resistant against O_2 attack because of the formation of the six-coordinate Ni complex. This finding suggests that the proximal Fe–S cluster functions not only as a component of the electron-transfer pathway but also as an oxidative stress sensor to protect the Ni–Fe active site from O_2.

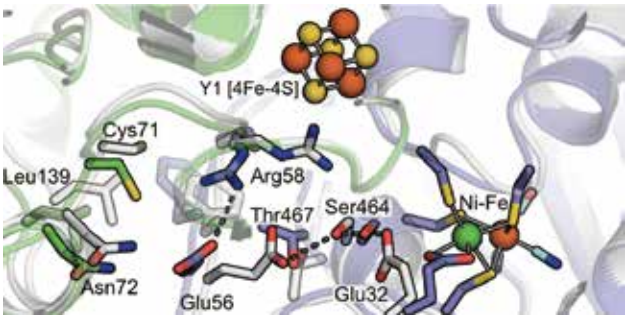

Fig. 3. Structure comparison of SH in the air-oxidized and H_2-reduced states. The air-oxidized state is shown in the same colors as in Fig. 2, and the H_2-reduced state is shown in white. For clarity, the Ni–Fe active site and Y1 cluster are shown only for the air-oxidized state.

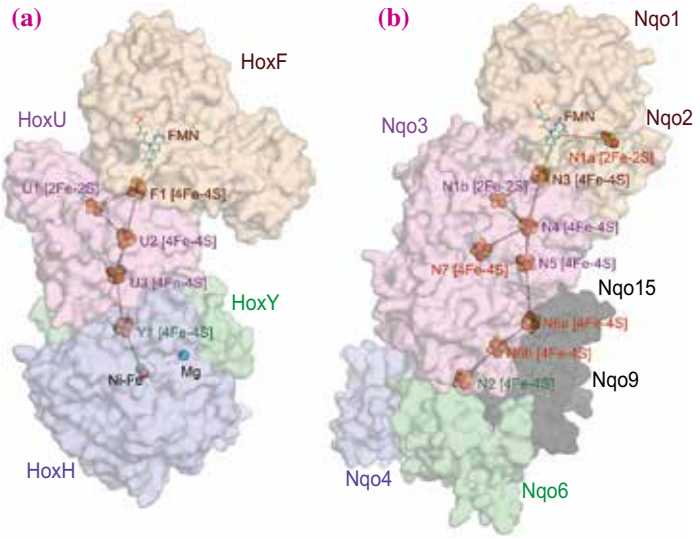

Fig. 2. Structure comparison of SH **(a)** and soluble part of *Tt*-complex I **(b)**. Surface representations of the protein molecules and sphere/stick models of the redox centers are shown. Homologous subunits are represented in the same color. The Fe–S clusters in red characters in (b) are not found in SH.

Yasuhito Shomura[a,*] and Yoshiki Higuchi[b,c]

[a] Institute of Quantum Beam Science, Ibaraki University
[b] Department of Picobiology, University of Hyogo
[c] JST/CREST

*Email: yasuhito.shomura.s@vc.ibaraki.ac.jp

References

[1] K. Schneider *et al.*: Biochim. Biophys. Acta - Enzymol. **452** (1976) 66.
[2] R. Böhm *et al.*: Mol. Microbiol. **4** (1990) 231.
[3] *Y. Shomura, M. Taketa, H. Nakashima, H. Tai, H. Nakagawa, Y. Ikeda, M. Ishii, Y. Igarashi, H. Nishihara, K-S. Yoon, S. Ogo, S. Hirota, Y. Higuchi: Science* ***357*** *(2017) 928.*
[4] M. Taketa *et al.*: Acta Crystallog. Sect. F **71** (2015) 96.
[5] R. Baradaran *et al.*: Nature **494** (2013) 443.

Multi-wavelength anomalous diffraction *de novo* phasing of serial femtosecond crystallography data using two-color pulses at SACLA

Serial femtosecond crystallography (SFX) at XFELs offers unprecedented possibilities for macromolecular structure determination of systems prone to radiation damage. However, *de novo* structure determination, i.e. without prior structural knowledge, is complicated by the inherent inaccuracy of SFX data. By its very nature, SFX data collection entails shot-to-shot fluctuations in X-ray wavelength and intensity as well as variations in crystal size and quality that must be averaged out. Hence, to obtain accurate diffraction intensities for *de novo* phasing, very large numbers of diffraction patterns are required — the multiplicity of measurements for a given reflection being typically several 100- to 1000-fold depending on the phasing method and signal strength — and, concomitantly large amounts of sample and long XFEL beamtimes. Since both are typically precious and often limited, improved use of one or both is essential to future evolution of XFEL-based structural biology.

The recently established two-color operation of SACLA [1] opened up a novel possibility of collecting two SFX datasets simultaneously, without doubling the amount of sample used. Due to the unprecedentedly large energy separation of the two tunable colors of the XFEL beam [1], two distinct and spatially well separated diffraction patterns can be recorded simultaneously on one diffraction image of the same crystal. The simultaneous arrival of the two XFEL pulses precludes damage effects from the first pulse affecting the diffraction of the second pulse. This allows simultaneous same-crystal acquisition of two-wavelength datasets for multiple wavelength anomalous dispersion (MAD) phasing. (This is in marked contrast to data collection at synchrotron sources where they are typically collected sequentially.)

In principle, given the availability of more information, MAD phase angles are expected to be more accurate than those from single wavelength anomalous dispersion (SAD) experiments. To explore whether this can be put to use for XFEL-based *de novo* phasing with the added benefit of halved sample consumption and beamtime, we performed a two-color SFX experiment at SACLA **BL3**. We used microcrystals of the well-established model system lysozyme, in complex with a lanthanide compound and collected SFX diffraction data in the DAPHNIS chamber using a multiport charge coupled device (MPCCD) detector (see Fig. 1). SACLA operated at

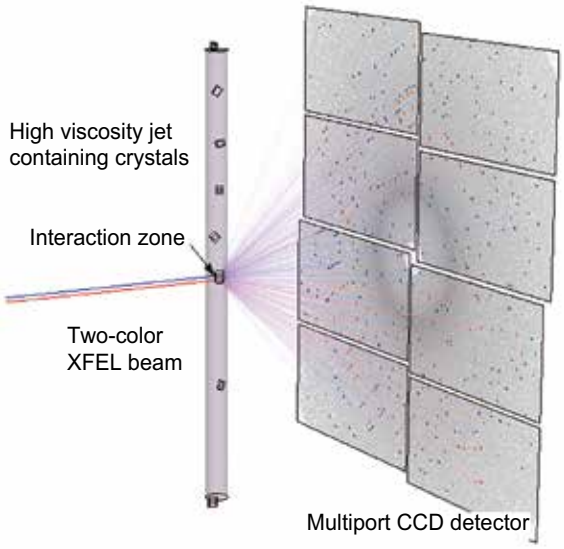

Fig. 1. Two-color serial femtosecond crystallography experiment. Experimental setup.

30 Hz and simultaneously delivered two-color X-ray pulses of nominally 7.0 keV and 9.0 keV photon energy, which are above the *M*- and *L*-edges of gadolinium, respectively. We collected 570,000 diffraction patterns in ~12 hours. Online data analysis was performed with CASS [2] and the Graphic User Interface to the offline data processing pipeline Cheetah Dispatcher was used to identify 208,373 hits (37% hit rate). A wide range inline spectrometer was used to simultaneously record the spectral information for the 7 keV and 9 keV colors for each XFEL pulse.

The analysis of two-color SFX data is not straightforward. In fact, direct processing with CrystFEL [3] was unsuccessful, since only a minute fraction of the hits could be indexed in both colors. Despite aiming for similar pulse energies for the two colors and compensating for the difference in detector quantum efficiency by inserting an aluminium filter, the intensity distribution of the two patterns in the diffraction image varied. One diffraction pattern typically dominated and could be indexed in one color, but indexing of the weaker second diffraction pattern in the other color typically failed. To index the weaker diffraction pattern, the threshold for identifying peaks had to be lowered and the previously indexed peaks were eliminated

from the list of all identified peaks. Using this approach we successfully indexed and integrated 11.1 % of the hits in both colors (Fig. 2). Phases were determined automatically using data to 1.9 Å resolution (Fig. 3).

We deliberately used a model system with an unusually strong anomalous signal. In spite of this we see a significant increase in the data information content of the two-color data used for MAD phasing, as evidenced by the higher figure of merit indicating more accurate initial phases, and easier model building compared to the single color data SAD phasing approach [4]. This difference is particularly striking at 5000 images, which is a comparatively low number for SFX data collection. Hence, these diffraction intensities are of lower precision than those derived from a larger number of images, as evidenced by the data statistics. At 5000 images, the first round of automated building essentially failed in the SAD case, whereas in the MAD case most of the structure was built. It has been suggested that for suboptimal data, density modification might more easily improve even inaccurate phases provided by MAD, which are unimodal, rather than SAD phases which are additionally compromised by a handedness ambiguity. This could help explain the superiority of the MAD phases during the later stages of structure determination. We expect the difference between SAD and MAD to be even larger for more challenging cases with weaker anomalous signals.

In conclusion, we have demonstrated that XFEL-based two-color phasing is not only feasible but also advantageous [4,5]. Using a well-characterized model system we show that significantly fewer indexed patterns are required for *de novo* phasing using two-color data compared to single color data. This should reduce the requisite amounts of sample and beamtime. We expect two-color data collection to be particularly useful for difficult-to-phase projects where it may make the crucial difference between being able to solve the structure and not.

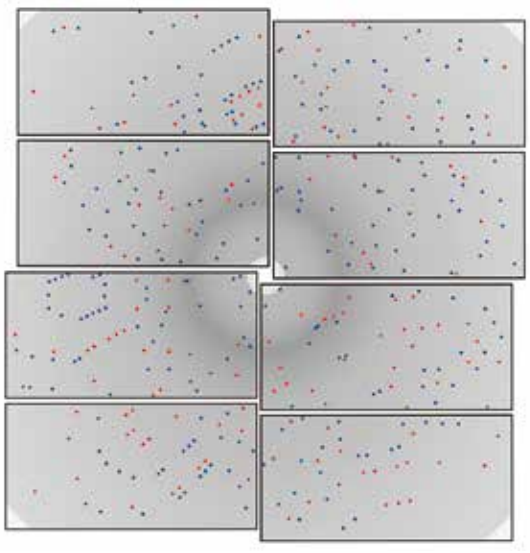

Fig. 2. Indexing of the two-color diffraction patterns.

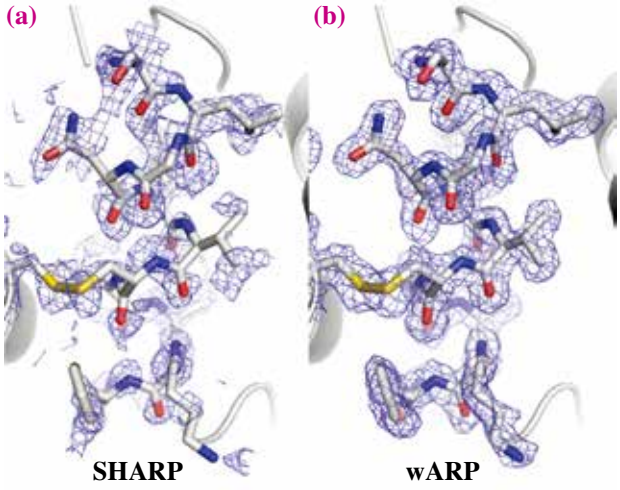

Fig. 3. Progression of the MAD phasing process with 5000 images. **(a)** Initial phases obtained with SHARP. **(b)** Phases after automatic building and -refinement by ARP/wARP. All maps are contoured at 1 sigma and are superimposed onto the final, refined structure (PDB code 5OER).

Alexander Gorel and Ilme Schlichting*

Max-Planck-Institut für medizinische Forschung, Germany

*Email: Ilme.Schlichting@mpimf-heidelberg.mpg.de

References

[1] T. Hara *et al.*: Nat. Commun. **4** (2013) 2919.
[2] L. Foucar: J. Appl. Cryst. **49** (2016) 1336.
[3] T.A. White: J. Appl. Cryst. **45** (2012) 335.
[4] *A. Gorel, K. Motomura, H. Fukuzawa, R.B. Doak, M.L. Gruenbein, M. Hilpert, I. Inoue, M. Kloos, G. Kovácsová, E. Nango, K. Nass, C.M. Roome, R.L. Shoeman, R. Tanaka, K. Tono, Y. Joti, M. Yabashi, S. Iwata, L. Foucar, K. Ueda, T.R.M. Barends and I. Schlichting: Nat. Commun. **8** (2017) 1170.*
[5] A. Gorel *et al.*: Scientific Data **4** (2017) 170188.

A vagal reflex mediates the lung aeration-induced increase in pulmonary blood flow at birth

At birth lung aeration not only allows pulmonary gas exchange to commence, but also stimulates a large increase in pulmonary blood flow (PBF) [1]. During fetal life, gas exchange occurs across the placenta and PBF is low due to a high pulmonary vascular resistance (PVR). Thus, PBF contributes little to the blood supply (preload) for the left ventricle in the fetus, whereas in the adult, PBF supplies 100% of this preload. Instead, in the fetus, preload for the left ventricle mostly comes from umbilical blood flow [2,3]. Following birth, umbilical venous return is lost with clamping of the umbilical cord and so PBF must rapidly increase to facilitate pulmonary gas exchange and supply preload for the left ventricle[2]. Thus, the increase in PBF is critical for the transition to newborn life and while it is clear that lung aeration is the trigger, the mechanism by which lung aeration stimulates PBF remains poorly understood.

Numerous factors are thought to contribute to the increase in PBF at birth, which include increased oxygenation, vasodilator release (e.g. nitric oxide (NO)) and mechanical factors. Increased oxygenation dilates pulmonary vessels through mediators such as NO, whereas air entry into the lung causes surface tension to develop at the air/liquid interface, which increases lung recoil and causes peri-alveolar capillaries to expand. Our recent studies have identified an additional, previously unrecognized, factor that contributes to the increase in PBF at birth [4,5]. These studies were conducted at SPring-8 using simultaneous angiography and phase contrast (PC) X-ray imaging and showed that partial lung aeration in the both presence and absence of O_2 increased PBF equally in both aerated and non-aerated lung regions [5]. These findings clearly demonstrated the existence of a previously unrecognized mechanism that could not be readily explained by any known mechanism [4].

As partial lung aeration triggers a global increase in PBF, we considered that a neural reflex may be responsible, which is triggered by the movement of liquid out of the airways and into the surrounding tissue during lung aeration. This is consistent with our previous studies performed at SPring-8 showing that during lung aeration liquid moves distally through the airways and eventually across the distal airway wall into lung tissue. It is also consistent with the finding that vagal stimulation causes pulmonary vasodilation in fetal sheep. In this study, we investigated the role of the vagus nerve in mediating the increase in PBF at birth using simultaneous PC X-ray imaging and angiography in newborn rabbits (Fig. 1). We hypothesized that, following partial lung aeration, vagotomy would disrupt vasodilation in non-aerated lung regions regardless of the O_2 content of the inspired gas.

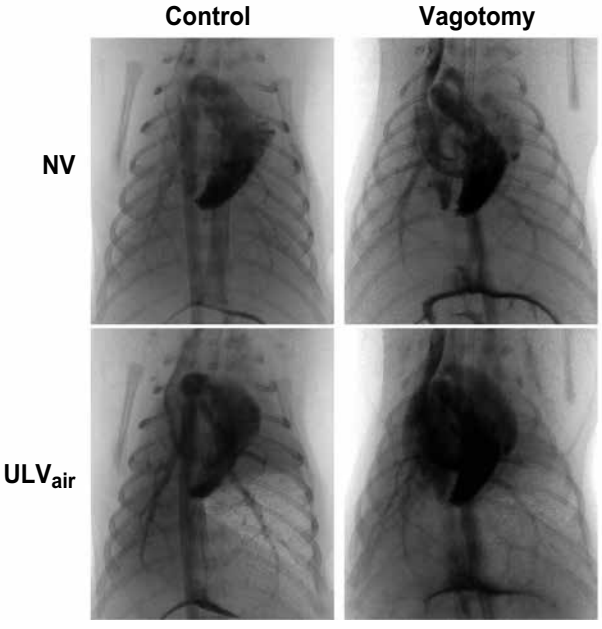

Fig. 1. Representative PC X-ray angiography image sequences of vagotomized and control newborn rabbits imaged prior to ventilation (NV) and following unilateral ventilation (ULV) of the right lung with air (ULV_{air}). Images were obtained 1–3 seconds following iodine bolus injection.

These experiments were performed at SPring-8 **BL20B2** in newborn rabbit kittens as previously described [4,5]. Newborn kittens were either vagotomized or sham operated prior to delivery and then imaged at 20Hz. Image sequences were acquired before lung aeration and following aeration of a single lung ventilated with either 100% N_2 (0% O_2), air (21% O_2) or 100% O_2 in different groups of kittens (Fig. 1). Kittens were imaged again after the ventilation gas was switched to air, then again after ventilation commenced with both lungs [6]. In contrast to sham operated kittens, PBF in vagotomized kittens did not increase in response to unilateral ventilation of the lung with both 100% N_2 and air (Fig. 2). Interestingly, PBF was not reduced in vagotomized animals ventilated with 100% O_2, demonstrating the independent stimulatory effects of oxygen and autonomic innervation to the increase in PBF at birth. The PBF findings were consistent with the changes in vessel diameter and PBF transit times measured from the image sequences, demonstrating that the increase in PBF was primarily due to downstream vasodilation.

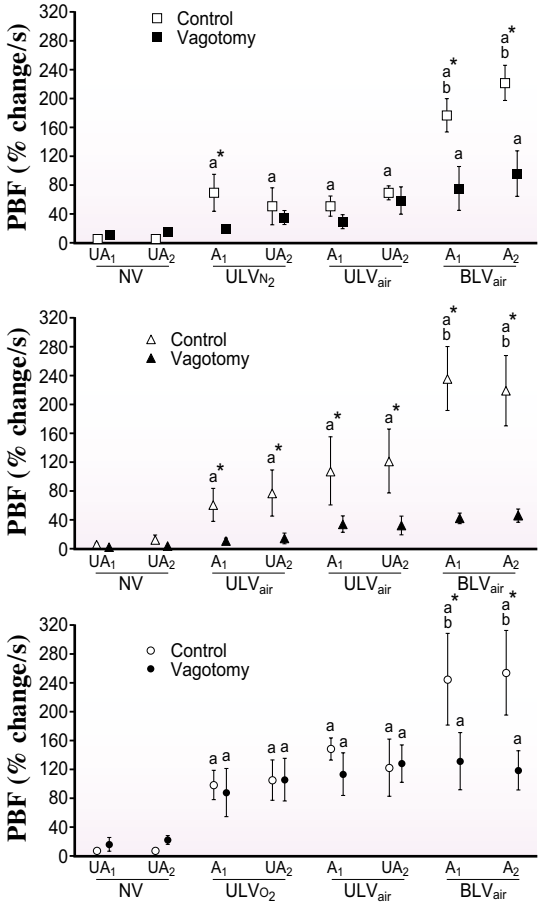

Fig. 2. Mean (±SEM) relative PBF (% change/s) levels in control (open symbols) and vagotomized (closed symbols) kittens initially ventilated with either 100% N_2 (squares; upper panel), air (triangles; middle panel) or 100% O_2 (circles; lower panel). Ventilation periods shown are non-ventilated (NV), unilateral ventilation ($ULV_{N_2/air/O_2}$), unilateral ventilation with air (ULV_{air}) and bilateral ventilation with air (BLV_{air}). Lungs are either unaerated (UA) or aerated (A) and ventilated first ($_1$) or second ($_2$). a: $p<0.05$ compared to the same lung at NV. *: $p<0.05$ control *vs.* vagotomy. Relative PBF was calculated by determining the maximum % change gray value in the main axial arteries divided by the arterial transit time.

The results of this study confirm that partial lung aeration induces a global increase in PBF across the entire lung, which is mediated by a neural reflex that signals via afferent nerve fibers that travel within the vagal trunk. Activation of these fibers are independent of oxygenation levels, which appears to act predominantly in localized manner to increased PBF only in affected tissues. While it remains unclear how lung aeration activates these nerve fibers and what receptors are involved, we speculate that the response involves activation of the lung's J-receptors. That is, during lung aeration, the movement of liquid out of the airways and into lung tissue causes lung tissue edema, which is known to activate J-receptors that signal via *c*-fibers within the vagal trunk. In summary, PC imaging and angiography can be utilized to demonstrate that partial lung aeration triggers a global increase in PBF, that is mediated via the vagal nerve. While this can lead to a potential mismatch between pulmonary ventilation and perfusion, at birth this is an advantage, not a disadvantage. That is, as the increase in PBF at birth is not dependent upon complete aeration of the lung, then the infant's cardiac output after birth (which depends on PBF for preload) is also not dependent upon complete lung aeration.

J. A.R. Lang[a,b], J. T. Pearson[c], M. J. Kitchen[d] and S. B. Hooper[a,b,*]

[a] The Ritchie Centre, Hudson Institute of Medical Research, Australia
[b] Department of Obstetrics and Gynaecology, Monash University, Australia
[c] Department of Cardiac Physiology at National Cerebral and Cardiovascular Center Research Institute, Japan
[d] School of Physics and Astronomy, Monash University, Australia

*Email: stuart.hooper@monash.edu

References

[1] S.B. Hooper *et al.*: Pediatr. Res. **77** (2015) 608.
[2] S. Bhatt *et al.*: J. Physiol. **591** (2013) 2113.
[3] K.J. Crossley *et al.*: J. Physiol. **587** (2009) 4695.
[4] J.A. Lang *et al.*: J. Appl. Physiol. **117** (2014) 535.
[5] J.A. Lang *et al.*: J. Physiol. **594** (2015) 1389.
[6] *J.A.R. Lang, J.T. Pearson, C. Binder-Heschl, M.J. Wallace, M.L. Siew, M.J. Kitchen, A.B. te Pas, R.A. Lewis, G.R. Polglase, M. Shirai and S.B. Hooper: J. Physiol.* ***595*** *(2017) 1593.*

Imaging of Br-labeled fatty acids in mammalian cells by scanning X-ray fluorescence microscopy

Fatty acids are taken up by cells and incorporated into lipids such as neutral lipids and glycerophospholipids (GPLs). GPLs are major constituents of cellular membranes of the various organelles, e.g. Golgi, ER, nucleus and lipid droplets (Fig. 1). There are more than 1,000 molecular species of GPLs having different polar head groups and fatty acid compositions. Fatty acids are efficient energy sources by themselves or components of cellular membranes. Such versatile functions of fatty acids are essential for cell survival, growth, and movement, and are related to diseases. Fatty acids have been well analyzed by mass spectrometry. However, intracellular imaging of fatty acids and GPLs has not been successful using conventional methods. Labeling with large molecules as chromophore may interfere with metabolism as a result of steric hindrance. Isotope labeling of fatty acids in combination with positron emission tomography and matrix-assisted laser desorption ionization or desorption electrospray ionization imaging mass spectrometry are inadequate to determine the intracellular localization of fatty acids owing to their low resolution (>5 μm). To overcome this issue, we employed the single-element labeling of fatty acids combined with scanning X-ray fluorescence microscopy (SXFM, Fig. 2(b)) technology at SPring-8 **BL29XUL**, which enables the imaging of multiple intracellular elements at the sub-organelle level by a sub-100-nm X-ray beam focusing system [1-3].

We prepared Br-palmitic acid (PA) and Br-stearic acid (SA), which possess Br at position Δ12 (Fig. 2(a)). Cells were treated with Br-SA for 24 h and subjected to SXFM (Fig. 2(b)). The Br-SA SXFM spectrum of cells showed that the Br X-ray fluorescence lines with different electron shells (Br-Kα and Br-Kβ) increased in a manner dependent on the Br-SA concentration, whereas the X-ray fluorescence energies of the rest of the elements including zinc (Zn) were relatively stable [4]. While untreated control cells showed background Br signals owing to the use of a serum-containing culture medium, Br-SA-treated cells exhibited more than 10-fold higher Br contents, which enabled mapping images ready for SXFM. The concentration range of bromine according to the results of SXFM was 0.0013–10 fg/μm^2. Spectra of Br-Kα and Zn-Kα were mainly used for mapping images. Mapping data (500 nm/pixel) indicated that Br signals were mostly detected in the perinuclear region of the cytoplasm in both Br-fatty acid (FA)-treated cells (Fig. 2(c)). The Br signals tended to be clustered on one side of the nucleus (arrows). In contrast, Zn signals were observed in the entire cellular region but mainly were concentrated in the nucleus, whereas the signals did not exceed the background levels in ethanol (EtOH)-treated cells. We observed cells for 72 h after Br-FAs addition. The cell number increased logarithmically and Br signals remained in the perinuclear region *via* three passages. Analyses using inductively coupled plasma mass spectrometry combined with column separation suggested that Br-FAs were mainly metabolized into GPLs in cells. Further liquid chromatography mass spectrometry showed that Br-PA and Br-SA produced different species of Br-labeled phosphatidylcholines, one of the major components of GPLs [4]. These data suggested that Br-FAs were metabolized in

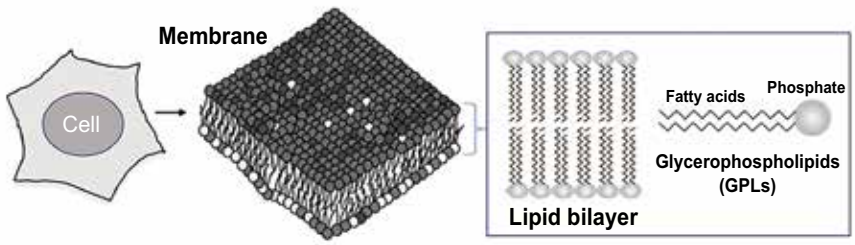

Fig. 1. Schematic structures of saturated glycerophospholipids (GPLs) in cells. GPLs are the most abundant lipid in the cellular membrane. Palmitic acid and stearic acid used in this study are the components of GPLs.

cells without alternation of cellular functions. Higher-resolution imaging (250 nm/pixel) revealed spotlike Br signals in the cytoplasm of cells, which were distinct from the Zn signals (arrows, Fig. 3). The size of the spotlike Br signals was <1 μm in diameter and the bromine signals were well co-localized with signals by staining of endoplasmic reticulum (ER) marker dye rather than mitochondrial one [4], which is consistent with previous findings that GPLs are produced by enzymes at ER.

In this study, we established a novel procedure for the imaging of intracellular FAs by single-element labeling combined with SXFM technology. The application of this new technology to unsaturated fatty acids will contribute to understanding of the dynamics of eicosanoids or other polyunsaturated fatty acid (PUFA)-derived lipid mediators in various fields of physiology and pathology, including inflammation, neurodegenerative diseases, and cardiovascular diseases.

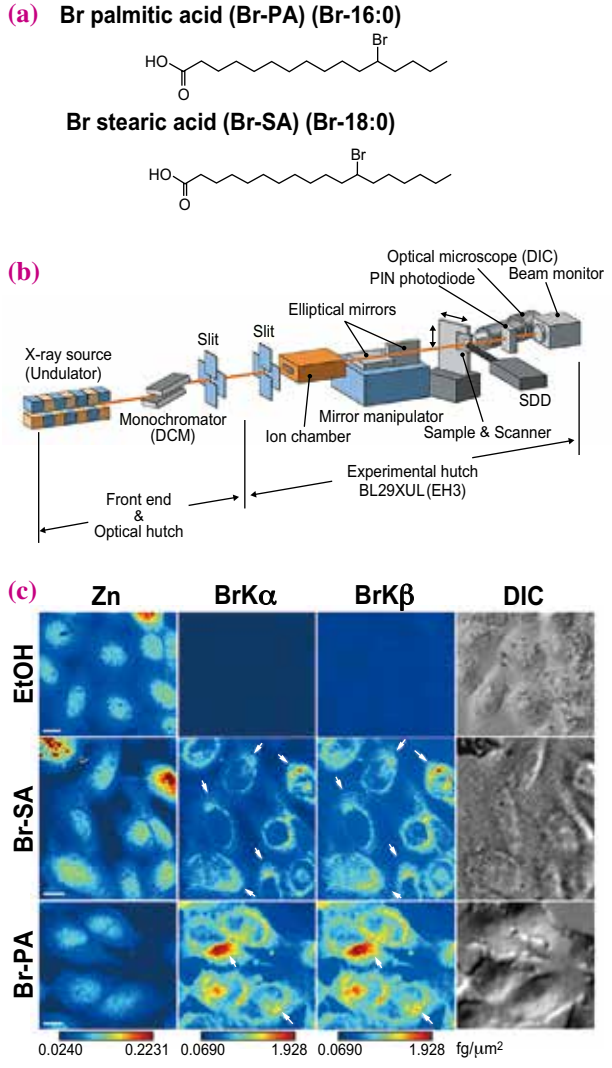

Fig. 2. X-ray fluorescence images of Br-labeled fatty acids. **(a, b)** Schematic views of the Br-labeled fatty acids and SXFM. **(c)** Zn- and Br-mapping images of Br-SA-, Br-PA-, and EtOH-treated CHO-K1 cells treated for 24 h. Arrows, clustered Br signals; BrKα and Brkβ, bromine X-ray emission lines; DIC, differential interference contrast image. A brighter color indicates higher signal intensity. Color bar, fg/μm^2; bar, 10 μm.

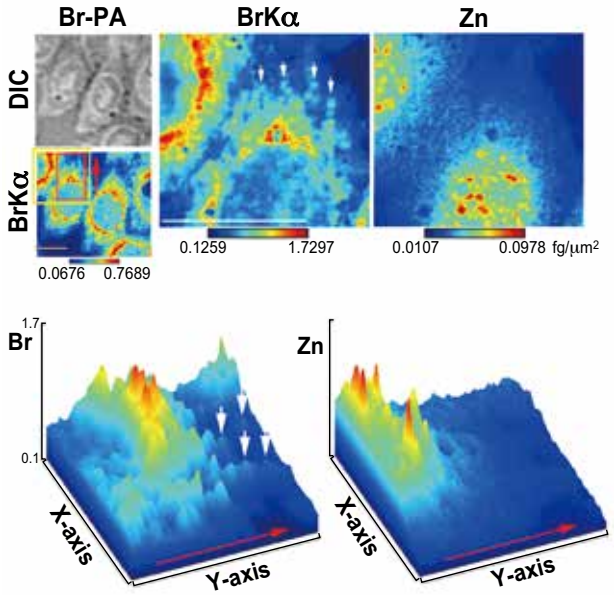

Fig. 3. Higher-resolution X-ray fluorescence images. Top, Br-PA. Bottom, surface plot generated on the basis of the red area in the top images. The yellow-framed area was measured at a higher resolution. Red arrows, direction presented in the surface plots; white arrows, spotlike Br distribution. A brighter color indicates higher signal intensity. Color bar, fg/μm^2; bar, 10 μm.

Mari Shimura

Department of Intractable Diseases,
National Center for Global Health and Medicine

Email: mshimura@ri.ncgm.go.jp

References

[1] H. Shindou *et al.*: J. Biol. Chem. **284** (2009) 1.
[2] S. Matsuyama *et al.*: Rev. Sci. Instrum. **77** (2006) 103102.
[3] M. Shimura *et al.*: Cancer Res. **65** (2005) 4998.
[4] *M. Shimura, H. Shindou, L. Szyrwiel, S.M. Tokuoka, F. Hamano, S. Matsuyama, M. Okamoto, A. Matsunaga, Y. Kita, Y. Ishizaka, K. Yamauchi, Y. Kohmura, R. Lobinski, I. Shimizu and T. Shimizu: FASEB J.* ***30*** *(2016) 4149.*

Direct observation of molecular orbital distribution by synchrotron X-ray diffraction

Molecular conductors exhibit various electronic states upon a small change in external field because the quantum parameters (transition integrals and electronic correlation energies) of substances are small and antagonistic. In order to understand physical properties correctly, it is necessary to clarify what type of interaction is cooperating/competing in a system. For that, precise information of the crystal structure and electron distribution state is indispensable.

In the case of molecular crystals, the observation of the molecular orbital distribution is considered to be very important in providing guidelines for material design. Today, quantum chemistry calculations play a major role in molecular design owing to the development of computational science. However, in the case of molecular crystals, since the number of constituent atoms is large and the number of independent parameters becomes enormous, it is difficult to experimentally obtain accurate crystallographic information including the electronic state.

The typical quasi-one-dimensional system $(TMTTF)_2PF_6$ consists of weak dimers of TMTTF stacked in the *a*-axis direction (Fig. 1(a)) and exhibits low-dimensional electronic properties and relatively strong electron-electron correlations. This compound shows a phase transition from the dimer-Mott phase to the charge ordering phase at approximately 67 K, which is called the mysterious "structureless transition" because the structural parameters are hardly affected by the transition [1]. Some experiments have been performed in an attempt to solve this mystery [2,3].

We first revealed the microstructural changes accompanying the charge ordering of $(TMTTF)_2PF_6$ by careful analysis using a device at SPring-8 **BL02B1**, where it is possible to collect diffraction data with high luminance and high resolution. Furthermore, using this high-quality data, we showed that direct observation of the molecular orbital distribution state is possible by electron density analysis by the core differential Fourier synthesis (CDFS) method [4].

Figure 1(d) shows the total electron density distribution of a TMTTF molecule calculated by a normal inverse Fourier transform of the high resolution data obtained at BL02B1. Even if short-wavelength (~0.35 Å) X-ray diffraction data is used, a marked truncation effect due to the inverse Fourier transform appears around atoms, meaning that atomic electron clouds cannot be identified.

Therefore, we used the CDFS method to separate the information of the core electrons that do not contribute to the bonding of atoms and the valence electrons that form the frontier orbital. Figure 1(e) shows the valence electron density distribution of a

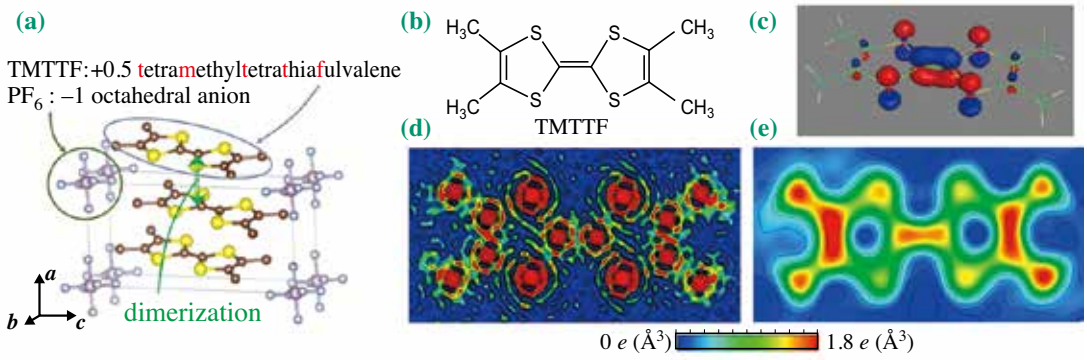

Fig. 1. **(a)** Crystal structure of $(TMTTF)_2PF_6$. **(b)** Molecular structure of a TMTTF molecule. **(c)** Molecular orbital obtained by quantum chemistry calculation of isolated molecules. Molecular orbitals do not represent the electron density and are painted red and blue depending on the sign of the quantum phase. The electron density of the square of the absolute value of the orbital was experimentally observed. **(d)**, **(e)** Total electron density distribution and valence electron density distribution of a TMTTF molecule, respectively.

TMTTF molecule obtained by the CDFS method. Both the smooth electron density of the bonding orbital on the C=C bond and the electron density node of the anti-bonding orbital of the C–S bond (Figs. 1(b) and 1(c)) are clearly shown.

By comparing the valence electron number of the two TMTTF molecules in the dimer obtained by the CDFS analysis in the atomic basins calculated by Bader's topological analysis, the amount of charge transfer was found to be δ_{CO}=0.20*e*. We directly revealed that the spatial charge ordering pattern formed a two-dimensional Wigner crystal state from the electron density distribution in the charge ordering phase called the "structureless transition" (Fig. 2).

This CDFS method can be applied not only to determine molecular orbitals in molecular crystals but also to determine the localized *d* orbitals of transition metals in inorganic crystals. By using the CDFS method, it becomes possible to discuss the detailed electronic state of a wider range of materials and to provide information for the development of functional materials.

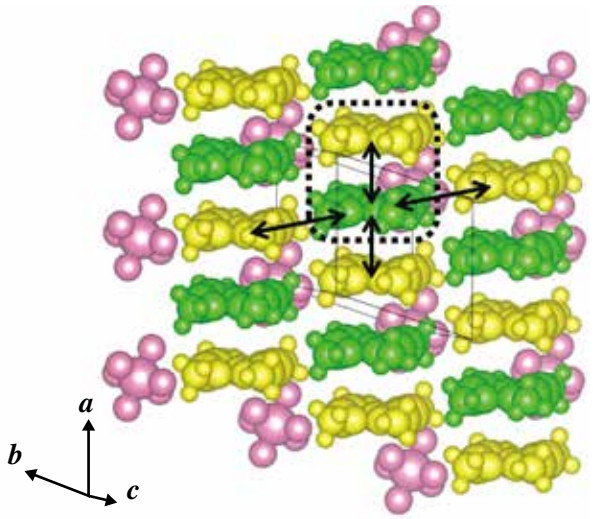

Fig. 2. Charge ordering patterns of hole-rich (yellow) and hole-poor (green) molecules, which indicate a two-dimensional Wigner crystal state. The region surrounded by the dotted line shows a TMTTF molecule dimer.

Shunsuke Kitou and Hiroshi Sawa*

Department of Applied Physics, Nagoya University

*Email: z47827a@cc.nagoya-u.ac.jp

References

[1] C. Coulon *et al.*: Phys. Rev. B **31** (1985) 3583.
[2] M. de Souza *et al.*: Phys. Rev. Lett. **101** (2008) 216403.
[3] P. Foury-Leylekian *et al.*: Physica B **405** (2010) 95.
[4] *S. Kitou, T. Fujii, T. Kawamoto, N. Katayama, S. Maki, E. Nishibori, K. Sugimoto, M. Takata, T. Nakamura and H. Sawa: Phys. Rev. Lett.* ***119*** *(2017) 065701.*

In situ observation of crystal structure dynamics in ferroelectric films under application of an electric field

Ferroelectric materials have a switchable spontaneous polarization and also have pyroelectric and piezoelectric properties. Using such properties, they have been widely applied to many electronic devices, including sensors and actuators. Recently, they have also been applied to energy harvesting devices using mechanical vibration from an environmental source. Therefore, they have become one of the key materials for sensor network systems to a sustain an aging society, for example, by monitoring the movements of elderly people living alone.

Thin films of $Pb(Zr_{1-x}Ti_x)O_3$ combined with a microelectromechanical system (MEMS) have been extensively studied for such applications because of a superior piezoelectric and ferroelectric properties. It has been pointed out that the electromechanical response of $Pb(Zr_{1-x}Ti_x)O_3$ under the application of an electric field is not only simple lattice elongation (the so-called intrinsic contribution of the piezoresponse) (see Fig. 1(a)) but also includes extrinsic contributions, which include the reorientation of the film as shown in Fig. 1(b). For example, (100)-oriented regions (*a*-domains) switch to (001)-oriented regions (*c*-domains) in tetragonal $Pb(Zr_{1-x}Ti_x)O_3$ films consisting of a mixture of the (100) and (001) orientations. This extrinsic contribution is responsible for more than 50% of the total piezoelectric response and is required for the design of high-performance piezoelectric devices for MEMS applications.

The dynamics of the crystal structure in $Pb(Zr_{1-x}Ti_x)O_3$ films while applying an electric field have been measured by *in situ* X-ray diffraction (XRD) measurement. However, it has not yet been clarified how fast the reorientation proceeds. In particular, the relationship between the lattice elongation and geometrical domain structure deformation in tetragonal $Pb(Zr_{1-x}Ti_x)O_3$ thin films has not been determined from the viewpoint of the response speed. In our study, we investigated the change in the crystal structure under the application of an electric field in 600-nm-thick (100)/(001)-oriented epitaxial tetragonal $Pb(Zr_{0.4}Ti_{0.6})O_3$ films [1].

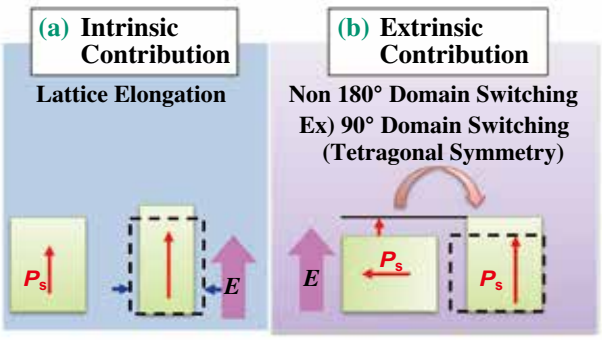

Fig. 1. Schematic drawing of two contributions to piezoelectric response in piezoelectric materials.

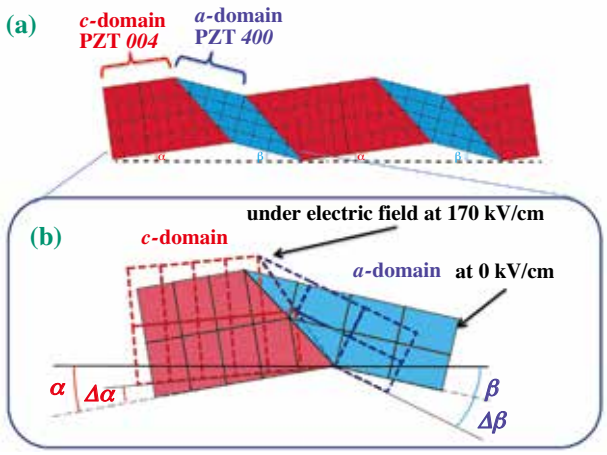

Fig. 2. Schematic drawing of crystal structures domain structures of (100)/(001)-oriented epitaxial tetragonal $Pb(Zr_{0.4}Ti_{0.6})O_3$ films.

The investigated film samples consisted of a combination of (100)-oriented domains (*a*-domains) and (001)-oriented domains (*c*-domains), as shown in Fig. 2(a), where the polar axis was perpendicular and parallel to the substrate surface for the (001)- and (100)-oriented domains, respectively. The average lattice parameters and the domain structure of the films under an electric field were measured using a time-resolved *in situ* synchrotron XRD system at SPring-8 **BL13XU** in conjunction with a high-speed pulse generator.

Figure 3 shows the XRD patterns before and under the application of an electric field. The *004* peak position of the (004) orientation shifts to a lower 2θ angle under the application of an electric field, as shown in Fig. 3(a), which demonstrates the elongation of the *c*-axis lattice parameter of the (100)-oriented region. This corresponds to the intrinsic response shown in Fig. 1(a). In contrast, the *400* peak shifts in the opposite direction (to a higher angle) as shown in Fig. 3(b), thus indicating a decrease in the *a*-axis lattice parameter of the (100)-oriented region. In addition to this change in the lattice parameters, the amount of reorientation of the crystal structure from

(100) to (001) was evaluated from the changes in the *400* and *004* diffraction peak intensities resulting from the application of an electric field (see Fig. 3). These changes also accompanied a tilt in the angles of the (100)- and (001)-oriented regions from the substrate surface normal direction as schematically illustrated by the dashed line in Fig. 2(b).

Figure 4 shows the electric charge (Fig. 4(a)) and the lattice strains (Fig. 4(b)), the tilting angles (Fig. 4(c)), and the peak intensity of each domain (Fig. 4(d)) as a function of time. Figures 4(b), 4(c), and 4(d) suggest that the elastic deformation, tilting motion, and ferroelastic domain switching were completed within 40 ns. When the electric field was removed, the tilt angles and intensities also returned to their original values at zero field in less than 40 ns. These data were acquired during the repeated application of electric pulses of 800 ns duration, which confirm that a ferroelastic reorientation is perfectly repeatable. More importantly, all these changes (charging, lattice strain, domain switching, and the change in the tilting angle) occurred simultaneously without delay when the electric field across the PZT film was changed. This means that the 90° domain switching from the (100) to (001) orientation can be exploited to enhance the piezoresponse response time, even to within 10 ns order. It should be noted that the response time in this study is less than that previously reported [2,3] for a sintered body, which is on the order of 100 ns. Moreover, the reorientation of thin films does not suffer from frequency dispersion, as seen in bulk ceramics, where it becomes inactive within a short pulse time of ns order. This observation proved that the (001) orientation switches to the (100) orientation within 40 ns under a high-speed pulsed electric field. Our direct observation of such high-speed switching paves the way for the design of piezo-MEMS devices for high-frequency operation.

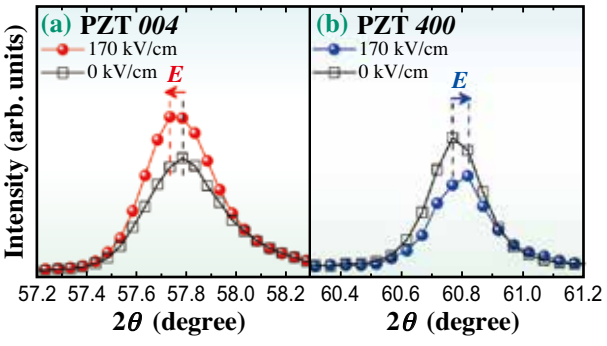

Fig. 3. HRXRD 2θ scans of (**a**) PZT *004* and (**b**) PZT *400* measured under a 200 ns pulsed electric field with amplitudes of 0 kV/cm (open squares) and 170 kV/cm (filled circles) for the $Pb(Zr_{0.4}Ti_{0.6})O_3$ films.

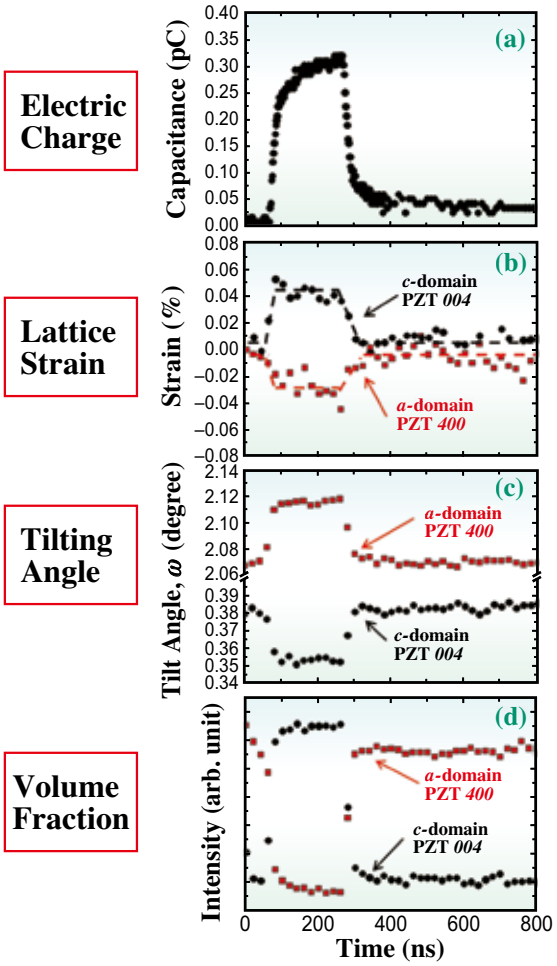

Fig. 4. (**a**) Electric charge, (**b**) lattice strains, (**c**) tilting angles, and (**d**) peak intensities of PZT *004* and PZT *400* as a function of time during the application of a 200 ns pulsed electric field with a magnitude of 170 kV/cm.

Hiroshi Funakubo[a,b,c,*], Takao Shimizu[b,c] and Osami Sakata[a,b,d]

[a] Department of Innovative and Engineered Material, Tokyo Institute of Technology
[b] Materials Research Center for Element Strategy, Tokyo Institute of Technology
[c] School of Materials and Chemical Technology, Tokyo Institute of Technology
[d] Synchrotron X-ray Station at SPring-8 and Synchrotron X-ray Group, National Institute for Materials Science (NIMS)

*Email: funakubo.h.aa@m.titech.ac.jp

References

[1] *Y. Ehara, S. Yasui, T. Oikawa, T. Shiraishi, T. Shimizu, Hi. Tanaka, N. Kanenko, R. Maran, T. Yamada, Y. Imai, O. Sakata, N. Valanoor and H. Funakubo: Sci. Rep. 7 (2017) 9641.*
[2] Y. Ehara *et al.*: Appl. Phys. Lett. **99** (2011) 182906.
[3] H.-H. Huang *et al.*: Adv. Mater. Interfaces **2** (2015) 1500075.

Crystallization and vitrification of strongly correlated electrons on a geometrically frustrated triangular lattice

Glassy materials are ubiquitous in nature [1]. The history of glassmaking traces back thousands of years and sophisticated glass-forming technology has been utilized by humans for centuries. Yet, the fundamental understanding of glassy dynamics remains one of the most important unresolved problems in both physics and materials science. So far, from various fields of condensed-matter physics, a rich variety of glass-formation phenomena have been observed, ranging from structural to spin, electric-dipole, and superconducting vortex glasses. The dynamics and mechanisms by which the materials acquire the glassy state, however, have been a long-standing issue in both theoretical and experimental physics. Here, we focus on a unique glassy state of electrons in solids realized in an organic molecular conductor, where the lack of periodicity of the strongly correlated electrons on the triangular lattice is caused by geometrical frustration and strong quantum effects.

The quasi-two-dimensional organic compound θ_m-(BEDT-TTF)$_2$TlZn(SCN)$_4$ studied here (henceforth θ_m-TlZn) undergoes a charge ordering (CO) transition at 170 K owing to strong electron correlations (Fig. 1(a)), where the charge carriers on the BEDT-TTF molecules are localized periodically with a diagonal stripe pattern (Fig. 1(c)) [2]. Such a periodic CO state can be regarded as a "charge-crystal" state. In contrast, above the CO transition temperature, the charge of +0.5 per BEDT-TTF molecule is distributed uniformly in space; therefore, such a delocalized state can be referred to as a "charge-liquid" state (Fig. 1(b)). In θ_m-TlZn, when the sample is cooled faster than a critical cooling rate (~50 K/min), charge crystallization is kinetically avoided, leading to a "charge glass" state where the charge is randomly quenched (Fig. 1(d)). The mechanism of formation of the glassy electronic state has been investigated experimentally and theoretically in terms of the geometrically frustrated triangular lattice, but still remains rather elusive [3,4].

To clarify the origin of charge-glass formation in θ_m-TlZn, we utilized various complementary experimental techniques. Among them, infrared optical spectroscopy has provided important information on the local charge distribution on the BEDT-TTF molecules at a microscopic level. The brilliance of synchrotron radiation light at **BL43IR** in SPring-8 is more than two orders of magnitude higher than that of a laboratory light source, which enables accurate optical measurements for tiny single crystals such as organic compounds.

Figure 2(a) shows the charge-sensitive vibrational mode ν_{27} of the BEDT-TTF molecule. The ν_{27} mode is known as a local probe of the molecular charge and splits into two modes in the presence of a difference in charge between the A and B sites in the unit cell (Figs. 1(b) and 1(c)). A clear peak around 1420 cm^{-1} is assigned to the charge-rich mode of ν_{27} (Fig. 2(b)). A sizable intensity was observed above T_m (Fig. 2(c)), indicating the presence of charge disproportionation. Because the A and B sites are crystallographically equivalent above T_m, the time-averaged charge distribution above T_m should be +0.5 per BEDT-TTF molecule (Fig. 1(b)). Therefore, the splitting of ν_{27} above T_m implies that charge disproportionation is not static but dynamically fluctuates on a time scale slower than that of the molecular vibrational ν_{27} motion. Because the intensity of the charge-rich mode reflects the volume of dynamically fluctuating charge clusters, its increase with decreasing temperature suggests that the heterogeneous slow dynamics grows towards the charge-glass transition.

The present results, combined with the X-ray structural analysis, revealed that the charge-glass state of θ_m-TlZn is described by the superposition of various chain-striped states as shown in Fig. 3(a). This situation can be understood by an energy landscape with multiple local minima, as illustrated in Fig. 3(b) — that is, a metastable state with an amorphous stripe-glass structure as proposed on the basis of recent theoretical calculations [4].

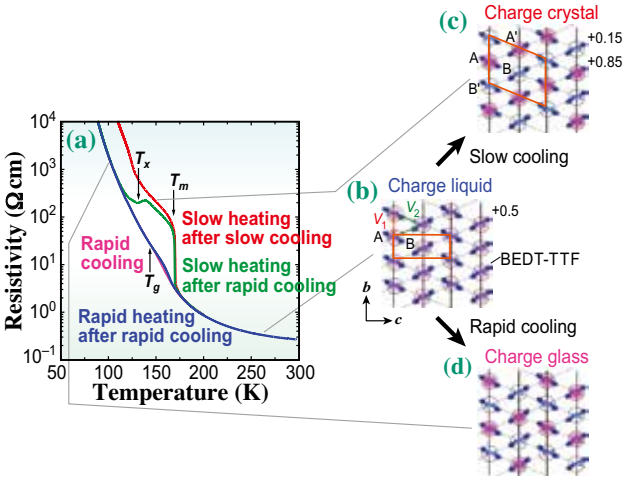

Fig. 1. **(a)** Temperature dependence of the resistivity for θ_m-TlZn measured in various cooling/heating processes. **(b)–(d)** Illustrations of **(b)** the charge-liquid state, **(c)** the charge-crystal state, and **(d)** the charge-glass state in θ_m-TlZn. V_1 and V_2 are the nearest-neighbor Coulomb interactions, where V_2/V_1 ~0.8.

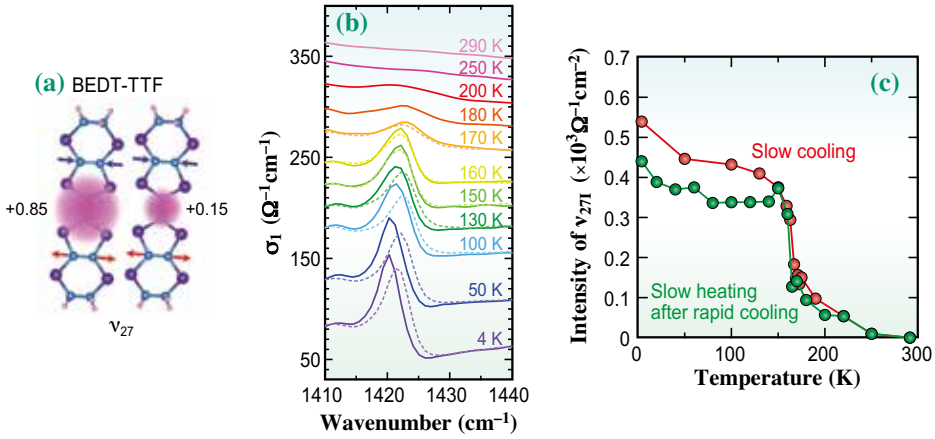

Fig. 2. **(a)** Sketch of the infrared active vibrational mode ν_{27} of the BEDT-TTF molecule. The charge-rich and charge-poor modes are observed at 1420 cm^{-1} and 1515 cm^{-1}, respectively. **(b)** Temperature dependence of the ν_{27} mode of the charge-rich site measured during slow cooling (solid line) and slow heating after rapid cooling (dashed line). **(c)** Temperature dependence of the intensity of ν_{27} of the charge-rich site.

Next we compared our organic molecular material containing 'frustrated' electrons with the atomic/molecular dynamics of glass formation in conventional glass-forming liquids. We quantitatively evaluated the CO volume fraction from the time evolution of the resistivity during the charge crystallization process from the supercooled charge-liquid or charge-glass state. Figure 3(c) displays the contour map of the CO fraction plotted in the time-temperature plane [a so-called time-temperature-transformation (TTT) diagram]. The relaxation time becomes faster with decreasing temperature, and then slower below ~160 K, which is referred to as the "nose temperature"; this characteristic temperature dependence of the relaxation time can be explained by the theory of nucleation and growth at a first-order liquid-crystal phase transition. Our observation demonstrates that the crystallization process of electrons in solids can be described by the nucleation and growth process of a liquid, as observed in conventional glass-forming liquids. The surprising similarities between our system and conventional glass formers highlight the universal nature of the liquid-glass transition.

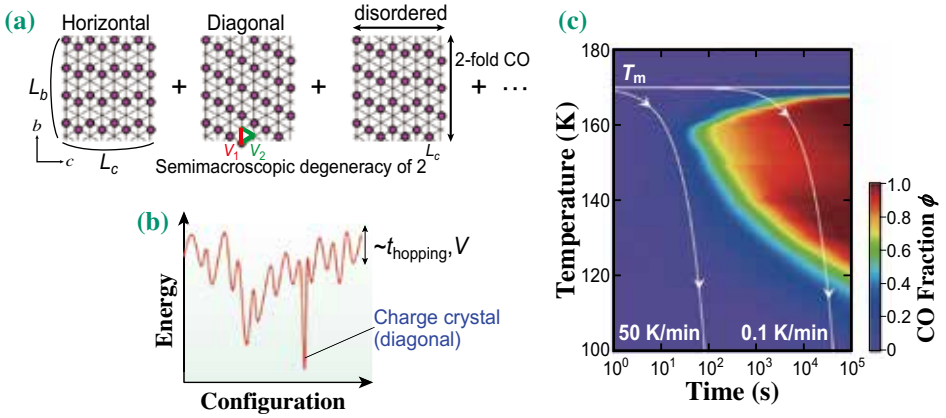

Fig. 3. **(a)** Schematics of various chain-striped CO patterns. The magenta circles represent the charge-rich sites. **(b)** Illustration of an energy landscape with multiple local minima separated by barriers having an energy scale of the hopping integral $t_{hopping}$ and/or the long-range Coulomb interaction V. The horizontal axis represents the various spatial configurations of charge patterns as illustrated in (a). **(c)** TTT diagram derived from the time evolution of the resistivity.

Kenichiro Hashimoto* and Takahiko Sasaki

Institute for Materials Research, Tohoku University

*Email: hashimoto@imr.tohoku.ac.jp

References

[1] P.G. Debenedetti and F.H. Stillinger: Nature **410** (2001) 259.
[2] *S. Sasaki, K. Hashimoto, R. Kobayashi, K. Itoh, S. Iguchi, Y. Nishio, Y. Ikemoto, T. Moriwaki, N. Yoneyama, M. Watanabe, A. Ueda, H. Mori, K. Kobayashi, R. Kumai, Y. Murakami, J. Müller and T. Sasaki: Science* ***357*** *(2017) 1381.*
[3] F. Kagawa *et al.*: Nat. Phys. **9** (2013) 419.
[4] S. Mahmoudian *et al.*: Phys. Rev. Lett. **115** (2015) 025701.

Probing the energy storage in Li ion batteries with hard X-ray Compton scattering

A comprehensive quantum mechanical understanding of the principles underlying rechargeable batteries is still evolving after several decades of research. In this connection, our recent work shows how X-ray Compton scattering experiments can help unravel relationships between useful battery characteristics and the nature of the electronic orbitals involved in ion intercalation reactions [1,2]. The discharge process in which positive lithium ions intercalate or lithiate the cathode and drive current in an external circuit lies at the heart of the Li-ion battery (LIB). The reverse reaction produces the charging of the battery and involves delithiation of the cathode material.

Compton scattering experiments using brilliant, high-energy X-rays at SPring-8 **BL08W**, provide a unique window for probing the electron momentum distributions (EMDs) of the redox orbitals involved in lithiation and delithiation processes. The measured spectra can be compared with model Compton profiles obtained from accurate electronic structure calculations based on Density Functional Theory (DFT) to extract redox wave functions associated with the Li electron transfer process. Along similar lines, we have previously investigated effects of doping in high temperature superconductors [3].

In this study, we focused on lithium iron phosphate (LFP) as an exemplar LIB cathode material. LFP was proposed for use in rechargeable batteries by Padhi, Nanjundaswamy and Goodenough about 20 years ago [4] and commercial LFP batteries are available today. The olivine crystal structure of LFP is composed of perfect PO_4 tetrahedra and distorted FeO_6 octahedra as shown in Fig. 1. The electronic and magnetic structure of LFP is interesting as it displays antiferromagnetic and insulating behavior. Moreover, delithiation of LFP is a two-phase process that leads to microscopic phase separation in equilibrium.

We have previously investigated LFP using X-ray absorption spectroscopy (XAS) and parallel DFT computations to monitor the evolution of the redox orbitals under different lithiation levels [5]. In this way, we identified spectroscopic signatures of the lithiation process in LFP, and obtained information on phase transformations, valence and spin states, and local structural distortions. XAS, however, can only access the energy dependencies of electronic states and the associated spectral functions. Compton scattering, in contrast, is capable of accessing the momentum characteristics of the correlated ground state, which are beyond the reach of XAS. In particular, the experimental Compton profile is directly related to a two-dimensional integral of the EMD. Since the EMD is given by an energy integral of the spectral function over occupied states, the spectral function and its momentum dependence near the Fermi level can be obtained via an energy derivative of the EMD. Compton scattering technique thus enables unique insight into the evolution of redox orbitals with lithiation and delithiation processes in battery materials.

The EMD (integrated along the [100] direction) of the orbital involved in lithium insertion in LFP is shown in Fig. 2. This visualization can be used to gain insight into voltage shifts in the LIB and how these shifts are connected with the modification of the bond between transition metal and oxygen atoms. For this purpose, we introduce a 'deformation profile,' *D(p)*, which isolates the contribution to the Compton profile from the effects of octahedral deformation, and reveals losses in redox potential generated by the shrinking of the FeO_6 octahedron produced by the delithiation, see Fig. 3 and discussion in Ref. [1]. Interestingly, strains and octahedral distortions present in olivine phosphate compounds in which some iron atoms are substituted with other transition metals (Mn, Co and

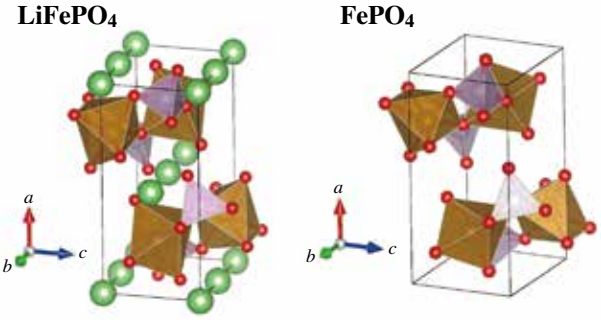

Fig. 1. Crystal structure of LFP. Li (green) and O atoms (red) are shown. Phosphorus and oxygen atoms form tetrahedral units, which link planes of corner-sharing FeO_6 octahedra.

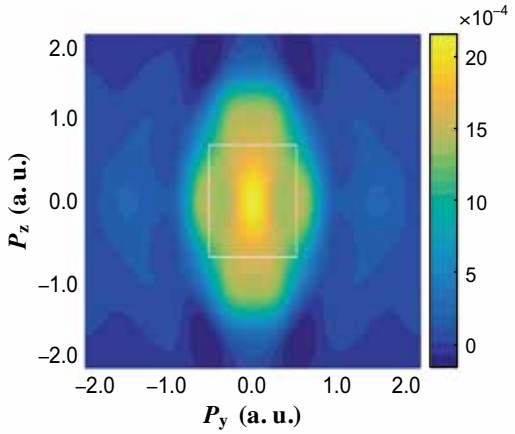

Fig. 2. Difference of 2D electron momentum densities of LFP and $FePO_4$. P_y and P_z axes are parallel to [010] and [001] direction, respectively. White rectangular box marks the boundary of the first Brillouin zone.

Ni) could improve the limited energy density of the pristine LFP and this trend can be monitored by using the deformation profile *D(p)*.

It is important to keep in mind that the energy density in a lithium battery pack in an electric car is about 0.4 MJ/liter, which is 100 times smaller than that in gasoline. This large difference indicates that there is much room for improving energy densities of rechargeable battery materials and that further work in this direction is needed. Since high-energy X-rays can easily penetrate closed electrochemical cells, Compton scattering experiments provide a unique spectroscopic tool for monitoring changes in redox orbitals during charging and discharging processes, and thus facilitate the design and development of high-performance rechargeable batteries.

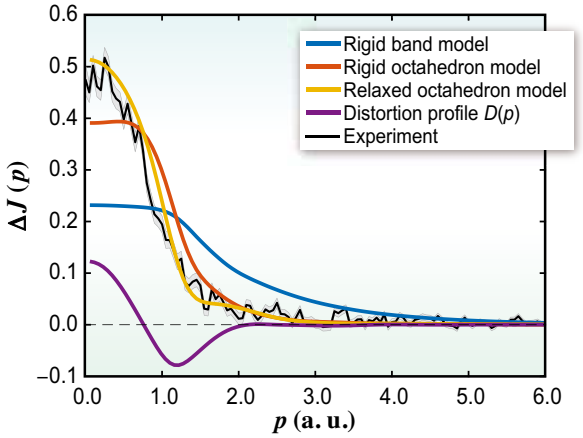

Fig. 3. Compton profile difference $\Delta J(p) = J_{LiFePO_4}(p) - J_{FePO_4}(p)$ for various models of LFP introduced in Ref. 1, along with the corresponding experimental results. Deformation profile, *D(p)*, gives the contribution to the theoretical profile from effects of octahedral distortion.

Bernardo Barbiellini[a,b,*], Arun Bansil[a] and Yoshiharu Sakurai[c]

[a] Department of Physics, Northeastern University
[b] Lappeeranta University of Technology
[c] Japan Synchrotron Radiation Research Institute (JASRI)

*Email: benardo.barbiellini@lut.fi

References

[1] *H. Hafiz, K. Suzuki, B. Barbiellini, Y. Orikasa, V. Callewaert, S. Kaprzyk, M. Itou, K. Yamamoto, R. Yamada, Y. Uchimoto, Y. Sakurai, H. Sakurai and A. Bansil: Sci. Adv.* ***3*** *(2017) e1700971.*
[2] K. Suzuki *et al.*: J. Appl. Phys. **119** (2016) 025103; B. Barbiellini *et al.*: Appl. Phys. Lett. **109** (2016) 073102.
[3] Y. Sakurai *et al.*: Science **332** (2011) 698.
[4] A.K. Padhi *et al.*: J. Electrochem. Soc. **144** (1997) 1188.
[5] X. Liu *et al.*: J. Am. Chem. Soc. **134** (2012) 13708.

X-ray magnetic circular dichroism spectroscopy for voltage-controlled magnetic anisotropy in FePt/MgO multilayer system

An electric field at a surface is known to exhibit useful phenomena, such as the pinch-off phenomenon in field-effect transistors and the induction of Mott transitions, superconducting phases, ferromagnetic phases, and magnetic anisotropy. All of these phenomena are attributable to one or both of two factors: electron accumulation or electric dipole induction. In particular, electric-field control of magnetic properties at room temperature has attracted much attention because of its great potential for enabling the construction of ultralow-power-consumption electric devices. Voltage-controlled magnetic anisotropy (VCMA) in Fe/MgO-based tunnel junctions [1] has shown that the magnetization of nanomagnets can be controlled in fast periods (down to 0.1 ns) by electric fields, as indicated by bistable precessional magnetization switching [2] and ferromagnetic resonance excitation [3]. Because the microscopic origin of VCMA should be purely electronic, the VCMA effect can be an ultimate technology for the operation of spintronics devices, such as nonvolatile random access memory, where high-speed operation with high writing endurance is indispensable.

In this research [4], we showed a mechanism to enhance electronic VCMA proved by X-ray magnetic circular dichroism (XMCD) spectroscopy at SPring-8 **BL39XU** and **BL25SU** beamlines. We prepared monatomic layers of Pt at an Fe-MgO interface by molecular-beam epitaxy in an ultrahigh vacuum as shown in Fig. 1. Since the Pt atoms have a considerable amount of spin polarization because of their hybridization with Fe and large spin-orbit interactions, the influence of the modified electron orbitals of Pt on the level of magnetocrystalline anisotropy energy (MAE) should be significant.

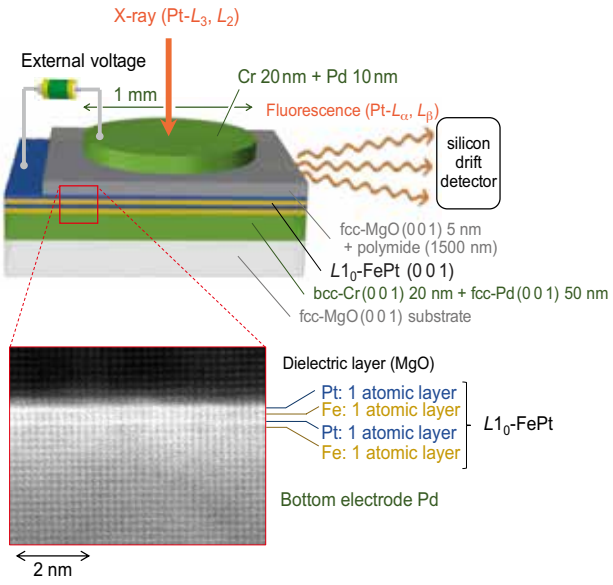

Fig. 1. Schematic of sample structure and experimental design.

An $L1_0$-FePt/MgO system was prepared to conduct XMCD spectroscopy as shown in Fig. 1. X-ray absorption spectroscopy (XAS) and its XMCD spectra were recorded *in situ* at the Pt L_3 and L_2 edges by detecting the X-ray fluorescence yields. In this configuration, positive external voltages induce electron accumulation at the Pt-MgO interface. As shown in Fig. 2, a clear VCMA effect, that is, a change in the magnetization hysteresis curve, was observed. Then, conventional sum-rule analysis can characterize the magnetic moments from XAS/XMCD spectra at the Pt absorption edge. The results confirm clear external voltage induction of the effective spin magnetic moment $m_S - 7m_T$ and an increase in the number of hole in Pt. While voltage application does not contribute a significant difference to the orbital magnetic moment m_L, the effective spin magnetic moment increased by 13%, and the hole number of Pt in the 5*d*-orbital increased by 0.019 when the external voltage was switched from positive to negative. From the magnetization angle dependence, we conclude that the voltage-induced changes in the effective spin magnetic moment originate from voltage-induced changes in the magnetic dipole T_z term m_T in the Pt atom, which has been revealed by high-precision XAS/XMCD measurements in SPring-8.

Equation 1 shows the perpendicular MAE (ΔE) when the spin-orbit interaction is treated in the second order [5] to discuss the MAE.

$$\Delta E \cong \frac{\lambda'}{4\mu_B}\left(\Delta m_{L,\downarrow} - \Delta m_{L,\uparrow}\right) - \frac{21}{2\mu_B}\frac{\lambda'^2}{E_{ex}}\Delta m_T \qquad (1)$$

$\Delta m_{L,s}\left(= m_{L,s}^{\perp} - m_{L,s}^{//}\right)$ and $\Delta m_T\left(= m_T^{\perp} - m_T^{//}\right)$ express the changes in the orbital magnetic moment and the magnetic dipole moment between the perpendicularly ($\perp$) and in-plane ($//$) magnetized electronic states, respectively. Here $\Delta m_{L,\downarrow(\uparrow)}$ expresses the contribution from the minority (majority) spin band. The measured orbital magnetic moment equals $m_L^{\perp(//)} = \Delta m_{L,\downarrow}^{\perp(//)} + \Delta m_{L,\uparrow}^{\perp(//)}$. In this case, λ' is the effective spin-orbit interaction coefficient in the *d*-band.

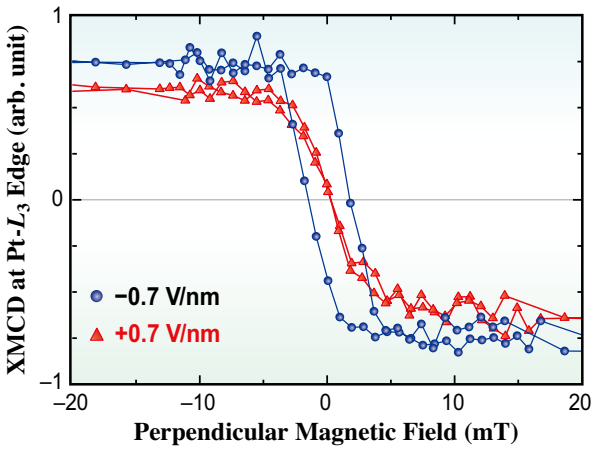

Fig. 2. Voltage-controlled magnetic anisotropy in FePt/MgO multilayer.

The first term is the MAE related to the orbital magnetic moment. When the majority spin band is full, $m_{L,\uparrow}^{\perp(//)}$ can be neglected. Then, the perpendicular MAE is proportional to the measured changes in the orbital magnetic moment; this relation is known as Bruno's model. This mechanism originates from the charge doping inducing anisotropy in the orbital magnetic moment as shown in Fig. 3(a). Note that $m_{L,\uparrow}^{\perp(//)}$ cannot be neglected in the case of Pt because of the small size of the exchange splitting.

The second term represents the perpendicular MAE related to the changes in the magnetic dipole T_z term m_T. It accounts for the spin-flip excitations between the exchange-split (E_{ex}) majority and minority spin bands. Because an electric field applied to a metal/dielectric is inhomogeneous because of the strong electrostatic screening effect in metals, such an electric field, including higher-order quadratic components, can couple with the electric quadrupole correlated to the magnetic dipole T_z term. The induced energy splitting of each orbital changes the MAE through spin-flip excitation, as shown by the second term in Eq. 1 and in Fig. 3(b).

From our first-principles study, the VCMA effect in the FePt/MgO system mainly originates from the second term in Eq. 1 for the Pt atom, which corresponds to the experimentally observed changes in the magnetic dipole T_z term m_T. However, in our FePt/MgO system, the VCMAs from the orbital magnetic moment and the electric quadrupole partially cancel one another. It should be noted that the VCMA from the electric quadrupole mechanism is larger than that of the orbital magnetic moment. However, the total VCMA is only 9% of the VCMA from the electric quadrupole mechanism. If a material with both VCMAs having the same polarity is to be designed, an electronic VCMA larger by more than a factor of 10 would be feasible [4,5].

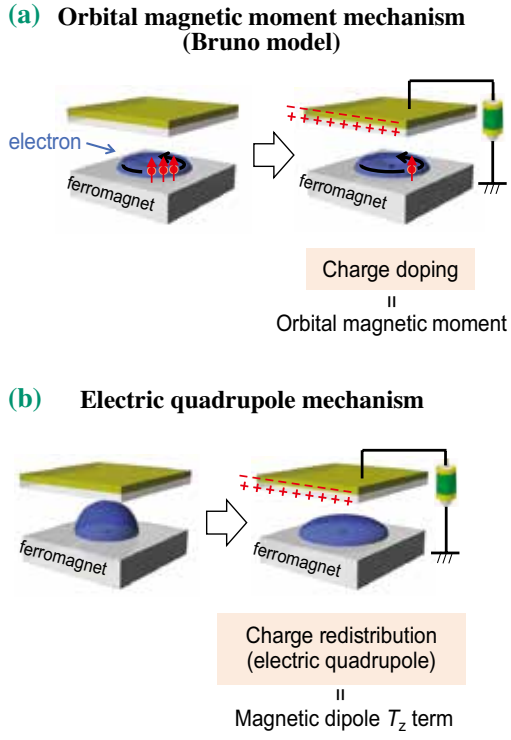

Fig. 3. Microscopic origin of VCMA in ultrathin ferromagnetic metals.

Shinji Miwa[a,b]

[a] Graduate School of Engineering Science, Osaka University
[b] The Institute for Solid State Physics, The University of Tokyo

Email: miwa@issp.u-tokyo.ac.jp

References

[1] T. Maruyama *et al.*: Nat. Nanotechnol. **4** (2009) 158.
[2] Y. Shiota *et al.*: Nat. Mater. **11** (2012) 39.
[3] T. Nozaki *et al.*: Nat. Phys. **8** (2012) 492.
[4] *S. Miwa, M. Suzuki, M. Tsujikawa, K. Matsuda, T. Nozaki, K. Tanaka, T. Tsukahara, K. Nawaoka, M. Goto, Y. Kotani, T. Ohkubo, F. Bonell, E. Tamura, K. Hono, T. Nakamura, M. Shirai, S. Yuasa and Y. Suzuki: Nat. Commun.* ***8*** *(2017) 15848.*
[5] G. van der Laan: J. Phys. Condens. Matter **10** (1998) 3239.

Gigantic spin waves induced by ultrashort laser pulses

Recently, spintronics, a field of electronic engineering utilizing the degrees of freedom of both electrons and spins of materials, has been actively studied. In particular, its application to information transmission techniques that use spin waves is highly expected.

In this study, we discovered remarkable spin waves with more than ten times the amplitude of those previously reported. This was realized by temporally and spatially observing the behavior of spins in a ferrimagnetic Gd–Fe–Co thin film immediately after the irradiation of ultrashort laser pulses [1].

Usually, spin directions can be switched by applying magnetic fields or electric pulses. Likewise, spin waves can be generated by applying radio-frequency magnetic or electric fields. In this study, however, we applied a recently developed method to manipulate spins by using ultrafast laser pulses (pulse width: ~100 fs). Because light-induced spin wave generation is theoretically a nonthermal process, it may lead to the development of new electronic devices with lower power consumption. Conversely, the discovery of new magnetization control methods, for example, spin manipulation using spin-lattice coupling, is also expected by making use of thermal activation by laser beams.

To effectively control spin directions, ferrimagnetic Gd–Fe–Co alloy films are used as materials because of their strong magneto-optical interaction. Gd–Fe–Co alloys have different angular-momentum compensation temperatures (T_A) depending on their composition. In addition, it is known that anomalously strong precession damping takes place at T_A. Therefore, as shown in Fig. 1, light-induced spin dynamics depends on the ambient temperature of the sample relative to its T_A; when T_A is below or above the experimental temperature, we expect prolonged magnetization precession and rapid magnetization reversal, respectively [2].

Experiments were performed at SPring-8 **BL25SU** soft X-ray beamline [3] by visualization of the X-ray magnetic circular dichroism effect using a photoemission electron microscope (XMCD-PEEM) combined with a pump-probe technique [4]. Figures 2(a) and 2(b) show time-dependent XMCD-PEEM images of $Gd_{26}Fe_{66}Co_8$ and $Gd_{22}Fe_{70}Co_8$ thin films, respectively. In the $Gd_{26}Fe_{66}Co_8$ sample (Fig. 2(a)), the magnetization mostly settled to its final state approximately 1 ns after the excitation. However, in the $Gd_{22}Fe_{70}Co_8$ sample (Fig. 2(b)), a packet of wavelike spin modulation propagated isotropically along the radial direction from 800 ps to 5 ns post-irradiation. Precise analysis of the modulation of the XMCD signals revealed that precession angle of the spin waves was extremely large, approximately 20° (±10°) (Fig. 2(c)). Taking into account the temporal resolution of the present study, the actual precession angle may be approximately double this value up to ~40° (±20°). This value is orders of magnitude higher than that ever observed in spin waves generated by either electric fields or optical excitation, where precession angles are typically in the range of ~0.1–1°.

We proved by some other simulations and comparative experiments that this unusual phenomenon is triggered by resonant magnetization precession as

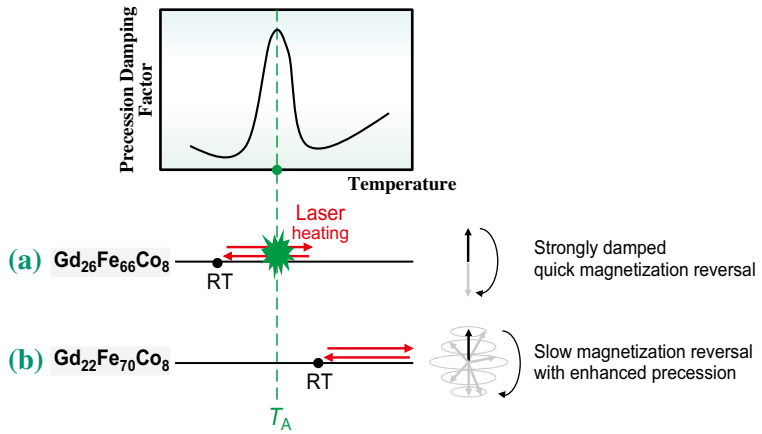

Fig. 1. Schematic of magnetization reversals induced by laser pulses of Gd–Fe–Co thin films. When the Gd content is 26% ($Gd_{26}Fe_{66}Co_8$, T_A>RT), smooth spin reversal with strong damping is expected. When the Gd content is 22% ($Gd_{22}Fe_{70}Co_8$, T_A<RT), the sample temperature does not intercept T_A and long-lasting spin precession is expected.

explained in Fig. 1(b). However, nonzero propagation momentum (*traveling* of the wavefronts) is likely produced by extrinsic factors such as lateral shifting of the precession phase due to a laser-induced radial heat gradient, considering (i) the large wavelength (on the order of 10 μm), which cannot be explained by intrinsic magnons generated in metallic systems, (ii) the limitation of the observed modulation to the irradiated spot, and (iii) the contraction and inward movement of the wavefronts toward the center of the spot (note that backward-volume magnetostatic waves are ruled out by the experimental geometry, which directs the magnetization perpendicular to the propagation direction of the waves). Nevertheless, we believe that the present observation provides a new point of view regarding how to generate spin waves. Considering that this phenomenon occurs as a consequence of a mixture of spin precession and heat excitation, experimental and theoretical searches for the possibility of spin-phonon coupling may also be worthwhile.

In fact, the Gd–Fe–Co system has previously been regarded as a good candidate capable of "ultrafast spin switching" (Fig. 1(a)), in other words, a "low" T_A condition (Fig. 1(b)) has been thought to be unfavorable for this purpose. In this study, however, we unexpectedly discovered a completely new functionality in Gd–Fe–Co ferrimagnets, *giant spin waves*, under this condition. Discoveries of highly pronounced novel phenomena sometimes accelerate the development of practical devices. For example, the giant magnetoresistance (GMR) effect was first reported as a tiny effect. Meanwhile, a phenomenon with the same mechanism was found by another research group at nearly the same time but the magnetoresistance ratio was approximately ten times larger than that observed by the other group [5]. The series of discoveries attracted much attention, leading to the development of GMR recording heads as well as the exponential improvement of recording density. We believe that the gigantic spin waves introduced here can serve as a trigger for the development of high-speed on-chip magnetic signal processing and control in spin-electronics applications.

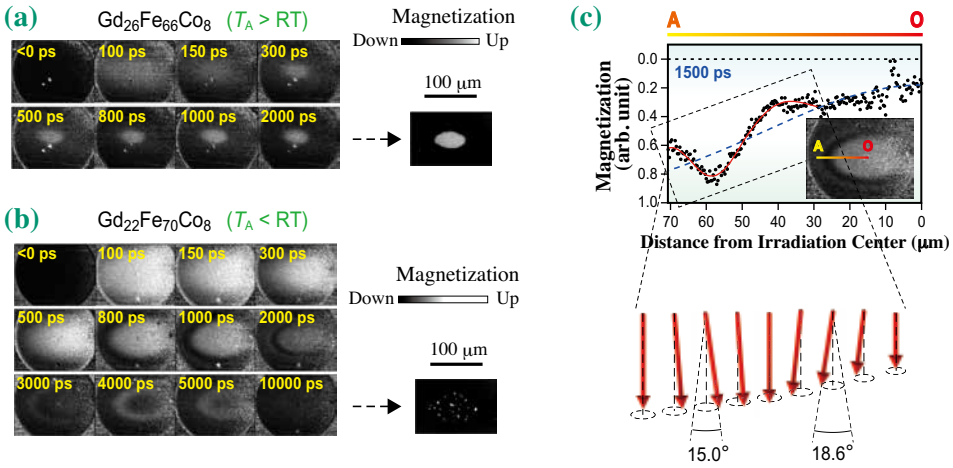

Fig. 2. Time-dependent magnetic images of the **(a)** $Gd_{26}Fe_{66}Co_8$ and **(b)** $Gd_{22}Fe_{70}Co_8$ samples. In the $Gd_{26}Fe_{66}Co_8$ sample, clear spin reversal is observed. However, in the $Gd_{22}Fe_{70}Co_8$ sample, wavelike magnetization modulation propagated isotropically along the radial direction. **(c)** Spin distribution of the $Gd_{22}Fe_{70}Co_8$ sample 1500 ps after the laser pulse duration. A line profile of the magnetization distribution (main graph), an XMCD-PEEM image snapshot (inset image), and the calculated distribution of spin directions (lower drawings) are shown. One can see propagating spin waves whose precession angle is in the range of 20° (±10°).

Takuo Ohkochi

Japan Synchrotron Radiation Research Institute (JASRI)

Email: o-taku@spring8.or.jp

References

[1] *T. Ohkochi, H. Fujiwara, M. Kotsugi, H. Takahashi, R. Adam, A. Sekiyama, T. Nakamura, A. Tsukamoto, C.M. Schneider, H. Kuroda, E.F. Arguelles, M. Sakaue, H. Kasai, M. Tsunoda, S. Suga and T. Kinoshita: Appl. Phys. Exp.* ***10*** *(2017) 103002.*
[2] C.D. Stanciu *et al.*: Phys. Rev. B **73** (2006) 220402(R).
[3] Y. Saitoh *et al.*: Rev. Sci. Inst. **71** (2000) 3254.
[4] T. Ohkochi *et al.*: Jpn. J. Appl. Phys. **51** (2012) 073001.
[5] G. Binasch *et al.*: Phys. Rev. B **39** 4828 (1989); M.N. Baibich *et al.*: Phys. Rev. Lett. **61** 2472 (1988).

Hydride complex with ninefold H-coordination

Hydrogen, although being the simplest element, exhibits an exceptionally rich chemistry, forming various types of chemical bonds in materials. The chemical flexibility is a source of many interesting properties of hydrides, such as hydrogen storage, fast ionic conductivity, magnetism, and the metal–insulator transition [1]. In particular, the recent discovery of the superconductivity at 203 K in the sulfur hydride system [2] has spurred tremendous research activity toward the exploration of hydrogen-rich materials.

Complex transition-metal hydrides represent a class of hydrogen-rich materials, wherein a number of H atoms covalently bind to the transition metals to form a varied set of homoleptic transition-metal hydride complexes with a remarkably rich variety of H coordination modes. These complexes are stabilized by charge transfer from electropositive counterions, such as alkali and alkaline earth metals, to form insulating hydrides [1]. In general, the H-coordination number increases from right to left along a given period of the periodic table because of the trend of increasing atomic size, which allows more hydrogen binding. At the same time, despite research spanning the past several decades, the elements capable of forming hydride complexes had been thought to be limited to those in Groups 7–12 [3]. This limitation had precluded the further discovery of hydride complexes with higher H-coordination numbers; however, the recent high-pressure and high-temperature technique overcame this limitation, and we successfully synthesized the novel hydrogen-rich material Mg_3CrH_8 as the first Group 6 hydride complex $[CrH_7]^{5-}$ [4]. The results strongly indicate that there is no *a priori* reason for the limitation and pave the way for the discovery of hydride complexes with higher H-coordination comprising unexplored elements to the left of Group 7, as illustrated in Fig. 1.

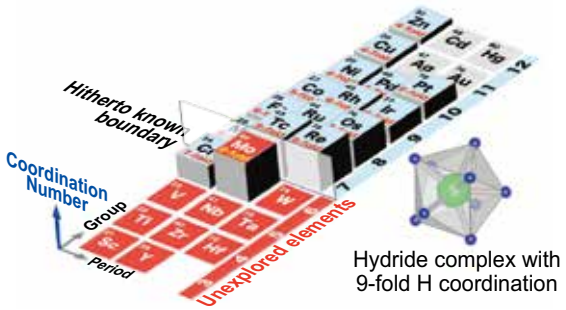

Fig. 1. Strategy for obtaining hydride complexes with high H-coordination.

On the basis of the above strategy, we examined the formation of novel transition-metal hydride complexes of the Group 6 element Mo [5]. Lithium was selected as a counterion because of its low electronegativity, which is expected to thermodynamically stabilize the complex hydride phases. Our density functional theory (DFT) calculations predicted that tricapped trigonal prismatic H-coordination (Fig. 1) allows the formation of strong σ-bonds between Mo and H, thus enabling the formation of the novel hydride complex $[MoH_9]^{3-}$ with ninefold H-coordination in Li_5MoH_{11}. Subsequently, the optimized synthesis conditions were effectively determined by *in situ* synchrotron radiation X-ray diffraction measurements using a cubic-type multianvil press installed at SPring-8 **BL14B1**. The crystal structure of the synthesized sample was investigated using a combined experimental and *ab initio* approach.

Figures 2(a) and 2(b) illustrate the DFT ground-state structure of Li_5MoH_{11}. The nine H atoms (H1) form a tricapped trigonal prism around the Mo atoms located at the (0, 0, 0) and (0, 0, 1/2) coordinates of the hexagonal lattice, and two isolated H atoms (H2) are located at the approximate centers of the trigonal prisms formed by the six Mo atoms. The four Li atoms coordinate to the H2 atoms, forming a two-dimensional network of corner-sharing tetrahedra between the layers of MoH_9 units.

Figure 2(c) shows the neutron diffraction (ND) profile of a sample obtained by the hydrogenation of a powder mixture of LiD and Mo at 5 GPa and 973 K for 48 h (open circles). We performed Rietveld refinement on the profile (black line in Fig. 2(d)) and obtained the *P*6cc structure (No. 184) of Li_5MoD_{11} with nine D atoms statistically distributed around the Mo atom, as depicted in Fig. 2(e). The statistical distribution is reasonably well reproduced by first-principles molecular dynamics (FPMD) calculations at 298 K, wherein the nine H1 atoms significantly rotate around the Mo atoms, generating a spherical shell-like distribution (Fig. 2(f)), as observed by the comparison of the simulated profile obtained from the FPMD trajectory (red line in Fig. 2(e)) with the Rietveld refinement fit. From these results, we concluded that the novel complex transition-metal hydride Li_5MoH_{11} containing the first reported ninefold H-coordination Group 6 hydride complex $[MoH_9]^{3-}$ was successfully synthesized.

Qualitatively, the electronic structures of complex transition-metal hydrides can be viewed as consisting of low-lying H 1*s*- and high-lying transition-metal (*T*) *spd*-derived states (Fig. 3). The ligand field induced

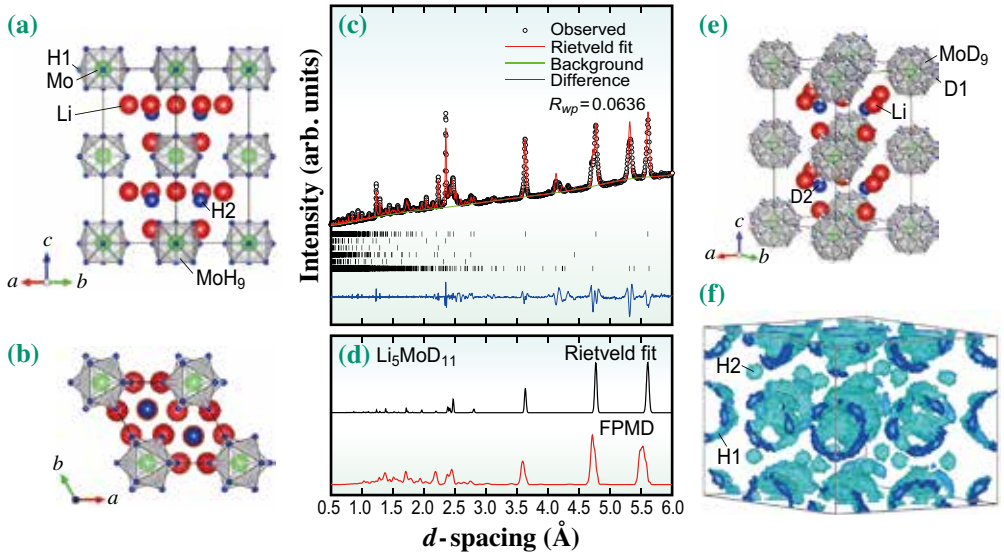

Fig. 2. DFT ground-state structure of **(a)** Li_5MoH_{11}/Li_5WH_{11} and **(b)** $Li_6NbH_{11}/Li_6TaH_{11}$. **(c)** Experimental ND profile of Li_5MoD_{11} measured at room temperature. The positions of Bragg reflections (tick marks) are shown for Li_5MoD_{11} (top), LiD (second), Mo (third), LiOD (third from bottom), Li_2O (second from bottom), and the unknown phase (bottom). **(d)** Rietveld fit of experimental profile (black line) and simulated profile obtained from FPMD trajectory at 298 K (red line). **(e)** Crystal structure of Li_5MoD_{11} determined by Rietveld analysis. **(f)** Time-averaged atomic-density profile obtained from the FPMD trajectory of H atoms at 298 K.

by the H-coordination divides the *T spd* states into nonbonding and antibonding states, and E_F normally falls in the ligand-field gap in order to accommodate the so-called 18-electron rule. The most striking point here is that the contribution from the H 1*s*-derived states in the valence bands increases with an increasing H-coordination number, reaching E_F at ninefold coordination. Such hydrogen-rich materials are very rare among solid-state hydrides containing transition metals and might be of interest in terms of high-T_c superconductivity if the band gaps close under compression.

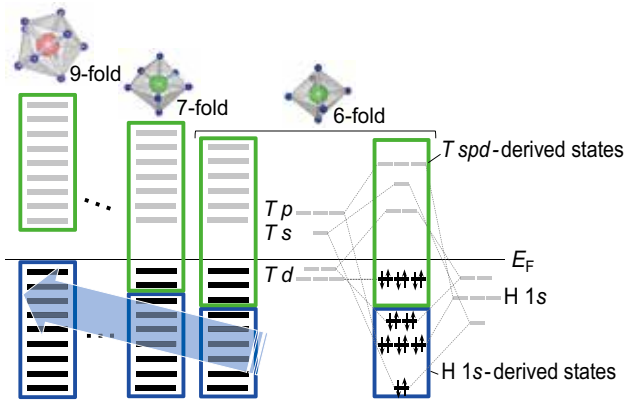

Fig. 3. Strategy for obtaining complex transition-metal hydrides with H 1*s*-derived states reaching the Fermi level (E_F). The electronic structures roughly comprise low-lying H 1*s*- and high-lying *T spd*-derived states. The contribution from H 1*s*-derived states to the valence bands increases with increasing H-coordination number and reaches E_F at ninefold H-coordination.

In addition to the above electronic feature, Li_5MoH_{11} has a characteristic phonon property such that the ninefold hydride complexes exhibit significant rotational motion even at room temperature, as demonstrated by our FPMD calculations. This type of motion has never been observed in complex transition-metal hydrides, but has often been discussed in relation to the occurrence of fast ion conduction in alkali metal *closo*-polyborane salts. Although we observed no obvious translational diffusion of Li^+ ions in our FPMD calculations because of the limited simulation time (12 ps) and the unit cell size (136 atoms), the significant rotational motion of $[MoH_9]^{3-}$ ions, as observed in Fig. 2(f), suggests the potential for fast lithium ion conduction even at room temperature.

Shigeyuki Takagi

Institute for Materials Research, Tohoku University

Email: shigeyuki.takagi@imr.tohoku.ac.jp

References

[1] S. Takagi and S. Orimo: Scripta Mater. **109** (2015) 1.
[2] A.P. Drozdov *et al.*: Nature **525** (2015) 73.
[3] K. Yvon: Chimia **52** (1998) 613.
[4] S. Takagi *et al.*: Angew. Chem. Int. Ed. **54** (2015) 5650.
[5] *S. Takagi, Y. Iijima, T. Sato, H. Saitoh, K. Ikeda, T. Otomo, K. Miwa, T. Ikeshoji and S. Orimo: Sci. Rep. 7 (2017) 44253.*

Charge transfer to ground-state ions in Ne-Kr mixed clusters producing slow electrons

When X-rays irradiate a light atom, an inner-shell electron is ejected, followed by the emission of one or several Auger electrons of relatively high energy (>200 eV). When X-rays irradiate condensed matter, however, the majority of emitted electrons have low kinetic energy (<20 eV). These slow electrons are traditionally believed to be secondary electrons produced via inelastic scattering of a photoelectron or Auger electrons at the surroundings atoms. In a biological system, a high potency for genotoxic effects has been assigned to these slow electrons [1].

About 20 years ago, new pathways were proposed to produce slow electrons in a loosely bound system. If an ion in the excited state is included in such a system, it may relax to the ground state, emitting an electron from a neighbor. This process is called interatomic/intermolecular Coulombic decay (ICD) [2]. Alternatively, an electron may be transferred from a neighbor to the ion, accompanied by electron emission from another neighbor. This process is called electron-transfer-mediated decay (ETMD) [3]. ETMD has been considered as a minor decay channel since it cannot compete with ICD [3]. It can, however, become a dominant relaxation pathway for configurations in which ICD is energetically forbidden. As an example, Stumpf *et al.* presented *ab initio* calculations for a NeKrKr trimer [4] and showed that ETMD takes place between Ne dications in their ground state and the Kr neighbors (Fig. 1). In this study, we report the experimental identification of this process using Ne-Kr mixed clusters [5].

The experiment was carried out at SPring-8 **BL17SU**. The photon energies were set to 878 eV and 888 eV, corresponding to 8 eV and 18 eV above the Ne 1*s* ionization threshold of 870 eV, respectively. A Ne-Kr mixed cluster beam was prepared by expanding a mixed gas through an 80 μm nozzle at a stagnation pressure of 0.6 MPa. The molar mixing ratio of Ne:Kr was 60:1. The temperature of the nozzle was 160 K. The resulting Ne:Kr ratio in the clusters estimated from the experiment was 4:1.

To measure ions and electrons originating from a cluster after a series of events, we used an electron-ion three-dimensional momentum coincidence spectrometer. The spectrometer consisted of two time-of-flight (TOF) spectrometers equipped with delay-line-type position-sensitive detectors. One of them detected ions and the other detected electrons. They faced each other with the crossing point of the X-rays and cluster beams between them. Knowledge of the position and arrival time at the detectors allowed us to extract information about the three-dimensional momentum of each particle.

We expected the production of three singly charged ions (one Ne ion and two Kr ions) and three electrons (photoelectron, Auger electron, and ETMD electron). To search for the target processes, we selected only the events in which we measured these three ions, and identified the photo- and ETMD electrons from electron spectra in coincidence with the events.

Figure 2 shows the TOF spectra of ions. Different

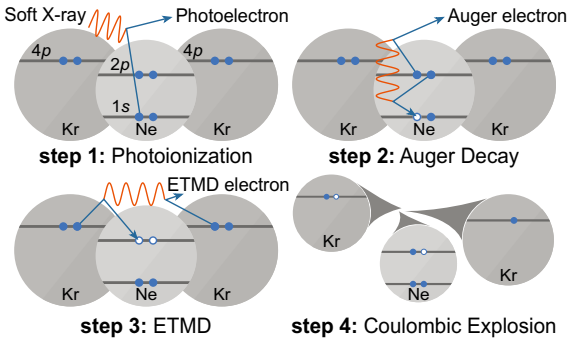

Fig. 1. Schematics of process investigated. First step (photoionization): an ionizing X-ray photon ejects a Ne 1*s* electron (photoelectron) from a Ne atom in a Ne-Kr mixed cluster. Second step (Auger effect): Auger decay of the resulting Ne ion leads to a dication with two holes in the valence shell and an ejected electron (Auger electron). Third step (ETMD): one of the electrons of a neighboring Kr atom fills one of the Ne valence holes, and one of the valence electrons of another Kr atom is ejected (ETMD electron). Fourth step (Coulomb explosion): the cluster explodes by Coulomb repulsive forces, and releases one singly charged Ne ion and two singly charged Kr ions. Filled blue discs indicate active electrons, and the positive charges are indicated by empty blue circles. [5]

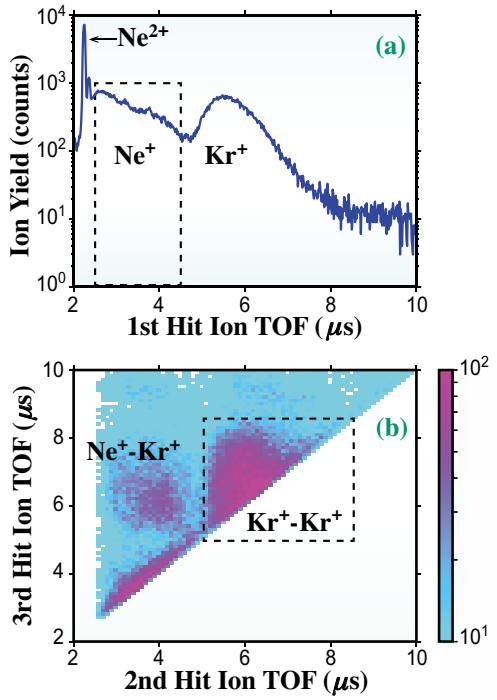

Fig. 2. TOF spectra of ions released from Ne-Kr mixed clusters showing results filtered for events in which three ions were detected in coincidence. The photon energy used was 888 eV. (**a**) TOF of the first ion arriving at the detector. The region surrounded by a dashed line was used to select events for a Ne monocation. **(b)** TOFs of the second ion versus the third ion detected in coincidence with the Ne ion as the first ion. The region surrounded by a dashed line was used to select events in which two Kr monocations were detected. The scale bar indicates counts. [5]

mass-to-charge ratios give rise to peaks at different TOF values. The initial velocities of ions broaden the peaks. We expected Ne and Kr monocations to appear around 3.2 μs and 6.5 μs, respectively, and selected only events in which we detected the target three ions.

Figure 3 shows the electron kinetic energy spectra. The regions around 8 eV and 18 eV in Fig. 3(a) correspond to Ne 1*s* photoelectrons. These regions provide evidence that the ion triples are indeed produced after Ne 1*s* photoionization. In addition to the photoelectrons, significantly enhanced intensity is seen around 0–5 eV. After subtracting the contributions from photoelectrons (Fig. 3(b)), we can more clearly see that the same low-energy component appears at both photon energies. The intensity of the 0–11 eV electrons, which is the energy corresponding to ETMD, is around 70% of that of the photoelectrons. This implies that a slow electron is almost always emitted from the cluster when a Ne 1*s* photoionization event occurs at the Ne-Kr interface.

Our results apply to relaxation pathways after interaction with energetic particles in a broad range of weakly bonded systems, for example, aqueous solutions. We show that non-local autoionization may occur even from states with no or a small amount of electronic excitation energy. Taking these processes into account is very important for understanding the chemical effect of radiation on a microscopic level.

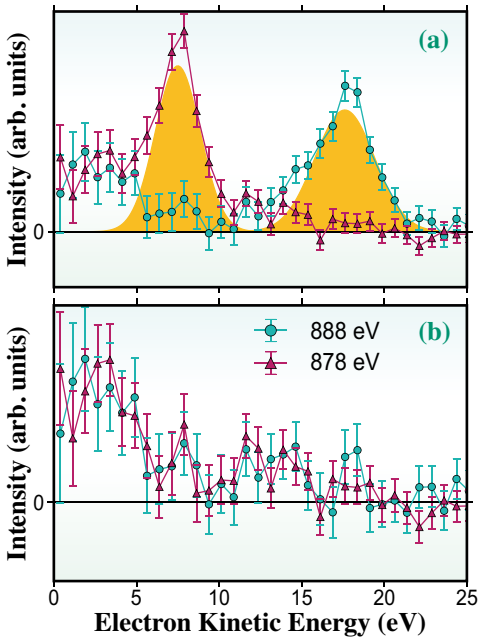

Fig. 3. Electron spectra in coincidence with the target ions. **(a)** Kinetic energy of electrons detected in coincidence with the ion triple. The two Gaussian functions fitted to the photoelectron peaks are also shown as yellow regions. **(b)** The same as (a) subtracting the contributions from photoelectrons, fitted by two Gaussian functions. The error bars in (a) and (b) are defined as standard deviations. [5]

Daehyun You[a,b], Hironobu Fukuzawa[a,b] and Kiyoshi Ueda[a,b,*]

[a] Institute of Multidisciplinary Research for Advanced Materials, Tohoku University
[b] RIKEN SPring-8 Center

*Email: kiyoshi.ueda.a2@tohoku.ac.jp

References

[1] B. Boudaïffa *et al.*: Science **287** (2000) 1658.
[2] L.S. Cederbaum *et al.*: Phys. Rev. Lett. **79** (1997) 4778.
[3] J. Zobeley *et al.*: J. Chem. Phys. **115** (2001) 5076.
[4] V. Stumpf *et al.*: Phys. Rev. Lett. **110** (2013) 258302.
[5] *D. You, H. Fukuzawa, Y. Sakakibara, T. Takanashi, Y. Ito, G.G. Maliyar, K. Motomura, K. Nagaya, T. Nishiyama, K. Asa, Y. Sato, N. Saito, M. Oura, M. Schöffler, G. Kastirke, U. Hergenhahn, V. Stumpf, K. Gokhberg, A.I. Kuleff, L.S. Cederbaum and K. Ueda: Nat. Commun.* ***8*** *(2017) 14277.*

Multi-photon superradiance from a nuclear ensemble

Understanding the response of large collections of atoms to external stimuli, based on the response of a single atom, is one of the interesting and fundamental problems in physics. One class of such problems is the decay of two-level atoms. An early, and now famous, treatment of this was Dicke's theory of superradiance [1]. He showed that the decay time of a collection of two-level atoms was strongly affected both by the number of atoms and the number of photons in the system. Specifically, for the case when all the atoms are very close to each-other, he showed that a system of n_a atoms or nuclei of which n_γ are excited, decays at an enhanced rate given by

$$\frac{I}{I_0} = n_\gamma n_a \left(1 - \frac{n_\gamma - 1}{n_a}\right) \approx n_\gamma n_a$$

where I/I_0 is the rate relative to the decay rate, I_0, of single atom or nucleus in isolation, and the approximate equality holds for small numbers of photons, $n_\gamma \ll n_a$. More generally [1] the response to pulse excitation of a (slightly) extended collection of oscillators behaved similarly, with $I/I_0 \approx n_\gamma n_a$ (again $n_\gamma \ll n_a$) with, now, n_a replaced by a geometric factor that scales as a phased sum over atom positions. In both cases, the enhanced decay rate relative to the single photon case for the system, I_1, by a factor

$$\frac{I}{I_1} = n_\gamma \left(1 - \frac{n_\gamma - 1}{n_a}\right) \approx n_\gamma$$

This enhanced decay rate, relative to the one-photon response, is what we investigated.

Nuclear resonant scattering of synchrotron radiation [2] offers a body of techniques that can be used to investigate the change in lifetime of a collection of oscillators. Indeed, it has been well demonstrated that the time response of a collection of nuclei after single photon excitation is rather different than that of isolated nuclear decay, with, in many cases a faster response, often called “speed-up”, that is found to be in excellent agreement with calculations. But the dependence on the number of photons, n_γ in the system, has not been investigated. Here, unfortunately, synchrotron based experiments are not much help, as the number of photons per pulse in the nuclear resonance bandwidth is only extremely rarely larger than 1.

The SACLA Free Electron Laser provides pulses with enough intensity so that one can begin to investigate the nuclear multi-photon response, at least for small numbers (<100) of photons/pulse. In particular, we performed the first nuclear scattering experiment at a Free Electron Laser beamline SACLA **BL3** to investigate the multi-photon aspect of the response [3]. The setup, Fig. 1, used the pure nuclear (111) reflection in a highly enriched perfect crystal of iron borate, $^{57}FeBO_3$, to select only the nuclear scattered radiation from the beam. A typical scope trace of one of the stack of 4 APD detectors, showing 18 photons detected after a single pulse is given in

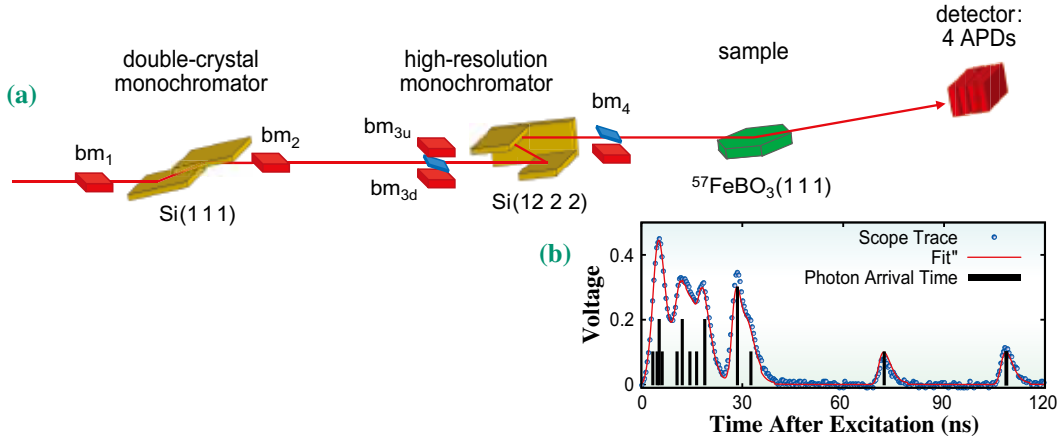

Fig. 1. **(a)** Experimental setup showing optical components, the sample, and beam intensity monitors (bm) and **(b)** scope trace of the response of the first diode after a pulse.

Fig. 1, confirming the multi-photon response. Figure 2 then shows an enhanced decay rate for the first photon observed as the number of detected photons increase, with the rate plotted in detail in the lower panel. One finds reasonably good agreement with the linear dependence expected from [1].

It turns out that the enhanced decay rate with increasing photon number is well explained by a statistical model, something that is not obvious from Dicke's treatment. Very simply, if one considers the probability distribution for the emission of a photon after the pulse to be given, in a small photon number limit, by $f(t)$, and then one considers a large number of photons placed into that distribution, then rather naturally, the time to the first photon is reduced, so the observed initial decay rate is enhanced. This is easy to see, either from Monte-Carlo simulations, or the analytic approach of [3]. Notably, the decay of the entire energy in the system keeps the shape of the single photon response, $f(t)$, (Fig. 3) so, when the number of photons in the system is not too large ($n_\gamma \ll n_a$), the time response, in the sense of the decay of the total energy in the system, not just the time to the first photon, still can be calculated using the usual formalism for nuclear scattering. This then also opens the door to single-shot hyperfine spectroscopy [3].

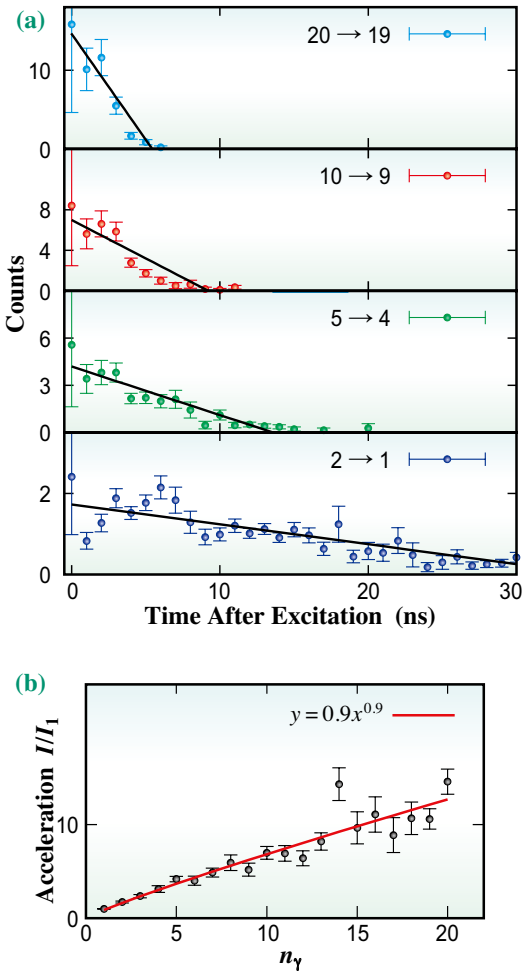

Fig. 2. **(a)** I/I_1 for different numbers of total detected photons. **(b)** Decay rate *versus* photon number.

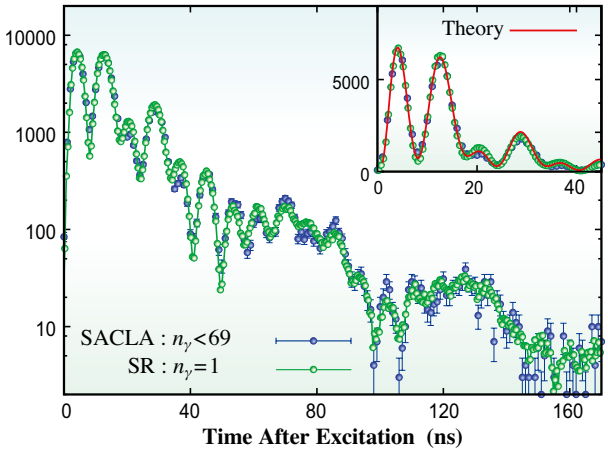

Fig. 3. Comparison of the time response for a multi-photon excitation at SACLA and the single photon excitation at a storage ring. The inset shows both data sets and a theory curve.

Alfred Q. R. Baron[a,*] and Aleksandr I. Chumakov[b]

[a] RIKEN SPring-8 Center
[b] European Synchrotron Radiation Facility (ESRF), France

*Email: Baron@spring8.or.jp

References

[1] R.H. Dicke: Phys. Rev. **93** (1954) 99.
[2] E. Gerdau and H. de Waard: Hyperfine Interact. **123-125** (2000).
[3] *A.I. Chumakov, A.Q.R. Baron, I. Sergueev, C. Strohm, O. Leupold, Y. Shvyd'ko, G.V. Smirnov, R. Rüffer, Y. Inubushi, M. Yabashi, K. Tono, T. Kudo and T. Ishikawa: Nat. Phys.* ***14*** *(2017) 261.*

Water molecules in action, in real space and time

Water is arguably the most important substance to life. Yet, its properties are shrouded in mystery. For instance, usually liquid becomes denser as it is cooled. But the density of water peaks at 4°C and then decreases. This and other strange behaviors arise in large part because of hydrogen bond which is highly quantum-mechanical in nature. To elucidate such behaviors the traditional axiom in materials science to figure out the structure-property relationship does not help, because a liquid does not have a "structure"; strictly speaking the intensity of elastic neutron or X-ray scattering from a liquid is zero. Instead the snapshot (equal-time) pair-density function (PDF), $g(r)$, is used as the substitute for the "structure". But trying to guess at the dynamics based upon the snapshot structure is like buying stocks knowing only today's stock prices. It does not work.

Atomic dynamics has been described either in terms of collective excitations, such as phonons, or diffusion. Collective dynamics is studied by measuring the dynamic structure factor, $S(Q, E)$, where Q and E are the momentum and energy transfers in scattering, using inelastic neutron or X-ray scattering. Diffusion is measured by quasi-elastic scattering. However, the dynamics in liquid is neither collective nor purely diffusive. Phonons are strongly overdamped due to dynamic disorder, and diffusive motions are highly correlated because liquid is not a gas, but is a condensed matter with strong atomic correlation.

In order to observe such locally correlated dynamics directly we applied the double-Fourier-transformation from Q to r (real space) and E to t (time), to $S(Q, E)$, and obtained the Van Hove function, $G(r, t)$ [1]. The Van Hove function describes the time evolution of the distribution of the atomic distance, $r_{AB}(t) = |\boldsymbol{r}_A(0) - \boldsymbol{r}_B(t)|$, where $\boldsymbol{r}_A(0)$ is the position of the atom A at $t = 0$, and $\boldsymbol{r}_B(t)$ is the position of the atom B at time t. At $t = 0$ it is equal to the snapshot PDF; $G(r, 0) = g(r)$, and $G(r, t)$ describes how the correlations become weaker as t is increased. The Van Hove function was defined in 1954, but nobody used it because it has been difficult to measure it. In order to determine the Van Hove function we have to know $S(Q, E)$ over a wide Q-E space, whereas the inelastic scattering measurements were slow. With a reactor neutron source and a triple-axis-spectrometer it takes a few hours just to get one energy scan at a constant Q.

However, the advent of pulsed neutron source with a two-dimensional detectors for inelastic neutron scattering (INS) [2] and progress in the instrumentation of inelastic X-ray scattering (IXS) [3] made it possible to determine $S(Q, E)$ over a Q-E space wide enough for accurate Fourier-transformation. We used the high-resolution IXS beamline **BL35XU** at the SPring-8 facility to determine $S(Q, E)$ over $1.3\ \text{Å}^{-1} \leq Q \leq 9.5\ \text{Å}^{-1}$ and $-10\ \text{meV} \leq E \leq 100\ \text{meV}$ for water (H_2O) at room

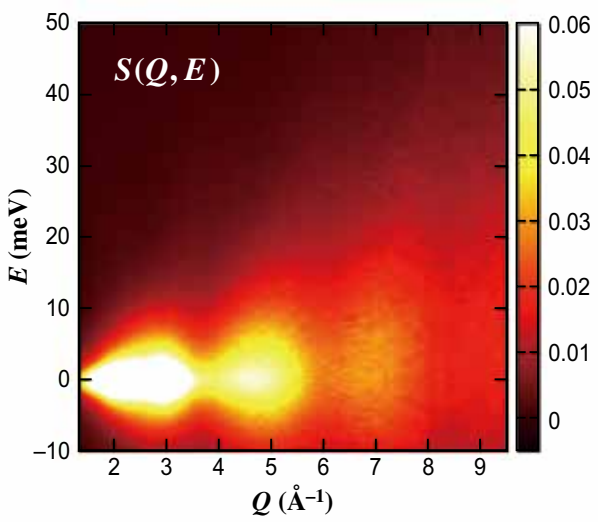

Fig. 1. The dynamic structure factor $S(Q,E)$ of water at room temperature determined by IXS measurement at SPring-8 BL35XU [4].

temperature, as shown in Fig. 1 [4]. We chose IXS to focus on the molecular dynamics, because hydrogen hardly scatters X-ray, so the Van Hove function obtained by IXS is dominated by the oxygen-oxygen, thus inter-molecular, correlations.

As shown in Fig. 1 $S(Q,E)$ of water is totally dominated by the quasi-elastic scattering (QEXS). Phonons are there (27 meV at 1.3 Å^{-1}), but are all but invisible in this intensity scale, because they are overdamped and their spectral density is quite low. The QEXS intensity is nearly featureless and is it hard to figure out what information it can provide.

However, once $S(Q,E)$ is converted to the Van Hove function as shown in Fig. 2, it conveys rich information regarding the local dynamics. In Fig. 2 the intensity around $r = 0$ is due to self-correlation. At $t = 0$ the nearest neighbor peak is seen at 2.8 Å and the second and third peaks at 4.5 and 6.8 Å. Surprisingly the first and the second peaks come closer and appear to merge as t increases. It means that as soon as the neighbor molecule goes away the second neighbor comes in to take its place, because water molecules want to maintain its four neighbors environment. Water molecules do not do random walk, but their footsteps are highly correlated.

From this result we were able to determine the time it takes for one nearest neighbor of a molecule to go away by cutting the hydrogen bond. This time, τ_{LC}, was found to be equal to the Maxwell relaxation time, $\tau_M = \eta/G_\infty$, where η is viscosity and G_∞ is the high-frequency shear modulus. τ_M is the time-scale which characterizes the time-dependent mechanical response of liquid. Earlier we have shown that $\tau_M = \tau_{LC}$ through computer simulation [5]. This work provides the first experimental confirmation of this prediction, and proves that the origin of viscosity in liquid is the excitation in the local topology of atomic connectivity network [5].

This work demonstrated that local atomic and molecular dynamics can be directly studied by IXS. We are now examining how addition of salt and other ionic compounds will modify the local dynamics in water. This work opens up a huge new field of study for local dynamics in liquid and other soft matter, impacting soft-matter physics, chemistry, and possibly biology and even medical sciences.

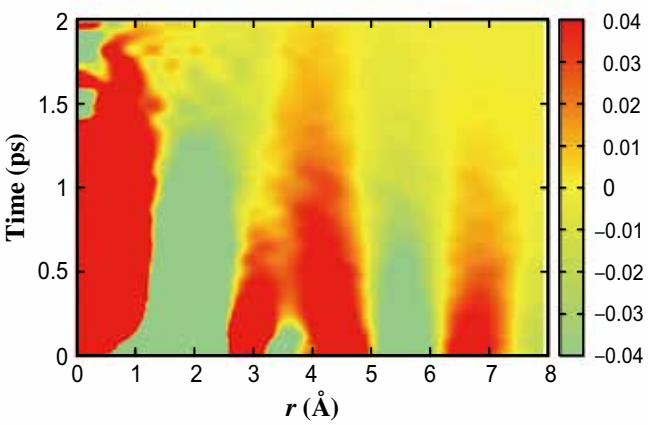

Fig. 2. The Van Hove function of water at room temperature determined by the IXS measurement [4].

Takeshi Egami[a,b]

[a] Shull-Wollan Center – Joint Institute for Neutron Sciences, University of Tennessee and Oak Ridge National Lab., USA
[b] Department of Physics and Astronomy, University of Tennessee, USA

Email: egami@utk.edu

References

[1] L. Van Hove: Phys. Rev. **95** (1954) 249.
[2] T.E. Mason *et al.*: Physica B **385-386** (2006) 955.
[3] A.Q.R. Baron *et al.*: J. Phys. Chem. Solids **61** (2000) 461.
[4] *T. Iwashita, B. Wu, W.R. Chen, S. Tsutsui, A.Q.R. Baron and T. Egami: Science Adv. **3** (2017) e1603079.*
[5] T. Iwashita *et al.*: Phys. Rev. Lett. **110** (2013) 205504.

Use of Kramers–Kronig relation in phase retrieval calculation in X-ray spectro-ptychography

Coherent diffraction imaging (CDI) is a method for reconstructing the complex-valued images of objects from their diffraction intensities by using iterative phasing methods. CDI provides information on both the phase shift and the absorption of incident beams due to the interaction with electrons in objects. It is therefore considered that CDI substitutes computational image reconstruction for an image-forming lens. Ptychography, which is a scanning CDI method, is the most practical approach to CDI at third-generation synchrotron facilities since it is free from limitations on the sample size. X-ray ptychography can also provide us with chemical information of a sample by using an X-ray absorption edge, i.e., multiple-energy ptychographic diffraction data are collected in the vicinity of the absorption edge, and then element-specific images are reconstructed, which is often referred to as X-ray spectro-ptychography. An ultimate form of X-ray spectro-ptychography is to reconstruct the X-ray absorption fine structure (XAFS) at the nanoscale. Recently, the XAFS of Fe_3O_4 nanoparticles [1] has been reconstructed by soft X-ray spectro-ptychography. Extending this approach to the hard X-ray region will enable us to visualize the chemical state of nanostructures buried within thick samples. However, a limitation of this method is the weak absorption of incident X-rays in the hard X-ray region. In order to improve the convergence of the phase retrieval for complex-valued images in X-ray spectro-ptychography, we proposed the addition of a constraint based on the Kramers-Kronig relation (KKR) to phase retrieval algorithms [2]. In this study, we also performed a proof-of-principle experiment on the reconstruction of near-edge XAFS spectra by X-ray ptychography.

A nanostructured object composed of Mn_2O_3 was used as the test sample. A 600-nm-thick Mn_2O_3 layer was deposited on a 500-nm-thick Si_3N_4 membrane chip, and then both a pattern comprising the characters of “SPring-8” and a square hole were fabricated using a focused ion beam. Figure 1(a) shows a field-emission scanning electron microscopy (FE-SEM) image of the sample. Ptychographic diffraction data of the sample were collected at SPring-8 **BL29XUL**. Figure 1(b) shows a schematic drawing of the experimental setup. A monochromatic X-ray beam was generated by an in-vacuum undulator device and a Si(111) double-crystal monochromator. Fourteen X-ray energies were selected between 6.530 keV and 6.588 keV, around the *K* absorption edge of Mn. The incident

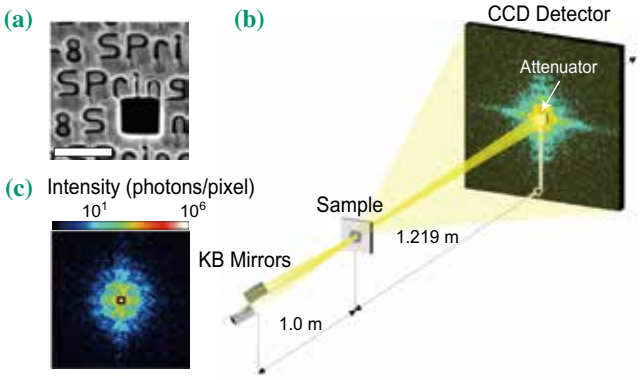

Fig. 1. **(a)** FE-SEM image of the test sample. The scale bar is 1 μm. **(b)** Experimental setup at BL29XUL. **(c)** Coherent diffraction pattern of the sample at 6.554 keV.

X-rays were two-dimensionally focused to a ~500 nm (FWHM) spot size using a pair of Kirkpatrick–Baez (KB) mirrors. The sample was positioned at the focal plane and mounted on piezoelectric stages inside a high-vacuum chamber. A diffraction dataset was collected at each position using an in-vacuum front-illuminated CCD detector with a pixel size of 20×20 μm^2, placed 1219 mm downstream of the sample position. To measure the bright field and increase the effective dynamic range of the diffraction intensity, 10-μm-thick Ta with a size of 640×640 μm^2 was installed in front of the CCD detector as a semitransparent central stop. The exposure time at each position was 2.8 s and it took ~1 h to collect 49 patterns at each X-ray energy, which includes the readout time from the detector and the time required for position correction. The illumination position was corrected at each scanning column by the drift compensation method. This method allows us to radiate the focused X-ray beam with greater accuracy than 10 nm, which was smaller than the pixel size of the reconstructed image. The fluctuation of the incident X-ray energies was much less than 1 eV, which was smaller than the minimum step of the present experiment. Figure 1(c) shows the coherent diffraction pattern of the sample at 6.554 keV. The dynamic range of the diffraction intensity was 1.0 photon/pixel to 1.9×10^6 photons/pixel.

Both the sample image and the probe were reconstructed by using a phase retrieval algorithm with and without the KKR constraint. The initial inputs of the object function were constant values and the initial input of the probe was estimated by considering

our experimental parameters. Figures 2(a) and 2(b) show the reconstructed amplitude and phase images at 6.542 keV and 6.554 keV, respectively, after 2×10^3 iterations using the KKR constraint every 100 iterations. The reconstructions were in good agreement with the FE-SEM image of the sample. The spatial resolution of the images was determined to be 41.1 nm using the phase retrieval transfer function. The amplitude image showed better contrast at 6.554 keV, which is above the Mn *K* absorption edge. Next, near-edge XAFS spectra were derived from the absorption images. Figures 3(a) and 3(b) show four near-edge XAFS and phase spectra without and with using the KKR constraint, respectively, which were extracted from the 40×40 nm^2 regions indicated by the arrows in Fig. 2(b). The top spectrum in Fig. 3(a) is the reference spectrum measured in the transmittance mode. Without using the KKR constraint, a strong subpeak appears in addition to the main peak. On the other hand, using the KKR constraint, the intensity of the subpeak decreases and the spectra become closer to the reference spectrum. The RMS error between the reference spectrum and average of the spectra obtained by X-ray spectro-ptychography was improved from 0.232 to 0.178 by using the KKR constraint. It is clear that the KKR constraint works well and provides us with more precise XAFS spectra.

When the range of the X-ray energy in X-ray spectro-ptychography is extended to much higher regions, an extended X-ray absorption fine structure (EXAFS) appears in the absorption images. The EXAFS enables us to directly determine the local atomic structure around a specific element. The signal of the EXAFS is extremely small compared with that of the near-edge XAFS, and the present reconstruction algorithm with the KKR constraint will be useful for reconstructing the EXAFS signal. In the near future, we believe that the present approach will provide a novel way to understand the relationship between the local atomic structure and the chemical state in unprecedentedly small amounts of materials.

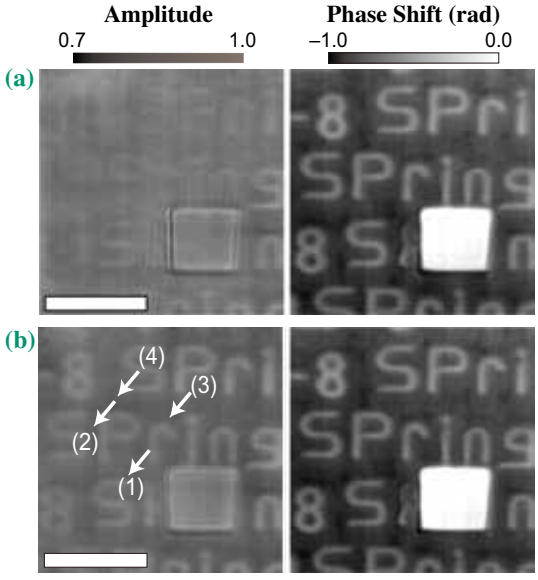

Fig. 2. **(a, b)** Amplitude (left) and phase (right) images reconstructed from the ptychographic diffraction patterns at **(a)** 6.542 keV and **(b)** 6.554 keV. The scale bar is 1 μm.

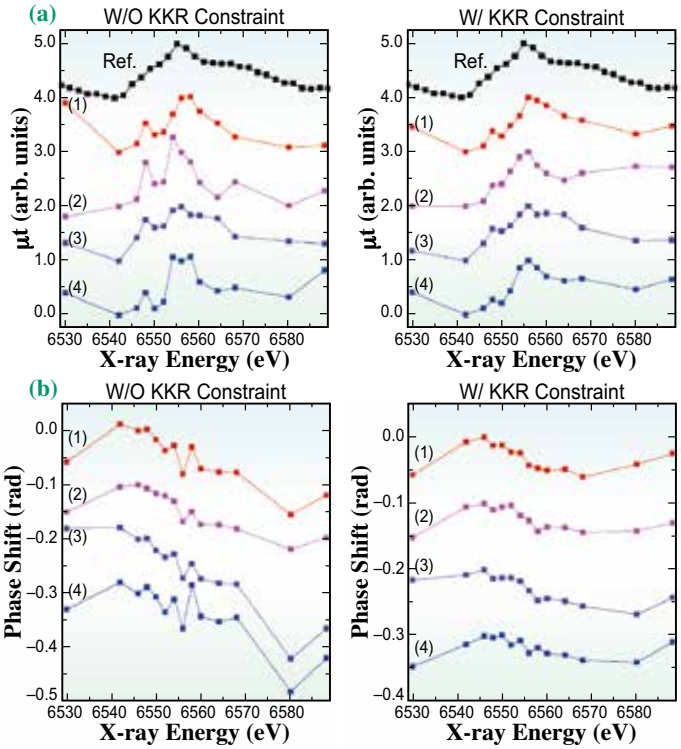

Fig. 3. **(a)** Near-edge XAFS spectrum of the sample measured in transmittance geometry using a focused X-ray beam (top). Near-edge XAFS spectra reconstructed by X-ray ptychography without (left) and with (right) using the KKR constraint. The spectra were extracted from the 40×40 nm^2 regions (2×2 pixels) indicated by the arrows in Fig. 2(b). **(b)** Near-edge phase spectra at the same positions without (left) and with (right) using the KKR constraint.

Yukio Takahashi[a,b]* and Makoto Hirose[a,b]

[a] Graduate School of Engineering, Osaka University
[b] RIKEN SPring-8 Center

*Email: takahashi@prec.eng.osaka-u.ac.jp

References

[1] X. Zhu *et al.*: Proc. Natl. Acad. Sci. USA **113** (2016) 8219.
[2] *M. Hirose, K. Shimomura, N. Burdet, Y. Takahashi: Opt. Express* ***25*** *(2017) 8593.*

Damage micromechanisms in dual-phase steel investigated by combined phase- and absorption-contrast tomography

In general, the ductile fracture process in alloys consists of the nucleation, growth and coalescence of microvoids. The nucleation of microvoids is attributable to particle fracture and/or particle/matrix interfacial decohesion. The ductile fracture process might also be interrelated with various microstructural heterogeneities, such as pre-existing microdefects [1], particle clustering [2], microstructural anisotropy [3] and dual-phase (DP) microstructures [4]. It is reasonable to assume that the ductile fracture process is appreciably affected in the case of a DP microstructure, which is seen in DP steels that consist of a hard martensitic phase and a soft ferritic phase. In spite of extensive research activity, a variety of interpretations remain concerning the micromechanisms of damage nucleation in DP steels. With the advent of state-of-the-art imaging techniques, a thorough understanding of the detailed damage processes is expected, even when practical materials with three-dimensional (3D) complexity in their DP microstructures are investigated. Phase-contrast X-ray microtomography (XMT) techniques are capable of revealing such DP microstructures with reasonable spatial resolution. The present authors applied the single-distance phase retrieval technique to 3D observations of a DP stainless steel consisting of austenitic and ferritic phases [5,6], In the present study, the single-distance phase retrieval technique was applied to contrast-enhanced imaging of the DP microstructure of a ferrite/martensite DP with only 1.4% difference in density between the two phases [7]. The XMT experiments were performed at SPring-8 **BL20XU** beamline.

The loading step at which each microvoid was nucleated was identified by tracking the microvoid throughout the application of tension, together with its nucleation site. The growth curves of individual microvoids are collated and classified according to their nucleation site in Fig. 1. Wider variation in the growth rate is apparent in the case of microvoids nucleated due to martensitic cracking. The four microvoids with high growth rates were nucleated by martensitic cracking at an applied strain of 23.9%, and later propagated in oblique directions with respect to the loading direction.

The largest microvoid seen in Fig. 1 has been extracted in Fig. 2, together with adjacent martensitic particles. The microvoids shown in Fig. 2 were nucleated where the martensitic phase exhibited morphological complexity such as a notch or neck.

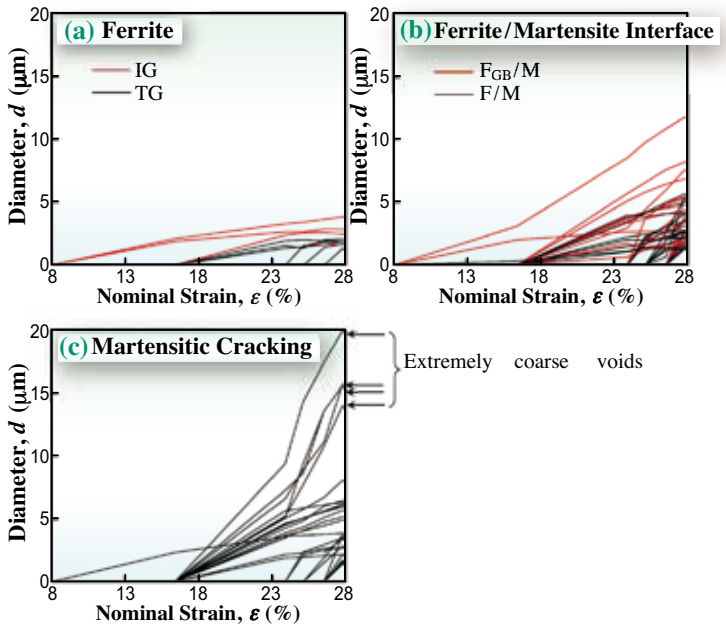

Fig. 1. Growth behavior of individual microvoids extracted from a unit box located at the center of the specimen. The growth data were organized according to the microvoid nucleation sites: **(a)** microvoids nucleated in the ferritic phase, which have been classified into intergranular (IG) and transgranular (TG) fracture; **(b)** the interfaces between the ferritic and martensitic phases, in which the intersections between martensite and the ferritic grain boundaries have been distinguished; and **(c)** the martensite fracture itself.

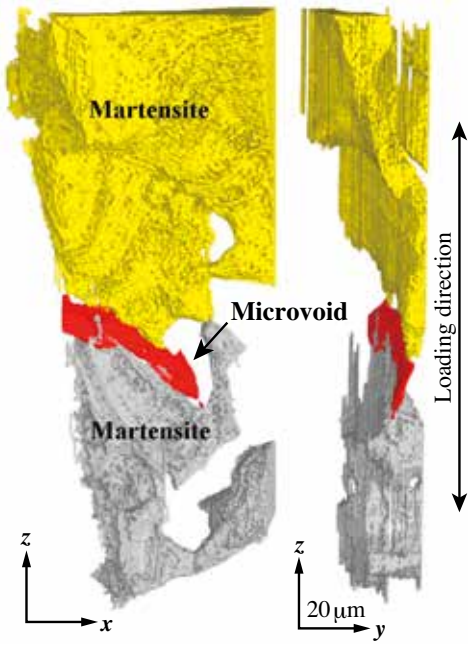

Fig. 2. 3D perspective views of a typical microvoid. The underlying ferritic phase is not displayed, and only the microvoid and the martensitic phase are shown.

No such morphological features were obvious at the other nucleation sites. It is clearly demonstrated that necked portions were sampled as a result of intense strain localization, and that the driving forces for subsequent rapid growth may arise from stress redistribution after martensitic cracking. In order to quantitatively evaluate the effects of the martensitic morphology, 3D strain mapping was performed for the interior of the martensitic phase. Tetrahedra, whose vertices were sites of morphological features such as concave and convex portions of the martensitic phase, were generated by the Delaunay tessellation technique, and normal and shear strains were then calculated on the basis of the deformation of each tetrahedron, assuming a linear displacement field inside it. The local strain distribution was illustrated in the form of a 3D color contour map, as shown in Fig. 3. It is interesting to note that in this figure, although the macroscopic applied strain range is only 11.4% (i.e., between the third and the last loading steps), high strain regions reach more than 50% in terms of the equivalent strain shown in Fig. 3(b).

Premature damage initiation was observed at a relatively early stage at various nucleation sites, such as the ferrite interior, martensitic interior and ferrite/martensite interfaces; however, the subsequent growth of such microvoids was relatively moderate. On the other hand, microvoids were also initiated later by martensitic cracking after the maximum load was reached, and these microvoids subsequently exhibited rapid growth. The martensite cracking induced additional damage evolution, mainly along nearby ferrite/martensite interfaces and intersections between the martensite and the ferrite grain boundaries. It is notable that the microvoids originating from martensitic cracking exhibited characteristic shear-dominated growth under macroscopic tension, whereas those originating from the other nucleation sites exhibited traditional triaxiality-dominated growth. It was concluded that the ductile fracture was dominated by the substantial force driving the growth of microvoids located on morphologically characteristic martensitic particles.

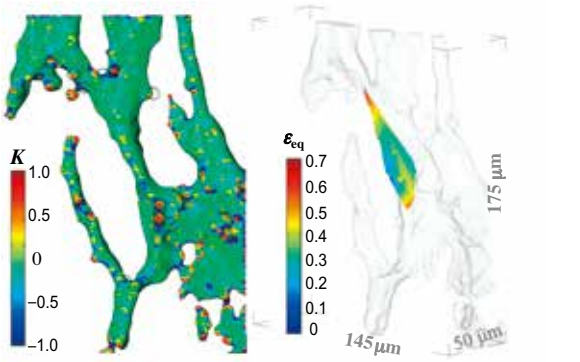

(a) Gaussian Curvature **(b) Local Strain Map for an Applied Strain Change of 11.4%**

Fig. 3. Results of 3D strain mapping of cracked martensite, which was measured between an applied strain of 16.4 and 27.8%. **(a)** Spatial distribution of Gaussian curvature value superposed on the extracted image of a martensitic phase region. **(b)** 3D contour of equivalent strain. Circles in **(a)** denote morphological features used for the 3D strain mapping.

Kyosuke Hirayama[a,*], Hiroyuki Toda[a] and Masakazu Kobayashi[b]

[a] Department of Mechanical Engineering, Kyushu University
[b] Department of Mechanical Engineering, Toyohashi University of Technology

*Email: hirayama@mech.kyushu-u.ac.jp

References

[1] H. Toda *et al.*: Metall. Mater. Trans. A **45** (2014) 765e776; L. Margulies *et al.*: Science **291** (2001) 2392.
[2] D. Steglich *et al.*: Eng. Fract. Mech. **75** (2008) 3692.
[3] C.Y. Tang *et al.*: J. Mater. Proc. Tech. **91** (1999) 270.
[4] E. Ahmad *et al.*: J. Mater. Eng. Perform. **21** (2012) 382.
[5] H. Toda *et al.*: ISIJ Int. **56** (2016) 883.
[6] H. Toda *et al.*: Proc. 4th Int. Symposium Steel Sci. (2014) 32.
[7] *H. Toda, A. Takijiri, M. Azuma, S. Yabu, K. Hayashi, D. Seo, M. Kobayashi, K. Hirayama, A. Takeuchi, K. Uesugi: Acta Materialia* ***126*** *(2017) 401.*

Mathematical design of molecular self-assembly

Molecular self-assembly is a phenomenon in which multiple molecular subunits autonomously assemble into an ordered structural form or pattern without any external direction. Self-assembled monolayer (SAM) films and mesoporous materials are the well-established examples that harness the mechanism of molecular self-assembly. Molecular machines, which were the topic of the 2016 Nobel Prize in Chemistry, are also closely related to molecular self-assembly. Accordingly, many people are increasingly likely to recognize the word "self-assembly" as a topic in chemistry. The concept of self-assembly has, however, never been limited to chemistry. Indeed many aspects of biological activity inside a cell can be appreciated as the ultimate form of molecular self-assembly. We have a lot to learn from such biological systems to realize more advanced technology. Unfortunately, it is not yet common to discuss the relationship between chemical and biological self-assembly. This is presumably because the number of subcomponents participating in self-assembly substantially differs in chemical and biological self-assembly. More specifically, the maximum number of subcomponents that can be handled in a chemically designed system is typically about ten, with the maximum number of components reported in the literature only being on the order of 10. In nature, on the other hand, there are many self-assembly systems that assemble hundreds of subcomponents even as discrete molecules. For instance, the capsid structure of Bluetongue virus shown in Fig. 1 consists of 900 protein subunits. Such a level of self-assembly has been a daunting challenge and beyond the reach of chemists. What we have achieved in our recent work is a proposal and demonstration of a geometric design strategy that enables self-assembly with a large number of components, which had previously been unachievable. It is not common to exploit the knowledge of mathematics in synthetic chemistry, but such a new approach was found to be effective. A mathematical description based on a geometric theorem clearly explained a previously reported self-assembly. Moreover, we succeeded in actually synthesizing a structure that was predicted by the theory. This is a structure self-assembled from 144 components, which is the largest self-assembled supramolecular cage ever reported. The methodology and the synthesis were described in Ref. 1. The following paragraphs summarize the results of the research.

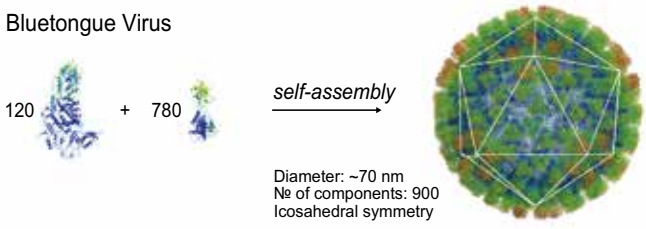

Fig. 1. Bluetongue virus. An example of a self-assembled molecule in nature.

The greatest challenge in a designing multi-component self-assembly is the "dispersion" of the number of components participating in the assembly. Similarly to micelles, vesicles, and polymers, upon assembling subunits, the dispersion of the number of subunits, and accordingly the dispersion of the resultant structure, is generally unavoidable. Such dispersion is a major obstacle to designing and implementing a precise function. Nonetheless, this issue can somehow be overcome in nature to achieve an accurate 900-component assembly, as shown in Fig. 1. How can it be? We focused on the fact that most spherical virus capsids have icosahedral symmetry. In geometry, restrictions such as congruity of the shape of faces or vertices significantly limit the number of possible polyhedra, for example regular and semiregular polyhedra are limited to only 5 and 13 species, respectively. Our hypothesis was as follows. If we can embed the nature of polyhedra within a system of a molecular assembly, only discrete products with limited numbers, sizes, and shapes of components will be realizable, thus enabling a molecular assembly without structural dispersion. We tested this hypothesis using a self-assembly system, in which bent ditopic organic ligands (L) and divalent palladium ions with square planar coordination sites (M) assemble into discrete M_nL_{2n} metal complexes [2]. The bend angle of L is the key to obtaining closed spherical structures rather than infinite networked structures (Fig. 2(a)). If we view the positions of metal ions (M) as vertices and those of organic ligands (L) as edges, each of the previously reported self-assembled structures can be recognized as semiregular polyhedra. In fact, when we fix the valency of vertices to four, which originates from the square planar coordination nature of palladium ions, only one of the regular polyhedra and four of the semiregular polyhedra fulfill the condition. Three of the five structures had been synthesized and the other two structures, the icosidodecahedron and rhombicosidodecahedron, were unprecedented. We

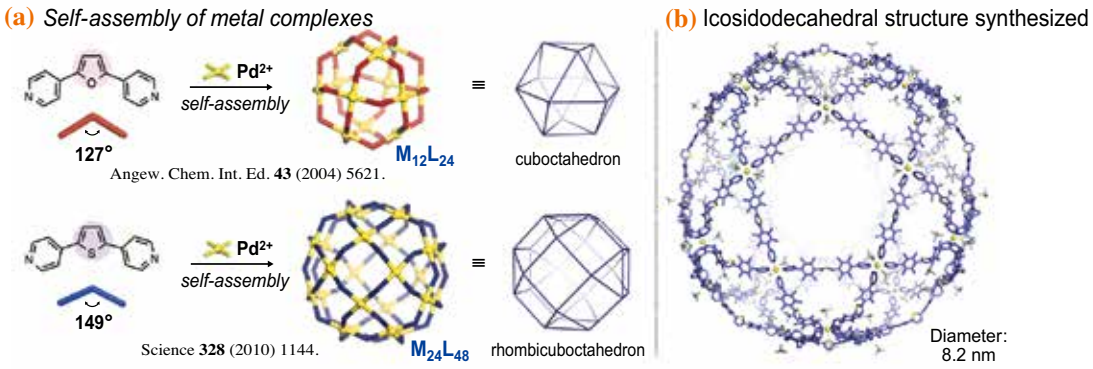

Fig. 2. Components and assembled structures of polyhedra.

then targeted the realization of the icosidodecahedron structure. If our hypothesis is correct, the fabrication of the icosidodecahedron structure will be challenging but theoretically feasible. We lack space to discuss the details here; however, by carefully tuning the structure of the organic ligand on the basis of the polyhedral design, we succeeded in synthesizing the icosidodecahedron structure at beamlines **BL38B1** and **BL41XU** in SPring-8 and at BL1A in Photon Factory (Fig. 2(b)) [3].

This approach based on the knowledge of polyhedra was further developed by combining it with more detailed mathematical discussion. The preceding discussion was limited to regular and semiregular polyhedra without a convincing theoretical justification. Also, the designable structures have an upper limit in terms of the number of subcomponents. We thus reconstructed the design theory based on the deduction from two chemical requirements: 1) all the vertices are tetravalent — a palladium ion has square-planar coordination sites, 2) all the edges are equilateral — the chemical structure of organic ligands remains unchanged on assembly, and one symmetrical postulation. As a result, by defining the $F(h, k)$ index (h, k = natural numbers) and the Q value ($Q = h^2 + k^2$) as a representative value, we realized that it clearly described the reported products of the M_nL_{2n} self-assembly without any defect or overlap. (Mathematically, such a discussion corresponds to the tetravalent Goldberg-Coxeter construction in combination mathematics.) This discussion is not limited to the analysis of observed phenomena and can be exploited as a design tool for creation. As predicted from the Q value, we succeeded in synthesizing an $M_{48}L_{96}$ structure consisting of 144 subcomponents, which is the largest synthetic supramolecular structure ever reported (Fig. 3) [1].

The methodology we developed has opened up a new landscape in the field of molecular self-assembly, where no logical synthetic strategy previously existed. It revealed that a mathematical approach is beneficial for predicting or designing unknown self-assembled structures. We expect that this research will accelerate the development of the field of molecular self-assembly.

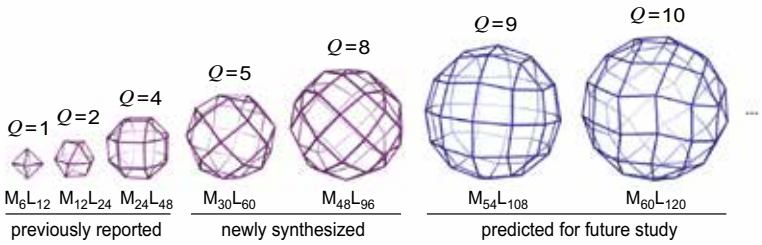

Fig. 3. The family of M_nL_{2n} polyhedra.

Daishi Fujita and Makoto Fujita*

Department of Applied Chemistry, The University of Tokyo

*Email: mfujita@appchem.t.u-tokyo.ac.jp

References

[1] *D. Fujita, Y. Ueda, S. Sato, N. Mizuno, T. Kumasaka, M. Fujita: Nature* ***540*** *(2016) 563.*
[2] K. Harris *et al.*: Chem. Commun. **49** (2013) 6703.
[3] *D. Fujita, Y. Ueda, S. Sato, H. Yokoyama, N. Mizuno, T. Kumasaka, M. Fujita: Chem* ***1*** *(2016) 91.*

Magnetic circular dichroism in X-ray emission

Advanced hard and soft magnets are key devices in modern technologies and are widely used in our everyday lives. Permanent magnets with high flux density and high coercivity are used in the motors in electric vehicles; electrical steel with high permeability and low core loss is used in transformers that supply electricity to houses. In order to improve the magnetic properties of these materials, it is necessary to observe the spatial distribution of magnetic domains under static and oscillating magnetic fields. In particular, observation of magnetic domains well below the surface of bulk magnetic materials is required from the viewpoint of industrial applications.

X-ray magnetic circular dichroism in the hard X-ray region (HXMCD) is a powerful technique suitable for the above-mentioned purpose. It utilizes a phenomenon that the X-ray absorption cross section of magnetized materials depends on whether the magnetization and the helicity of circularly polarized incident X-rays are parallel or antiparallel, particularly near the absorption edges. The use of highly collimated synchrotron X-rays in HXMCD makes it possible to provide a moderate spatial resolution of a few hundreds nanometers without a large loss of incident flux. The attenuation length of X-rays ranging from 5 to 10 keV, at which the *K* absorption edges of 3*d* transition-metal (TM) elements and *L* absorption edges of rare-earth elements reside, is approximately on the order of 10 μm. Accordingly, bulk-sensitive and element-selective magnetic microscopy is realized using HXMCD [1].

However, a disadvantage of HXMCD is a very small dichroic effect (about 0.5%) for 3*d* TMs, such as Fe, Co, and Ni, despite the fact that they are crucial elements in ferromagnetic materials. This difficulty has been overcome by using phase-sensitive detection for thin films [2], whereas it is still a problem for measurements of bulk materials. Therefore, there has been strong demand to find a new principle that enables magnetic circular dichroism measurement to be performed with a large dichroic effect for 3*d* TMs in the hard X-ray region. In this research, a new magneto-optical effect in the X-ray region is proposed and experimentally confirmed [3]. The new effect is that the dichroic effect is exhibited in X-ray emission, in sharp contrast to conventional XMCD, in which the dichroic effect is observed in X-ray absorption.

The basic idea of the new magneto-optical effect is presented below and also illustrated in Fig. 1. A spin-orbit coupling is a key requisite in magnetic circular dichroism. For instance, a small dichroic effect at the *K* absorption process of 3*d* TMs ($1s \rightarrow 4p$) stems from the fact that there is no large effective spin-orbit coupling in both 1*s* and 4*p* orbitals. In contrast, a large spin-orbit coupling exists in the final $2p^5$ state in the $K\alpha$ emission process ($2p \rightarrow 1s$). The $2p^5$ state splits into a $2p_{1/2}$ doublet and a $2p_{3/2}$ quartet owing to the large spin-orbit coupling, where the $2p_{3/2} \rightarrow 1s$ transition corresponds to the $K\alpha_1$ emission. The $2p_{3/2}$ quartet further splits because of the spin polarization in the 3*d* orbital through the sizable 2*p*3*d* exchange interaction. The resulting spin splitting of the $2p_{3/2}$ quartet also produces orbital splitting since the orbital state tightly couples to the spin state. Accordingly, because of this orbital splitting, a large dichroic effect is expected in the $K\alpha_1$ emission of 3*d* TMs.

The validity of this idea was established in experiments at SPring-8 **BL22XU**. The experimental setup is introduced below in detail and is illustrated in Fig. 2. The sample was an iron single crystal, which was inserted between permanent magnets in order to saturate the magnetization. The sample was illuminated by intense incident X-rays generated from an undulator and emitted fluorescence X-rays, which were collimated by an exit slit down to a divergence of 120 μrad in order that the optical elements mentioned below could operate. The quarter-wave plate (QWP)

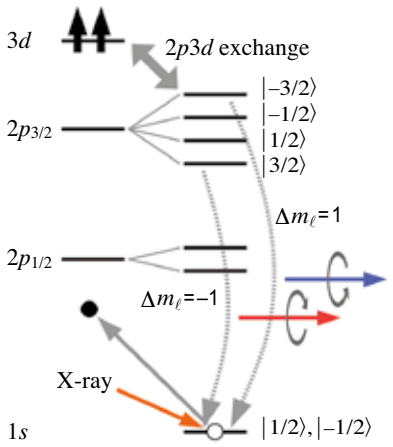

Fig. 1. $K\alpha_1$ emission process of a 3*d* TM ferromagnet. A 1*s* electron is promoted by an incident photon, and then a 2*p* electron fills the 1*s* core hole, emitting a $K\alpha$ photon. Representative two transitions are shown. The final $2p^5$ state splits into a $2p_{3/2}$ quartet and a $2p_{1/2}$ doublet owing to a spin-orbit coupling and further splits owing to a 2*p*3*d* exchange interaction. Numbers are the magnetic quantum numbers of sublevels and Δm_ℓ is the change in the orbital magnetic quantum number at the transition.

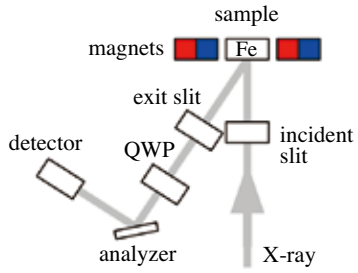

Fig. 2. Top view of the experimental layout. QWP: diamond phase retarder that acts as a quarter-wave plate. Analyzer: Ge(400) single crystal that is used as both an energy and polarization analyzer.

was a diamond single crystal and is a device that mutually converts circularly polarized X-rays and linearly polarized X-rays. The polarization analyzer that reflected the vertical component of the incoming fluorescence X-rays was a Ge single crystal and also functioned as an energy analyzer. The combination of a QWP and a polarization analyzer is a standard device for detecting the circular polarization of a beam of photons. In short, the device transmits right (left) circularly polarized X-rays and 50% linearly polarized X-rays when the QWP generates a $\pi/2$ ($-\pi/2$) phase shift.

The obtained Fe $K\alpha_1$ emission spectra are indicated in Fig. 3(a). I^+ (red open circles) and I^- (blue closed circles) are data observed when the $\pi/2$ and $-\pi/2$ phase shifts are induced by the QWP, respectively. The magnetic field is applied as shown in the inset (positive direction). It is clear that the I^+ spectrum is shifted to the low-energy side by about 0.3 eV compared with the I^- spectrum. The difference between the two spectra is direct evidence that the $K\alpha_1$ emission is circularly polarized. When the magnetic field is reversed, the tendency is reversed as shown in Fig. 3(b). The difference spectra I^+-I^- normalized by the peak intensity of the sum of the spectra are also shown in Fig. 3(c).

These results clearly illustrate that (i) the energy-resolved $K\alpha_1$ spectrum of ferromagnetic Fe indicates finite circular polarization and (ii) the circular polarization is inverted when the magnetization of the sample is inverted. These two features unambiguously indicate the existence of XMCD in the Fe $K\alpha_1$ emission. The flipping ratio $(I^+-I^-)/(I^++I^-)$ is a measure of the size of the dichroic effect and was 12 ± 4% at 6.405 keV. If the corrections for the scattering angle and the efficiency of the QWP are taken into account, the value would amount to 18 ± 6%.

To summarize, it was experimentally confirmed that magnetic circular dichroism actually exists in X-ray core-level emission and that the dichroic effect is quite large even in the *K*-edge of 3*d* TMs. Hence, this magneto-optical effect may open a new way to perform element-selective and truly bulk-sensitive measurements of the magnetization of 3*d* TMs.

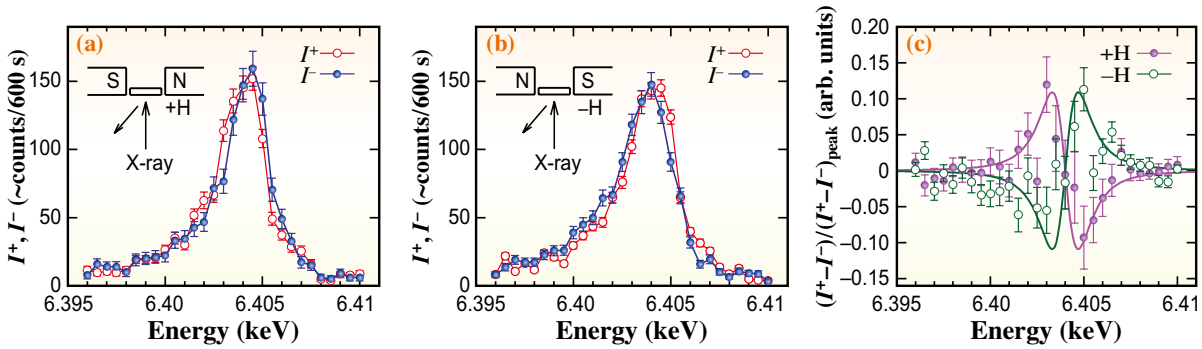

Fig. 3. **(a)** Fe $K\alpha_1$ emission spectra I^+ and I^- for a phase shift of $\pi/2$ (red open circles) and $-\pi/2$ (blue solid circles), respectively. The lines connect the data points to guide the eye. The magnetic field is applied as shown in the inset and the direction is defined as positive. The I^+ spectrum is shifted to the low energy side compared with the I^- spectrum. **(b)** Fe $K\alpha_1$ emission spectra I^+ and I^- when the magnetic field is applied along the negative direction. In contrast to (a), the I^+ spectrum is shifted to the high energy side. **(c)** Difference spectra between I^+ and I^- normalized by the peak intensity of the sum of the spectra. Magenta solid circles and green open circles are measurements when the magnetic field is directed along the positive and negative directions, respectively. Solid lines are a guide to the eye.

Toshiya Inami

National Institutes for Quantum and Radiological Science and Technology (QST)

Email: inami.toshiya@qst.go.jp

References

[1] M. Suzuki *et al.*: Acta Mater. **106** (2016) 155.
[2] T. Nakamura and M. Suzuki: J. Phys. Soc. Jpn. **82** (2013) 021006.
[3] *T. Inami: Phys. Rev. Lett.* ***119*** *(2017) 137203.*

Crystal-site-selective spectrum of Fe_3O_4 obtained by synchrotron Mössbauer diffraction

^{57}Fe Mössbauer spectroscopy is a local and dynamic probe that is very useful for investigating iron compounds. Through the hyperfine structure obtained by analysis of the spectrum, such as the isomer shift, quadrupole splitting, and hyperfine field, we can examine the electronic state, local crystal structure, and magnetic structure of Fe. In many cases, materials contain several Fe-sites, and their Mössbauer spectra are composed of the superposition of the corresponding subspectra. As a result, it often becomes difficult to analyze the spectrum and to determine precise hyperfine parameters. On the other hand, diffraction measurements, such as X-ray and neutron diffraction, provide information on each crystallographic site because their intensities are given by the structure factors of constituent atoms. The combination of both techniques, i.e., Mössbauer diffraction, enables us to obtain a crystal-site-selective spectrum.

The synchrotron Mössbauer source at SPring-8 **BL11XU**, where the ^{57}Fe energy domain spectrum is directly obtained, is very suitable for studying Mössbauer diffraction. The γ-ray (π-polarized, wavelength 0.8603 Å) emitted from the $^{57}FeBO_3$ nuclear Bragg monochromator has high directivity (angular divergence 3.0") and extremely high brilliance (10^5 times that of a usual radioactive source). Recently, using this source, we have developed a Mössbauer diffractometer by installing a θ–2θ goniometer as a sample stage between the nuclear monochromator and a detector [1,2]. A crystal-site-selective spectrum can be obtained by using only a selected γ-ray reflection, which enables us to determine precise hyperfine parameters in multi-Fe-site compounds. There still remains a problem that the reflected γ-ray from a specimen consists of the γ-ray scattered by the nuclei after the resonance (nuclear resonant scattering) and that scattered by the electrons of the atoms (electron scattering). The former gives a crystal-site-selective emission spectrum, while the latter only gives a usual transmission spectrum regardless of the reflection index. Therefore, in order to obtain a site-selective Mössbauer spectrum, only the nuclear resonant scattering should be extracted, or the electron scattering should be suppressed. For this purpose, we propose three methods:

(a) *Use of a pure nuclear Bragg reflection (pure nuclear method)*

When the Fe magnetic structure has a lower symmetry than the crystal symmetry, the pure nuclear Bragg reflection can be obtained, where the electron scattering is completely suppressed. A typical example is a forbidden reflection of a collinear antiferromagnet.

(b) *Use of a reflection having a Bragg angle (θ_B) near 45° (45° method)*

This method utilizes the nature of a π-polarized γ-ray where the polarization factor of the electron scattering $P_e = \cos 2\theta_B$ vanishes when $\theta_B = 45°$.

(c) *Use of a reflection from a polarization analyzer (polarization analyzer method)*

This method is essentially the same as the 45° method, except that an extra diffraction at a polarization analyzer, installed between the sample and the detector, is used. As an analyzer crystal, the Si(840) plane (θ_B = 45.1°) is suitable. The analyzer cuts off the electron scattering (π-polarization) regardless of the reflection index of the sample.

In the present research, we applied the 45° method to a typical multi-Fe-site compound, magnetite (Fe_3O_4) [3]. Magnetite has a cubic inverse-spinel structure (space group $Fd\bar{3}m$, lattice constant a = 8.396 Å at room temperature). The crystal structure is shown in Fig. 1. The A-site (8a, site symmetry $\bar{4}3m$) is occupied by an Fe^{3+} ion, while the B-site (16*d*, site symmetry $\bar{3}m$) is occupied by equal numbers of Fe^{2+} and Fe^{3+} ions. A schematic view of the experimental setup is illustrated in Fig. 2. A single-crystal specimen of 95% enriched $^{57}Fe_3O_4$ fabricated by the floating zone melting method (FZ) in a controlled oxygen pressure was mounted on a goniometer. The reflected γ-rays with 666 ($\theta_B = 32.26°$) and 10 10 0 ($\theta_B = 46.48°$) reflections were used to collect the spectra at room temperature with measurement times of 6 and 18 h, respectively. The Fe nuclear structure factors of the

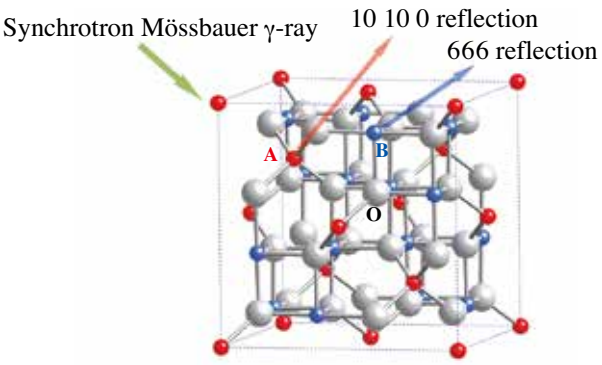

Fig. 1. Crystal structure of Fe_3O_4. A, B, and O denote A-site Fe, B-site Fe, and oxygen, respectively. The diffraction image for the 666 and 10 10 0 reflections is also illustrated.

666 and 10 10 0 reflections consist of only B-site and A-site Fe, respectively. The diffraction image is also illustrated in Fig. 1.

The Mössbauer diffraction spectrum collected by using only the 666 and 10 10 0 reflected γ-ray is shown in Figs. 3(a) and 3(b), respectively. The 666 reflection spectrum is mainly composed of the B-site emission spectrum due to the nuclear resonant scattering. However, there are some small dips due to the electron scattering since P_e is not zero but 0.43 for this reflection. The interference effect between the nuclear resonant scattering and the electron scattering, i.e., broadening of the lines, asymmetric line shapes, and a slope of the base line, is also notable. In such a case, the spectral shape can be expressed by the Fano function. We successfully analyzed the spectrum as shown by the smooth red curve in the figure. The assignments B(n), A(e), and B(e) denote the B-site spectrum due to the nuclear resonant scattering and the A- and B-site spectra due to the electron scattering, respectively. On the other hand, the 10 10 0 reflection spectrum is only composed of the A-site emission spectrum due to the nuclear resonant scattering and there is no interference effect ($P_e = -0.05$). As a first-order approximation, the spectrum can be analyzed by the Lorentzian function as shown by the smooth red curve in the figure.

Note here that we also succeeded in obtaining the crystal-site-selective spectrum by using the other two methods (a) and (c) [4,5]. For the pure nuclear method, another typical multi-Fe-site compound, the collinear antiferromagnet Fe_3BO_6, was used. Well-resolved 300, 500, and 700 reflection spectra were quantitatively analyzed using a formula based on the dynamical theory of diffraction. The intensity ratio of Fe1 to Fe2 subspectra originating from two different Fe sites in Fe_3BO_6 was in accordance with the nuclear structure factor. For the polarization analyzer method, the 222 reflection of Fe_3O_4 was used and only the B-site emission spectrum was obtained. Synchrotron Mössbauer diffraction is a clearly powerful tool for analyzing the highly complex Mössbauer spectrum in multisite materials.

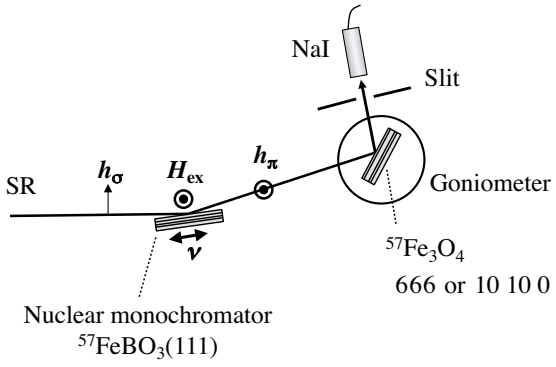

Fig. 2. Schematic view of the experimental setup at BL11XU. SR: synchrotron radiation. h_σ and h_π: unit magnetic field vectors of the incident (σ-polarized) and diffracted (π-polarized) radiation at the $^{57}FeBO_3$ nuclear monochromator, respectively. H_{ex}: external field (150 Oe) applied to the nuclear monochromator. NaI: scintillation detector.

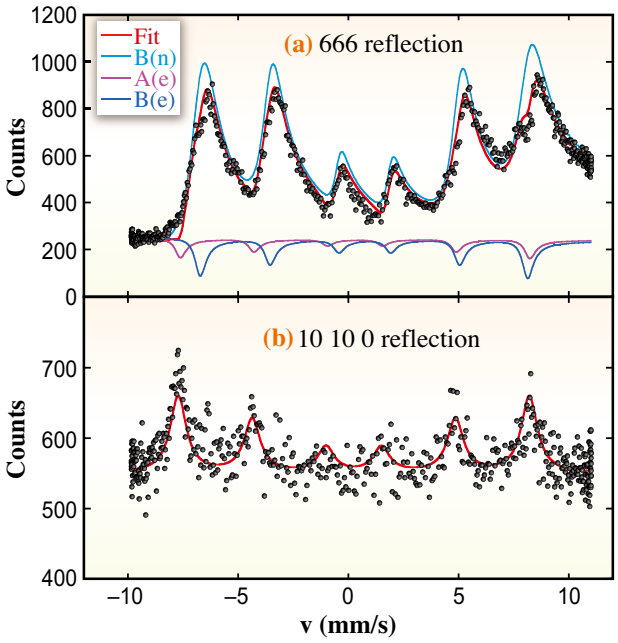

Fig. 3. Mössbauer diffraction spectrum of $^{57}Fe_3O_4$ collected by using **(a)** 666 and **(b)** 10 10 0 reflected γ-ray at room temperature. The assignments B(n), A(e), and B(e) denote the B-site spectrum due to the nuclear resonant scattering and the A- and B-site spectra due to the electron scattering, respectively.

Shin Nakamura[a,*], Takaya Mitsui[b] and Susumu Shimomura[c]

[a] Department of Science and Engineering, Teikyo University
[b] National Institutes for Quantum and Radiological Science and Technology (QST)
[c] Department of Physics, Kyoto Sangyo University

*Email: shin@koala.mse.teikyo-u.ac.jp

References

[1] T. Mitsui *et al.*: J. Phys. Soc. Jpn. **85** (2016) 054705.
[2] S. Nakamura *et al.*: Hyperfine Interact. **237** (2016) 157.
[3] *S. Nakamura, T. Mitsui, K. Fujiwara, N. Ikeda, M. Kurokuzu, and S. Shimomura: J. Phys. Soc. Jpn. **86** (2017) 023707.*
[4] *S. Nakamura, T. Mitsui, K. Fujiwara, N. Ikeda, M. Kurokuzu and S. Shimomura: J. Phys. Soc. Jpn. **86** (2017) 084701.*
[5] S. Nakamura and T. Mitsui: Solid State Phys. **52** (2017) 551. (in Japanese)

Formation of metallic cation-oxygen network in binary phosphate glass with anomalous thermal expansion coefficients

Oxide glass prepared by melt-quenching is usually composed of network former (NWF) and network modifier (NWM) groups [1]. P_2O_5 is generally classified as NWF groups from the viewpoint of glass-forming ability. However, P_2O_5 differs from other NWF oxides since the P=O bond allows delocalized electrons in phosphate glasses. Phosphate glasses are often considered for practical applications because of their durability but also have significant potential for several other uses owing to their distinctive physical and structural properties. Understanding the network structure of a phosphate glass system is therefore one of the most important unresolved issues facing glass science.

In contrast to the conventional NWF group, several metal oxides, which are classified as intermediate groups, can act as either NWF or NWM groups [1], depending on the glass composition. Zinc oxide is classified as being part of the intermediate group. Zinc phosphate (ZP) glass is a promising material for use as lead-free sealing glass or as a good host for emitting centers. The structure of ZP glass has been extensively analyzed using various methods. Several groups have also performed structural analyses using neutron and X-ray diffraction with the aid of reverse Monte Carlo (RMC) modeling [2,3]. However, previous investigations have shown that metal oxides have a small oxygen coordination in glass since the rigid glass network enables the metastable species of metal oxides to be sustained in the glass matrix. Therefore, the modeling of a reliable atomic arrangement in glass based on metal-cation-specific experimental data and conventional diffraction data is essential. In this article [4], we report on the reliable atomic configuration of ZP glass from the viewpoint of 3D network linkage, i.e., the connectivity of each oxide. We use a combination of ^{31}P magic angle spinning (MAS) NMR, Zn *K*-edge extended X-ray absorption fine structure (EXAFS), and X-ray and neutron diffraction data [2] to determine the dependence of this connectivity on the chemical composition and on the zinc coordination. Moreover, we discuss the relationship between several properties and the glass structure and find that the thermal expansion coefficient is sensitive to the substitution of the phosphate chain network by a network consisting of Zn-O units in zinc-rich glass.

Figure 1(a) shows the thermal expansion curves for xZnO-(100-x)P_2O_5 (xZP) glasses (x = 58, 60, 65, and 70). Figure 1(b) shows the linear thermal expansion coefficients of these glasses as a function of the amount of ZnO. The thermal expansion coefficients increase with increasing ZnO fraction. If the glass network is similar, i.e., if the glass has the same NWF, the lower T_g glass generally exhibits a higher thermal expansion coefficient. However, the obtained results show that a higher T_g glass exhibits a higher thermal expansion coefficient. The anomaly of the thermal expansion coefficients suggests that the glass networks might change depending on ZnO fraction.

We performed RMC modeling using data of XRD measured at SPring-8 **BL04B2**, neutron diffraction [2], and EXAFS measured at **BL01B1** with several constraints on the coordination numbers to identify several chemical coordination states around phosphorus in order to reveal the behavior of the oxygen coordination around zinc. The modeling was based on the results of ^{31}P MAS NMR, which revealed a significant change in Q^2 species between the 60ZP and 70ZP glasses. Figure 2 shows the experimentally determined X-ray and neutron structure factors, $S(Q)$ and EXAFS $k^3\chi(k)$, respectively, of the 60ZP and 70ZP glasses along with those obtained by the RMC modeling. Since there is good agreement between the experimentally determined and RMC-modeled data, we have succeeded in modeling atomic configurations that reproduce the X-ray, neutron, EXAFS, and NMR data.

To understand the 3D atomic configuration in ZP glasses, the connectivity of PO_4 and Zn-O polyhedra was analyzed. Figures 3(a) and 3(b) show the 3D linkage of the phosphate network in terms of the chain length, as calculated from the total number of atoms in each phosphate. Figure 3(a) shows the fraction of Q^1 units and Q^2 chains of PO_4 polyhedra in the 60ZP glass and a typical RMC-modeled Q^2 chain. As can be seen in Fig. 3(b), the 70ZP glass consists of only isolated PO_4 tetrahedra (Q^0) and P_2O_7 dimers (Q^1). Thus, our RMC models reproduce the modification of the 3D phosphate network as observed

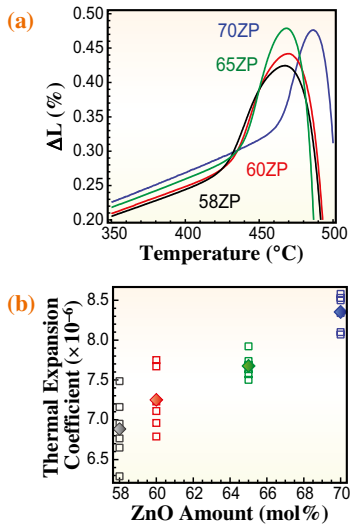

Fig. 1. Linear thermal expansion coefficients of ZP glasses. **(a)** Thermal expansion curves of 58ZP, 60ZP, 65ZP, and 70ZP glasses. **(b)** Thermal expansion coefficients below T_g as a function of ZnO. The 70ZP glass exhibits a higher T_g and a higher thermal expansion coefficient below and above T_g than those of 60ZP glass. Closed squares indicate mean values [4].

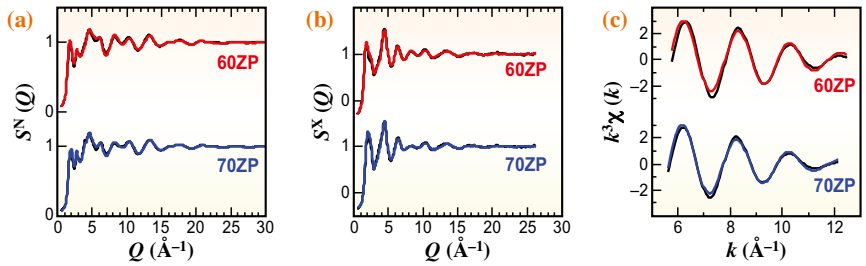

Fig. 2. Comparison between neutron/synchrotron X-ray data and RMC model for the ZP glasses. **(a)** Neutron total structure factor $S^N(Q)$, **(b)** X-ray total structure factor $S^X(Q)$, and **(c)** EXAFS $k^3\chi(k)$. The EXAFS $k^3\chi(k)$ data were obtained by back Fourier transformation of |FT(R)| for the first correlation peak. Black curve, experimental data; colored curve, RMC model [4].

by ^{31}P MAS NMR. The probabilities of the formation of polyhedral connections between PO_4 tetrahedra and Zn-O polyhedra were calculated in order to elucidate the mechanism of glass formation in binary oxide glasses with low amounts of network former. The total number of atoms constituting the Zn_xO_y units was estimated to determine the origin of the glass network in the glass. As the figure shows, the Zn_xO_y units do not form a network in 60ZP glass, and the size of the fragments (consisting of up to 41 atoms, as shown in the inset of Fig. 3(c)) is <20 Å. In contrast, 10% of the Zn_xO_y units in the 70ZP glass form networks consisting of more than 40 atoms, as manifested by their atomic configurations consisting of up to 1,300 atoms, as shown in the inset of Fig. 3(d). The unusual network structure units formed by the Zn_xO_y polyhedra can be attributed to the smaller oxygen coordination of the zinc than that of the ZnO crystal; the high glass-forming ability of the 70ZP glass stems from this small oxygen coordination. On the other hand, it is suggested from our RMC model that the small Zn-O coordination is a signature of the network former, according to Zachariasen's rule [1], in our model for 70ZP glass.

In summary, by performing structural modeling based on a combination of an advanced quantum beam technique and spectroscopic measurement, we found that the thermal expansion coefficient reflected the substitution of the network of phosphate by a network consisting of Zn_xO_y units in zinc-rich glasses. The results obtained in this study via several structural analysis methods are significant since they clearly reveal the fundamental properties that determine the functionality of these types of glass. The results obtained in the current study should constitute a significant milestone in the design of phosphate glasses for practical applications.

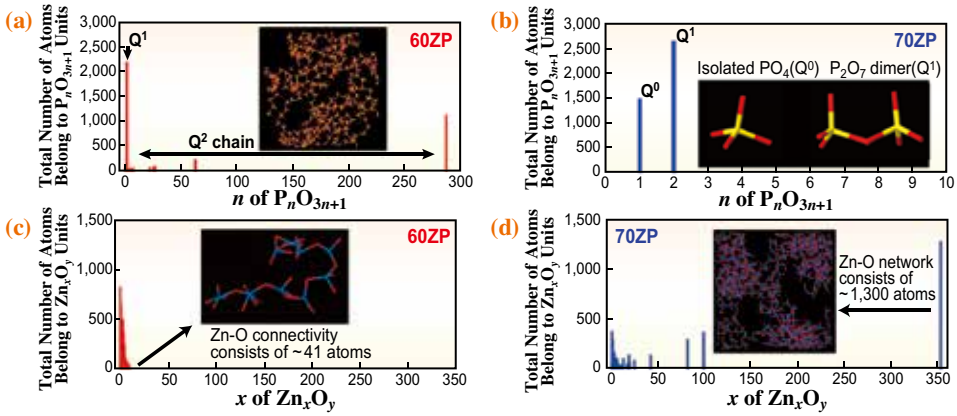

Fig. 3. Connectivity of PO_4 tetrahedra and Zn_xO_y polyhedra in the ZP glasses. Size distribution of PO_4 tetrahedral chains in **(a)** 60ZP glass and **(b)** 70ZP glass. Size distribution of Zn_xO_y polyhedral chains in **(c)** 60ZP glass and (d) 70ZP glass. P, Zn, and O atoms are shown in yellow, blue, and red, respectively [4].

Hirokazu Masai[a,*], Yohei Onodera[b] and Shinji Kohara[c,d,e,f]

[a] National Institute of Advanced Industrial Science and Technology (AIST)
[b] Inst. for Integrated Radiation and Nuclear Science, Kyoto Univ.
[c] Research Center for Advanced Measurement and Characterization, NIMS
[d] Center for Materials Research by Information Integration, NIMS
[e] JST/PRESTO
[f] Japan Synchrotron Radiation Research Institute (JASRI)

*Email: hirokazu.masai@aist.go.jp

References

[1] W. H. Zachariasen: J. Am. Chem. Soc. **54** (1932) 3841.
[2] K. Suzuya *et al.*: J. Non-Cryst. Solids **345** (2004) 80.
[3] U. Hoppe *et al.*: J. Non-Cryst. Solids **351** (2005) 1020.
[4] *Y. Onodera, S. Kohara, H. Masai, A. Koreeda, S. Okamura, T. Ohkubo: Nat. Commun. **8** (2017) 15449.*

Structural characterization of nanoparticulate GaN-ZnO electrode for artificial photosynthesis

The artificial photosynthesis technology known as the Honda-Fujishima effect, which produces oxygen and hydrogen or organic energy from sunlight, is an effective energy and environmental technology. The key component for the increasing the efficiency of this reaction system is the anode electrode, generally composed of a photocatalyst on a glass substrate coated by electrically conductive fluorine-doped tin oxide (FTO).

Recently, we applied aerosol-type nanoparticle deposition (NPD) techniques to form a GaN-ZnO electrode, and by controlling the deposition conditions, we obtained films with a narrower band gap than the raw material powder. We confirmed that the films produced a current approximately 100 times larger than those produced by conventional processes. In this study, we analyzed the structural difference between such a high-current film and the raw powder by applying XRD, HAXPES, and XAFS techniques using SPring-8 **BL16XU** and **BL16B2** (Sunbeam) beamlines. These results are discussed with those of a first-principles simulation [1].

The nanoparticle deposition equipment [2,3] was composed of an aerosol-generation system, a deposition chamber, and a vacuum system. Raw ceramic powder was set in the aerosol-generation system. Then, a pressurized carrier gas was introduced into the vessel to transfer the generated aerosol from the nozzle to the substrate in the deposition chamber. This method is suitable for forming a nanoparticle crystal film of complex ceramic.

A GaN-ZnO-based material is a solid solution of hexagonal wurtzite structure crystals that continuously changes its composition as Ga-Zn and N-O are substituted in the crystal structure. It is known that a GaN-ZnO solid solution has a narrower band gap than pure GaN or ZnO, and its absorption wavelength edge expands to the long-wavelength side as the amount of ZnO dissolved into the GaN increases [4].

To synthesize a $Ga_{1-x}Zn_xN_{1-x}O_x$ ($x = 0$ to 1) solid solution, we adopted a general solid-state reaction using oxide raw materials (Ga_2O_3, ZnO) at a high temperature (1123 K) in an ammonia gas flow. It was, however, difficult to increase the amount of ZnO to more than $x = 0.45$.

In the NPD deposition, we applied two types of condition. As the first condition, nitrogen carrier gas with a speed of 50 m/s was used to transfer the source powder to the substrate, and the resulting film is called NPD_0. As the second condition, helium gas with a speed of 100 m/s was used and the film is called NPD*.

Figure 1 shows the appearances of the raw material powder with $x = 0.45$, and the NPD_0 film and NPD* film formed on an FTO substrate using this raw material powder. In the same figure, the Kubelka-Munk values are plotted, which were obtained from the diffuse reflectance spectrum by using UV and visible light. The reflection absorption edge of the raw material powder was at 490 nm (band gap: 2.53 eV) and that of the NPD_0 film was at 545 nm (band gap: 2.27 eV). The raw material powder and the NPD_0 film have almost the same yellow color, and a small difference in the band gap values was detected. The NPD* film is brown and its absorption edge was at 635 nm (band gap: 1.97 eV), which is significantly smaller than that for the original raw powder.

Figure 2(a) shows the hard X-ray photoelectron spectroscopy (HAXPES) spectra near the top of the valence band for the NPD* films with $x = 0$, 0.24, 0.45, and 1. The end of each spectrum is a valence band maximum (VBM). According to the figure, the VBM increased with increasing ZnO content, which indicates that the electron level of the solid solution is highest at $x = 0.45$. Also, we observed similar dependences for the raw material powder and the NPD_0 film.

We performed XAFS measurement at the Ga *K*-edge and Zn *K*-edge of the raw powder and NPD* film with the composition $x = 0.45$. The XAFS spectrum $\chi(k)$ was extracted from the measured data. In Fig. 2, the Fourier transformed Ga $\chi(R)$ with the compositions $x = 0$ (b) and 0.45 (c) are shown. The peaks in the figures correspond to the bond

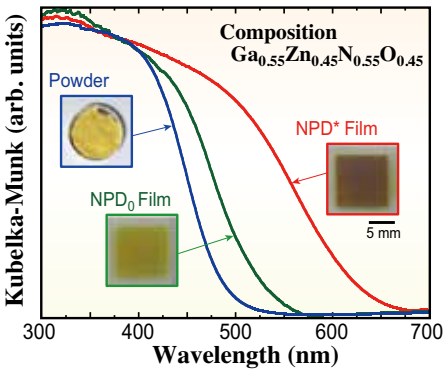

Fig. 1. Kubelka-Munk values of the raw material powder (blue), NPD_0 film (green), and NPD* film (red) for the composition $x = 0.45$ obtained from the diffuse reflectance spectra measured by using UV and visible light.

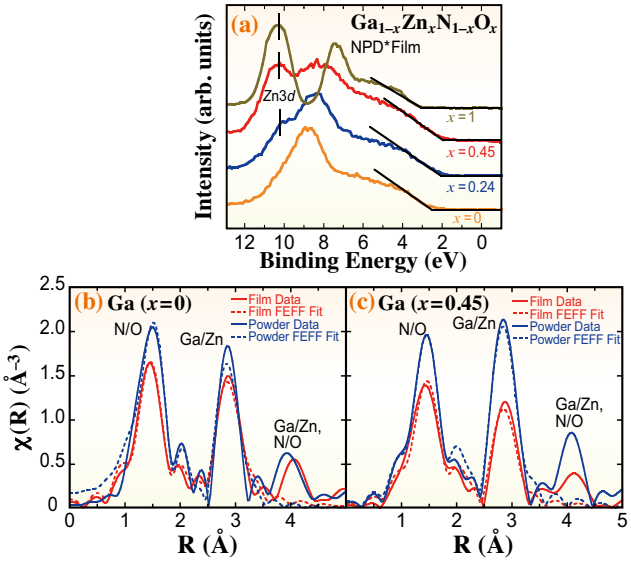

Fig. 2. **(a)** Hard X-ray photoelectron spectroscopy (HAXPES) spectra around the top of the valence band for the NPD* film. Effective bond length distributions of the raw material powder and the NPD* film for compositions $x = 0$ **(b)** and 0.45 **(c)** obtained from Ga *K*-edge XAFS.

length and the intensity decreases with the structural disorder. For the composition of $x = 0$ (b), the intensity of the first nearest peak, which corresponds to the Ga-(N/O) bond, was lower for the NPD* film than for the powder. For the composition of $x = 0.45$ (c), in addition to the first nearest peak, the intensity was also lower for the second nearest peak, which corresponds to the Ga-(Ga/Zn) bond. From these results, we confirmed that in the NPD* film, the atomic disorder is greater than that in the raw material powder, and the disorder is further increased by the substitution of ZnO. The most likely reason for the increase in the atomic disorder is the local strain due to the different ion radii of Ga and Zn, which is largest for the composition $x = 0.45$, and the soft distortion occurring in the film formation process.

As the increase in atomic disorder may have contributed to the decrease in the band gap, we carried out a first-principles simulation using the crystal structure model with composition $x = 0.5$. To reproduce the crystal disorder, we used the model of the partial crystal structure shown in Fig. 3(a). In the model, we introduced the displacement *d* in the *c*-axis direction for the bonding pair composed of a given cation and a neighboring anion. From the simulation, we found that the band gap energy decreases as the displacement increases, regardless of the displacement direction. In this simulation, when a pair of atoms was displaced by only 0.2 Å, the band gap energy decreased by approximately 0.2 to 0.3 eV. Figure 3(b) shows schematic diagrams of the electronic structure with and without the displacement. With the displacement, the conduction band formed by 4*s* and 4*p* orbitals of Ga and Zn expands and the conduction band minimum (CBM) is lowered, which results in the decrease in the band gap.

As described above, we have proven that the application of the NPD process to photocatalyst materials can form nanoparticulate films with a narrower band gap, and this method is applicable to various other photocatalysts.

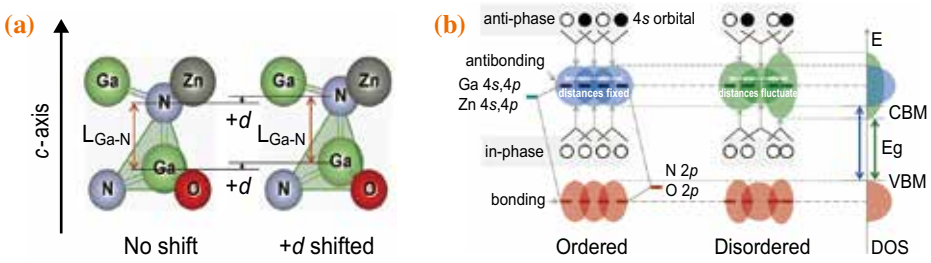

Fig. 3. **(a)** Partial structure with the atom displacement in the crystal model. **(b)** Schematic diagrams explaining the decrease in the band gap energy due to the displacement of the atom positions.

Yoshihiko Imanaka* and Naoki Awaji

Fujitsu Laboratories, Ltd.

*Email: Imanaka@jp.fujitsu.com

References

[1] *Y. Imanaka, T. Anazawa, T. Manabe, H. Amada, S. Ido, F. Kumasaka, N. Awaji, Ga. Sánchez-Santolino, R. Ishikawa and Y. Ikuhara: Sci. Rep.* ***6*** *(2016) 35593.*
[2] Y. Imanaka *et al.*: Ad. Eng. Mat. **15** (2013) 1129.
[3] Y. Imanaka *et al.*: J. Nanopart. Res. **18** (2016) 102.
[4] K. Maeda and K. Domen: J. Phys. Chem. C **111** (2007) 7851.

Dehydration processes of metal cations during electrodeposition

Metal deposition is an important subject from industrial viewpoints such as electrolytic refining, corrosion, and plating. Recently, well-designed plating techniques have become necessary for various fields, including the nanofabrication of electrodes for electronic devices and the surface modification of nanoparticles for catalysts. Underpotential deposition (upd) can achieve atomically controlled single- or double-layer modification of metal cations, which has been applied for the preparation of nanocatalysts [1].

During electrodeposition, counter anions often promote or inhibit metal deposition. Moreover, solvent species as well as ionic species also affect the approach of metal cations to a surface because of diffusion across an electrical double layer (EDL). In the EDL, ionic species are located at the Helmholtz layer and the solvent species are highly oriented by the layer structure of the charged species with a huge electric field. In an electrochemical reaction, when the reaction species approach the surface, these layered structures are destroyed. Since metal cations are hydrated in solution, the dehydration process is also important during deposition. However, these approaching and dehydration processes of metal cations are unknown. X-ray diffraction is the best method for the structural determination of ionic species in an EDL and can also carry out detection with high time and spatial resolution. In this study, we performed time-resolved X-ray diffraction to observe the upd process of various metal cations on Au(111) in real time.

X-ray diffraction measurements were performed with a multi-axis diffractometer at SPring-8 **BL13XU**. For the time-resolved experiment, a rectangular potential wave between non-upd and upd potentials with a frequency of 1.0 Hz was applied to an Au electrode. Diffracted photons were detected by a Ce-doped yttrium aluminum perovskite (YAP:Ce) detector, and the discriminated pulses were counted by a multichannel scaler synchronized with a function generator used for potential control [2].

We performed time-resolved measurements at peak positions along a crystal truncation rod (CTR). For Cu upd, a potential step was applied from the non-upd potential of 1.05 V *versus* standard hydrogen electrode (SHE), at which a well-ordered sulfate layer on Au (111) was formed, to the upd potential of 0.45 V, at which a $\sqrt{3} \times \sqrt{3}$ upd layer was formed. Figure 1 shows the time-resolved intensity transient along the specular CTR after the potential step. After 100 ms, the intensity around $L = 1.2$ had decreased, whereas that around $L = 4.2$ had increased. These changes can be ascribed to the deposition of $\sqrt{3} \times \sqrt{3}$ Cu. However, an abnormal enhancement of the intensity appeared between $L = 1.2$ and 2.7 immediately after the potential step to 100 ms that cannot be attributed to the formation of an adsorbed layer. We constructed time-resolved structure factors along the specular CTR from the intensity transient in order to refine the structural parameters at each time. The structure factors were conventionally corrected from the integrated intensity measurement along the CTR. Figure 2 shows the time dependence of the structural parameters during Cu upd. The initial enhancement of the intensity after the step to the upd potential can be ascribed to the layer formation of the Cu species at a distance of around 0.32 nm from the surface. When Cu was deposited on a Au(111) surface directly, the distance between the first Au layer and the adsorbed Cu layer was 0.21 nm. Therefore, the distance of 0.32 nm indicates that this Cu species was not adsorbed directly but was located at the outer Helmholtz layer as a hydrated state [3]. During Cu deposition, hydrated Cu ions approached the outer Helmholtz layer, and Cu ions were then adsorbed on the Au(111) surface by the destruction of the hydration shell. The adsorbed

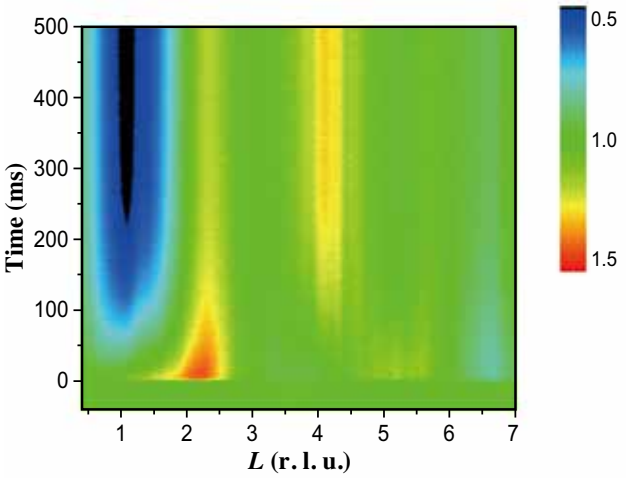

Fig. 1. Time-resolved specular CTR in 0.5 M H_2SO_4 + 1.0 mM $CuSO_4$ after the potential step from 1.05 V to 0.45 V with a time resolution of 500 μs. The transient intensities were normalized by those at the non-upd potential of 1.05 V. Red and blue regions indicate increases and decreases of intensity, respectively.

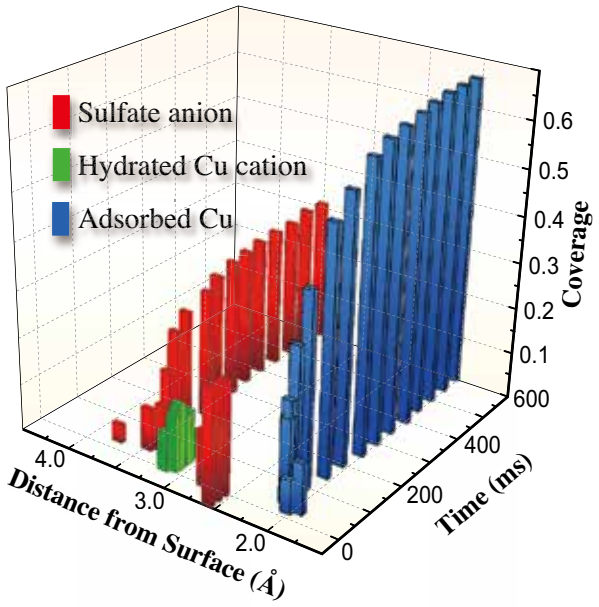

Fig. 2. Time dependence of the structural parameters optimized using the time-resolved specular CTR. The position of the adsorbed (bi)sulfate indicates the sulfur atom of tridentate (bi)sulfate.

sulfate species at the non-upd potential were located 0.27 nm from the Au(111) surface. After the potential was decreased stepwise to 0.45 V, the sulfate species desorbed within 1 ms, and then the hydrated Cu^{2+} was immediately accumulated with a maximum coverage of 0.14. The coverage of the hydrated Cu^{2+} decreased after 40 ms, and the Cu and the sulfate anion were then adsorbed on Au(111) over the next 400 ms. The coverages of the adsorbed Cu and sulfate species correlated strongly, suggesting that these ions interacted in a complementary manner.

The initial deposition process was investigated for the upd of different metal cations (Tl^+, Ag^+, Zn^{2+}, Cd^{2+}, and Bi^{3+}). The time constants of metal deposition were estimated from the transient intensities at the reciprocal lattice point of 0 0 1.4. As described above, the metal cation with the hydration shell was metastably layered in the EDL before the deposition step. Therefore, the destruction of the hydration shell may have been the kinetically controlled step during deposition. Figure 3 shows a plot of the coordination energies of the hydrated water estimated by DFT calculations against the time constant of the intensity transient. The coordination energy is strongly correlated to the ionic valence due to the electrostatic interaction. The deposition rate of the metal cations has a linear relationship with the coordination energy, except in the case of Cu upd; this indicates that strong interaction between water and the metal cation delays the adsorption on the surface. However, the decay time of the Cu deposition is longer than that of Bi showing a higher coordination energy. Since the decay of Cu upd becomes faster as the concentration of sulfuric acid increases, the slow decay of Cu upd is due to its complex formation with the sulfate anion. The complex formation process of Cu on Au(111), which requires SO_4 delays the Cu deposition and makes it slower than Bi upd.

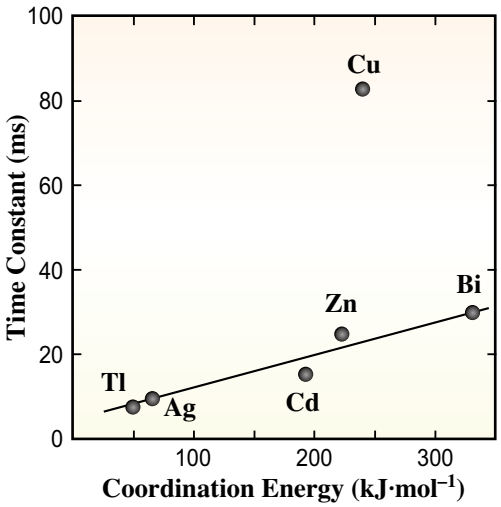

Fig. 3. Correlation between the time constant of X-ray intensity decay and the coordination energy of each hydration water of $M(H_2O)_6^{n+}$.

Masashi Nakamura[a,*], Osamu Endo[b] and Osami Sakata[c]

[a] Graduate School of Engineering, Chiba University
[b] Graduate School of Engineering, Tokyo University of Agriculture and Technology
[c] Synchrotron X-ray Station at SPring-8, National Institute for Materials Science (NIMS)

*Email: mnakamura@faculty.chiba-u.jp

References

[1] F. Calle-Vallejo *et al.*: Chem. Soc. Rev. **42** (2013) 5210.
[2] M. Nakamura *et al.*: J. Phys. Chem. C **118** (2014) 22136.
[3] *M. Nakamura, T. Banzai, Y. Maehata, O. Endo, H. Tajiri, O. Sakata, N. Hoshi: Sci. Rep. 7 (2017) 914.*

Photochromic hollow crystals showing scattering of crystals and dispersal of included objects mimicking *Impatiens*

Diarylethene derivatives are photochromic compounds whose colorless open-ring isomers undergo cyclization to colored closed-ring isomers upon UV irradiation and revert to the original open-ring isomers by a cycloreversion reaction upon visible light irradiation. Diarylethenes are known by their following excellent photochromic properties: 1) high thermal stability of both isomers, 2) fatigue resistance to repeated photochromic reaction cycles, 3) high sensitivity (high absorption coefficients and photochromic quantum yields), 4) photochromic reactivity even in the crystalline state. Owing to these specific properties, diarylethene derivatives have been paid much attention in the research field of molecular memories and switches [1].

In 2007, a paper on the photoinduced bending phenomena of diarylethene crystals was published in Nature [2]. The macroscopic movement due to crystal bending was induced by the sum of the changes in each molecular volume from open-ring to closed-ring isomers. The dramatic movement of crystals upon alternate irradiation with UV and visible light attracted much interest. Then a new research field to develop systems that exhibit photoinduced macroscopic events attributed to the assumption of microscopic molecular movements was started and developed.

In addition to photochromic crystalline systems, other macroscopic phenomena called salient effects have been reported [3]. Salient phenomena refer to crystals showing jumping, breaking, or scattering into small pieces upon heating or photoirradiation. Salient phenomena induced by heating are called “thermosalient” phenomenon and those induced by photoirradiation are called “photosalient” phenomenon. Salient phenomena are much more dramatic than the photoinduced bending of crystals, i.e., in the bending the crystal lattice is maintained, while in salient phenomena the lattice is broken. When breaking the lattice, all the strained energy is released and transferred into kinetic energy. Therefore, the crystals jump or are scattered at a high speed.

Although the phenomena are dramatic and interesting to observe, they do not undergo any functions, and only breaking or jumping in unexpected directions occurs. The photoinduced bending of crystals is much slower, but some of them can be used for actual functions such as rolling gears or switching electronic devices.

We have studied the synthesis of new diarylethene derivatives to search for new photofunctions. We prepared a new derivative **1o** having a six-membered perfluorocyclohexene ring at the ethene moiety

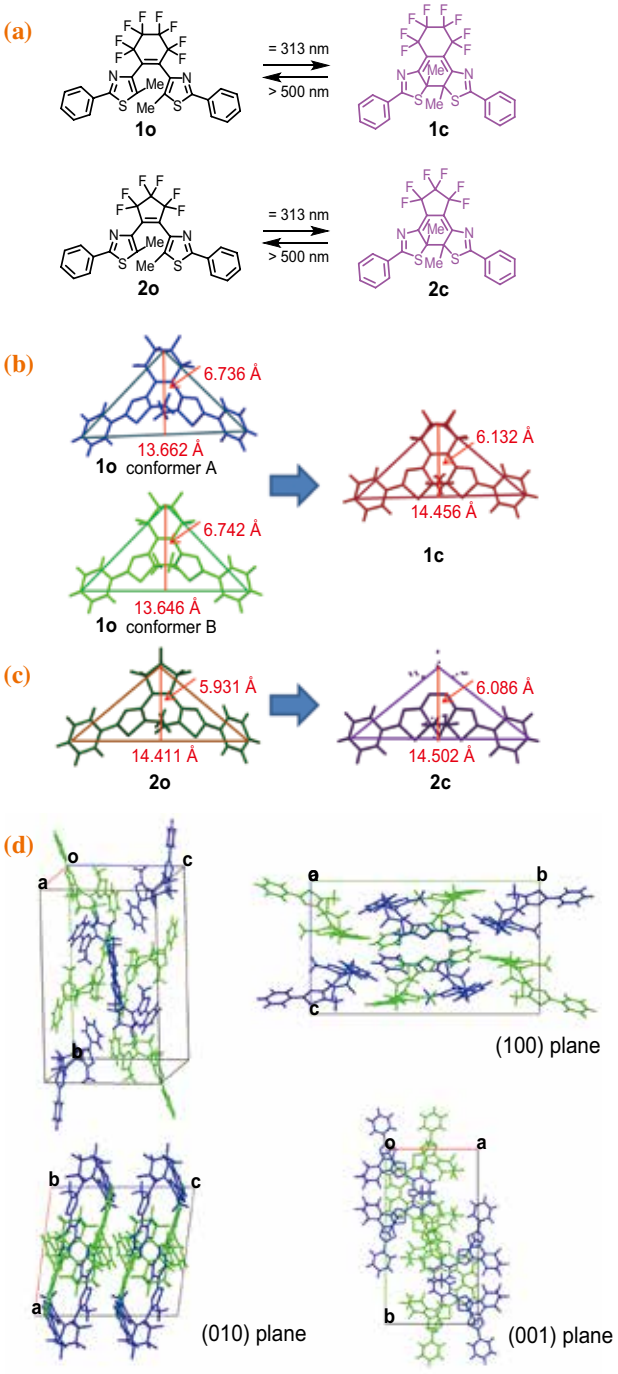

Fig. 1. Molecular movement of diarylethenes in the crystals. **(a)** Molecular structural changes of diarylethenes (1) and (2), **(b, c)** changes in structure size during the reaction from open-ring (**1o, 2o**) to closed-ring (**1c, 2c**) isomers, **(d)** molecular packing of two conformers (A and B) of **1o** in the unit cell.

instead of the five-membered perfluorocyclopentene ring of the previously prepared derivative (**2o**) (Fig. 1(a)); derivative **2o** is the compound whose single crystal showed photoinduced bending [2]. The crystal of **1o** showed the photosalient phenomena of jumping and scattering into small pieces upon UV irradiation. The reason for this was clarified by X-ray analysis. In a unit cell of the crystal of **1o**, there are two conformers (depicted in blue (conformer A) and green (conformer B)). Upon UV irradiation, they undergo a cyclization reaction to form the closed-ring isomer **1c**. Comparing the sizes of **1o** and **1c**, the height of the molecules decreased by 9.0% for both conformers, while the widths of the molecules increased by 5.8 and 5.9% for conformers A and B, respectively (Fig. 1(b)). These changes are almost three times larger than those for the conversion from **2o** to **2c** (0.6% increase in width and 2.6% increase in height) (Fig. 1(c)). These larger structural changes induced stress in the crystal upon UV irradiation, leading to photoinduced salient phenomena [4].

Unexpectedly, **1o** formed crystals with hollow structure by sublimation on a hot plate under atmospheric pressure. We analyzed the hollow crystals at SPring-8 beamlines **BL02B1** and **BL40XU**, and found that the hollow crystals have the same molecular packing as the non-hollow crystals as shown in Fig. 1(d).

This finding inspired us to devise a function for the hollow crystals. *Impatiens* (touch-me-not) are known to have a specific biofunction. The *impatiens* plant disperses its seeds over a distance as the seedpod explodes open. We attempted to mimic this function. The dimensions of the largest hollow crystal were 5 to 30 μm in width and around 100 μm in length. Upon UV irradiation, hollow crystals were deformed as in Fig. 2(a) and finally broke down in small pieces [5]. In addition, small plastic beads (1.0 μm diameter) containing a fluorescent dye were packed into the hollow (Fig. 2(b)), and UV light was irradiated to the crystal. Then the beads inside the hollow were immediately scattered along with the deformation and breaking of the walls in the manner of the seeds of natural *impatiens* (Fig. 2(c)). This phenomenon implies that the photoresponsive hollow acts as a kind of artificial *impatiens*. With the help of SPring-8, we were able to clarify the mechanism of the photosalient phenomena of hollow crystals, which led to the generation of a new photoresponsive system mimicking *impatiens*.

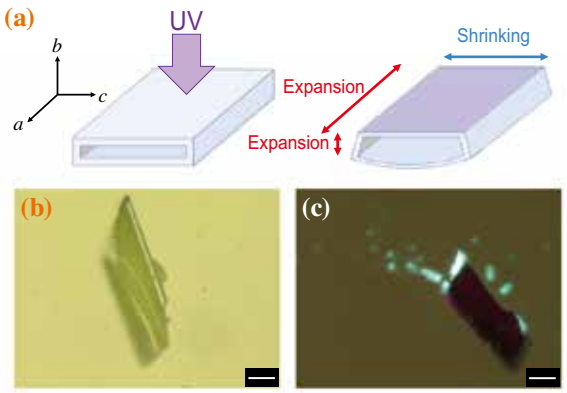

Fig. 2. **(a)** Deformation of the hollow crystal upon UV irradiation, **(b)** hollow crystal packed with fluorescent polystyrene beads with 1 μm diameter, **(c)** UV-induced scattering of fluorescent beads. Scale bars: 20 μm.

Kingo Uchida[a,*], Eri Hatano[a] and Masakazu Morimoto[b]

[a] Department of Materials Chemistry, Ryukoku University
[b] Department of Chemistry and Research Center for Smart Molecules, Rikkyo University

*Email: uchida@rins.ryukoku.ac.jp

References

[1] M. Irie *et al.*: Chem. Rev. **114** (2014) 12174.
[2] M. Irie *et al.*: Nature **446** (2007) 778.
[3] P. Naumov *et al.*: Chem. Rev. **115** (2015) 12440.
[4] K. Uchida *et al.*: Chem. Eur. J. **22** (2016) 12680.
[5] *E. Hatano, M. Morimoto, T. Imai, K. Hyodo, A. Fujimoto, R. Nishimura, A. Sekine, N. Yasuda, S. Yokojima, S. Nakamura and K. Uchida: Angew. Chem. Int. Ed.* ***56*** *(2017) 12576.*

X-ray photoelectron spectroscopy under ambient pressure conditions

X-ray photoelectron spectroscopy (XPS) is a powerful tool for measuring the physical and chemical properties of surfaces. A conventional photoelectron spectroscopy analyzer can only operate under high vacuum. One of the reasons for this is that the discharge of the analyzer occurs at low vacuum and the other reason is that the number of photoelectrons decreases quickly when photoelectrons pass through the gas atmosphere because of the electron scattering by gas molecules. Attempts to perform XPS measurement in a gas atmosphere began in the early 1970s. In several cases, differential evacuation was performed between the electron energy analyzer and the sample to prevent the gases from entering the analyzer and to maintain the vacuum under which the analyzer can be operated safely. In addition, a short working distance (WD) between the sample surface and the detector orifice (aperture) was adopted to prevent electrons from passing through a long distance in the high-pressure region. This technique is known as ambient pressure X-ray photoelectron spectroscopy (AP-XPS) [1].

The AP-XPS technique has advanced with the use of third-generation synchrotron radiation light sources. High brightness and small focused beams have allowed the diameter of the aperture to be reduced. Furthermore, by introducing an electron lens into a differentially pumped chamber to increase photoelectron transmission, it has become possible to lengthen the chamber and exhaust residual gases with numerous pumps. These techniques can increase the working pressure in the measurement chamber to 3000 Pa, close to the saturation vapor pressure of water at room temperature. In recent years, AP-XPS has been used in various research areas such as solid-gas reactions, solid-liquid interfaces, fuel cells, and batteries. However, the upper limit of the working pressure is about 3% of atmospheric pressure. Considering that many practical chemical reactions occur under atmospheric pressure or higher, it is desirable to further increase the pressure limit in AP-XPS.

The key requirements for increasing the pressure limit in AP-XPS are a high-brightness light source, a small focused beam, a small aperture, a short WD, and high-energy photoelectrons generated by a high-energy excitation light. Using a small aperture to increase the pressure limit in AP-XPS has two advantages. First, it can prevent gases from flowing into the analyzer, and second, it can shorten the WD without decreasing the actual pressure at the sample surface. Regarding the inflow of gases, we investigated the pressures at a differentially pumped chamber and an analyzer chamber during XPS measurement under atmospheric pressure for apertures of various sizes. We found that an aperture diameter of ≤70 μm can maintain the gaseous pressure in both chambers at a value allowing the spectrometer to be operated safely during the measurement at atmospheric pressure. Concerning such a short WD, the number of photoelectrons with a kinetic energy of 8 keV is decreased to ~0.3% as a result of scattering at nitrogen molecules when they pass through a distance of 60 μm in the atmospheric pressure region. Therefore, a WD close to this value is required in AP-XPS measurement at atmospheric pressure to detect signals with sufficient intensities. The actual pressure at the sample surface, however, may differ from the apparent value measured far from the aperture if the aperture is too close to the sample. Previous AP-XPS experiments suggested that the WD should be twice the aperture diameter in order not to perturb the gas environment at the sample surface. Namely, it is necessary to use an aperture with a diameter of 30 μm to set the WD to 60 μm.

The AP-XPS measurements were conducted at SPring-8 **BL36XU** beamline [2]. Excitation light of 7.94 keV focused to a beam size of 20 μm × 20 μm was used. An AP-XPS system with a commercial differential pumping-type spectrometer (R4000 HiPP-2, Scienta Omicron Inc.) was installed in the beamline [3]. The equipment comprises a pre-lens in a differentially pumped chamber evacuated with several vacuum pumps and a standard hemispherical electron energy analyzer. The standard aperture

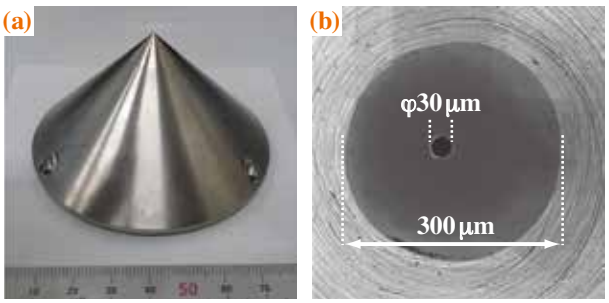

Fig. 1. **(a)** Front cone of the electron energy analyzer. **(b)** Scanning electron microscope image of the aperture shape at the top of the front cone.

at the top of the front cone in the spectrometer has a diameter of 300 μm. In this report, we replaced the front cone with our custom-made one with an aperture diameter of 30 μm, which was shaped by focused ion beam processing, to increase the pressure limit in the AP-XPS measurement (Fig. 1).

We measured the XPS spectra of a Au(111) surface grown on a mica substrate with a WD of 60 μm under various gas pressures using the AP-XPS equipment [4]. The signal intensity obtained by the spectrometer with the 30 μm aperture was ~5% of that obtained with the 500 μm aperture due to the small acceptance angle. Figure 2 shows the intensity decay of the Au 4*f* spectra with increasing gas pressure from 1 Pa to 100 kPa. Here we use 100 kPa as atmospheric pressure. The XPS measurement was not affected by the ambient gas at a pressure of 1 Pa. As the gas pressure increased, the signal intensity decreased because the photoelectrons were scattered by the ambient gas while passing through the sample to the detector. Although the signal intensity was very weak, the appearance of the $4f_{7/2}$ peak was confirmed at atmospheric pressure. The attenuation of the signal from its signal level at 1 Pa was 0.5% at 100 kPa. However, the signal-to-noise ratio can be improved by increasing the acquisition time. Figure 3 shows the Au 4*f* spectrum recorded at atmospheric pressure. The $4f_{7/2}$ and $4f_{5/2}$ peaks can be clearly observed in the spectrum. The Shirley background was subtracted from the spectrum, and the plots were fitted with a Voigt function. The curve-fitting result shows that the energy difference between the $4f_{7/2}$ and $4f_{5/2}$ peaks is 3.7 eV and the intensity ratio $4f_{7/2}$:$4f_{5/2}$ is approximately 4:3. These values are in good agreement with the standard values for Au 4*f* peaks. Thus, accurate photoelectron spectroscopy measurement is possible even under atmospheric pressure using a differential-pumping-type photoelectron spectrometer with an aperture of 30 μm.

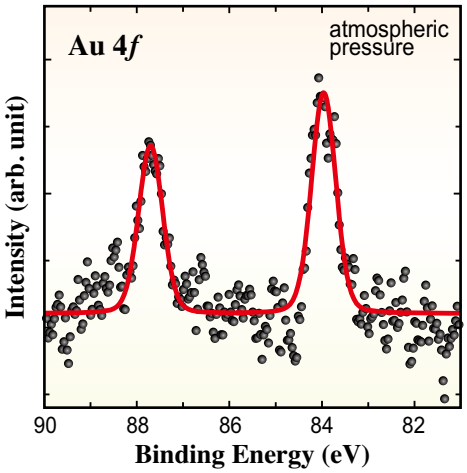

Fig. 3. Au 4*f* spectrum recorded at atmospheric pressure in an acquisition time of 30 min.

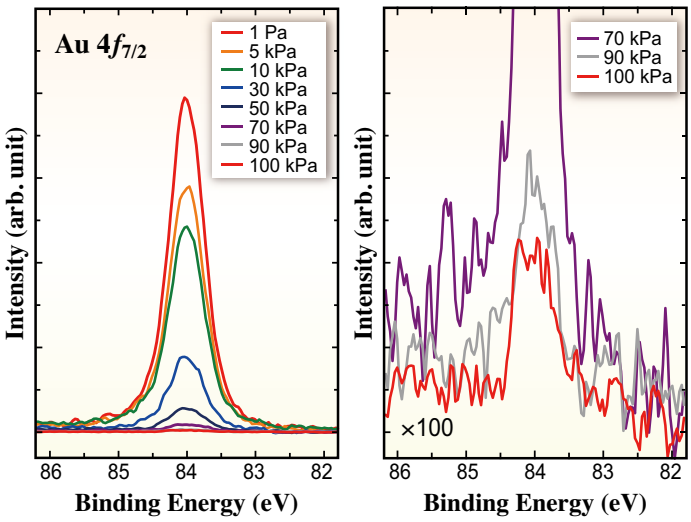

Fig. 2. Au $4f_{7/2}$ spectra recorded using 7.94 keV X-rays at pressures of 1 Pa to 100 kPa. Each spectrum was recorded in an acquisition time of 10 min.

Yasumasa Takagi[a,*,†], Toshihiko Yokoyama[a] and Yasuhiro Iwasawa[b]

[a] Institute for Molecular Science
[b] Innovation Research Center for Fuel Cells, The University of Electro-Communications

*Email: ytakagi@spring8.or.jp

[†] Present address: Japan Synchrotron Radiation Research Institute (JASRI)

References

[1] L. Trotochaud *et al.*: J. Phys: Condes. Matt. **29** (2017) 53002.
[2] O. Sekizawa *et al.*: J. Phys.: Conf. Ser. **712** (2016) 012142.
[3] Y. Takagi *et al.*: App. Phys. Lett. **105** (2014) 131602.
[4] *Y. Takagi, T. Nakamura, L. Yu, S. Chaveanghong, O. Sekizawa, T. Sakata, T. Uruga, M. Tada, Y. Iwasawa and T. Yokoyama: App. Phys. Exp.* ***10*** *(2017) 076603.*

Operando three-dimensional XAFS imaging of the degradation of a polymer electrolyte fuel cell Pt/C cathode electrocatalyst

The 3D visualization of heterogeneous catalysts is one of the most challenging subjects in catalytic chemistry and would be helpful for solving serious problems faced in the practical use of heterogeneous catalysts. X-ray absorption fine structure (XAFS) using hard X-rays is a powerful technique for analyzing the chemical state and local coordination of heterogeneous catalysts, and the high transmission of hard X-rays enables *operando* XAFS measurements under catalyst working conditions. We have developed 3D XAFS imaging combining computed tomography (CT) and XAFS spectroscopy (CT-XAFS) [1] and used it to visualize the degradation process of Pt cathode electrocatalysts in a polymer electrolyte fuel cell (PEFC) under PEFC operating conditions.

PEFCs are promising next-generation energy devices that can realize high energy conversion, on-site power generation, a sustainable clean power source, and so forth. For the practical application and commercialization of PEFCs, the durability of the cathode electrocatalyst must be improved. It is well known that the dissolution and degradation of the cathode electrocatalyst, such as Pt nanoparticles, proceeds under the practical operation conditions of fuel-cell vehicles, consisting of repeated cell voltage operations. We performed *operando* CT-XAFS at the Pt L_{III}-edge for a Pt/C cathode electrocatalyst in a practical membrane electrode assembly (MEA) under PEFC operating conditions, and the distribution and oxidation states of the Pt catalyst before and after an accelerated degradation test (ADT) were successfully visualized [2].

The *operando* CT-XAFS measurements were performed at SPring-8 **BL36XU** [3]. X-rays were monochromatized by Si(111) channel-cut crystals through a paper rotation diffuser, and X-ray transmission images of the sample (I_1) and I_0 images were recorded by a high-resolution X-ray imaging unit (Fig. 1). A PEFC cell designed for the CT-XAFS measurements was rotated between angles of –80° and +80° perpendicular to the optical path and 1,600 X-ray projection images were recorded at 184 X-ray energies around the Pt L_{III}-edge. The total measurement time was less than 2.5 h. We used a commercial MEA (EIWA Co., Ltd.; 3 × 3 cm^2) with a Pt/C cathode catalyst and a Pd/C anode catalyst (0.5 $mg \cdot cm^{2}_{\text{-Pt/Pd}}$). The MEA was conditioned and aged in the PEFC cell by supplying H_2 (150 $mL \cdot min^{-1}$) at the anode and N_2 (600 $mL \cdot min^{-1}$) at the cathode. *Operando* CT-XAFS measurements were performed for the MEA before and after the 20,000 cycles of the ADT (rectangular voltage cycling between 0.6 and 1.0 V for 3 s) at 1.0 V.

We reconstructed 3D images of three structural parameters from the series of CT-XAFS data: morphology images, Pt distribution images, and Pt

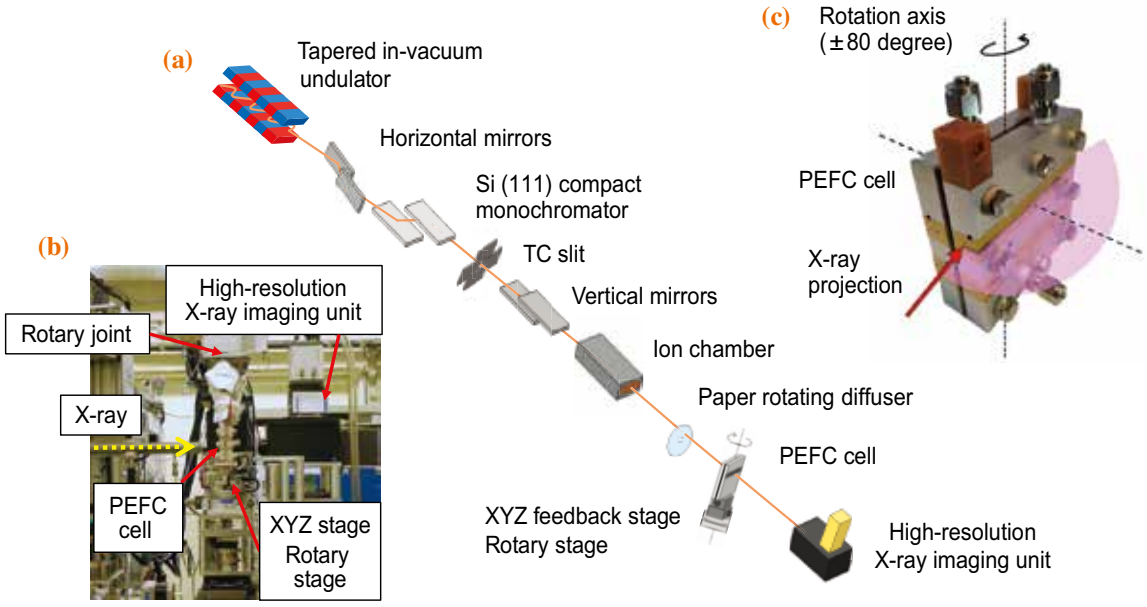

Fig. 1. **(a,b)** Schematic and image of CT-XAFS experimental setup at beamline BL36XU. **(c)** Image of the PEFC cell designed for the CT-XAFS measurements. [2]

valence state images in the MEA. The morphology images were obtained by the reconstruction of CT data measured at 11.497 keV, which was lower than the energy of the Pt L_{III}-edge (Figs. 2(A1, B1)). We found the clear contrasts derived from the structures of the components in the MEA, and a heterogeneous structure with random cracks was clearly imaged in the cathode catalyst layer.

Then, we reconstructed the Pt L_{III}-edge jump, which corresponds to the amount of Pt. Figures 2(A2, B2) show 3D reconstructed images of the Pt L_{III}-edge jump, where the distribution of the Pt catalyst in the MEA was clearly visualized before and after the ADT. Before the ADT, the distribution of the Pt catalyst was observed as tiny spots in the whole of the cathode catalyst layer, suggesting that the Pt catalyst was originally dispersed in the cathode catalyst layer. The 3D images of the distribution of the Pt catalyst markedly changed after the 20,000 ADT cycles. The observed tiny structures almost disappeared and the dissolution of the Pt catalyst from the cathode catalyst layer to the Nafion membrane was also observed. Severe aggregation was observed in some parts, whereas the Pt catalyst was lost in parts around the crack structures. The 3D images of the Pt distribution before and after the ADT showed the migration and degradation of the Pt cathode catalyst caused by the ADT cycles.

Figures 2(A3, B3) show 3D images of the Pt valence at 1.0 V obtained by the reconstruction of the white-line height of the Pt L_{III}-edge. After the ADT cycles, it was clear that the 3D image had changed from yellow to blue, showing decreases in the Pt valence caused by the ADT. This was observed in the entire cathode catalyst layer, indicating that Pt aggregation proceeded in the cathode catalyst layer with reduction in the active surface area of the Pt catalyst.

Briefly, we have succeeded in measuring *operando* CT-XAFS data of an MEA of a PEFC with a Pt/C cathode catalyst and reconstructing the Pt distribution and valence state in the MEA under PEFC operating conditions for the first time. The *operando* 3D-CT-XAFS images before and after the ADT showed that the dissolution, migration, and aggregation of the Pt cathode catalyst occurred in the entire cathode layer and spread to the Nafion membrane in the MEA during the ADT. The 3D visualization by CT-XAFS is a promising method for visualizing heterogeneous catalyst migration and the degradation of electrocatalysts in PEFCs to obtain a deeper understanding of catalyst degradation in PEFCs and for developing new catalysts and PEFC systems for practical use.

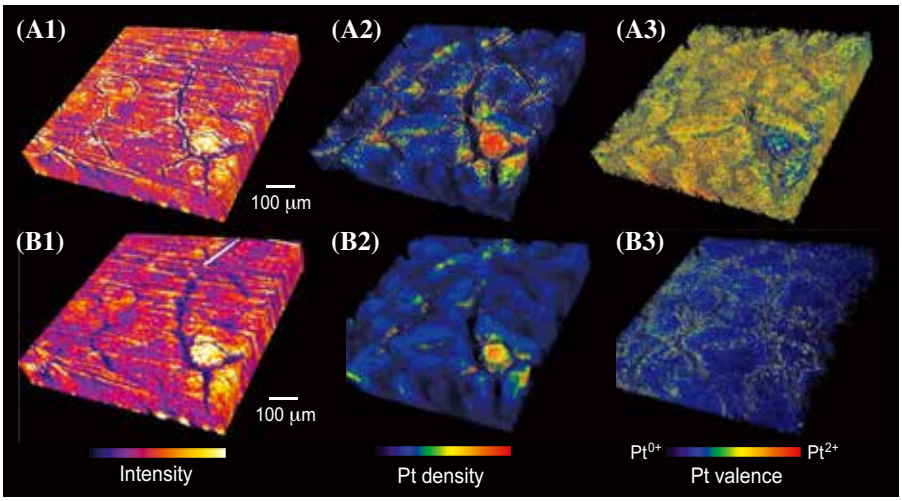

Fig. 2. Set of 3D images of (1) morphologies, (2) Pt densities, and (3) Pt valence states for the MEA **(A)** before and **(B)** after the 20,000 cycles of the ADT. [2]

Hirosuke Matsui[a,*], Nozomu Ishiguro[b] and Mizuki Tada[a,b]

[a] Graduate School of Science & Research Center for Materials Science (RCMS), Nagoya University
[b] RIKEN SPring-8 Center

*Email: h-matsui@chem.nagoya-u.ac.jp

References

[1] T. Saida *et al.*: Angew. Chem. Int. Ed. **51** (2012) 10311.
[2] *H. Matsui, N. Ishiguro, T. Uruga, O. Sekizawa, K. Higashi, N. Maejima, M. Tada: Angew. Chem. Int. Ed.* ***56*** *(2017) 9371.*
[3] O. Sekizawa *et al.*: J. Phys: Conf. Series **849** (2017) 012022(1-4).

Platonic micelles: A new concept of micelles since their discovery 100 years ago

Surfactants and lipids comprise hydrophilic polar headgroups and hydrophobic tails, which are commonly long hydrocarbon chains. When these molecules are dispersed in aqueous solutions, the hydrophobic tails tend to avoid unfavorable interactions with polar water, while the headgroups favorably interact with water. This consequently leads to the formation of aggregates with a certain size called "micelles." This term was first used by J. W. McBain in 1913 to describe an aggregate of soap molecules, and the first model of spherical micelles was proposed by G. S. Hartley [1]. In Hartley's micelle model, the polar headgroups usually form the exterior of the aggregate and the hydrophobic moieties form the interior.

Tanford was the first to formulate the thermodynamics of micelle formation [2]. His theory and its improvements, and also recent computer simulations based on these theories are reasonably consistent with various experimental results for a wide range of materials. It is generally accepted that the aggregation number (N_{agg}) gradually changes with the surfactant concentration and other solvent conditions such as the ionic strength and that N_{agg} has a certain distribution. However, we recently observed an interesting phenomenon that seemingly cannot be rationalized within the above framework.

We have newly synthesized calix[4]arene-based amphiphiles, all of which consist of four headgroups and four alkyl tails and have a conical shape, as presented in Fig. 1(a). Synchrotron small angle X-ray scattering (SAXS) measurement was carried out at SPring-8 **BL40B2** to determine the micelle shape composed of the amphiphile as well as the N_{agg}.

We first identified that a calix[4]arene-based amphiphile bearing amines and propyl chains forms hexamer micelles at pH = 3 without any distribution in N_{agg} [3]. We also found that some calix[4]arene-based amphiphiles self-assemble into spherical micelles exhibiting similar monodispersity of N_{agg}. The monodispersed aggregation numbers that we have so far identified are 4, 6, 8, 12, 20. It is quite surprising that those numbers coincide with the vertex numbers of regular polyhedral structures, i.e., Platonic solids, as illustrated in Fig. 1(a), and we name them "Platonic micelles." The monodispersity and discreteness of N_{agg} have been found in another micellar system composed of surfactin, which consists of a heptapeptide unit (Glu-Leu-D-LeuIVal-Asp-D-Leu-Leu) and a beta-hydroxy fatty acid. The

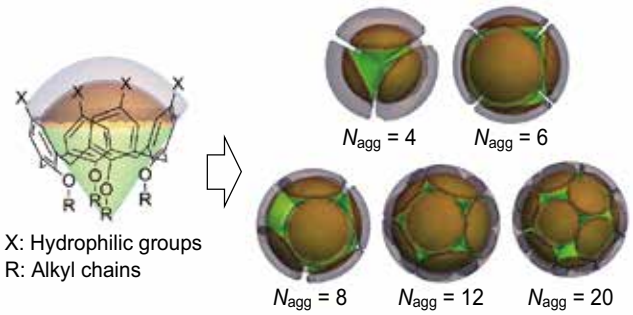

Fig. 1. Chemical structure of a calix[4]arene-based amphiphile and schematic illustration of calix[4]arene-based micelles whose N_{agg} values match the vertex numbers of regular polyhedra.

present results indicate that a suitable combination of amphiphile tail length, head volume, and sufficiently small N_{agg}, as well as some rigidity of the building block, is necessary to produce Platonic micelles, which are monodisperse with a defined N_{agg} whose values are chosen from the vertex numbers of regular polyhedra [4].

There have been no reports of such discreteness and monodispersity in conventional micelles. Generally, normal micelles have larger N_{agg} values than the present systems. If the interfacial area (a_e) between a hydrophilic domain and a hydrophobic domain is large and N_{agg} is small, the way in which the hydrophobic tails are covered to achieve the minimum free energy may differ from the systems with a large N_{agg}. This issue is probably related to the mathematical problem of how to efficiently cover a spherical surface with multiple identical spherical caps. In geometry, this is called the "best packing on a sphere" or the Tammes problem. For example, as illustrated in the right of Fig. 2(a), the maximum coverage with three spherical caps is $D(N) = 0.75$. For 12 caps (left of Fig. 2(a)), we can have a larger coverage of $D(N) = 0.90$ and the centers of the caps have the same configuration as the vertices of a regular icosahedron. Here, $D(N)$ is defined as the ratio of the sum of the cap areas to the area of the sphere surface.

Figure 2(b) plots $D(N)$ against the number of caps N. For small N, larger $D(N)$ values are obtained at certain numbers such as N = 4, 6,12, and 20. It is surprising that these numbers coincide with our observed values of N_{agg}. In an analogy to the above, it can be reasonably assumed that there are certain

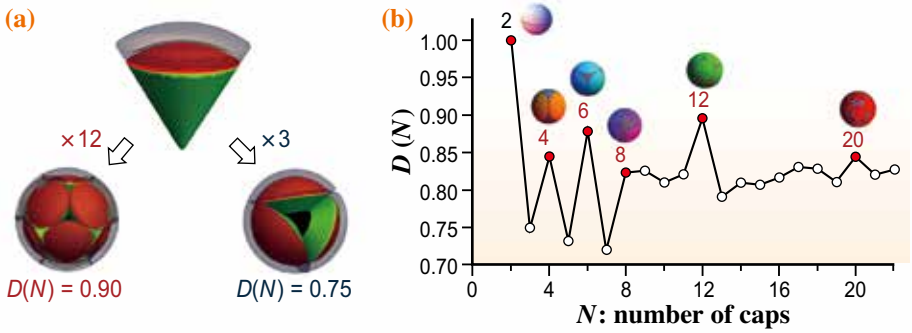

Fig. 2. **(a)** Two examples of the best packing of multiple circles on a sphere surface (N = 3 and 12). The Tammes problem and its analogy of how multiple cone-shaped surfactants form spherical micelles to cover their hydrophobic tail domain (green) with the interface area (red) acting as spherical caps. **(b)** Coverage $D(N)$ of the Tammes problem plotted against the number of caps N.

numbers of molecules that can more efficiently cover spherical micelles than other numbers. One may think that real molecules do not behave like rigid spherical caps, but the hard-core potential (i.e., Tammes problem) is not a necessary condition for an oscillating $D(N)$ pattern. A similar simulation with the Coulomb potential exhibits local maxima at the same values of N as those in the Tammes problem. Therefore, we can presume that N_{agg} = 4, 6,12, and 20 are more likely to be encountered in real micelles. The monodispersity can be explained in the same framework. When a certain N_{agg} is strongly favorable, most aggregates will consist of this number of molecules and the system becomes monodisperse.

We have also observed a very interesting kinetic transition from calix[4]arene-based dodecamer micelles to icosamer ones when increasing the salt concentration (Fig. 3(a)) [5]. N_{agg} remained unchanged during the first 60 s after the increase in NaCl concentration, and then abruptly increased to 20 (Fig. 3(b)). We surmise that this phenomenon is probably due to the fact that only a few N_{agg} values are thermodynamically allowed in the system of Platonic micelles.

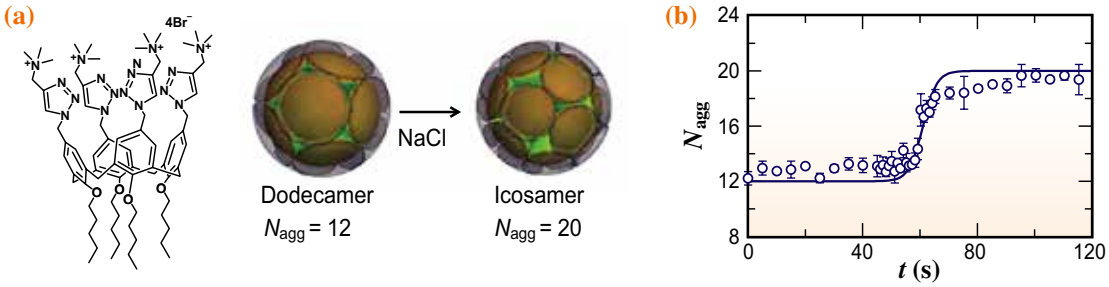

Fig. 3. **(a)** Chemical structure of the calix[4]arene-based amphiphile bearing quaternary amines and schematic illustration of the salt-induced transition of the micelles from dodecamer to icosamer. **(b)** Time evolution of N_{agg} (circles) and the fitting curve.

Shota Fujii, Rintaro Takahashi and Kazuo Sakurai*

Department of Chemistry and Biochemistry,
University of Kitakyushu

*Email: sakurai@kitakyu-u.ac.jp

References

[1] B. Vincent: Adv. Colloid Interface Sci. **203** (2014) 51.
[2] J.N. Israelachvili: Intermolecular and Surface Forces. Vol. 450 (Academic press London, 1992).
[3] S. Fujii *et al.*: Langmuir **28** (2012) 3092.
[4] *S. Fujii, S. Yamada, S. Matsumoto, G. Kubo, K. Yoshida, E. Tabata, R. Miyake, Y. Sanada, I. Akiba, T. Okobira, N. Yagi, E. Mylonas, N. Ohta, H. Sekiguchi and K. Sakurai: Sci. Rep. **7** (2017) 44494.*
[5] *R. Takahashi, S. Matsumoto, S. Fujii, T. Narayanan and K. Sakurai: Angew. Chem. Int. Ed. **56** (2017) 6734.*

In situ analysis of Cs species in an alkali-activated solid waste incineration fly ash and pyrophyllite-based system

Alkali-activated materials (AAMs) synthesized from aluminosilicates under highly alkaline conditions, such as geopolymers and zeolites, have been researched as alternatives to cement, concrete, and ceramics [1]. One of the alternative uses is as a solidification agent in the treatment of various wastes. Recently, there has been much interest in the use of AAMs obtained from aluminosilicates for the treatment of radionuclide-contaminated waste from the Fukushima Daiichi Nuclear Power Plant (FDNPP) accident. In particular, radioactive cesium (^{134}Cs and ^{137}Cs) in radionuclide-contaminated solid waste incineration fly ash (SWIFA), a residue from thermal treatment of the waste, is soluble and cannot be stabilized sufficiently by general solidification using ordinary Portland cement [2].

The solidification process of an AAM obtained from aluminosilicates may involve the dissolution of aluminosilicates in a highly alkaline solution, gelation, reorganization, polymerization/crystallization, and hardening (Fig. 1(a)) [1]. Kinetic analysis of the process is essential for the design of curing conditions and important for understanding the reaction mechanism for the effective stabilization of hazardous substances. Although kinetic analyses have been reported, almost all of them focused on changing the AAM matrix such as the environment around Si and Al, which form a Si–O–Al chain or an amorphous phase. In the stabilization of Cs, Cs species before and after the stabilization are also important for understanding the mechanism. However, little research is available on kinetic analysis focusing on Cs and its species in AAMs obtained from aluminosilicates.

In this study, we focused on the Cs species during the reaction in an alkali-activated SWIFA and pyrophyllite-based system, which simulated the treatment of radionuclide-contaminated SWIFA from the FDNPP accident. We investigated the chemical kinetics of the Cs species during the reaction by performing an *in situ* X-ray absorption fine structure (*in situ* XAFS) experiment. Pyrophyllite was used in this system because there is little knowledge of its application to AAMs as an aluminosilicate source.

SWIFA that had not been treated with any flue gas control agents (e.g., slaked lime, activated carbon) was collected from a baghouse at an SWI plant in Japan. We added CsCl to the SWIFA so that the concentration of CsCl in the SWIFA was 5 wt% to simplify the identification of changes in the Cs species. Pyrophyllite was dehydrated for 12 h at 900°C. Pastes of the AMM system in this study were prepared by mixing the same weight of each of the municipal solid waste incineration fly ash (MSWIFA) with 5 wt% CsCl, dehydrated pyrophyllite, sodium silicate solution, and 14 mol/L aqueous NaOH solution. To evaluate the stabilization of Cs in the system, the Japanese leaching test (JLT-46) for solid products obtained from 30 g of the pastes was performed at intervals of 0 to 24 h during 48 h curing at four different temperatures (room temperature, 60°C, 80°C, and 105°C) in batch experiments. The *in situ* XAFS experiments for the system were conducted at SPring-8 **BL01B1** (Fig. 1(b)). Approximately 200 g of each paste was

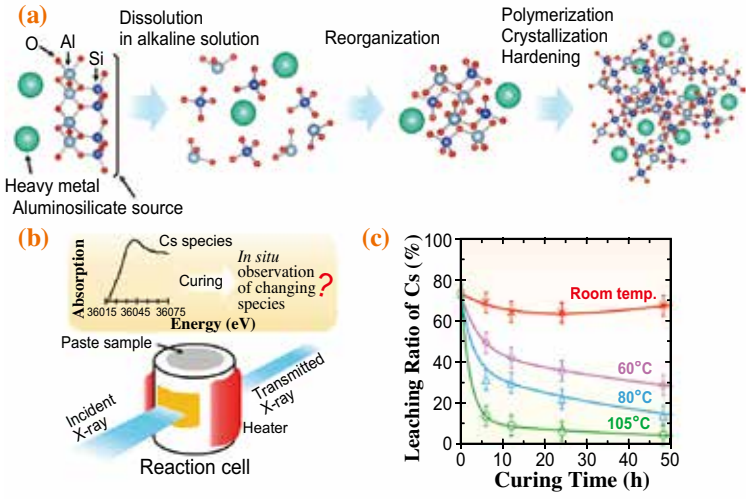

Fig. 1. **(a)** Scheme of a reaction process of an AAM obtained from aluminosilicates [1]. **(b)** Schematic illustration of *in situ* X-ray absorption fine structure (*in situ* XAFS) experiment. **(c)** Leaching ratio of Cs from products in an alkali-activated municipal solid waste incineration fly ash and pyrophyllite-based system obtained from Japanese leaching test (JLT-46). 'Leaching ratio' means the weight percentage of Cs in the leachate to the total Cs in a product.

placed in four custom-built reaction cells, which were cured under the four curing conditions. The *in situ* XAFS spectra at the Cs-*K* edge were collected in transmission mode at intervals of approximately 1 to 10 h (6 runs for 34 h) for each curing condition [3].

The leaching ratio of Cs from the product under room temperature curing decreased very little during JLT-46, by contrast, that of the product cured at 105°C decreased the most to less than 10% of its initial value after 12 h (Fig. 1(c)). These results showed that the AAM system in this study can be stabilized to a greater extend and faster by employing a higher curing temperature and longer curing time.

The results of *in situ* XAFS experiments on samples subjected to 60°C and 105°C curing are shown in Figs. 2(a) and 2(b). The spectra for both curing conditions markedly changed and became increasingly similar to that of pollucite with increasing curing time. The changes in the spectra were greater and the similarity to pollucite was observed earlier for curing at 105°C than for curing at 60°C. We estimated changes in the pollucite content in this system from all the spectra obtained from the *in situ* experiments using factor analysis and linear combination fitting technique using the spectra of reference materials (Fig. 2(c)). The pollucite content in the case of room temperature curing was below the detection limit. By contrast, that in the case of 105°C curing increased fastest to approximately 60 mol% of the total Cs species after 12 h. These results and further analyses of the reaction rate using a simple reaction model (not shown, see Ref. 3) showed that the pollucite formation rate was faster under a higher curing temperature. In addition, the pollucite content had a negative correlation with the Cs leaching ratio, which suggested that the formation of pollucite during the change in the Cs species played an important role in its stabilization using the system. By calculating the rate constants of pollucite and the slope of its Arrhenius plot [3], the activation energy of pollucite formation in the system was estimated to be 31.5 kJ/mol, which is similar to the values for geopolymers or zeolite materials in some alkali-activated systems [4,5]. This result indicates that pollucite can form as a result of the reaction energy in the alkali-activated system in this study.

As shown above, we demonstrated the chemical kinetics of Cs species in an alkali-activated MSWIFA and pyrophyllite-based system and revealed a quantitative relationship between the stabilization of Cs and the formation of pollucite.

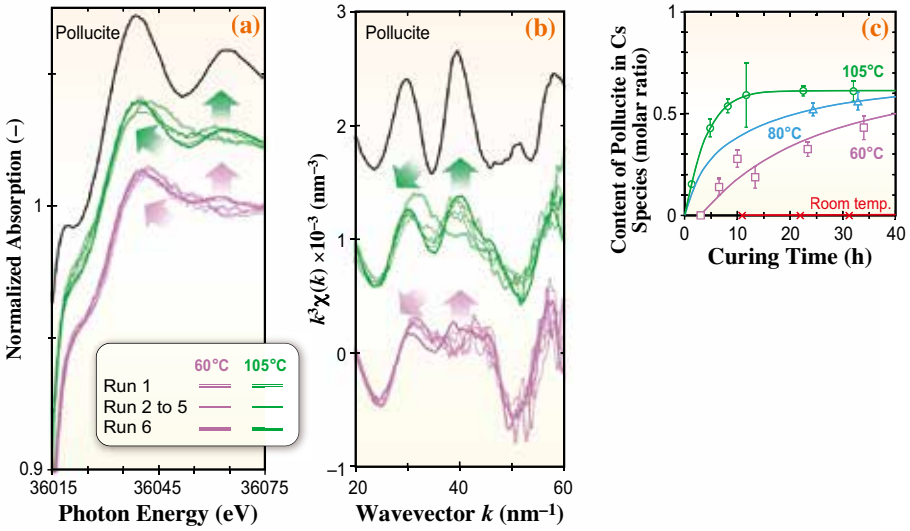

Fig. 2. **(a)** Cs *K*-edge X-ray absorption near edge structure (XANES) of pollucite and result of *in situ* experiments (60°C and 105°C). **(b)** Cs *K*-edge $k^3\chi(k)$ extended X-ray absorption fine structure (EXAFS) of pollucite and result of *in situ* experiments (60°C and 105°C). **(c)** Estimated content of pollucite during *in situ* experiments. Arrows indicate changes in spectral features during the *in situ* experiments.

Kenji Shiota[a,*] and Masaki Takaoka[a,b]

[a] Department of Environmental Engineering, Kyoto University
[b] Graduate School of Global Environmental Studies, Kyoto University

*Email: shiota.kenji.4x@kyoto-u.ac.jp

References

[1] J.L. Provis and S.A. Bernal: Ann. Rev. Mater. Res. **44** (2014) 299.
[2] K. Shiota *et al.*: Chemosphere **187** (2017) 188.
[3] *K. Shiota, T. Nakamura, M. Takaoka, K. Nitta, K. Oshita, T. Fujimori, T. Ina: Spectrochim. Acta Part B* ***131*** *(2017) 32.*
[4] H. Rahier *et al.*: J. Mater. Sci. **42** (2007) 2982.
[5] S.M. Holmes *et al.*: J. Chem. Soc., Faraday Trans. **94** (1998) 2025.

The pyrite-type high-pressure form of FeOOH

Hydrogen (H) is the most abundant element in the universe and it has played an important role in the structure, dynamics, and evolution of the Earth. About 70% of the Earth's surface is covered with water (H_2O) and a huge amount of water is also estimated to be maintained in the Earth's interior. However, the actual amount, distribution, and origin of the water deep in the Earth's interior are unclear. Although liquid water is generally present on the surface of the Earth, hydrous phases (which contain hydrogen in their crystal structure) can retain water in the deep mantle. Therefore, a significant amount of water has been transported into the Earth's interior via the subduction of hydrous phases in the cold oceanic lithosphere since the initiation of plate tectonics in the Archaean. Our research group previously contributed to understanding of the stability of hydrous phases at high pressures [1]. Several recent studies have suggested that δ-AlOOH - phase H ($MgSiO_4H_2$) solid solution can retain water without dehydration even at high pressures and temperatures corresponding to the base of the mantle [2]. Thus, the surface water may be transported as far as the core–mantle boundary (2,900 km depth) [1,2]. However, the strong dependence of the stability of hydrous minerals on the chemical composition may prevent the passage of water to such a great depth. For example, one of the possible hydrogen carriers, iron hydroxide ε-FeOOH, was recently reported to decompose at 80 GPa (corresponding to 1,900 km depth) to form FeO_2, releasing H_2 [3]. This reaction suggests that the separation of hydrogen and oxygen is cyclic and that water cannot reach the deeper regions of the lower mantle. In this study [4], we further examined the high-pressure behavior of iron hydroxide FeOOH and obtained data showing the formation of a new hydrous phase under the conditions of the deep lower mantle.

First, we conducted first-principles calculations to determine the stability of FeOOH phases at high pressures. The calculated relative enthalpies indicated that the pyrite - type structure may be stabilized at above ~70 GPa (Fig. 1), although the previous study suggested that FeOOH decomposes into FeO and H_2 under such conditions.

On the basis of these first-principles predictions, we performed *in situ* XRD measurements using a laser-heated diamond anvil cell (DAC) system at SPring-8 **BL10XU**. We used symmetric diamond anvil cells with 90 μm and 200 μm culet diamond anvils

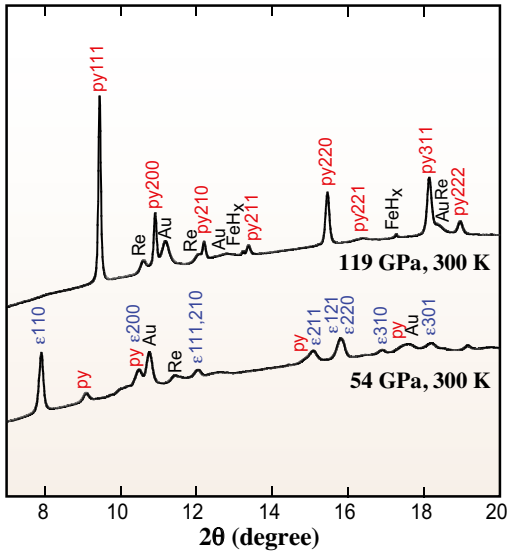

Fig. 1. Typical XRD patterns obtained by *in situ* observations at high pressure after heating at 1,500 K. ε, ε-FeOOH; py, pyrite-type FeOOH; FeH_x, dhcp-FeH_x; Au, gold; Re, rhenium.

to generate high pressures. Pellets of α-FeOOH with thickness 10–15 μm were used as the starting material. Each sample was coated with sputtered gold (Au) films on both sides, which acted as an internal pressure standard and a laser absorber. The sample was loaded into a sample chamber in a pre-indented rhenium gasket with insulation provided by layers of fine-grained SiO_2 glass. We used two 100 W single-mode fiber lasers and heated the sample from both sides. The temperatures were maintained for 3–30 min and measured using spectroradiometry. Angle-dispersive *in situ* XRD patterns were obtained at high pressures and temperatures with an imaging plate (Rigaku) and an X-ray flat panel detector (PerkinElmer) with typical exposure times of 30 s and 1 s, respectively. The wavelengths of the monochromatic incident X-ray beam were 0.415–0.416 Å. Pressures were calculated from the various equations of state for gold.

XRD patterns obtained at ~120 GPa at room temperature only showed diffraction peaks for sputtered gold owing to the amorphization of goethite during the compression process. After the heating of the sample to ~1500 K, the *in situ* XRD pattern showed clear diffraction peaks that can be accounted for by a simple cubic symmetry (Fig. 2), which

matches that predicted by theoretical calculation for the pyrite-type framework of FeO_6 octahedra. In order to determine the stability fields of this phase, we reheated this sample after decompression. The peaks corresponding to the pyrite-type FeOOH remained as the stable phase in the pressure range between 90 GPa and 129 GPa. Upon heating after further decompression to ~60 GPa, we observed the transition of pyrite-type FeOOH to ε-FeOOH, which is known as the polymorph in FeOOH. Thus, the phase boundary between ε-FeOOH and pyrite-type FeOOH is located between 60 GPa and 90 GPa at 1,500 K. XRD patterns of the pyrite-type FeOOH were also obtained in additional *in situ* experiments up to 2,400 K using the same starting material at ~96 GPa with weak peaks corresponding to double hexagonal-close-packed (dhcp) FeHx. When the sample was heated to temperatures of above 2,400 K, the pyrite-type FeOOH dehydrated into an assemblage containing an Fe_2O_3 post-perovskite phase.

Although anhydrous FeO_2 with a pyrite-type structure was recently reported to be stable above 80 GPa [3], the cell volume of pyrite-type FeOOH is approximately 8% greater than that of FeO_2 synthesized by a reaction between Fe_2O_3 and O_2 at about 80 GPa (Fig. 3). Moreover, our first-principles calculations clearly indicate that pyrite-type FeOOH is a thermodynamically stable phase since the enthalpy of the mixture of FeO_2 plus H_2 is much higher than that of pyrite-type FeOOH. Thus, pyrite-type FeOOH or the recently proposed $FeOOH_x$ (a partially solid solution between FeO_2 and FeOOH) [5] may deliver water to the deep lower mantle. The deep-seated pyrite-type FeOOH may release the free water by dehydration to form Fe_2O_3 when the slabs warm up during a long period of stagnation at the core-mantle boundary, as we observed. This dehydration process at the bottom of the lower mantle may cause partial melting at this depth. Further studies are required to test this hypothesis.

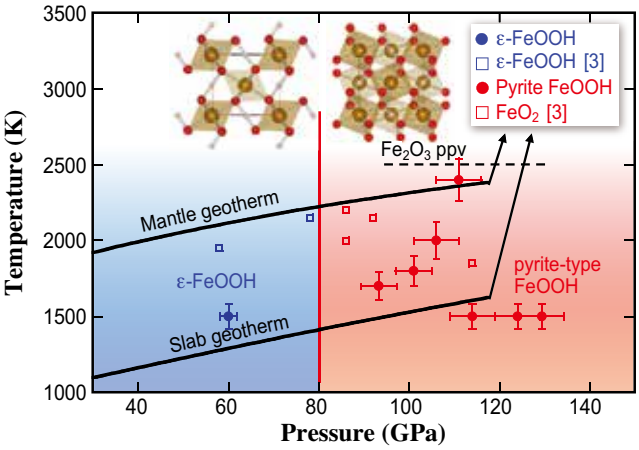

Fig. 2. Crystal structures and stability fields of ε-FeOOH and pyrite-type FeOOH. The appearance of Fe_2O_3 post-perovskite (ppv) associated with the dehydration process was observed above 2,400 K. Geotherms for cold subducted slabs and the mantle are shown by thick solid curves.

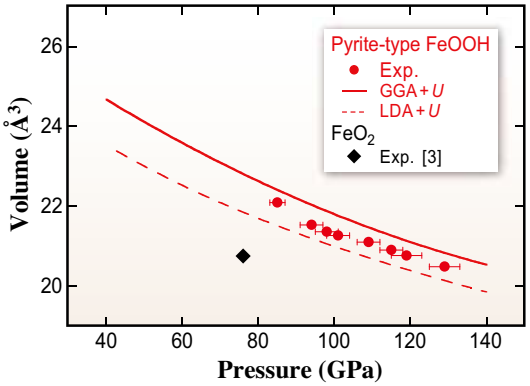

Fig. 3. Volume of pyrite-type FeOOH as a function of pressure. The experimental data at 300 K derived from XRD patterns after annealing at 1500–2400 K shows a larger volume of pyrite-type FeOOH than that of anhydrous FeO_2 [3]. Calculated volume compression curves of pyrite-type FeOOH at 0 K obtained using GGA+*U* and LDA+*U* (solid and dashed lines, respectively) are shown for comparison.

Masayuki Nishi

Geodynamics Research Center, Ehime University

Email: nishi@sci.ehime-u.ac.jp

References

[1] M. Nishi *et al.*: Nat. Geosci. **7** (2014) 224.
[2] I. Ohira *et al.*: Earth Planet. Sci. Lett. **401** (2014) 12.
[3] Q. Hu *et al.*: Nature **534** (2016) 241.
[4] *M. Nishi, Y. Kuwayama, J. Tsuchiya, T. Tsuchiya: Nature **547** (2017) 205.*
[5] J. Liu *et al.*: Nature **551** (2017) 494.

Intermediate-depth earthquakes triggered by localized heating in peridotites

The surface plates of Earth (thickness, ~60 km), on which we live, move and subduct along with the flow of the mantle (depths greater than 60 km). Earthquakes occur through the collision and subduction of plates. Earthquakes can be divided into three types according to the depth of hypocenter: i) interplate or crustal earthquakes (depths <50 km); ii) intermediate-depth earthquakes (50–300 km); and iii) deep earthquakes (>300 km). Intermediate-depth earthquakes often occur in subduction zones, and sometimes magnitude 7-class ones result in serious disasters. However, the occurrence of intermediate-depth earthquakes in subducting slabs has long puzzled geoscientists because these earthquakes require some mechanism to accelerate the fault movement at pressures above 1.8 GPa (i.e., depths ≥50 km). The frictional strength is so high that fault movement is inhibited without a "lubricant" at such high pressures. Since 1960s, a generally accepted hypothesis has been that aqueous fluid released from the breakdown reaction of hydrous minerals (e.g., antigorite and lawsonite) triggers intermediate-depth earthquakes. However, the distribution of hydrous minerals, and thus the aqueous fluid, is limited to the upper part of subducting slabs, namely, aqueous fluid does not account for the occurrence of earthquakes in the lower part of slabs. Here we show that intermediate-depth earthquakes could be caused by the drastic weakening of peridotites (i.e., the main constituent of slabs) through localized heating followed by partial melting [1].

My colleagues and I have conducted uniaxial deformation experiments on peridotite samples combined with synchrotron *in situ* X-ray observations at pressures of 1.0–2.6 GPa, temperatures of 860–1350 K and strain rates of 10^{-5}–10^{-4} s^{-1} using a deformation-DIA apparatus at SPring-8 **BL04B1**. The temperature and pressure ranges were equivalent to the conditions in the shallower part of subducting slabs. Acoustic emissions (AEs) were monitored using six piezoceramic lead-zirconate titanate transducers, each attached to the rear side of a second-stage anvil. Our AE monitoring technique (Fig. 1) allowed us to evaluate the three-dimensional location and magnitude of microcracks (i.e., hypocenters of AEs) in a deforming peridotite sample. The mechanical and statistical similarities between AEs and earthquakes have been verified on the basis of the Gutenberg-Richter relationship and the accelerated moment release model. In particular, the dependence of the critical nucleation size of failure on the duration of quasi-dynamic rupture is known to follow a scaling relationship in a wide range of scales from micrometers (i.e., microcracks) to kilometers (i.e., earthquakes) [2].

The plastic deformation of peridotite samples was followed by faulting and AEs at an accelerated strain rate (>5×10^{-5} s^{-1}). A decrease in the Gutenberg–Richter *b*-value and increases in the AE amplitude and AE rate were usually observed around the timing of faulting, probably due to the subcritical growth of cracks. Strong AE activity was also observed to continue after the faulting (i.e., aftershocks). Gouge layers consisting of ultrafine-grained olivine and orthopyroxene (down to 20 nm) developed along faults. Amorphous films were frequently observed on the grain interfaces (Fig. 2). Taking into account the possibility of localized heating (i.e., adiabatic instability caused by the weakening-feedback mechanism wherein localized deformation caused further heating), the origin of the amorphous phase must be evaluated from the viewpoint of the partial melting of peridotite. In fact, the following theoretical equation (Eq. 1) [3] predicts that localized heating is effective when the strain rate exceeds a threshold value (>10^{-4} s^{-1} in a laboratory scale):

$$\dot{\varepsilon}_c > \frac{h\rho C_p \kappa RT^2}{\sigma H^* L^2} \qquad (1)$$

where h is the work hardening coefficient (= 1), ρ is the density (~3.4 g/cm^3 at 1.5 GPa), C_p is the specific

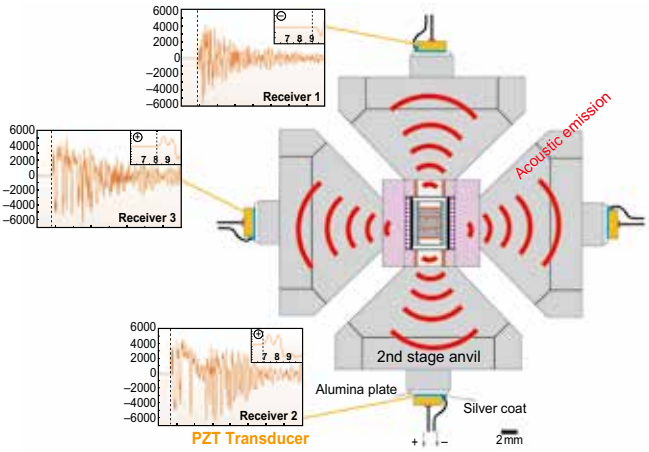

Fig. 1. Cell assembly viewed as a cross section from the direction parallel to the X-ray path. A cylindrical peridotite sample (diameter: 3 mm; length: 5 mm) is placed in the central part of the cell assembly. Piezoceramic lead-zirconate titanate (PZT) transducers are attached to the rear side of second-stage anvils made from tungsten carbide or cubic boron nitride. The transducers are separated from the anvils by alumina plates. Representative waveforms detected by transducers are also shown.

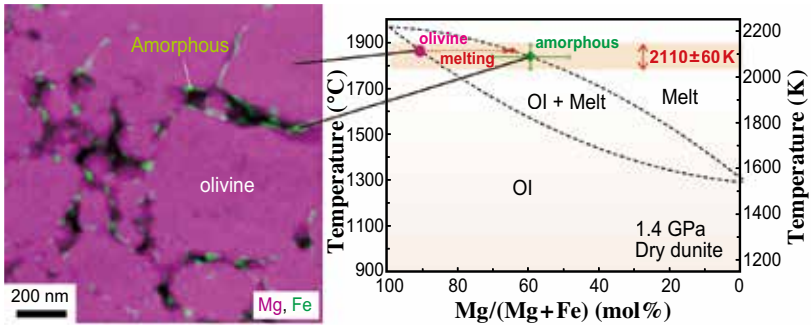

Fig. 2. Element map of ultrafine grains in a gouge layer formed in a failed dunite sample. The map was acquired using a field-emission TEM JEOL-2100F equipped with an EDS detector system at Ehime University. In the element map, the grayscale corresponds to the concentration of elements (pink: magnesium; green: iron). Chemical compositions of olivine and the amorphous phase are plotted in an equilibrium diagram of the Mg_2SiO_4–Fe_2SiO_4 system at 1.4 GPa under dry conditions. The iron content of the amorphous phase shows that the melting temperature is 2110±60 K.

heat (= 817 J/kg·K), κ is the thermal diffusivity (= 0.7 mm^2/s), H^* is the activation enthalpy for deformation (= 554 kJ/mol at 1.5 GPa), and L is the sample size (= 5.5 mm). *In situ* X-ray observations showed that the fault slip rate observed in the peridotites was sufficient to trigger localized heating. The partitioning of iron between olivine and the melt (i.e., amorphous phase) is useful for estimating the melting temperature in dry dunite (i.e., a monomineralic peridotite that consists of olivine). Using the calibration line determined from the chemical composition of olivine (Mg/(Mg+Fe) = 91 mol%), the concentration of iron in the amorphous phase was determined to be Mg/(Mg+Fe) = 59±11 mol%. The estimated iron content is consistent with the ideal iron content of the partial melt of olivine within the error bar (i.e., Mg/(Mg+Fe) = 65 mol%). Thus, the peak temperature during the localized heating in the dry dunite was estimated to be ~2110±60 K from the iron concentration in the amorphous phase (Fig. 2). At the peak temperature, the creep strength of the faults in dry dunite is thought to decrease to ~35 MPa or less.

Localized heating, which is required for the initiation of faulting, can be achieved in subducting slabs (temperatures of 873–973 K and pressures up to 6.5 GPa). It is obvious that the critical strain rate at a laboratory scale (i.e., ~10^{-4} s^{-1}) is much higher than that at a natural scale (1–10 km thickness for each plane of the double seismic zone) (see Eq. 1). Taking into account the fact that the plastic deformation of peridotites follows a power-law form in the shallow upper mantle, localized heating is considered possible once the background strain rate exceeds a threshold value in the range from 10^{-15} to 10^{-13} s^{-1}. The strain rate can be easily increased to the threshold value in shear zones as a result of dynamic recrystallization (i.e., grain size reduction via dislocation creep) followed by diffusion creep (Fig. 3). Localized heating induced by strain localization in the fine-grained peridotite shear zone has also been verified by a numerical model [4] and geological observations [5]. Thus, we conclude that the formation of fine-grained shear zones may be important for the occurrence of intermediate-depth earthquakes triggered by localized heating in subducting slabs.

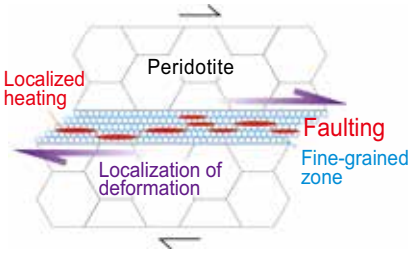

Fig. 3. Schematic diagram showing faulting caused by accelerated strain localization in peridotite with a fine-grained shear zone. The dominant deformation mechanisms are dislocation creep and diffusion creep in the coarse-grained wall rock (gray) and in the fine-grained shear zone (blue), respectively. Accelerated strain localization triggers localized heating in the fine-grained shear zone.

Tomohiro Ohuchi

Geodynamics Research Center, Ehime University

Email: ohuchi@sci.ehime-u.ac.jp

References

[1] *T. Ohuchi, X. Lei, H. Ohfuji, Y. Higo, Y. Tange, T. Sakai, K. Fujino and T. Irifune: Nat. Geosci.* ***10*** *(2017) 771.*
[2] X. Lei *et al.*: Phys. Earth Planet. Inter. **137** (2003) 213.
[3] S. Karto: An Introduction to the Rheology of Solid Earth (2008) Cambridge Univ. Press.
[4] P.B. Kelemen, G. Hirth: Nature **446** (2007) 787.
[5] T. Ueda *et al.*: Geology **36** (2008) 607.

Effect of ferrous iron on elasticity of bridgmanite: Possible origin of anticorrelated seismic velocity anomaly observed in the lower mantle

A seismological study revealed that some regions show an increase in bulk sound velocity ($V_B = \sqrt{K_s/\rho}$) and a decrease in shear wave velocity ($V_S = \sqrt{G/\rho}$): $\Delta V_B > 0 > \Delta V_S$, and others show a decrease in V_B and an increase in V_S: $\Delta V_B < 0 < \Delta V_S$ (K_S, G, and ρ are the adiabatic bulk modulus, shear modulus, and density, respectively) in the deep mantle between depths of 2000 and 2891 km [1]. This feature is called an anticorrelated seismic velocity anomaly. The regions showing this anomaly, which are beneath Africa and the central Pacific, have attracted attention as large low shear velocity provinces (LLSVPs) characterized as $\Delta V_B > 0 > \Delta V_S$.

In the 200 km layer at the bottom of the lower mantle, known as the D″ layer, the anomaly can be explained by the post-perovskite (pPv) phase transition of bridgmanite, the most abundant material of the lower mantle with the perovskite structure, since V_B and V_S for the post-perovskite phase are lower and higher than those for bridgmanite, respectively [2]. However, this cannot explain the anomaly in the shallower part from 2000 to 2700 km where the pPv phase cannot exist.

There have been several proposals for the origin of the LLSVPs [3]. Thermal heterogeneity has been considered, but exclusively thermal effects are insufficient to explain the LLSVPs because usually both V_B and V_S decrease with temperature. It is thus suggested that the LLSVPs have a very different chemical composition from that of the average mantle.

Although bridgmanite is an iron-aluminum bearing magnesium silicate, the effects of cation substitution, especially Fe^{2+}, have not been well investigated. To address these issues, the elastic properties of iron-bearing bridgmanite have been investigated under ambient conditions. For this purpose, the inelastic X-ray scattering (IXS) technique was used [3]. Iron-bearing bridgmanite is a colored material. A single crystal of bridgmanite is usually tiny (< a few hundred μm). Therefore, the elastic properties of iron-bearing bridgmanite should be measured using appropriate methods. X-rays can be focused relatively easily and do not basically limit a sample. The valence state of a bridgmanite has been evaluated by synchrotron-based ^{57}Fe Mössbauer spectroscopy [3].

The measured samples were single crystals synthesized at 24 GPa and 1500°C using a Kawai-type multianvil apparatus. The lattice constants were refined using a four-circle diffractometer with a laboratory source. The chemical composition was analyzed using an electron microprobe and determined as $Mg_{0.943}Fe_{0.045}Al_{0.023}Si_{0.988}O_3$ (FeAl-Bdg). It is important to identify the valence state of iron in the crystal. Although the present samples were not enriched with ^{57}Fe but had iron isotopes with natural abundance, a Mössbauer spectrum was collected in the energy domain at SPring-8 **BL10XU** (Fig. 1). Taking some constraints imposed by the crystal structure into account, the absorption lines in this spectrum are interpreted as an asymmetric doublet. On the basis of this interpretation, the isomer shift and quadrupole splitting were determined to be 1.05(6) and 1.8(1) mm/s, respectively. These values indicate that the iron in this sample was in a divalent high-spin state and substituted for magnesium. The intensity

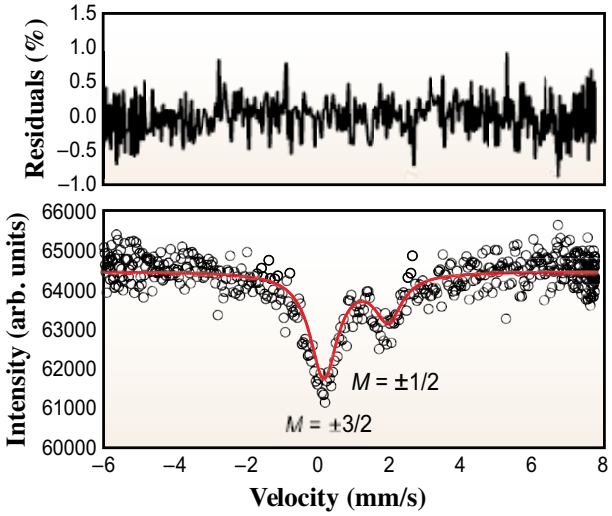

Fig. 1. Mössbauer spectrum of ^{57}Fe in FeAl-Bdg. Black circles are raw data from which the backgrounds have been subtracted. The red line indicates one doublet fitted to the data. (Top panel) Fitting residuals.

Table 1. Elastic moduli (Voigt-Reuss-Hill average of C_{ij} values) and elastic wave velocities of bridgmanites under the ambient conditions.

	Mg-Bdg	FeAl-Bdg	
K_S	236(4)	244(3)	
G	166(2)	165(1)	(GPa)
V_B	7.58(6)	7.66(5)	
V_S	6.37(4)	6.32(2)	(km/s)

asymmetry of this doublet is most probably due to the sample being a single crystal.

IXS measurements were carried out at SPring-8 **BL35XU**; $MgSiO_3$ bridgmanite (Mg-Bdg) was also measured at **BL43LXU** as well as at BL35XU as a reference. Elastic stiffness constants, C_{ij}, were determined from phonon energies and momenta obtained from the IXS spectra on the basis of the Christoffel equation. The number of phonon modes used to determine the six C_{ij} values was 461 and 319 for Mg-Bdg and FeAl-Bdg, respectively. The rather redundant data enabled us to determine the C_{ij} values precisely. Table 1 shows the determined K_S and G together with V_B and V_S. V_B for FeAl-Bdg is higher than that for Mg-Bdg, whereas V_S for FeAl-Bdg is lower than that for Mg-Bdg. Some cation substitutions in Mg-Bdg caused the anticorrelation between V_B and V_S, though the measurements were carried out under ambient conditions.

The present results have been applied to a geochemical and geothermal model assuming a perovskite mantle [4]. The seismic anomaly observed in the LLSVPs may be explained by the variation of Fe^{2+} and the temperature. When ΔT is about 226 K, the LLSVPs can be explained by only 5.4 atom% of Fe^{2+} (Fig. 2). These numbers are probably upper limits as the effect of aluminum has not been taken into account. The anticorrelated behavior of the elastic wave velocities has been successfully interpreted on the basis of the results of laboratory experiments.

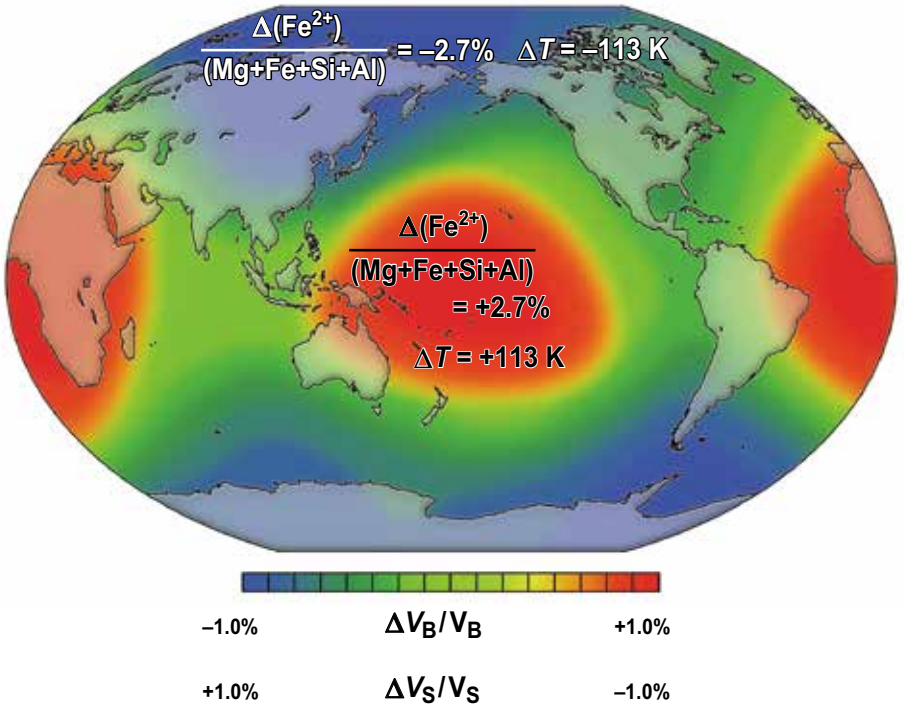

Fig. 2. Schematic image of regional variation of seismic velocities, ferrous iron composition of bridgmanite, and temperature variation at depths between 2000 and 2891 km. The map outline was made using CraftMAP *(http://www.craftmap.box-i.net/)*.

Hiroshi Fukui[a,*], Seiji Kamada[b] and Akira Yoneda[c]

[a] Center for Novel Material Science under Multi-Extreme Conditions, University of Hyogo
[b] Frontier Research Institute for Interdisciplinary Sciences, Tohoku University
[c] Institute of Planetary Materials, Okayama University

*Email: fukuih@sci.u-hyogo.ac.jp

References

[1] J. Trampert *et al.*: Science **306** (2004) 853.
[2] A. R. Hutko *et al.*: Science **320** (2008) 1070.
[3] *H. Fukui, A. Yoneda, A. Nakatsuka, N. Tsujino, S. Kamada, E. Ohtani, A. Shatskiy, N. Hirao, S. Tsutsui, H. Uchiyama and A.Q.R. Baron: Sci. Rep.* ***6*** *(2016) 33337.*
[4] M. Murakami *et al.*: Nature **485** (2012) 90.

Melting experiments on Fe–Fe_3S system to 254 GPa

Sulfur has been considered to be an important light element in the Earth's core because of the low melting temperature of Fe–S alloys and its wide presence in iron meteorites [1]. Previous density measurements of liquid Fe–S alloys under high pressure demonstrated that the outer core density profile is explained by Fe containing 10 wt.% S. The melting phase relations in the Fe–FeS system, in particular at 330 GPa corresponding to the pressure at the solid/liquid core boundary, are of great importance, because the outer core liquid composition must be on the iron-rich side of the eutectic if sulfur is a predominant impurity element.

Fe and FeS exhibit a simple eutectic system at 1 bar, while intermediate compounds are formed at high pressures; Fe_3S_2 above 14 GPa and Fe_2S and Fe_3S above 21 GPa [2]. Based on *in situ* X-ray diffraction (XRD) measurements in a laser-heated DAC, the eutectic temperature and composition in the Fe–Fe_3S system have been previously determined up to 123 GPa [3]. However, they have not been examined at the core pressure range above 136 GPa yet.

Melting experiments were performed on the Fe–Fe_3S binary system at high pressures between 34 and 254 GPa in a laser-heated diamond-anvil cell (DAC). We used starting materials of fine-grained homogeneous mixtures of Fe and FeS (<500 nm) prepared by induction melting and rapid quenching techniques. Melting phase relations and the liquid/solid partitioning of sulfur were examined on the basis of a combination between X-ray diffraction measurements at SPring-8 **BL10XU** and electron microprobe analyses on recovered samples. Angle-dispersive XRD spectra were collected on a flat panel detector (FPD) (Perkin Elmer) with typical exposure time of 1 s. Visible fluorescence light induced by X-rays in a diamond was used to precisely align the laser-heated spot with an X-ray beam.

First, we have examined subsolidus phase relations by XRD measurements before exploring melting phase relations. Using Fe + 5.9 wt% S starting material, four new peaks from the B2 (CsCl-type) structure appeared on heating to 2370 K at 270 GPa, in addition to the hexagonal-close-packed (hcp) phase (Fig. 1). The B2 structure indicates the ordering of sulfur atoms. When we further increased the temperature to 3570 K at 278 GPa, the Debye rings of both hcp Fe and B2 phases became spotty, indicating the grain growth and thus the stability of hcp + B2 at this *P-T* condition. The peaks from the B2 phase diminished, consistent with an increase in sulfur concentration in solid Fe with increasing temperature under subsolidus conditions. The coexistence of the hcp and B2 phases suggests that the solubility of sulfur in hcp Fe is lower than the starting composition (5.9 ± 0.2 wt% S) at 278 GPa. These indicate that the system we examined in the present experiments is Fe–Fe_3S binary only up to 254 GPa (see below).

Next, we performed ten separate melting experiments in a pressure range from 34 to 278 GPa. Melting of a sample was confirmed by a characteristic texture. A homogeneous portion with a non-stoichiometric composition was found at the center, the hottest part of a laser-heated sample, representing quenched liquid. Either solid Fe or Fe_3S in direct contact with liquid alloys should represent a liquidus phase. Interestingly, we sometimes observed both Fe and Fe_3S solids (see Fig. 2 for experiment at 254 GPa) in contact with liquid, indicating that it represents a eutectic liquid. Based on liquid compositions and coexisting solid phases, we constrain the eutectic liquid composition in the Fe–Fe_3S binary system to 254 GPa (Fig. 3). The sulfur concentration in the eutectic liquid decreases substantially with increasing pressure; it contains only 5.7 wt.% S at 254 GPa. Our data also demonstrate that solubility of sulfur in solid

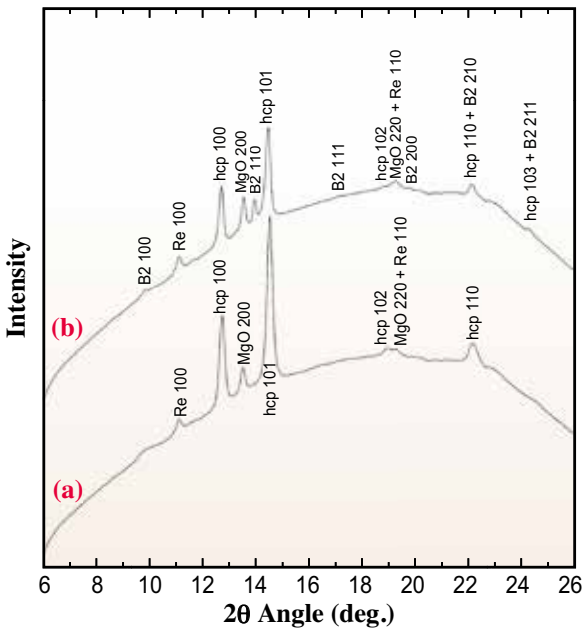

Fig. 1. XRD patterns of Fe + 5.9 wt% S **(a)** at 270 GPa and 300 K before heating and **(b)** during heating at 270 GPa and 2370 K.

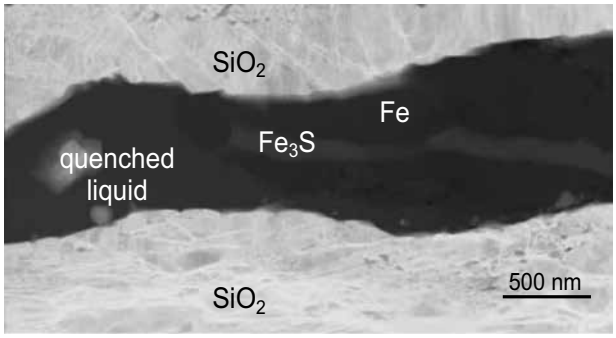

Fig. 2. STEM bright field image of the Fe+5.9 wt% S sample recovered from 254 GPa and 3550 K, showing the coexistence of liquid, solid Fe and Fe_3S. The presence of SiO_2 crystals indicates that the liquid part was molten.

iron is enhanced at higher pressures. It increases from <2 wt% S below 50 GPa to 3.4 ± 0.4 wt% S at 80 GPa. The present experiments further show that solid iron coexisting with eutectic liquid includes 3.9 ± 0.4 wt% S at 254 GPa.

Previous studies suggested that seismologically-deduced liquid outer core density profile is consistent with that of Fe containing 10 to 14 wt.% S at relevant conditions. On the other hand, the present study demonstrates that the eutectic liquid in the Fe–Fe_3S binary system includes only less than 6 wt.% S at 254 GPa, which should not be much different at 330 GPa, indicating that the liquid Fe with ≥10 wt.% S previously proposed for the outer core composition crystallizes the S-rich phase, Fe_3S at least to 254 GPa and the CsCl (B2)-type phase at higher pressure including solid/liquid core boundary conditions. It suggests that crystallizing solid is less dense than coexisting liquid at the ICB, which is not consistent with seismic observations. Our experiments also show that liquid Fe+5.7 wt.% S coexisted with hcp Fe containing 3.9 wt.% S at 254 GPa, showing a relatively small difference in sulfur concentration between coexisting liquid and solid at mid-outer core conditions. The sulfur contents in coexisting liquid and solid will be even closer at the solid/liquid core boundary. The density jump across the solid/liquid core boundary is not reconciled with such a small difference in impurity concentration in addition to the difference in density between solid and liquid. These indicate that sulfur is not a predominant light element in the core, although it could still be one of the alloying components.

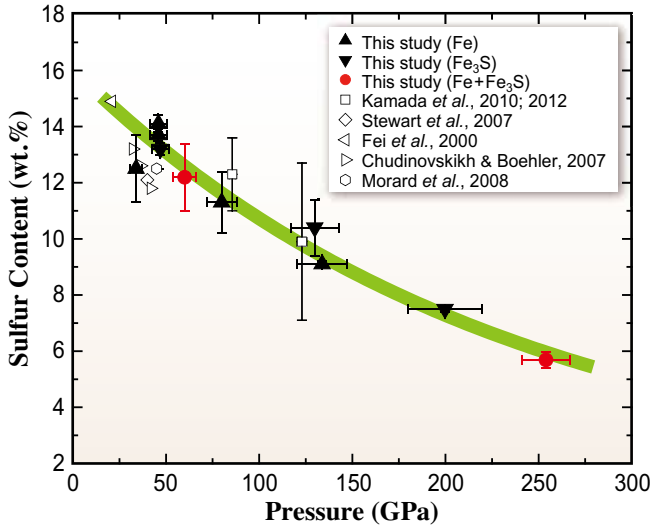

Fig. 3. Liquid compositions plotted as a function of pressure. Sulfur concentrations in eutectic liquids should be more or less than those when coexisting with Fe or Fe_3S, respectively. The change in eutectic composition in the Fe–Fe_3S system is shown by green curve. Liquid compositions obtained in this study are shown by triangles when coexisting with solid Fe, inverse triangles when in contact with Fe_3S, and red circles when both were found.

Kei Hirose[a,b]

[a] Earth-Life Science Institute, Tokyo Institute of Technology
[b] Department of Earth and Planetary Science, The University of Tokyo

Email: kei@elsi.jp

References

[1] K. Hirose *et al.*: Annu. Rev. Earth Planet. Sci. **41** (2013) 657.
[2] Y. Fei *et al.*: Am. Miner. **85** (2000) 1830.
[3] S. Kamada *et al.*: Earth Planet. Sci. Lett. **359** (2012) 26.
[4] *Y. Mori, H. Ozawa, K. Hirose, R. Sinmyo, S. Tateno, G. Morard, Y. Ohishi: Earth Planet. Sci. Lett.* ***464*** *(2017) 135.*

Ancient glassware that traveled the Silk Road

The Niizawa Senzuka Tumulus Cluster is one of the most famous large tumulus clusters consisting of over 600 burial mounds located at Kashihara City, Nara Prefecture, Japan [1]. The burial mounds were constructed from the end of the 4th century through to the 7th century AD. In 1963, two pieces of glassware, comprising a transparent pale green facet-cut glass bowl (Fig. 1(a)) and a deep blue glass dish, were excavated as grave goods from Tumulus No.126 in the cluster. The burial date of Tumulus No.126 is considered to be in the late 5th century AD based on the structural features and associated artifacts of the tumulus. Because no evidence of primary glass production from raw materials in Japan dating prior to the late 7th century AD has previously been found, it is believed that all earlier glass products were imports produced overseas. Based on the typological features of these two pieces of glassware, it is considered that they were derived from two huge empires prospered a far distance to the west of Japan: the Sasanian Empire (*ca.* 3rd–7th century AD) in West Asia and the Roman/Byzantine Empire (*ca.* 1st–6th century AD) in the Mediterranean region. Although the specific provenances of these glasses have not yet been identified, they can provide important evidence demonstrating how varied cultures were introduced to and accepted by ancient Japan. This study thus aims to reveal the specific provenances of the glassware based on their chemical compositions. However, it is not easy to chemically investigate the glassware as they are designated as important national cultural properties in Japan and are now stored in the Tokyo National Museum.

Therefore, in this study, the author focused on the rest of the fragments from the glassware excavated from Niizawa Senzuka Tumulus No.126 in the previous scientific research conducted by the National Museum of Nature and Science [1]. The author decided to analyze not the real bodies of the glassware but rather fragments believed to be sampled from them. Two small glass fragments, specimens A and B, were collected from the rest of the previous scientific research. Specimen A (Fig. 1(b)) is a transparent pale-green glass fragment believed to be sampled from the facet-cut glass bowl (Fig. 1(a)). Meanwhile, specimen B is a tiny blue platelike fragment possibly sampled from the blue glass dish. Several X-ray fluorescence (XRF) analytical techniques – a laboratorial XRF analysis using custom-made spectrometers and a highly sensitive XRF analysis excited by synchrotron radiation – were applied to these specimens to establish their detailed chemical composition nondestructively. The specific provenances of these specimens were verified by a comparison between our analytical results and the literature data of Roman and Sasanian glass artifacts. Note that only part of the analytical results obtained for specimen A, the glass fragment believed to be sampled from the facet-cut glass bowl, are given in this article. Please refer to author's original paper [2] for further discussion including the results for specimen B.

The principal chemical composition of specimens A and B was quantified using two XRF spectrometers, 100FA-IIL and 100FA-V, in a laboratory. These spectrometers were developed by Ourstex Co. Ltd. in collaboration with the author. To analyze the trace

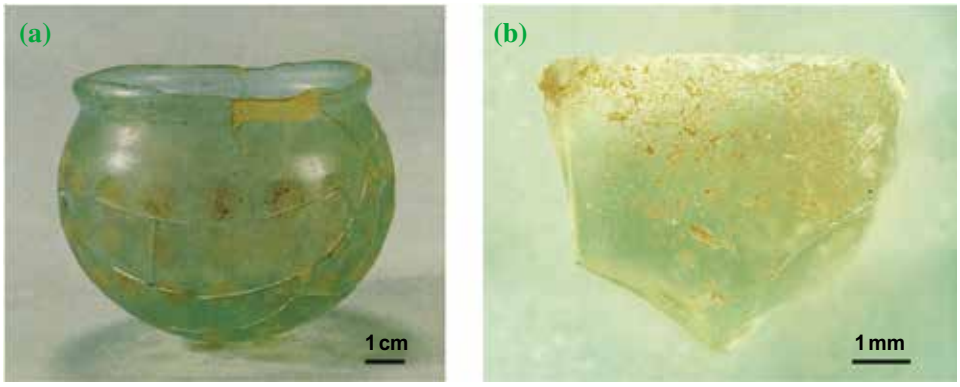

Fig. 1. **(a)** Facet-cut glass bowl excavated from Niizawa Senzuka Tumulus No.126. Reprinted from the excavation report by Archaeological Institute of Kashihara [1]. **(b)** Microscope photograph of specimen A, a piece of glass fragment believed to be sampled from the facet-cut glass bowl.

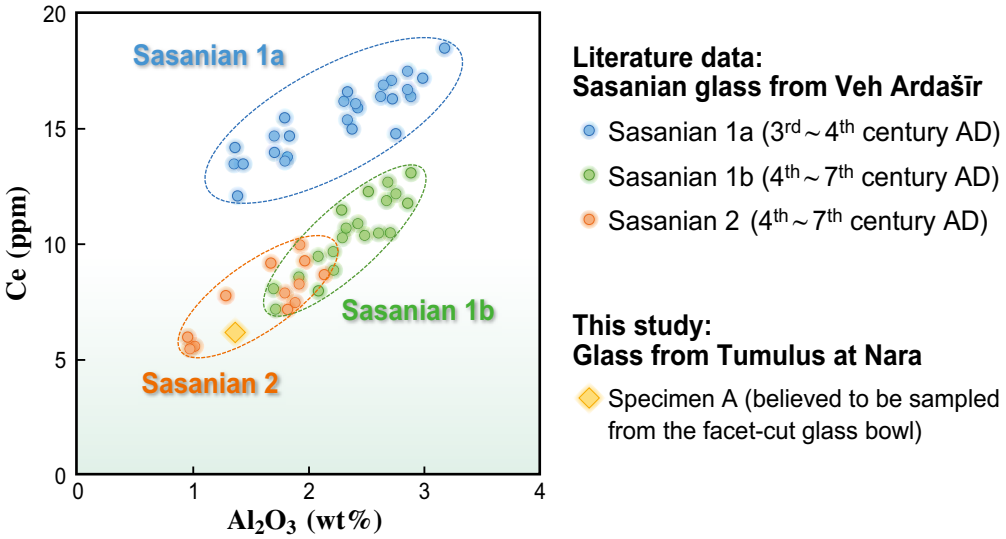

Fig. 2. Comparison of chemical composition between specimen A and Sasanian glass from Veh Ardašīr, Iraq [3].

heavy elemental composition, including rare earth elements (REEs), a high-energy synchrotron radiation (SR) XRF analysis was applied to specimens A and B in a nondestructive manner. The SR experiment was conducted at SPring-8 **BL08W**, the only wiggler beamline and the highest X-ray energy beamline in SPring-8. The use of its 116 keV monochromated X-ray enables the excitation of *K*-edges of all heavy elements up to uranium (*K*-edge: 115.6 keV). All measurements were carried out in a nondestructive manner.

From the principal chemical composition obtained by the laboratorial XRF, it is suggested that specimen A has a similar chemical composition to Sasanian glass, characterized by the use of a plant ash soda flux containing highly concentrated Mg and K. Through a series of recent scientific investigations of Sasanian glasses excavated from the royal town of Veh Ardašīr in Iraq, detailed chemical compositional features of Sasanian glass have become well understood in relation to their raw materials. The Sasanian glass excavated at Veh Ardašīr can be classified into three compositional groups – named Sasanian 1a, Sasanian 1b and Sasanian 2 – according to the use of different raw materials (plant ashes and silica sources) and the principal production period. Figure 2 shows a bi-plot focusing on elements derived from the silica source (aluminum and cerium) for comparison of the chemical composition between specimen A and the three compositional groups in the Sasanian glass from Veh Ardašīr [3]. As evidenced by Fig. 2, the chemical composition of specimen A is characterized by the use of a highly pure silica source; the chemical compositional feature of specimen A closely matches that of Sasanian 2 glass. This indicates that the glass bowl found in Japan was originally manufactured using glass produced in the Sasanian Empire. Considering the discovery of similar facet-cut glass bowls in the Sasanian region, it is also possible that both the primary and secondary glass production of the glass bowl were conducted at workshop(s) in the Sasanian region. Even if it took several decades for the bowl to be transferred from the Sasanian glass workshop to Nara, the possible production period of Sasanian 2 glass (4th–7th century AD) corresponds to the burial date of Tumulus No.126 (late 5th century AD).

In conclusion, on the basis of nondestructive X-ray analysis of a small fragment using the highly brilliant and high-energy X-rays of SPring-8, this study demonstrated the possibility that the precious glass bowl discovered at a tumulus in Japan was glassware manufactured in the Sasanian Empire and transported to Japan along the Silk Road around the same time.

Yoshinari Abe

Department of Applied Chemistry,
Tokyo University of Science

Email: y.abe@rs.tus.ac.jp

References

[1] Archaeological Institute of Kashihara: Tomb No. 126 of Niizawa (1977).
[2] *Y. Abe, R. Shikaku, I. Nakai: J. Archaeol. Sci. Rep.* ***17*** *(2018) 212.*
[3] P. Mirti *et al.*: J. Archaeol. Sci. **36** (2009) 1061.

Disruption of human stratum corneum lipid structure by sodium dodecyl sulfate

The skin maintains the body temperature and forms the outer barrier of the human body, protecting it against various environmental hazards, including exposure to chemical stimulants, poisons, microbial invasions, hazardous ultraviolet radiation, and other possible physical and chemical hazards. Furthermore, its low permeability to water protects the body from excessive dehydration. Maintenance of an optimal functional state requires that the skin be kept clean. Detergents are major ingredients of body soaps and cleansers. However, harsh detergents can damage the skin. The stratum corneum (SC) is the outermost layer of the skin and it contains corneocytes and intercellular lipids, which form lamellar structures. These well-organized structures are especially important for the barrier function of the skin, and detergents may impair this function by disrupting the lamellar structure. We used X-ray diffraction to evaluate structural modifications in human SC resulting from sodium dodecyl sulfate (SDS) treatment, focusing on how SDS affects SC lipid structures such as the lamellar structure and the hydrocarbon-chain packing structures. We investigated structural changes in isolated human SC using small- and wide-angle X-ray diffraction.

Human SC sheets were obtained from Biopredic International (Rennes, France). The dried samples were rehydrated in an incubator until they were 25 wt% hydrated. Reagent-grade SDS was purchased from Wako (Japan). Solutions with 1 wt% and 10 wt% SDS were prepared in Carmody buffer (pH 7.0). The X-ray diffraction measurements were performed using SPring-8 **BL19B2** and **BL40B2** beamlines. The method used is particularly useful for detecting small changes in the SC structure [1]. The measurement specifications of BL19B2 were as follows. All samples were exposed to an X-ray beam at 28 keV for 30 s at approximately 25°C. An X-ray beam with 200 μm diameter was used to allow the observation of the whole SC sample. A photon-counting pixel array detector (PILATUS 2M, Dectris) was used. The camera length, i.e., the distance between the sample and the detector, was *ca.* 700 mm. The measurement specifications of BL40B2 were as follows. All samples were exposed to an X-ray beam at 15 keV for 30 s at about 25°C. The camera length was *ca.* 500 mm. The diffraction pattern was obtained with a 300 mm × 300 mm imaging plate (R-AXIS, Rigaku). A wide-*q*-range X-ray diffraction profile was recorded every 3 min.

The SAXD profiles for the long lamellar structure of human SC after treatment with 10 wt% SDS, 1 wt% SDS, and without SDS (i.e., with distilled water) up to 129 min are shown in Figs. 1(a), 1(b), and 1(c), respectively [2]. Treatment with 10 wt% SDS led to the third-order peak of the long lamellar structure at about $S = 0.22$ nm^{-1} being smeared out with time as shown in Fig. 1(a). Treatment with 1 wt% SDS led to similar behavior for the third-order peak. Without SDS, the third-order peak did not change. The very weak fourth-order peak of the long lamellar structure at about $S = 0.29$ nm^{-1} became weaker after the SDS treatments, similar to the behavior of the third-order peaks in both the 10 wt% and 1 wt% SDS treatments, and the peak at about $S = 0.29$ nm^{-1} remained unchanged when distilled water was applied. These

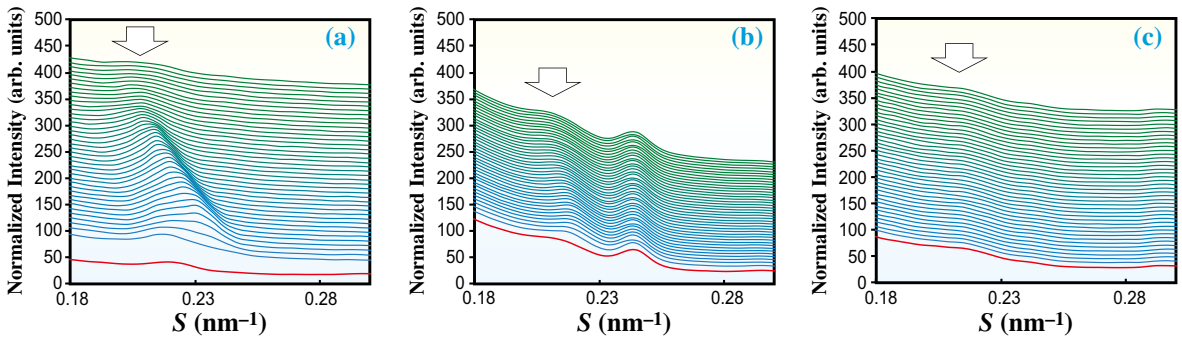

Fig. 1. SAXD profiles of human SC treated with 10 wt% SDS **(a)**, 1 wt% SDS **(b)**, and without SDS **(c)**. The profiles before treatment are indicated by a red curve. The profiles after treatment were recorded every 3 min up to 129 min. The illustrated intensity profiles are shifted in the vertical direction successively from blue to green curves with time. The white arrow denotes the third-order peaks for the long lamellar structure. The peak at 0.24 nm^{-1} in (b) is due to neutral lipids, which were sometimes observed.

results clearly indicate that the change in the long lamellar diffraction peak profile was caused by SDS. On the other hand, the short lamellar structure was not influenced by SDS treatment. Additionally, the intensities and the positions of peaks corresponding to hydrocarbon-chain packing structures did not change markedly both after SDS treatment of the SC and treatment without SDS. On the basis of these findings, we propose that the long lamellar structure is predominantly affected by the SDS treatment.

Upon 10 wt% SDS treatment, the X-ray diffraction peak for the long lamellar structure became broad and the intensity gradually diminished. To investigate this behavior further, the third-order X-ray diffraction profile at about $S = 0.22\ nm^{-1}$ was analyzed using two Gaussian functions. The final disordered lipid state was reached through two types of structural change, where one exhibits a strong diffraction peak and the other exhibits a weak peak. We propose that the disordered lipid state results from the incorporation of SDS into the long lamellar structure through the two processes. As shown in Fig. 2, the structural change for 1 wt% SDS treatment exhibited similar behavior to the strong diffraction peak for 10 wt% SDS treatment, but owing to the weak effect, the behavior corresponding to the strong peak predominantly occurred.

This study clearly demonstrated the process of human SC collapse caused by detergent. Bouwstra *et al.* [3] and Kuemple *et al.* [4] pointed out that the long lamellar structure in skin plays an important role in maintaining the skin barrier function. Therefore, the observed effect of surfactants on the long lamellar structure should be considered in the development of cleansers.

In an experiment involving washing women's arms in SDS, transepidermal water loss (TEWL) values temporarily increased and skin capacitance decreased. In other words, the change in the long lamellar structure plays a key role in the development of dry skin after using detergents. On the basis of these studies, we developed new body soap products that can maintain the skin capacitance after taking a bath.

Recently, Mojumdar *et al.* [5] pointed out that water molecules are stored in two crystallographic locations of the long lamellar structure. We also speculate that SDS was incorporated in the two locations and, as a result, two types of structural change took place. Further detailed study on the permeation of SDS in SC is now in progress.

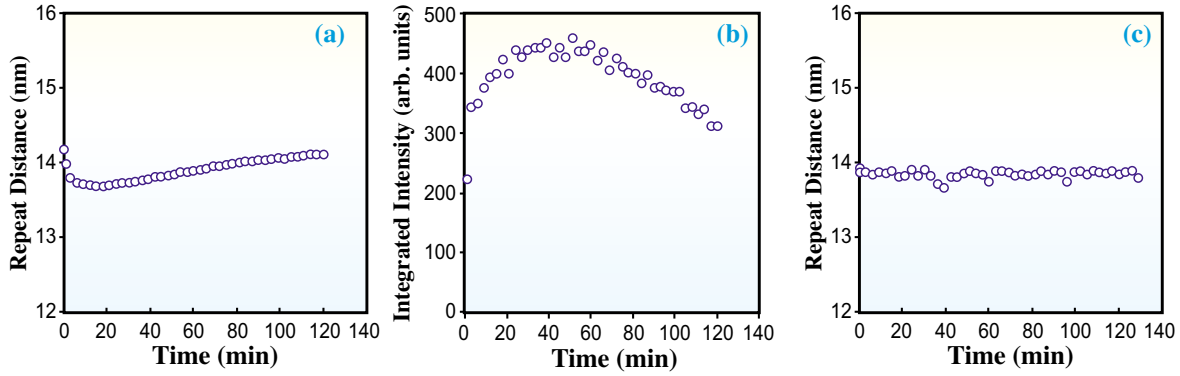

Fig. 2. Repeat distance **(a)** and intensity **(b)** of the third-order X-ray diffraction profiles obtained from the long lamellar structure of the SC treated with 1 wt% SDS. **(c)** Repeat distance of the third-order X-ray diffraction profiles obtained from the long lamellar structure of the SC without SDS treatment. (a) The repeat distance first decreased, then started to increase and finally saturated. (b) The intensity first increased and then decreased.

Kaori Yanase[a,*] and Ichiro Hatta[b]

[a] Kracie Home Products
[b] Nagoya Industrial Science Research Institute

*Email: k.yanase@khp.kracie.co.jp

References

[1] I. Hatta *et al.*: Chem. Phys. Lipids **163** (2010) 381.
[2] *K. Yanase and I. Hatta: Int. J. Cos. Sci.* ***40*** *(2018) 44.*
[3] J.A. Bouwstra *et al.*: Acta Derm. Venereol. Suppl. **208** (2000) 23.
[4] D. Kuemple *et al.*: Biochem. Biophys. Acta **1372** (1988) 135.
[5] E.H. Mojumdar *et al.*: Biochim. Biophys. Acta **1858** (2016) 1926.

HAXPES for a better tire performance: Chemical state analysis of adhesive interface between rubber and steel cords

Most of us routinely use vehicles for transportation, either by driving a car or by taking taxis and buses, and all of us rely on merchandise distribution services, where vehicles play an essential role. Nowadays, there are more than 1.2 billion registered vehicles (passenger cars and commercial vehicles) worldwide from remote regions to urban areas, and around 100 million vehicles are manufactured every year [1]. It is no exaggeration to state that our modern society is supported by vehicles. One of the key components of vehicles is rubber tires. The tires literally support the vehicle, and the tire performance affects the steering control, noise and vibration characteristics, fuel consumption, and other factors.

The present *de facto* standard of vehicular tires is the radial tire, in which twisted steel cords are embedded in a steel belt (Fig. 1(a)). The most important role of the steel belt is to suppress shape deformation of the tire in order for the tire to keep a tight grip on the road surface and to produce efficient transmission of the traction force from the vehicle to the road. However, if the rubber compound surrounding the steel cords fails to hold the cords, the tire will be deformed, making proper steering of the vehicle difficult. Therefore, it is vital to develop strong and durable adhesion between rubber and the steel cords.

To realize strong rubber-to-steel adhesion, brass-plated cords have been commercially used. This is because rubber-to-brass bonding is superior to rubber-to-steel bonding. Electron spectroscopy, such as X-ray photoelectron spectroscopy (XPS) and Auger electron spectroscopy (AES), has been utilized to elucidate the adhesion mechanism between rubber and brass since the late 1970s [2]. It was soon recognized that copper sulfide is a key chemical species to cause strong adhesion. However, details of the morphology and chemical composition of the adhesive interface still remain unclear.

XPS and AES are powerful tools for the chemical state analysis of solids. However, because of the short inelastic mean free paths of electrons in solid materials, the adhesive interface must be exposed to the surface when these techniques are used. Among several methods to expose a rubber/brass interface, the so-called “filter paper method” [3] is a novel method to obtain a sulfurized brass surface that imitates the rubber/brass adhesive interface without the rubber molecules. Figure 2 shows S 2*p* core-level spectra of two samples whose interface has been “exposed” by the filter paper method [4]: One was prepared under optimum reaction conditions (heating at 170°C for 10 min, which result in strong adhesion), and the other was obtained under overcuring conditions (170°C for 40 min). Lineshape analysis of the spectra enabled us to identify CuS and Cu_xS ($x \approx 2$) on the optimum sample. As the reaction time is prolonged and the adhesion strength is weakened, the amounts of both CuS and Cu_xS decreased while ZnS is increasingly formed. These observations support the already known fact that copper sulfide acts as an adhesive agent at the interface. The new finding is that, although Cu_xS is a minor species, there is a strong correlation between the adhesion strength and the amount of Cu_xS. This implies that Cu_xS ($x \approx 2$) is a more important adhesive agent than CuS.

Despite the fact that the XPS study in combination with the filter paper method has provided useful information on the chemical state at the adhesive interface, the “exposed” interfaces are not guaranteed to reflect the real chemical state of the buried interface. Therefore, bulk-sensitive hard X-ray photoelectron spectroscopy (HAXPES) was employed to directly

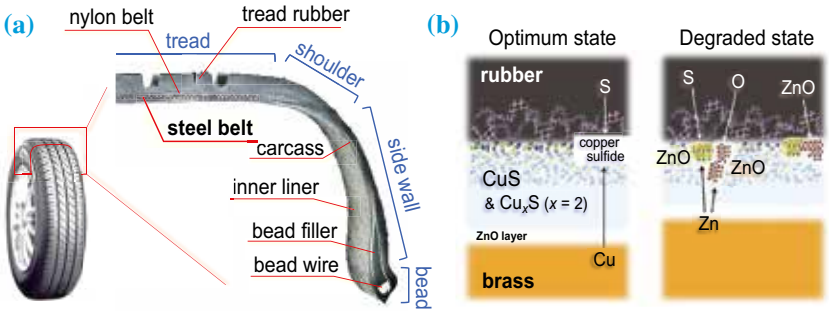

Fig. 1. **(a)** Cross-sectional view of a radial tire. **(b)** Schematic illustrations of the chemical compositions at rubber/brass interfaces proposed by the outcomes of the present study. In the optimum state (left), where strong adhesion is realized, the adhesive interface is mainly composed of copper sulfide. Degradation of the adhesion is characterized by the decomposition of copper sulfide and the accumulation of Zn-containing species (right).

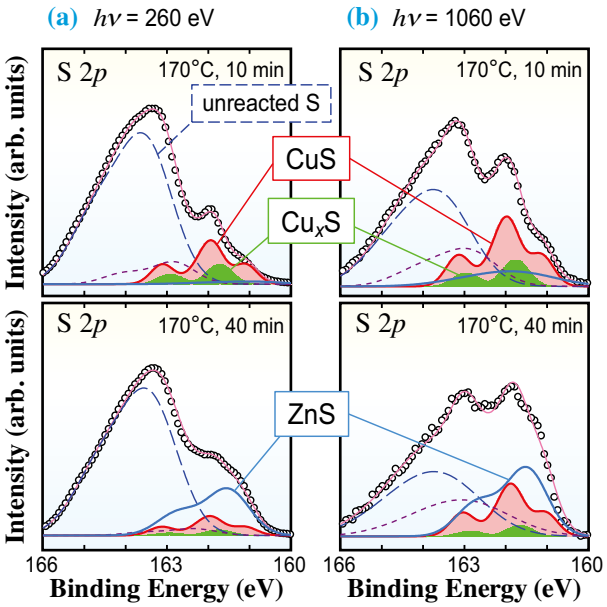

Fig. 2. S 2*p* XPS spectra of the exposed interfaces prepared under the optimum conditions (170°C, 10 min) and the overcuring conditions (170°C, 40 min). The photon energies used were **(a)** 260 eV and **(b)** 1060 eV.

investigate the rubber/brass adhesive interface buried beneath a 100-nm-thick rubber film [5]. The HAXPES measurements were carried out at SPring-8 **BL47XU**, and typical spectra are shown in Fig. 3(a). Here, angle-resolved measurements were concluded to distinguish between the species in the rubber compound and those at the adhesive interface. The S 1*s* spectrum is composed of at least two components: On the basis of the relative intensity variation as a function of the angle, the lower binding-energy (BE) component is assigned to the S species at the interface region, while the higher BE component is related to those in the rubber compound. The lower BE component of the sample prepared under the overcuring conditions is reproduced by a single-peak, whereas a double-peak structure is necessary for the optimum sample (Fig. 3(b)). The double-peak structure is characteristic of CuS. The transformation from the double-peak structure to the single-peak structure as the reaction time is prolonged reflects the decomposition of CuS and the formation of ZnS. Although the identification of Cu_xS ($x \approx 2$) was not possible in the present study, it was demonstrated that HAXPES is capable of following chemical changes at a buried rubber/brass adhesive interface.

On the basis of the results obtained from the present XPS and HAXPES studies, a more accurate view of the chemical composition of the adhesive interface between rubber and brass was obtained (Fig. 1(b)). With this newly proposed model, a technical solution can be found to realize stronger and more degradation-resistant adhesion, enabling the development of new tires with a better performance.

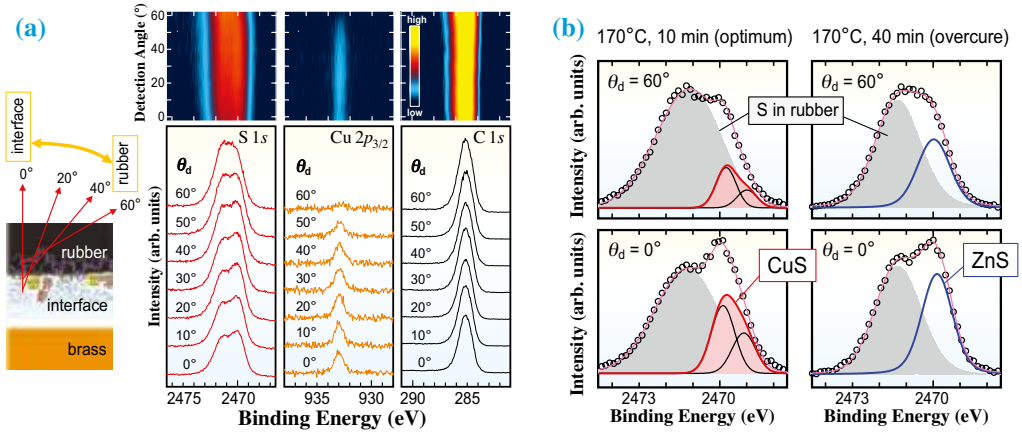

Fig. 3. **(a)** Angle-resolved HAXPES spectra of S 1*s*, Cu 2$p_{3/2}$, and C 1*s* core levels of the rubber-bonded brass sample subjected to heating at 170°C for 40 min. The photon energy was 7.94 keV. Upper panels show intensity plots of the spectra, and energy distribution curves are shown in the lower panels. **(b)** S 1*s* spectra of two differently prepared samples measured at detection angles (θ_d) of 0° and 60°. The interface component (the lower BE component) in the spectrum of the optimum sample consists of two subcomponents with a 1:2 intensity ratio, which is characteristic of CuS.

Kenichi Ozawa[a,*], Takashi Kakubo[b] and Naoya Amino[b]

[a] Department of Chemistry, Tokyo Institute of Technology
[b] The Yokohama Rubber Co., Ltd.

*Email: ozawa.k.ab@m.titech.ac.jp

References

[1] https://www.statista.com/statistics/281134/number-of-vehicles-in-use-worldwide/
[2] W. J. van Ooij: Surf. Sci. **68** (1977) 1.
[3] T. Hotaka *et al.*: Rubber Chem. Technol. **80** (2007) 61.
[4] K. Ozawa *et al.*: Appl. Surf. Sci. **264** (2013) 297.
[5] *K. Ozawa, T. Kakubo, N. Amino, K. Mase, E. Ikenaga, T. Nakamura: Langmuir* ***33*** *(2017) 9582.*

Effects of spinning speed and draw ratio on the fibril structure development of poly(ethylene terephthalate) fiber after neck-drawing

The properties of polymeric materials are strongly related to their higher-order structure. However, the higher-order structure is very complicated, that is, the molecular chains are considerably entangled with each other, part of them are oriented along certain axes, and part of them are crystallized. Thus, it is difficult to predict the properties of polymeric products quantitatively from the limited information of the higher-order structure. The mechanical and thermal properties, namely tensile strength and thermal shrinkage are particularly important properties of synthetic fibers and films, but they cannot be designed accurately from the ordinary higher-order structure parameters, such as the molecular orientation, crystallinity, crystal and amorphous orientations, crystallite size, and disorder parameters. For example, the tensile strength of industrial-grade poly(ethylene terephthalate) (PET) fibers is far below the theoretical value, less than 5% in general, despite the high crystal orientation and high crystallinity. This is due to the lack of information on the fibril structure, which is thought to be a bundle of highly oriented molecular chains and thought to bear the external force applied on the fibers and films. The bundle structure is formed by the orientation-induced crystallization during the melt-spinning and/or drawing processes with the extension of entangled molecular chain networks. Kikutani *et al.* [1] suggested that the uniformity of molecular chain networks determines the fibril structure and influences the tensile strength of the obtained PET fibers. It is difficult to observe the fibril structure directly by SAXS measurements of the obtained fibers because there is no obvious density difference between the fibrils and the surrounding matrix. However, we found a fibrillar-shaped smectic phase of nm-order width and 10-nm-order length during the development of the fiber structure less than 1 ms after necking [2]. This should be the embryo of the microfibrils and should influence the tensile strength of the resulting fiber [3]. Thus, in this study, we focused on the fibril structure development after necking and also on the effects of the processing conditions of the spinning speed of the fiber before the drawing and the draw ratio or drawing stress.

By obtaining WAXD and SAXS patterns during a continuous neck-drawing process, we analyzed the fibril structure development after the necking, i.e., the rapid extension of a fiber or film with a rapid change in diameter. The running fiber was drawn continuously by the speed difference between the fiber-feeding and take-up rollers while heating by CO_2 laser irradiation [4]. Owing to the rapid and homogeneous heating by laser irradiation, the location of the necking point hardly changed during the on-line measurement. Also, by moving the laser-irradiation point, we were able to change the distance between the necking point and the X-ray beam irradiation point, and analyze the fiber structure at a certain elapsed time after the necking. The ultrahigh intensity X-ray beam of SPring-8 **BL03XU** used in this study enable high-precision measurements not only with an improved S/N ratio but also with a 0.1 ms time resolution. The high time resolution allowed us to analyze the effects of processing conditions on the fibril structure development.

SAXS patterns obtained during drawing under the same drawing stress of about 100 MPa are shown in Fig. 1. The figure indicates the development of a long-period structure, involving phase separation from the fibrillar-shaped smectic phase to a series of crystallites and amorphous phases connecting them, that is, so-called microfibril. It is interesting that the structure development clearly depends on the spinning speed and laser irradiation on the spin-line, but the SAXS pattern of the drawn fiber does not change significantly among the samples. This reveals that the *in situ* measurement of fibril structure development

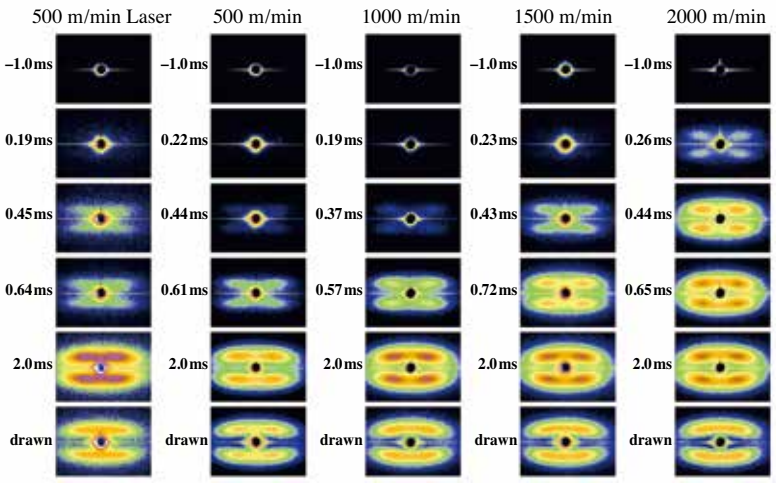

Fig. 1. SAXS patterns for certain elapsed times after necking. The drawing stress was about 100 MPa for all samples.

can provide more information about the fibril structure than structure analyses of the obtained products. This is because the effect of metastable fibrillar-shaped structure can be observed during the structure development, but it is obscured by the development of a density difference between the crystallites and the surrounding amorphous phase. For example, the long period obtained from the SAXS pattern is plotted against the elapsed time after necking in Fig. 2. Although the long period becomes almost the same for each drawn fiber regardless of the spinning speed, the development profiles are clearly different between the fibers taken-up at 500 m/min and 1000–2000 m/min. The fiber taken-up at 500 m/min required a longer time for the formation of long period structure, and showed a clear decrease in the long period with elapsed time. The delay of phase separation, or crystallization, can be explained by the effect of the smectic phase on inhibiting crystallization because more amount and a longer fibril length of the fibrillar-shaped smectic phase for the taken-up at 500 m/min than those at 1000–2000 m/min were observed by the WAXD measurement.

The model of fibril structure development based on the *in situ* WAXD and SAXS measurements is shown in Fig. 3. At the minimum drawing stress for stable drawing of about 30 MPa, at which the draw ratio is almost the same as the natural draw ratio, no smectic phase was formed, a clear X-shaped pattern was observed for the SAXS pattern about 0.3 ms after necking, and the X-shaped pattern was transformed into a four-point pattern within 1 ms after necking. This indicates that crystallites were formed along the shear-band-like structure formed by the necking. With increasing drawing stress for a low-speed spun fiber, so-called undrawn yarn (UDY), the fibrillar-shaped smectic phase tended to develop along the fiber axis, inhibiting the direct crystallization from the oriented amorphous phase. The fibrillar-shaped smectic phase was transformed into microfibrils composed of series of crystallite/amorphous structure until 2 ms after necking. In contrast, for the higher-speed spun fiber, so-called partially oriented yarn (POY), the oriented nuclei that formed in the spinning process are thought to inhibit the development of the smectic phase. As a result, POY is suitable for producing low shrinkage fibers because lamella crystals that mutually interlock with each other tend to be formed. In contrast, UDY is suitable for producing high-strength fibers because uniformly ordered fibrils tend to be formed.

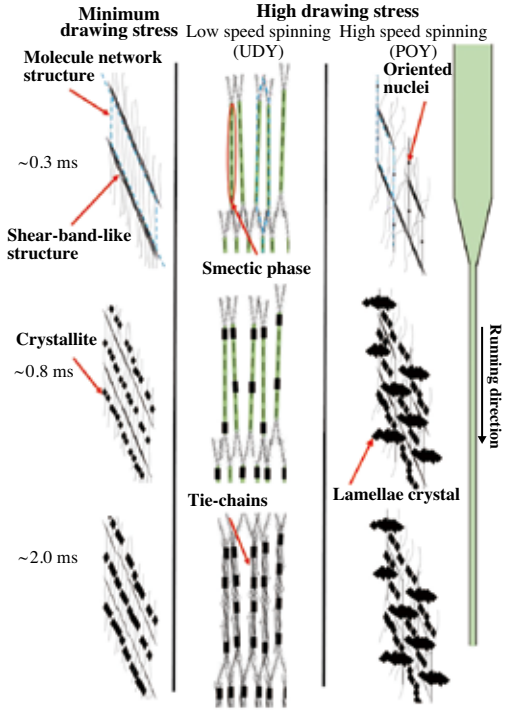

Fig. 3. Schematic diagrams of fiber structure development. The structures of the molecular network in the fibers are shown as blue lines.

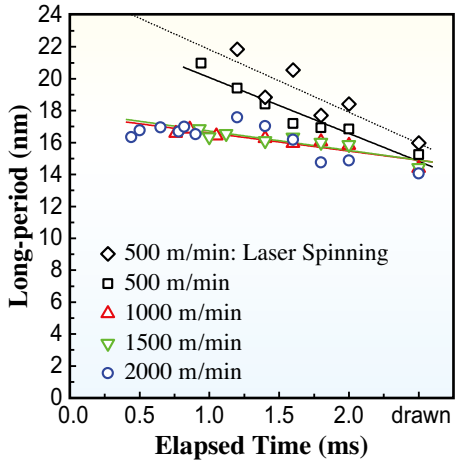

Fig. 2. Long periods obtained from SAXS patterns plotted against the elapsed time after necking.

Yutaka Ohkoshi*, Ren Tomisawa and Kyoung Hou Kim

Faculty of Textile Science and Technology,
Shinshu University

*Email: yokoshi@shinshu-u.ac.jp

References

[1] T. Kikutani: CMC Press (2008) 56.
[2] T. Yamaguchi *et al.*: J. Polym. Sci., Polym. Phys. **46** (2008) 2126.
[3] Y. Ohkoshi: SPring-8/SACLA Research Frontiers 2015, (2016) 86.
[4] *R. Tomisawa, T. Ikaga, K.H. Kim, Y. Ohkoshi, K. Okada, H. Masunaga, T. Kanaya, M. Masuda, Y. Maeda: Polymer* ***116*** *(2017) 357; ibid. 367.*

Accelerators & Beamlines Frontiers

SPring-8 Beam Performance

Recent update of accelerators

One of the recent works on the SPring-8 accelerator complex has been to renew the low-level radio-frequency (LLRF) system of the storage ring. The LLRF system is distributed at four RF stations along the storage ring, and the existing system based on analogue NIM modules has been dedicated to user operations since the SPring-8 accelerator complex was constructed in the 90s. Now we are aiming to replace the existing system with a new one based on the modern standard MicroTCA.4 before the existing system becomes unreliable due to its degradation over time. Also, one of our concerns is that some of the electric parts inside the system will no longer be available on the market.

This fiscal year we first tested our new LLRF system at the test RF stand, and its operation was successfully demonstrated. Therefore, we installed the new LLRF system in one of the four RF stations, called the A-station, after finishing this fiscal year's user operation in February 2018. From the beginning of user operation in fiscal year 2018, we plan to commence user operations with the new LLRF system at one of the four RF stations. Later, we intend to complete the installation of the new system in all four RF stations unless some unexpected problems occur. The new system is expected to provide more reliable and stable user operations by taking advantage of MicroTCA.4 [1].

Fig. 1. Permanent dipole magnet under magnetic field measurement. The magnet consists of four segments; the first and third segments are made of samarium-cobalt, and the second and fourth segments are made of neodymium-iron-boron (NdFeB).

Another recent work has been to replace one of the dipole electromagnets used in the beam transport from the booster synchrotron to the storage ring with a newly developed permanent magnet-based dipole magnet. At SPring-8, we have studied a possibility of applying permanent magnet-based dipole magnets for next generation light sources, especially SPring-8-II [2]. Permanent magnets are advantageous over conventional electromagnets in that they consume less power, are physically more compact, and there is less risk of a magnet-related accelerator failure due to, for example, a power failure or water leakage. It follows that a permanent magnet could be beneficial to both the facility and its users. However, there are also practical challenges in using permanent magnets as the main magnets for light sources. For example, the behavior of a permanent magnet is known to be temperature-dependent, which may result in a shift in the electron energy caused by ambient temperature drift in the accelerator tunnel. Radiation damage of the permanent magnet is also a concern when one considers the fact that the demagnetization of undulator permanent magnets has been observed at several accelerator facilities [3]. In recent years, we have designed, fabricated, and tested several kinds of permanent dipole magnets to overcome these challenges [2]. In this fiscal year, we fabricated a 2-m-long C-shaped permanent dipole magnet, in which the magnetic circuit was designed so that the dipole magnetic field was insensitive to temperature drift. After implementing several measurements in the magnet measurement room (see Fig.1), we replaced one of the beam transport magnets between the booster synchrotron and the storage ring, SSBT-BM5, with the permanent dipole magnet after the end of this fiscal year's user operation. We will start operations with the new permanent dipole magnet in fiscal year 2018.

Shiro Takano and Takahiro Watanabe*

Japan Synchrotron Radiation Research Institute (JASRI)

*Email: twatanabe@spring8.or.jp

References

[1] T. Ohshima *et al.*: Proc. IPAC2017(2017), THPAB117.
[2] T. Watanabe *et al.*: Phys. Rev. Acc. Beams **20** (2017) 072401.
[3] T. Bizen *et al.*: Sci. Rep. **6** (2016) 37937.

A new high-resolution X-ray spectrometer for studying electronic dynamics

Non-resonant inelastic X-ray scattering (NRIXS) is an interesting tool for spectroscopic investigations, with access to large momentum transfers allowing investigation beyond the dipole limit, and over atomic scale correlation lengths. NRIXS with ~eV resolution has been used to investigate valence structure, particle-hole excitations and plasmons. However, the method has significant practical constraints and it is only relatively recently that experimental work has begun to focus on narrower electronic (non-phonon) spectral features at ~eV energy transfers [1]. This, in large part, is due to instrumental limitations, as one needs both high resolution and high spectral intensity. However, given the possibility to directly investigate transitions of d electrons and the dispersion of such excitations (e.g., orbitons) there is significant interest.

Non-resonant scattering offers some advantages relative to resonant inelastic X-ray scattering (RIXS). NRIXS is *relatively* simple to interpret and calculate as the NRIXS cross section responds directly to the electronic charge density of the initial and final states via the non-resonant $\boldsymbol{A}^2$ term of the interaction Hamiltonian: avoiding the intermediate states from the resonant interaction, the $\boldsymbol{A}\cdot\boldsymbol{p}$ term, reduces count-rates but simplifies interpretation. The choice of X-ray energy in a non-resonant experiment is flexible, so it can be chosen to optimize optical performance to facilitate improved resolution. The energy can also be chosen to be relatively high to improve transmission into and out-of sample environments, and to increase the illuminated volume of a sample.

Here we used analyzers with a controlled temperature gradient (TG) [2] to allow good, 25 meV, resolution with a single element detector with a large space near the sample. The main elements of the spectrometer are shown in Fig. 1(a), and include the medium resolution monochromator, a bent cylindrical focusing mirror, stages and environment for the sample, and the analyzer system on the two-theta arm (Fig. 1(b)). This is installed at SPring-8 **BL43LXU** [3]. The operating energy of the spectrometer is 15816 eV, corresponding to the energy of the Si (888) back-reflection analyzer crystals. A TG of ΔT_g = 1.32 K/80 mm was applied over the analyzer with improvement as seen in the inset in Fig. 2(a), even using a single element detector placed 20 cm from the sample.

We use the new spectrometer to investigate a band of *d-d* excitations in NiO as we increase the temperature from 20 to 800 K, through the Neel point at T_N = 523 K [2]. The NiO crystal was placed inside of a closed-cycle cryofurnace. Measurements were done at **Q** = (2.5 2.5 2.5) reciprocal lattice units (rlu), $|\mathbf{Q}|$ = 6.52 Å^{-1}, with the acceptance of the analyzer being $\Delta\mathbf{Q}$ = (0.05 0.22 0.22) rlu. This **Q** is near the maximum intensity for this band of excitations.

The measured spectra are shown in Figs. 2(b) and 3(a), after background subtraction. At low temperatures, some structure is evident, and the

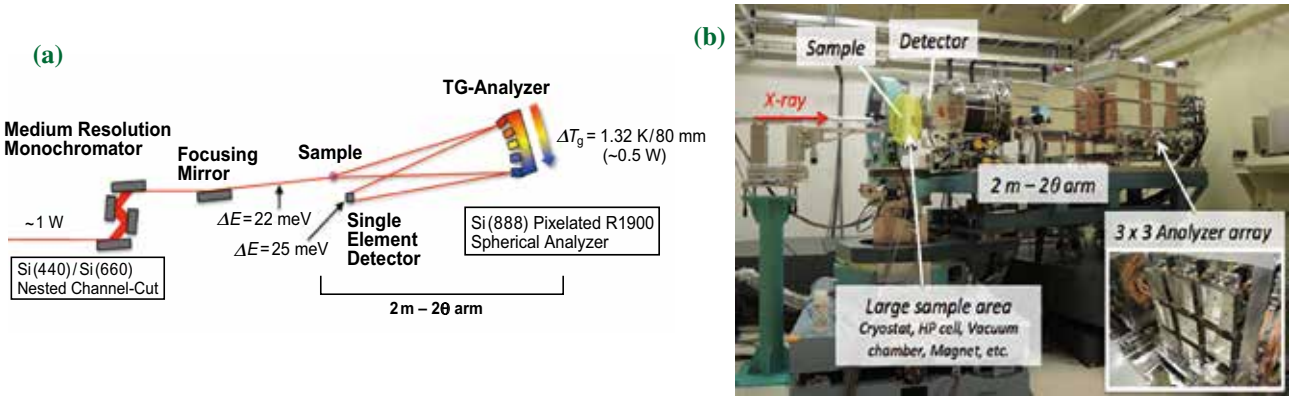

Fig. 1. 25 meV resolution Non-resonant IXS spectrometer with temperature-gradient (TG) analyzer. **(a)** Schematic showing the main components. **(b)** Photo of the spectrometer.

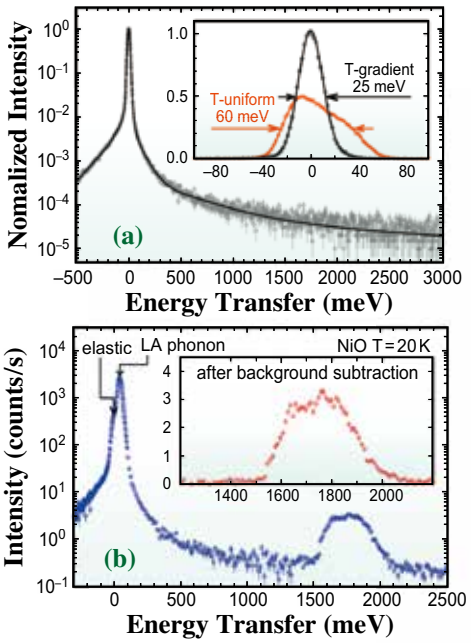

Fig. 2. Spectrometer response. **(a)** Measured scattering, with the TG, from plexiglass at its structure factor maximum where its response is predominantly elastic. The inset shows the resolution with and without TG. **(b)** The *d-d* excitation in NiO appears clearly above background.

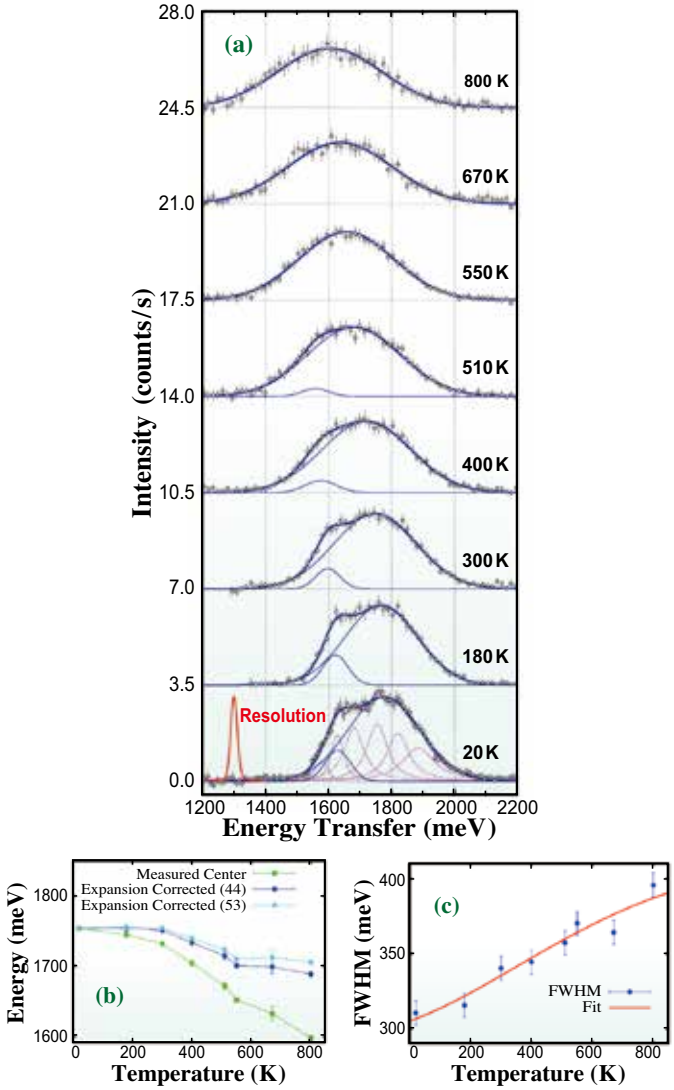

Fig. 3. **(a)** Temperature dependence of the *d-d* spectra of NiO measured at Q = (2.5 2.5 2.5) rlu. One TG analyzer (0.0024 sr) and single element detector 2×2 mm^2 were used. **(b,c)** Temperature dependence of the *d-d* excitation parameters. (b) Line position before and after correction for thermal expansion, using either the calculated value for the energy change (44 meV/pm) or the experimental value (53 meV/pm, see Ref. 2). Solid lines are guides for the eye. (c) Width of the excitation compared to the model in Ref. 2.

spectra can be fit using two Gaussian lines, or a more complex multiplet to reproduce all of the fine structure. At higher temperatures the response broadens, shifts to lower energies, and becomes increasingly Gaussian. The temperature dependence of the center and width of the response are shown in Figs. 3(b) and 3(c). The energy decreases steeply in the neighborhood of the Neel point, and then continues to drop (Fig. 3(b)). The width increases approximately linearly with temperature (Fig. 3(c)).

This data is the first to show the impact of phonons on electronic excitations: the linewidth increase is well fit using a simple model of thermally induced fluctuations with a scale factor of 53(3) meV energy shift per pm of Ni-O lattice constant expansion (solid line in Fig. 3(c)). Applying the same value for the thermal expansion then allows the Neel point to be more clearly observed in the temperature-induced shift of the center of the response (Fig. 3(b)). The experimental value of 53(3) meV is in reasonable agreement with the 44.5 meV/pm estimated from *ab initio* ligand field theory [4].

This work demonstrates the potential of a new high-resolution spectrometer now coming on line at the RIKEN SPring-8 Center.

Daisuke Ishikawa[a,b] and Alfred Q. R. Baron[a,*]

[a] RIKEN SPring-8 Center
[b] Japan Synchrotron Radiation Research Institute (JASRI)

*Email: baron@spring8.or.jp

References

[1] D. Ishikawa and A.Q.R. Baron: J. Synchrotron Rad. **17** (2010) 12.
[2] *D. Ishikawa, M.W. Haverkort and A.Q.R. Baron: J. Phys. Soc. Jpn.* ***86*** *(2017) 093706.*
[3] A.Q.R. Baron: SPring-8 Information **15** (2010) 14.
[4] M.W. Haverkort *et al.*: Phys. Rev. B **85** (2012) 165113.

Fresnel zone plate with apodized aperture for hard X-ray Gaussian beam optics

X-ray tomographic microscopy is a high spatial resolution three-dimensional (3D) computed tomography (CT) system using an X-ray full-field microscope optics. This system is called a nano-CT system because of its spatial resolution of from several tens to several hundreds of nanometers whereas the spatial resolution of a micro-CT system using a simple projection optics is limited to around 1 μm. X-ray nano-CT system using a Fresnel zone plate (FZP) as an objective are now open for user experiments at SPring-8 **BL37XU** and **BL47XU**, and are used in various fields such as materials, minerals, space/earth science, industrial use, and batteries.

An FZP is known as an approximately off-axis-aberration-free optics in the hard X-ray region [1]. However, it has been pointed out that some kinds of noises such as periodic fringes, edge enhancement, and streak noise tend to occur, particularly in the peripheral region of the field of view. Figure 1(a) shows an example of nano-CT measurement. Edge enhancement and contrast unevenness due to streak noise, which are severe obstacles to quantitative measurement, are observed in the CT image.

The reason for this is as follows. An image obtained with a full-field microscope optical system is expressed by the convolution of the transmittance function of the object and the point spread function (PSF) of the optical system. Here, the pupil function of the objective and the PSF are related by a Fourier transform. In general, since the objective has a circular or rectangular aperture, its PSF is expressed as a Bessel function or a Sinc function, respectively. These functions are known as having ripples (multiple side peaks) around the main peak that cause periodic noise called ringing. Although ringing is generally inconspicuous in the paraxial region corresponding to the central region of the field of view, it becomes more conspicuous in the off-axis region corresponding to the periphery of the field of view. Therefore, even if an ideal aberration-free lens is used, these noises are generated because of its finite aperture. Furthermore, since the ringing contains the phase information of the object, large contrast noise is generated even with a small absorption object.

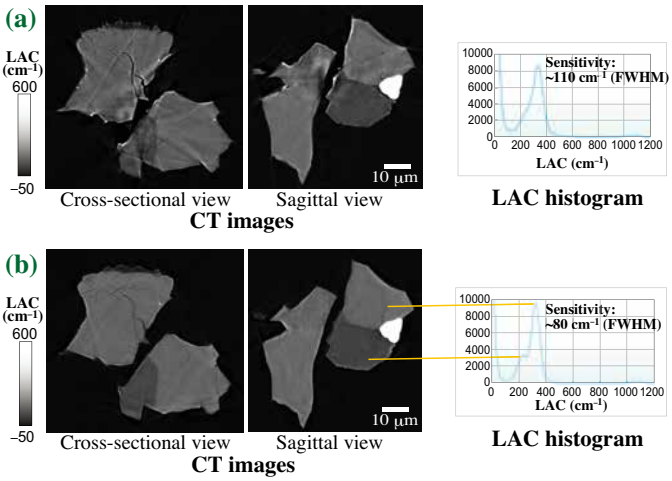

Fig. 1. Nano-CT images and CT value histograms of a Kilabo meteorite measured **(a)** by using a conventional FZP and **(b)** by using an apodization FZP as the objective. X-ray energy is 8 keV, voxel size is 83.7 nm, exposure time is 0.5 s, and CT scan time is 30 min for 1800 images/180 deg.

These noises can be effectively reduced by introducing a Gaussian beam optical system, whose electric field or intensity distribution can be regarded as approximately Gaussian. Therefore, its Fourier plane also has a Gaussian profile. Gaussian beam optics has some advantages such as (i) they are easy to handle mathematically, (ii) it is possible to remove high frequency speckle and fringe noises, and (iii) it is not necessary to set clear boundary conditions for the object. In recent years, several techniques for Gaussian beam optics in the X-ray region have been proposed [2,3]. In the case of a full-field microscope optical system, both the pupil function of the objective and the PSF are represented by their Gaussians. Since a Gaussian beam does not have ripples, no fringe noise is observed in the image. To convert a general objective aperture having a clear boundary into one with an ambiguous boundary, it is effective to install a filter whose transmittance gradually decreases from the central region to the peripheral region. This method of reducing the ripples by multiplying by an appropriate filter at the Fourier space is called apodization. An FZP with an apodization function (apodization FZP, A-FZP) was developed for introducing a Gaussian beam optical system into the optical system of an X-ray nano-CT system [4].

The aperture function of the FZP optics can be expressed as the first-order diffraction efficiency distribution. In the hard X-ray region, the zone depth is related to the diffraction efficiency distribution. In the case of a conventional FZP, which has a uniform zone depth, therefore, it has a pupil function defined as a definite circle or rectangle as shown in Fig. 2(a). On the other hand, as shown in Fig. 2(b), when an FZP has a structure in which the zone thickness decreases toward the periphery, the diffraction efficiency

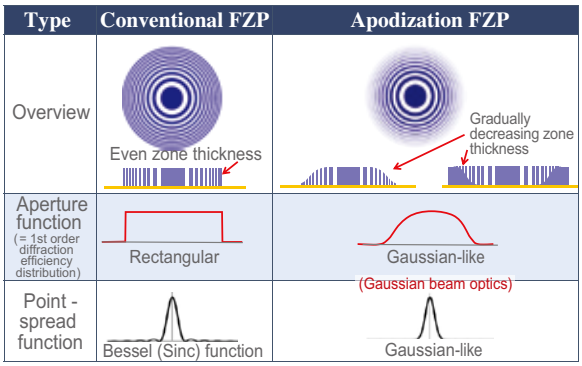

Fig. 2. Schematic drawings of conventional FZP (left) and A-FZP (right). A-FZP has a gradually decreasing zone thickness from the central region to the peripheral region, whereas conventional FZP has an even zone structure (upper). A-FZP has a Gaussian-like aperture function (middle) and also has a Gaussian-like PSF (lower), realizing a Gaussian beam optics.

gradually decreases in the peripheral region. This naturally realizes an FZP with an apodized aperture. Such a zone structure, which seems to be difficult to fabricate, however, it is not so difficult to realize. For a dry-etching process, which is one of the manufacturing processes used in the fabrication of FZPs by electron-beam lithography, it is known that the etching depth decreases with the patterns width. Such a phenomenon is called the microloading effect [5]. So far, this effect has been very problematic in fabricating an FZP having a uniform zone depth. Fortunately, however, it is a very convenient effect in fabricating an A-FZP. In other words, the zone structure that was previously recognized as a poorly finished FZP was actually an excellent A-FZP.

By actively employing the microloading effect, an A-FZP with an outermost zone width of 50 nm was fabricated by NTT Advanced Technology. Figure 3 shows the focal beam profile measured by a microbeam knife-edge scan as a performance test. The measured spot size was 55 nm in full width at the half maximum (FWHM), representing the nearly diffraction-limited resolution. This profile, in which ripples are considerably suppressed compared with the theoretical value for the conventional focus, has a shape resembling a Gaussian. An example of measurement using the nano-CT system with this A-FZP as an objective is shown in Fig. 1(b). The measured sample is the same as that of Fig. 1(a) measured with a conventional FZP. Edge enhancement, streak noise, and contrast unevenness, as can be seen in Fig. 1(a), are considerably suppressed in Fig. 1(b). Comparing the histograms of the linear absorption coefficient (LAC), Fig. 1(a) shows a single broad peak, whereas Fig. 1(b) clearly shows two separate peaks in the histogram. These results show that the introduction of a Gaussian beam realizes marked noise suppression and enables more quantitative and sensitive measurement.

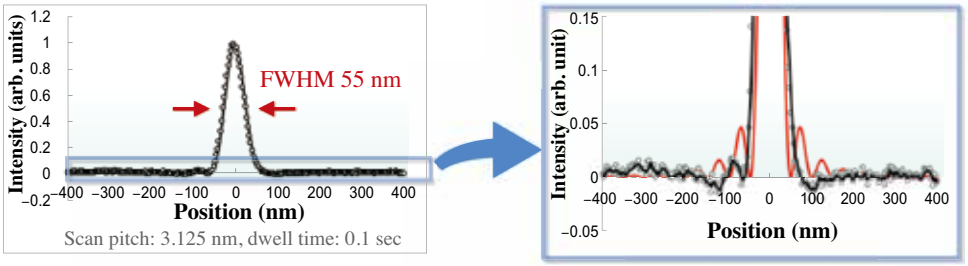

Fig. 3. Focused beam profile of A-FZP (with outermost zone width of 50 nm) measured by microbeam knife-edge scan (left) and magnified view of the bottom region of the profile (right). X-ray energy is 8 keV. Measured spot size was 55 nm, corresponding to the nearly diffraction-limited resolution of the FZP with an outermost zone width of 50 nm. Red line in the right view shows the theoretical value of the PSF of the conventional FZP. Measured value shows that the ripples were considerably suppressed compared with the red line.

Akihisa Takeuchi[a,*], Kentaro Uesugi[a] and Yoshio Suzuki[a,b]

[a] Japan Synchrotron Radiation Research Institute (JASRI)
[b] University of Tokyo

*Email: take@spring8.or.jp

References

[1] Y. Suzuki and H. Toda: Advanced Tomographic Methods in Materials Research and Engineering (Oxford University Press., Oxford, U.K. 2008) Sect. 7.1.
[2] Y. Suzuki and A. Takeuchi: Jpn. J. Appl. Phys. **51** (2012) 086701.
[3] K. Khakurel *et al.*: Opt. Express **23** (2015) 28182.
[4] *A. Takeuchi, K. Uesugi, Y. Suzuki, S. Itabashi and M. Oda: J. Synchrotron Rad. **24** (2017) 586.*
[5] M. Oda *et al.*: J. Vac. Sci. Technol. B **11** (1993) 37.

SACLA Beam Performance

A large jump in performance has been achieved by introducing BL2 and BL3 pulse-by-pulse switching operations in user experiments [1,2]. Since September 2017 [1], three FEL beamlines, BL1 for soft-X-ray FEL, and BL2 and BL3 for hard X-ray FELs, have been available simultaneously for a variety of experiments. This new operation standard significantly increases opportunities for user experiments, and the net user time in FY2017 across user shifts at BL1 to BL3 is expected to exceed 5000 hours, while maintaining high laser availability and short-pulse characteristics with efficient multi-beamline operations. Figure 1 shows the typical intensity stability at the three FEL beamlines.

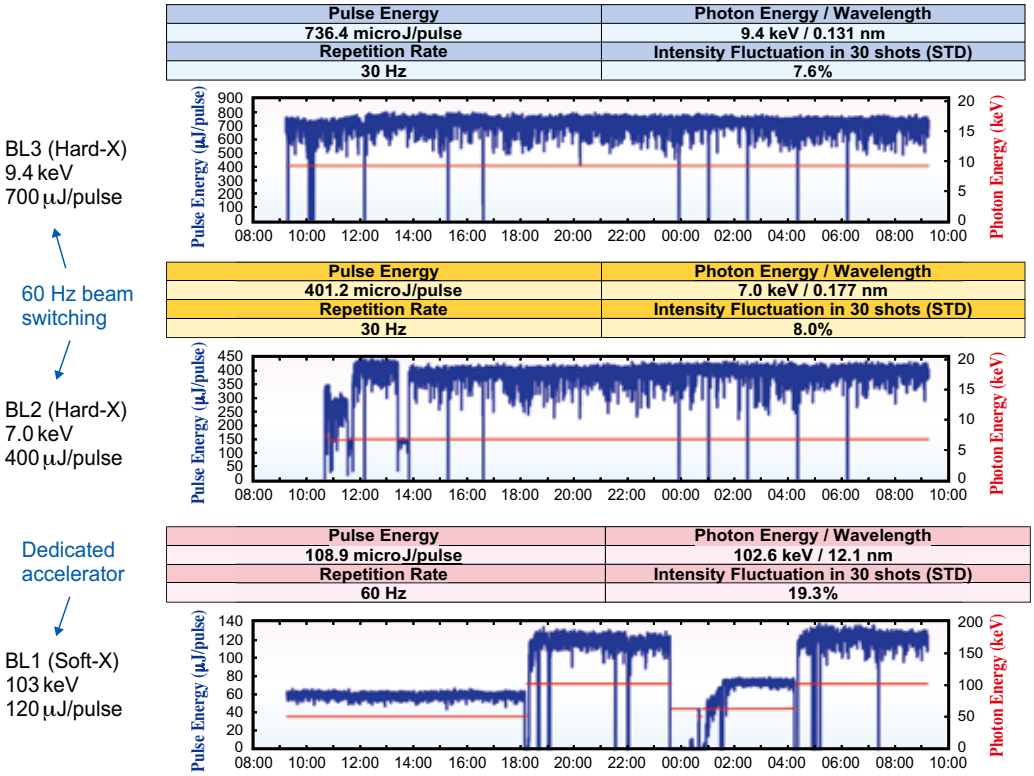

Fig. 1. Typical laser intensity trends during user experiments. The upper, middle, and lower graphs show the intensity stability at BL3, BL2, and BL1, respectively. The repetition rates of SACLA and BL1 dedicated accelerator are 60 Hz.

Hitoshi Tanaka

RIKEN SPring-8 Center

Email: tanaka@spring8.or.jp

References

[1] C. Kondo *et al.*: Proc. of IPAC2017, Copenhagen, Denmark (2017) pp. 3404.
[2] T. Hara *et al.*: Proc. of FEL2017, Santa Fe, USA (2017) - in press.

FACILITY STATUS

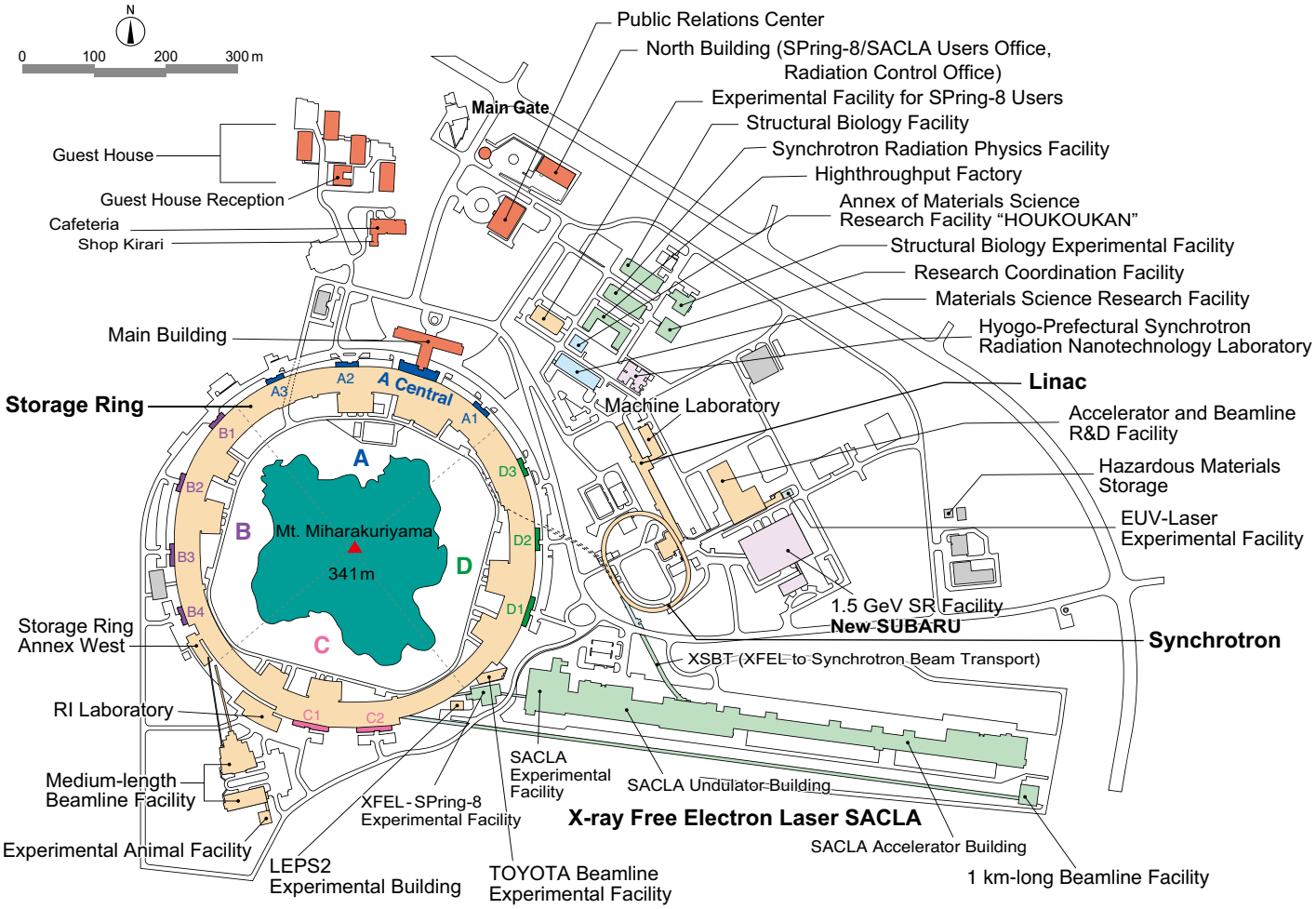

SPring-8

I. Introduction

It was the last year that SPring-8 celebrated the 20th anniversary since its start of operation in 1997. SPring-8 was stably operated throughout 2017 with the total operation time of the accelerator complex and the total user beam time of 5281.6 h and 4478.7 h, respectively, with the total down time of 29 h. SPring-8 had to complete all its operations by the middle of February 2018.

Regarding its research proposal system, SPring-8 designated the Cross-SR Facility Use Proposals for Industrial Application as a priority field of the priority research program on 25 September 2017. Concerning the contract beamlines, there were five interim reviews conducted for Research Center for Nuclear Physics, Osaka University (BL33LEP I), and the project was authorized to continue. Upon the expiration of their contract terms, reviews were also conducted for SUNBEAM Consortium (BL16B2, BL16XU), Hyogo ID (BL24XU, Hyogo Prefecture), and their proposals for the next term were approved.

At present, SPring-8 users number is as many as 13,000, all of whom are members of the SPring-8 User Community (SPRUC).

It is important for SPring-8 to jointly organize scientific events with SPRUC, such as the SPring-8 Symposium, to facilitate dialogue between users and the facility staff. In 2017, the SPring-8 Symposium was held at Hiroshima University on September 4–5, with a participant number of 267. SPring-8 also accelerates communication between users and the industry. The Joint Conference on Industrial Applications of SPring-8 was held in Kawasaki on August 31 to September 1, 2017, with 258 participants. As part of its continuous effort towards fostering of human resources in synchrotron sciences, SPring-8 organized the 17th SPring-8 Summer School with 90 students of graduate schools nationwide, in cooperation with Hyogo University, Kwansei Gakuin University, the University of Tokyo, Okayama University, Osaka University, Japan Atomic Energy Agency, National Institutes for Quantum and Radiological Science and Technology, and RIKEN. Furthermore, SPring-8 and SPRUC organized the 1st SPring-8 Autumn School with 43 participants which included 3rd year university students and researcher of companies.

II. Machine Operation

The operation statistics for the last five fiscal years are shown in Fig. 1. In FY2017, the total operation time of the accelerator complex was 5281.6 h. The operation time of the storage ring was 5270.4 h, 85.0% of which (4478.7 h) was for SR experiments. This excellent figure of the user time represents a storage ring availability of 99.3%, and a remarkable availability higher than 99% has been accomplished throughout the last five fiscal years. The downtime resulting from failure accounted for 0.64% (28.7 h) of the total user time. The intensity of the light source, i.e., the stored current is kept extremely stable within 0.1% thanks to the top-up operation, in which the current is filled up at any time on demand. In 93.4% of the user time in FY2017 the stored current stayed at 100 mA by the top-up operation, but in 5.8% at 70 mA as a result of failure of the RF system.

The variety of operation modes for SR experiments is one of the characteristics of SPring-8. The operation modes are grouped into several-bunch, and hybrid-filling modes. Several-bunch mode consists of equally spaced bunches or bunch-trains, i.e., 203 bunches, or 29 trains of 11 bunches, and hybrid-filling mode is composed of long bunch train and isolated single bunches as shown in Table 1, where a share of each operation mode is also shown. An isolated bunch impurity is routinely maintained better than 10^{-8} in the top-up operation by the bunch cleaning in the booster. The bunch current is also kept constant within 1% by means of the top-up operation. In the operation of the “11/29-filling+1single bunch” mode in the 8th cycle, failure of the timing system incurred a shift of the injection timing signal by one RF bucket, and it disabled us from maintaining the 5 mA single bunch for about 40h.

Table 2 summarizes the beam parameters of the storage ring.

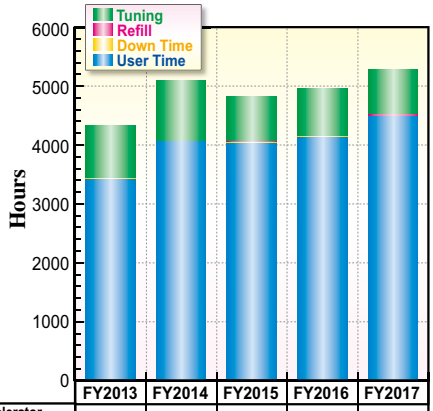

	FY2013	FY2014	FY2015	FY2016	FY2017
Accelerator Operation Time	4330.0	5099.3	4817.9	4951.7	5281.6
Storage Ring Operation Time	4265.4	5080.7	4804.8	4941.1	5270.4
Tuning & Study (Acc. & BL)	898.0	1019.3	767.2	803.1	769.6
Refill	3.5	5.1	5.3	3.4	4.6
Down Time	20.0	17.1	16.8	23.1	28.7
Mean Time Between Failures	213.0	163.2	202.8	229.2	194.7
Achieved User Time	3408.5	4057.8	4033.9	4125.5	4478.7
Planning User Time	3432.0	4080.0	4056.0	4152.0	4512.0
Availability (%)	99.3	99.5	99.5	99.4	99.3

Fig. 1. Operation statistics for most recent five fiscal years.

Table 1. Operation modes in FY2017

	Single bunch current (mA)	Share of operation time (%)
203 bunches		18.1
4 bunch-train × 84		7.4
11 bunch-train × 29		20.7
1/7-filling + 5 single bunches	3	8.0
2/29-filling + 26 single bunches	1.4	3.2
1/14-filling + 12 single bunches	1.6	14.4
4/58-filling + 53 single bunches	1	6.4
11/29-filling + 1 single bunch	5	21.8

Table 2. Beam parameters of SPring-8 storage ring

Energy [GeV]	8
Number of buckets	2436
Tunes (ν_x / ν_y)	41.14 / 19.34
Current [mA]:	
single bunch	12
multi bunch	100
Bunch length (σ) [psec]	13
Horizontal emittance [nm·rad]	2.4*
Vertical emittance [pm·rad]	4.8*
Coupling [%]	0.2
RF Voltage [MV]	14.4** ~ 16
Momentum acceptance [%]	3.2 (~256 MeV)
Beam size (σ_x / σ_y)* [μm]	
Long ID section	333 / 7
ID section	316 / 5
BM1 section	94 / 12
BM2 section	100 / 12
Beam divergence (σ_x' / σ_y')* [μrad]	
Long ID section	8 / 0.7
ID section	9 / 1.0
BM1 section	58 / 0.5
BM2 section	68 / 0.5
Operational chromaticities (ξ_x / ξ_y)	+2 / +2***
Lifetime [hr]:	
100 mA (multi bunch)	~ 250
1 mA (single bunch)	~ 30
Horizontal dispersion [m]:	
Long ID section	0.153
ID section	0.146
BM1 section	0.039
BM2 section	0.059
Fast orbit stability (0.1 – 200 Hz) [μm]	
horizontal (rms)	~ 4
vertical (rms)	~ 1

* Assuming 0.2% coupling
** Power saving mode
*** With bunch-by-bunch feedback

III. Beamlines

The SPring-8 storage ring can accommodate up to 62 beamlines: 34 insertion devices, 4 long undulators, and 24 bending magnets. At present, 57 beamlines are in operation, covering a wide variety of research fields involving synchrotron radiation science and technology. The beamlines are classified into the following three types.

(1) Public Beamlines (26 beamlines operating)
(2) Contract Beamlines (19 beamlines operating)
(3) RIKEN Beamlines (12 beamlines operating)

There are now 26 public beamlines in full operation. The beamlines that are proposed and constructed by external organizations, such as universities, research institutes, private companies and consortiums, are called contract beamlines and are exclusively used by the contractors for their own research purposes. At present, 19 contract beamlines are in operation. The beamlines constructed by RIKEN except for public beamlines are called RIKEN beamlines, and are mainly used for RIKEN's own research activities, with partial availability for public use. RIKEN is now operating 12 beamlines.

To illustrate the beamline portfolio of SPring-8, a beamline map is shown in Fig. 2 together with the beamline classification. The research fields of each beamline are presented in Table 3.

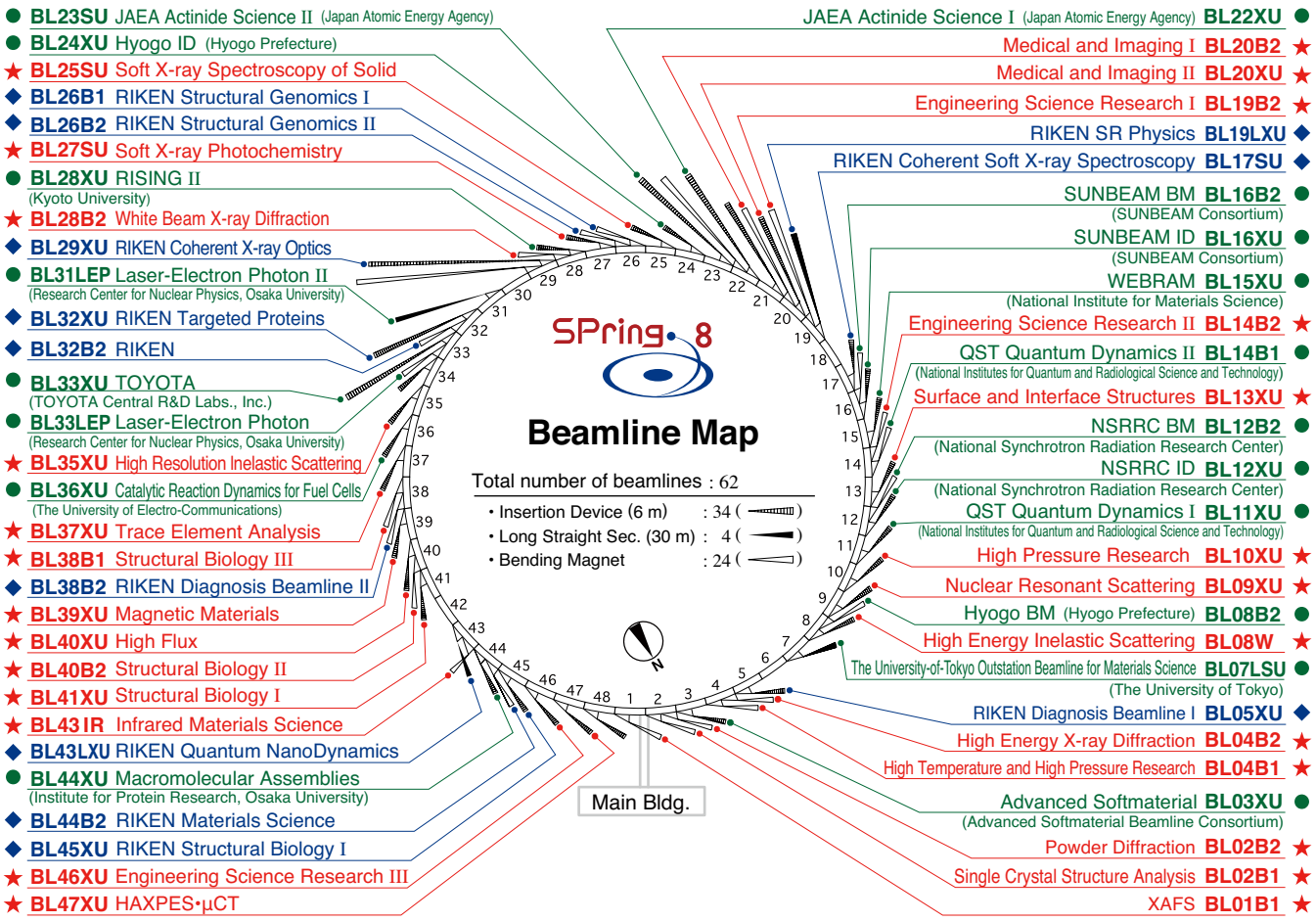

BL: Beamline
B1, B2: Bending Magnets
XU: X-ray Undulator
SU: Soft X-ray Undulator
W: Wiggler

IR: Infrared Radiation
LEP: Laser-Electron Photon
LXU: Long-length X-ray Undulator
LSU: Long-length Soft X-ray Undulator

★ : Public Beamlines
● : Contract Beamlines
◆ : RIKEN Beamlines

WEBRAM: Wide Energy Range Beamline for Research in Advanced Materials
NSRRC: National Synchrotron Radiation Research Center, Taiwan
RISING: Research & Development Initiative for Scientific Innovation of New Generation Batteries

Fig. 2. Beamline map.

Table 3. List of beamlines

BL #	Beamline Name	(Public Use) or (First Beam)	Areas of Research and Available Techniques
★ Public Beamlines			
BL01B1	XAFS	(Oct. 1997)	XAFS in wide energy region (3.8 to 113 keV). XAFS of dilute systems and thin films. Quick XAFS with a time resolution of seconds to tens of seconds.
BL02B1	Single Crystal Structure Analysis	(Oct. 1997)	Charge density study and crystal structure analysis from accurate single crystal X-ray diffraction. (X-ray energy range: 8 – 115 keV)
BL02B2	Powder Diffraction	(Sept. 1999)	Charge density study and phase identification of crystalline materials from accurate powder diffraction measurements. (X-ray energy range: 12.4 – 35 keV)
BL04B1	High Temperature and High Pressure Research	(Oct. 1997)	High temperature and high pressure research with the multi-anvil press by powder X-ray diffraction, radiography and ultrasonic measurement.
BL04B2	High Energy X-ray Diffraction	(Sept. 1999)	Pair distribution function analysis for glass, liquid, and amorphous materials. High-energy X-ray total scattering. Containerless levitation.
BL08W	High Energy Inelastic Scattering	(Oct. 1997)	Magnetic Compton scattering. High-resolution Compton scattering. High-energy Bragg scattering. High-energy fluorescent X-ray analysis.
BL09XU	Nuclear Resonant Scattering	(Oct. 1997)	Lattice dynamics using nuclear inelastic scattering. Mössbauer spectroscopy, especially for the surface/interface study and under the extreme conditions. Hard X-ray photoelectron spectroscopy (HAXPES). Depth analysis of HAXPES with high flux and energy resolution.
BL10XU	High Pressure Research	(Oct. 1997)	Structure analysis and phase transitions under ultra high pressure (DAC experiment). Earth and planetary science.
BL13XU	Surface and Interface Structures	(Sept. 2001)	Atomic-scale structural analysis of surfaces and interfaces of crystalline materials, ultra-thin films, and nanostructures. Surface X-ray diffraction (SXRD). Microbeam diffraction.
BL14B2	Engineering Science Research II	(Sept. 2007)	X-ray Imaging. XAFS in wide energy region (3.8 to 72 keV). XAFS of dilute systems and thin films.
BL19B2	Engineering Science Research I	(Nov. 2001)	Residual stress measurement. Structural analysis of thin film, surface, interface. Powder diffraction. X-ray imaging, X-ray topography. Ultra-small angle X-ray scattering.
BL20XU	Medical and Imaging II	(Sept. 2001)	Microimaging. Micro-/nano-tomography, phase-contrast microtomography, X-ray diffraction tomography (XRD-CT), hard X-ray microbeam/scanning microscopy, imaging microscopy, microtomography, phase-contrast microtomography X-ray diffraction tomography (XRD-CT), X-ray holography, coherent X-ray optics, and other experiments on X-ray optics and developments of optical elements. Refraction-enhanced imaging, phase-contrast CT. Ultra-small angle scattering.
BL20B2	Medical and Imaging I	(Sept. 1999)	Microimaging: microtomography, phase-contrast microtomography with grating interferometer for biological specimen and other kinds of specimen. Evaluation and development of various kinds of optical elements for novel imaging techniques. Large field X-ray topography.
BL25SU	Soft X-ray Spectroscopy of Solid	(Apr. 1998)	Study of electronic state of solids by soft X-ray photoemission spectroscopy (PES) including angle-resolved PES (ARPES). Atomic arrangement analysis of surfaces by photoelectron diffraction (PED) technique using two-dimensional photoemission analyzer. Magnetic state analysis by magnetic circular dichroism (MCD) of soft X-ray absorption and its element-specific magnetization curve measurements. Chemical and magnetic imaging by soft X-ray scanning microscopy and photoelectron emission microscopy (PEEM).
BL27SU	Soft X-ray Photochemistry	(May 1998)	Ambient atmospheric pressure soft X-ray photoabsorption spectroscopy. Chemical state analysis of light elements in dilute samples (NEXAFS). Elemental and chemical mapping using micro soft X-ray beam. Soft X-ray emission spectroscopy for solids.
BL28B2	White Beam X-ray Diffraction	(Sept. 1999)	White X-ray diffraction and topography. Time-resolved energy-dispersive XAFS (DXAFS) for studies of chemical and/or physical reaction process. Biomedical imaging and radiation biology studies. High energy X-ray microtomography.
BL35XU	High Resolution Inelastic Scattering	(Sept. 2001)	Materials dynamics on ~meV energy scales using inelastic X-ray scattering (IXS).
BL37XU	Trace Element Analysis	(Nov. 2002)	X-ray microbeam spectrochemical analysis. Ultra trace element analysis. High energy X-ray fluorescence analysis.
BL38B1	Structural Biology III	(Oct. 2000)	Structural biology. Macromolecular crystallography. Automatic data collection.
BL39XU	Magnetic Materials	(Oct. 1997)	X-ray magnetic circular dichroism (XMCD) spectroscopy and element-specific magnetometry under multiple-extreme conditions. XMCD/XAS using a 100 nm focussed X-ray beam. X-ray emission spectroscopy. Resonant X-ray magnetic scattering.
BL40XU	High Flux	(Apr. 2000)	Time-resolved diffraction and scattering experiments. Microbeam X-ray diffraction and scattering experiments. X-ray photon correlation spectroscopy. Fluorescence analysis. Quick XAFS. Submicrometer-scale single crystal structure analysis with high flux and zone plate focused X-ray beam. Single shot imaging with X-ray choppers. Laser pump-X-ray probe experiment.
BL40B2	Structural Biology II	(Sept. 1999)	Noncrystalline small and wide angle X-ray scattering.
BL41XU	Structural Biology I	(Oct. 1997)	Structural biology. Macromolecular crystallography. Microcrystallography. High resolution data collection.
BL43IR	Infrared Materials Science	(Apr. 2000)	Infrared microspectroscopy.
BL46XU	Engineering Science Research III	(Nov. 2000)	Structural characterization of thin films by X-ray diffraction and X-ray reflectivity measurement. Residual stress measurement. Time resolved X-ray diffraction measurement. Hard X-ray photoemission spectroscopy.
BL47XU	HAXPES·μCT	(Oct. 1997)	Hard X-ray photoelectron spectroscopy (HAXPES). Depth analysis of angle resolved HAXPES with wide acceptance lens. Projection type microtomography. Imaging type microtomography. Hard X-ray microbeam/scanning microscopy.

BL #	Beamline Name	(Public Use) or (First Beam)	Areas of Research and Available Techniques
	● Contract Beamlines		
BL03XU	**Advanced Softmaterial** (Advanced Softmaterial Beamline Consortium)	(Nov. 2009)	Structural characterization of softmaterials using small- and wide-angle X-ray scattering. Grazing-incidence small- and wide-angle X-ray scattering for thin films. X-ray diffraction and reflectivity measurements for softmaterials.
BL07LSU	**The University-of-Tokyo Outstation Beamline for Materials Science** (The University of Tokyo)	(Oct. 2009)	Time-resolved soft X-ray spectroscopy, nano-beam photoemission spectroscopy, ultra high-resolution soft X-ray emission spectroscopy, and any methods requiring the highly brilliant soft X-ray beam.
BL08B2	**Hyogo BM** (Hyogo Prefecture)	(Jun. 2005)	XAFS in a wide energy region. Small angle X-ray scattering for structural analyses of polymer and nanocomposite materials. X-ray topography. Imaging. Powder diffraction with a high angular-resolution.
BL11XU	**QST Quantum Dynamics I** (National Institutes for Quantum & Radiological Science & Technology)	(Oct. 1998)	Synchrotron radiation Mössbauer spectroscopy. XAFS. Resonant inelastic X-ray scattering spectroscopy. *In situ* X-ray diffraction during molecular-beam epitaxial growth.
BL12B2	**NSRRC BM** (National Synchrotron Rad. Res. Center)	(Oct. 2000)	X-ray absorption spectroscopy. Powder X-ray diffraction. High resolution X-ray scattering. Protein crystallography.
BL12XU	**NSRRC ID** (National Synchrotron Rad. Res. Center)	(Dec. 2001)	Non-resonant or resonant inelastic X-ray scattering. Hard X-ray photoemission spectroscopy.
BL14B1	**QST Quantum Dynamics II** (National Institutes for Quantum & Radiological Science & Technology)	(Dec. 1997)	Materials science under high-temperature and high-pressure, Energy-dispersive XAFS. X-ray diffraction for surface structure analyses.
BL15XU	**WEBRAM** (National Institute for Materials Science)	(Jan. 2000)	Hard X-ray photoelectron spectroscopy. High-precision X-ray powder diffraction.
BL16B2	**SUNBEAM BM** (SUNBEAM Consortium)	(Oct. 1998)	Characterization of secondary battery related materials, semiconductors, fuel cells, catalysts, and several industrial materials using X-ray absorption fine structure measurements, X-ray diffraction (including X-ray reflectivity technique) and X-ray topography.
BL16XU	**SUNBEAM ID** (SUNBEAM Consortium)	(Oct. 1998)	Characterization of secondary battery related materials, semiconductors, fuel cells, catalysts, and structural materials using X-ray diffraction, X-ray microbeam based evaluation techniques (including X-ray magnetic circular dichroism), hard X-ray photoemission spectroscopy and fluorescence X-ray analysis.
BL22XU	**JAEA Actinide Science I** (Japan Atomic Energy Agency)	(May 2002)	Materials science under high-pressure. Resonant X-ray scattering. Speckle scattering. Residual stress/strain distribution analysis.
BL23SU	**JAEA Actinide Science II** (Japan Atomic Energy Agency)	(Feb. 1998)	Surface chemistry with supersonic molecular beam. Biophysical spectroscopy. Photoelectron spectroscopy. Magnetic circular dichroism.
BL24XU	**Hyogo ID** (Hyogo Prefecture)	(May. 1998)	Surface/interface analysis for industry by fluorescent X-ray analysis, strain measurements and grazing incidence X-ray diffraction. Microbeam formation studies for material and life sciences. Scanning and imaging microscope. Micro-tomography. Micro-XAFS. Microbeam small- and wide-angle X-ray scattering for local structure analysis. Bright field X-ray topography. Near-ambient pressure hard X-ray photoelectron spectroscopy. 2016 Bright-field X-ray topography under multiple-beam diffraction condition.
BL28XU	**RISING II** (Kyoto University)	(Apr. 2012)	Characterization of rechargeable battery reactions and battery related materials by resonance X-ray diffraction, X-ray absorption spectroscopy (XAS), X-ray diffraction spectroscopy (XDS), and hard X-ray photoemission spectroscopy (HAXPES).
BL31LEP	**Laser-Electron Photon II** (RCNP, Osaka University)	(Oct. 2013)	Production of high intensity GeV photon beam by laser-backward Compton scattering. Hadron physics via photonucleon and photonuclear reactions. Test and calibration of detectors with GeV gamma-ray and converted electrons/positrons.
BL33LEP	**Laser-Electron Photon** (RCNP, Osaka University)	(Jun. 1999)	Meson photoproduction from nucleon and nucleus. Photoexcitation of hyperons, nucleon resonances, and other exotic states. Photonuclear reactions. Beam diagnoses. Test and calibration of detectors with GeV photon beam.
BL33XU	**TOYOTA** (TOYOTA Central R&D Labs., Inc.)	(Apr. 2009)	Time-resolved XAFS. Characterization of industrial materials, such as catalysts, secondary batteries, fuel cells.
BL36XU	**Catalytic Reaction Dynamics for Fuel Cells** (The University of Electro-Communications)	(Jan.2013)	Real time analysis of catalytic reaction dynamics for fuel cells: time resolved XAFS and X-ray diffraction, 2D scanning microscopic XAFS, 3D computed tomography/laminography XAFS, ambient pressure hard X-ray photoelectron spectroscopy.
BL44XU	**Macromolecular Assemblies** (IPR, Osaka University)	(May 1999)	Crystal structure analysis of biological macromolecular assemblies (e.g., membrane protein complexes, protein complexes, protein-nucleic acid complexes, and viruses).
	◆ RIKEN Beamlines		
BL05XU	**RIKEN Diagnosis Beamline I**	(Mar. 2004)	Accelerator beam diagnostics. R&D of accelerator components.
BL17SU	**RIKEN Coherent Soft X-ray Spectroscopy**	(Sept. 2003)	High resolution photoemission spectroscopy. Soft X-ray emission spectroscopy. Soft X-ray diffraction spectroscopy. Soft X-ray microspectroscopy.
BL19LXU	**RIKEN SR Physics**	(Oct. 2000)	SR science with highly brilliant X-ray beam.
BL26B1	**RIKEN Structural Genomics I**	(Apr. 2002)	Structural biology research based on single crystal X-ray diffraction.
BL26B2	**RIKEN Structural Genomics II**	(Apr. 2002)	Structural biology research based on single crystal X-ray diffraction.
BL29XU	**RIKEN Coherent X-ray Optics**	(Dec. 1998)	X-ray optics, especially coherent X-ray optics.
BL32XU	**RIKEN Targeted Proteins**	(Oct. 2009)	Protein microcrystallography.
BL38B2	**RIKEN Diagnosis Beamline II**	(Sept. 1999)	Accelerator beam diagnostics.
BL43LXU	**RIKEN Quantum NanoDynamics**	(Oct. 2011)	High resolution inelastic X-ray scattering for investigating atomic and electronic dynamics.
BL44B2	**RIKEN Materials Science**	(Feb. 1998)	Structural materials science research using powder X-ray diffraction.
BL45XU	**RIKEN Structural Biology I**	(Jul. 1997)	Time-resolved and static structures of non-crystalline biological materials using small-angle scattering and diffraction techniques.

IV. User Program and Statistics

SPring-8 calls for public use proposals twice a year, in principle. The submitted proposals are reviewed by the SPring-8 Proposal Review Committee (SPring-8 PRC). Since 1997, SPring-8 has accepted a variety of proposals. For the promotion of research on industrial applications at SPring-8, the Industrial Application Division was established in 2005. With consultation support for industrial users provided by the division's coordinators, currently, Industrial Application Proposals account for approximately 16%–20% of the total number of proposals conducted at the public beamlines. In addition, the Measurement Service was introduced in 2007B, wherein the personnel of the Industrial Application Division carries out XAFS measurements on behalf of users at BL14B2. SPring-8 also launched a Protein Crystallography Data Collection Service at BL38B1 and Powder X-ray Diffraction Measurement Service at BL19B2 in 2009B, a Hard X-ray Photoemission Spectroscopy (HAXPES) Measurement Service, and a Thin Film Analysis (GIXD/XRR) Measurement Service at BL46XU in 2012B, and a Small Angle Scattering (SAXS) Measurement Service at BL19B2 in 2014B.

SPring-8 has consistently provided ~4,500h of user beamtime per year. Since the start of its operation in 1997, SPring-8 has succeeded in providing users with a total beamtime of 79,401h. The beamtime available to users, the number of experiments conducted, and the number of user visits at the public and contract beamlines are summarized in Fig. 3. Part of the proposals are for proprietary use, for which refereed reports are not required. Figures 4 to 13 show the information on user programs.

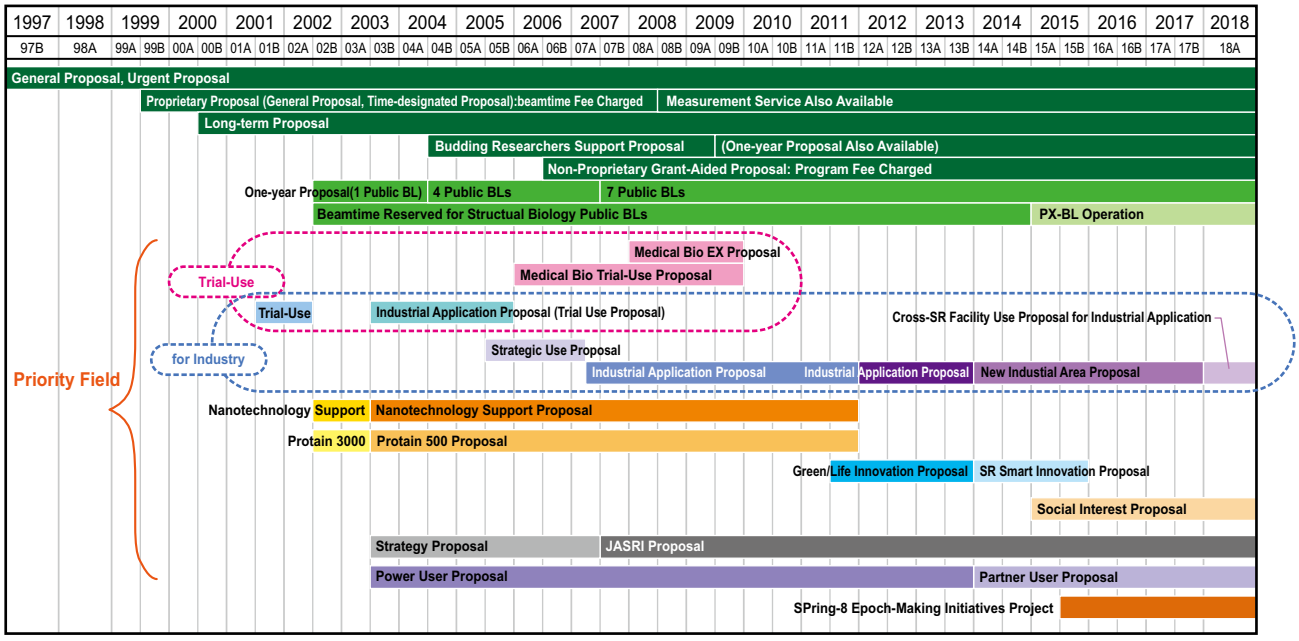

Fig. 3. Categories of proposals for the public beamlines.

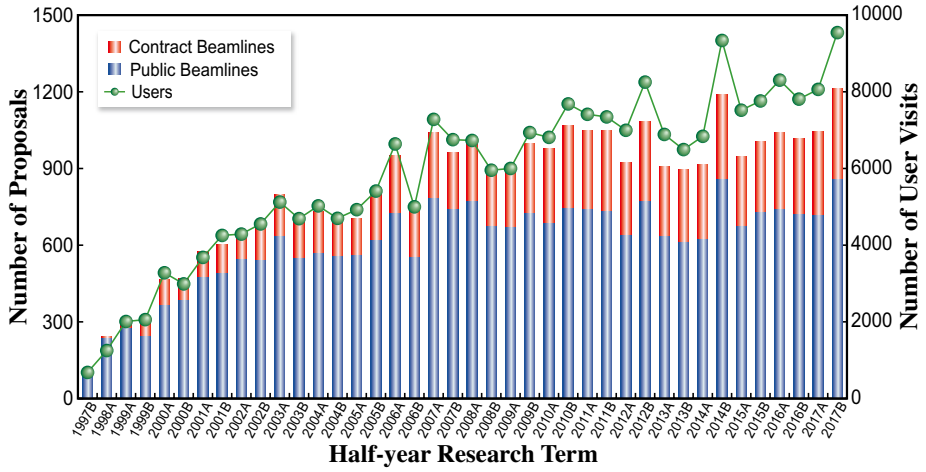

Fig. 4. Numbers of conducted experiments.

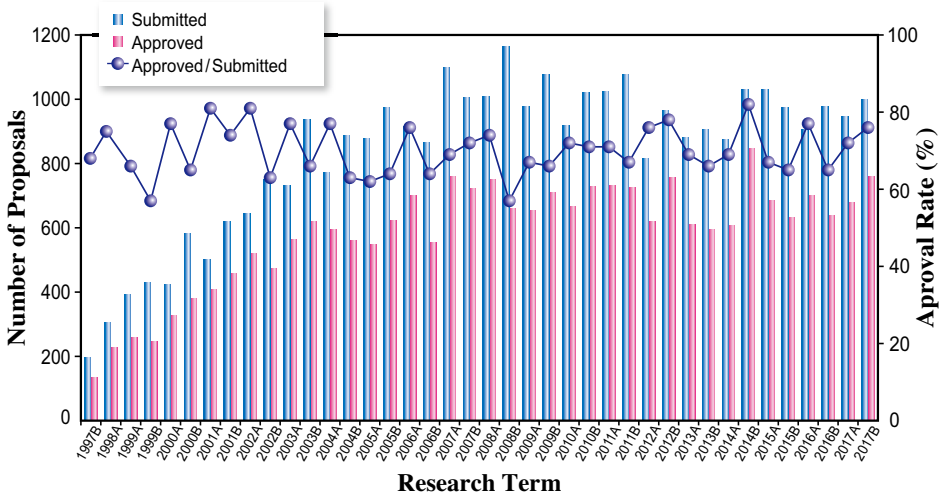

Fig. 5. Numbers of submitted proposals and approved proposals by research term (public beamlines).

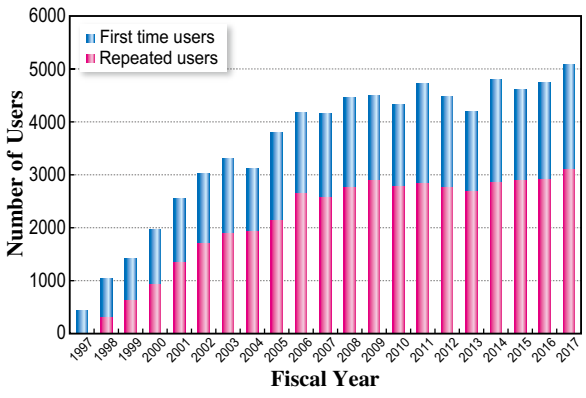

Fig. 6. Numbers of users by fical year.

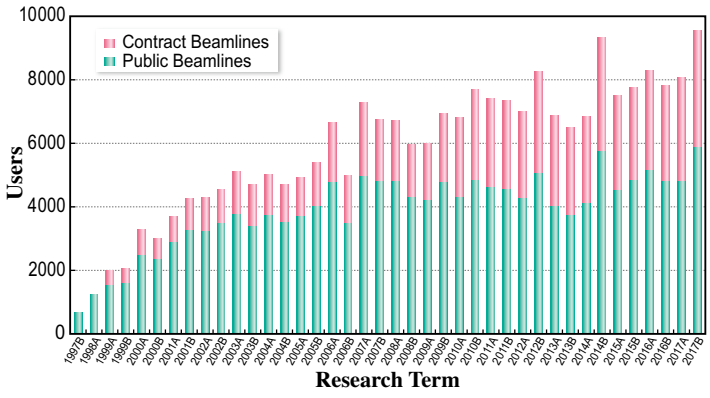

Fig. 7. Numbers of users visits by research term.

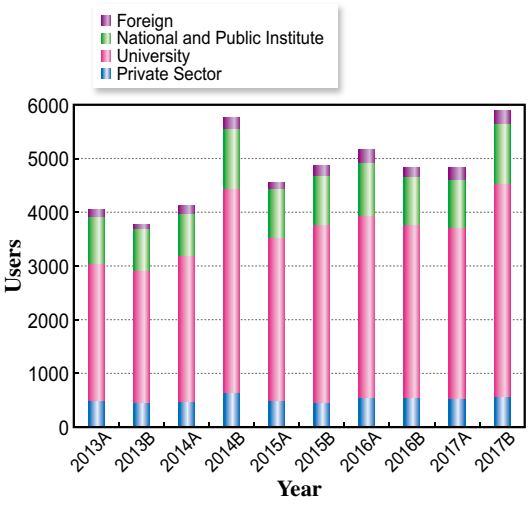

Fig. 8. Numbers of users by affiliation categories (public beamlines).

Fig. 9. Numbers of users by affiliation categories (contract beamlines).

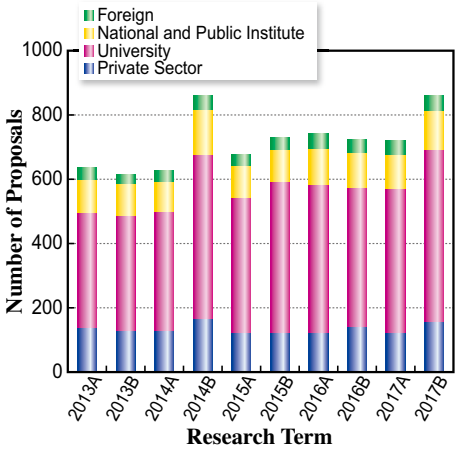

Fig. 10. Numbers of conducted proposals by affiliation (public beamlines).

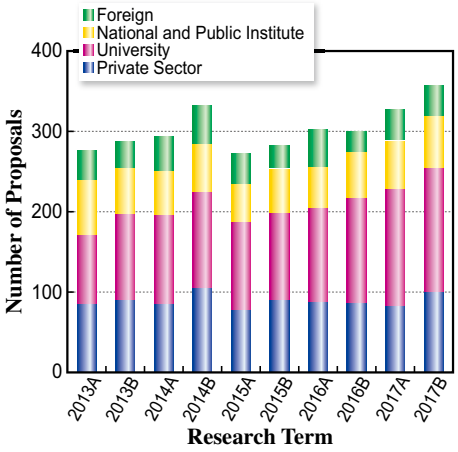

Fig. 11. Numbers of conducted proposals by affiliation categories (contract beamlines).

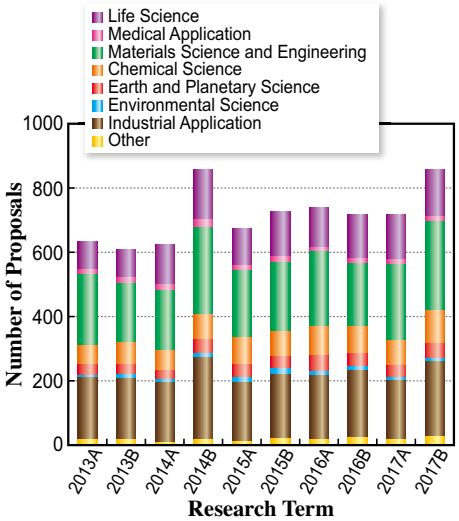

Fig. 12. Numbers of conducted proposals by research area (public beamlines).

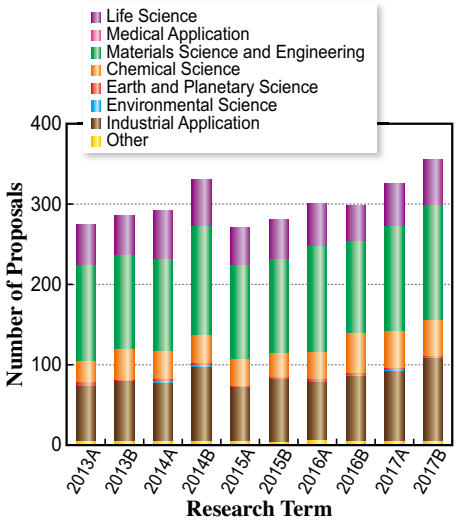

Fig. 13. Numbers of conducted proposals by research area (contract beamlines).

V. Research Outcome

As of March 2018, the total number of registered refereed papers from SPring-8 was 14,069. Figure14 shows the annual statistics of refereed papers.

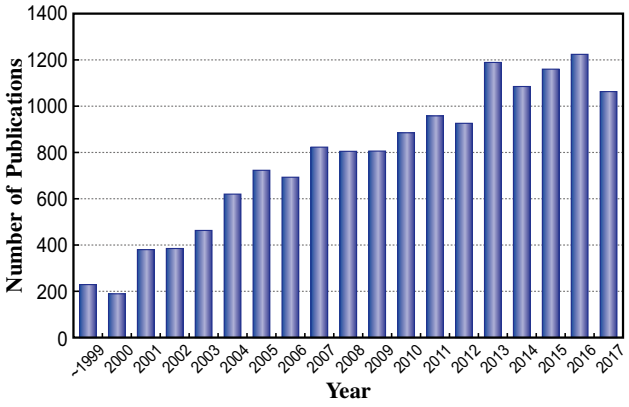

Fig. 14. Number of refereed publications.

VI. Budget and Personnel

When SPring-8 started operation in 1997, it was jointly managed by RIKEN, JAERI (now JAEA), and JASRI. However, JAERI withdrew from the management of SPring-8 on September 30, 2005. SPring-8 is currently administered by RIKEN and JASRI collaboratively.

The total budget for the operation of SPring-8 in FY2017 was about 9.4 billion yen. As of October 2016, RIKEN and JASRI have a total of 441 staff members. Figure 15 shows the annual budget allocated to operations, maintenance, and promotion of SPring-8. Figure 16 shows the manpower of RIKEN and JASRI.

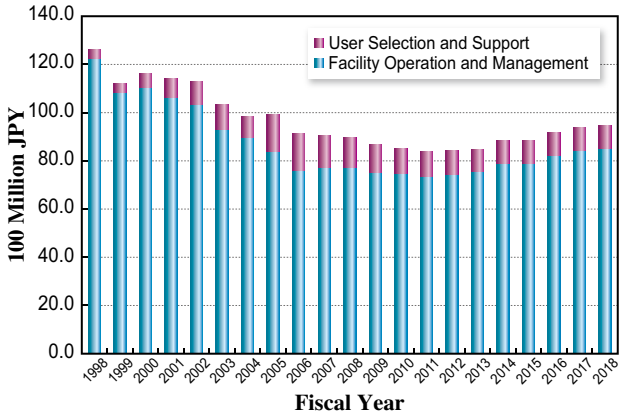

Fig. 15. SPring-8 budget.

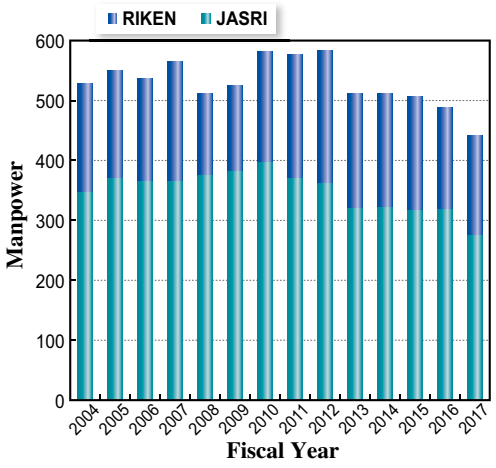

Fig. 16. Personnel at SPring-8: JASRI and RIKEN.

VII. Research Complex

The facilities of SPring-8, SACLA, and NewSUBARU form the Center of Excellence (COE) at the SPring-8 campus where JASRI, public beamline users, the contractors of contract beamlines, RIKEN, and the University of Hyogo work in close cooperation, forming a research complex where each member has their own role in delivering high-quality results to the field of synchrotron radiation science and technology. The organizational charts of RIKEN and JASRI, which are at the center of this research complex, are shown in Fig. 17 and Fig. 18, respectively.

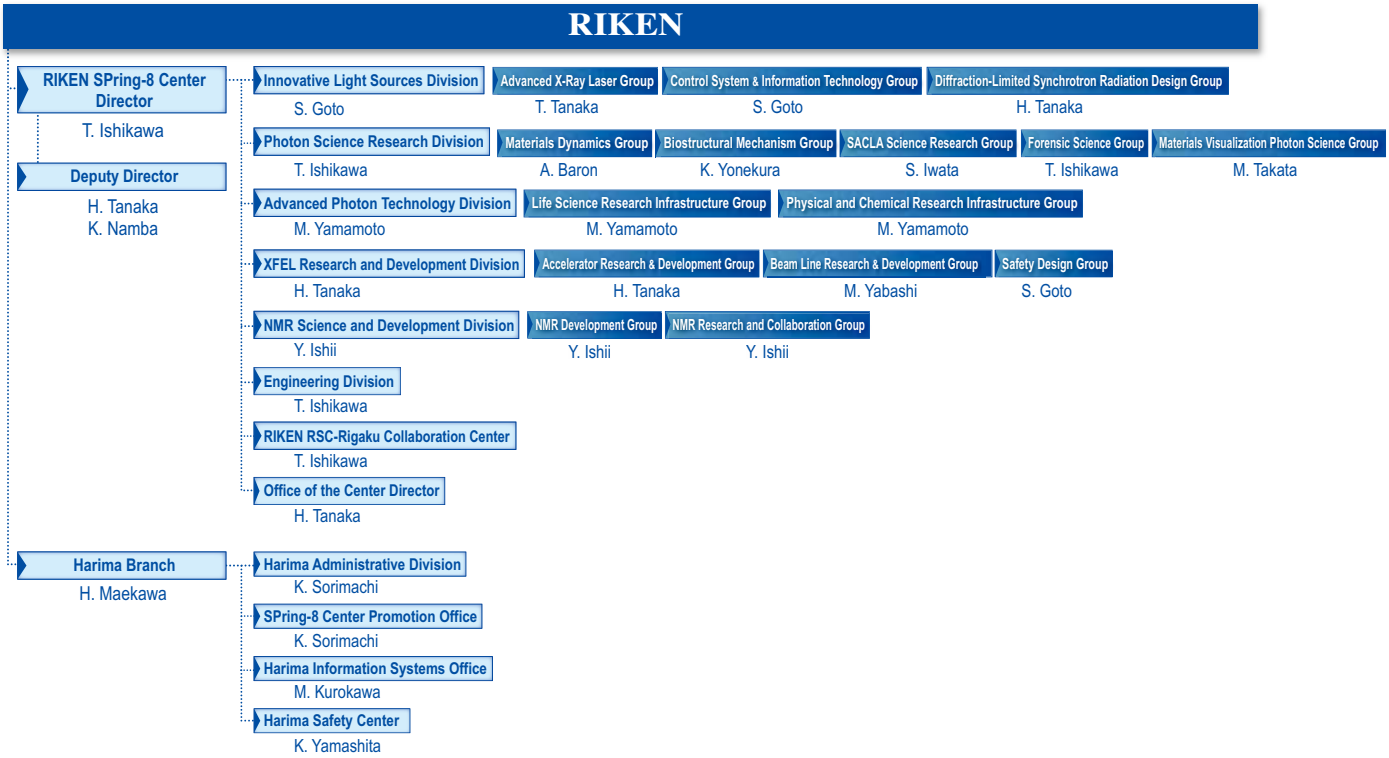

Fig. 17. RIKEN Harima Branch chart as of April 2018.

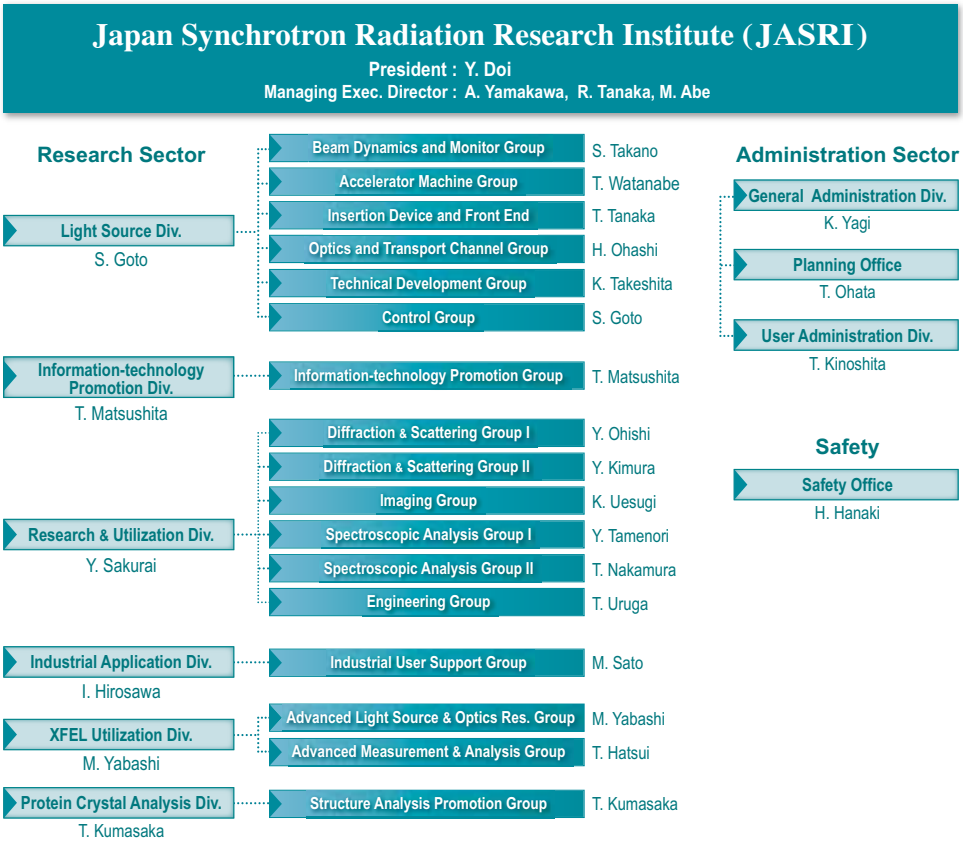

Fig. 18. JASRI chart as of April 2018.

VIII. SPring-8 Users Community (SPRUC)

The SPring-8 Users Community (SPRUC) is a user society that includes not only all users but also potential users who are interested in using SPring-8. In addition to these individuals, representative organizations comprising 26 institutes (principal universities, national/international research institutes, industries, beamline consortiums) participate in SPRUC to discuss further promotion of the utilization of SPring-8 from strategic and perspective viewpoints.

As one of the key activities of SPRUC, the SPring-8 Symposium is held annually at the site of one of the representing organizations jointly with RIKEN and JASRI. SPring-8 Symposium 2017, with the theme "Future vision of SPring-8", was held at Hiroshima University on September 4 and 5, 2017. In the symposium, a panel discussion was performed at the special session to debate on the theme. The award ceremony of SPRUC 2017 Young Scientist award which was conferred to two researchers (Dr. Shinji Miwa, Osaka University and Dr. Tatsuya Sakamaki, Tohoku University) was also held at the symposium. SPring-8 Symposium 2018 is scheduled to be held on August 25 and 26 at Himeji City Hall, jointly hosted by University of Hyogo.

SPRUC has continued to promote the activities of "SPRUC multidisciplinary research groups" in order to develop the use of SPring-8 in the new areas that will be important to future science and technology. Four multidisciplinary research fields were designated in 2014, and two multidisciplinary research groups for nanodevice science and application were launched in 2015. The groups actively performed an innovative use of SPring-8, and the nanodevice science research group is now preparing to launch the SPRUC Research Group at the next term. In addition, 3rd Term Research Groups each actively organized a workshop in FY2017.

In order to discuss medium- and long-term plans for the future performance of detectors and measurement systems, a SPRUC working group on high-performance beamline technologies was launched in December 2016. The working group sent out questionnaire about the comments to the plan for the high performance technologies to the SPRUC user group, and summarized the results. The result was submitted to the chair of SPRUC, Prof. Nakagawa, as "the Midterm report", and is now open on the SPRUC website.

At last, the two projects which started in FY2017 are described: First, the "SPring-8 Autumn School" was held on September 18–21, 2017, in order to open for beginners such as younger students and researchers who have never used SPring-8 beamlines. The school was a great success and will be held also in FY2018. The second is "SPRUC-RIKEN-JASRI 3-way meeting", which was organized in order to discuss the future issues and to feedback the opinions from SPRUC to the SPring-8 facility. At the meeting, the four representatives from each organizations come together at a pace of every two months.

Prof. A. Nakagawa
Osaka University
SPRUC Chairman FY2017

SPRUC 2017 Young Scientist Award
Prof. Y. Amemiya, Dr. T. Sakamaki, Dr. S. Miwa and Prof. A. Nakagawa

SPring-8 Symposium 2017

IX. Outreach Activities

To find new users in unexplored fields of application, SPring-8 holds various serialized seminars named "Workshop on Advanced Techniques and Applications at SPring-8". Here are some representatives.

- 15th: Novel functional materials using biological systems and the origins
  August 24, 2017 • Campus Plaza Kyoto (Kyoto)
- 16th Cultural property analysis with SPring-8
  June 10, 2017 • Tohoku University of Art and Design (Yamagata)
- 17th Current status and future prospects of protein structural biology at SPring-8
  August 3-4, 2017 • Osaka University (Osaka)
- 18th Frontiers of metal nanoparticle catalyst development – Controlling with the structure and the function – (Co-hosted by Industrial Users Society of SPring-8)
  December 1, 2017 • AP Shinagawa (Tokyo)
- 15th Novel functional materials using biological systems and the origins
  August 24, 2017 • Campus Plaza Kyoto (Kyoto)
- 23rd and 24th Acceleration of drug discovery with SPring-8 - the utilization and the usage system -
  (23rd) February 26, 2018 - Knowledge Capital Osaka (Osaka)
  (24th) March 5, 2018 - Fukurashia Tokyo Station (Tokyo)

SPring-8 Summer School

SACLA

I. Machine Operation & Beamlines

Our sixth year of operations proceeded without any significant issues. Operation statistics are summarized in Table 1. The ratio of downtime to user time was kept below 4%, a reasonably low rate for linac-based light sources.

Table 1. Operation Statistics for FY2017

	Time (h)
Total operation time	6281
User time	5466
Facility tuning time	701
Study time	4574
Downtime	234

In 2012, two beamlines, BL3 for XFEL and BL1 for broadband spontaneous light, were open for users, while all experiments were conducted with BL3. As the newest beamline, construction of BL2 was completed during the summer shutdown of 2014, and first laser amplification was achieved on October 21. An upgraded beamline for soft X-ray FEL, BL1, which combines the prototype accelerator of SACLA (SCSS), started operation in 2016. For more details, please refer to SACLA Beam Performance in this volume.

II. User Program and Statistics

SACLA calls for public user proposals twice per year.

In FY2016, JASRI introduced the proprietary research of General Proposals and the Proprietary Time-Designated Proposals. The project leaders of these proprietary proposals are not required to publish their research results, but required to pay each beamtime fee. In addition, to apply for the proprietary research the project leaders should be affiliated with a corporate enterprise located and registered in Japan.

Table 2, Figs. 1 and 2 provide statistics on proposals, users, and beamtime.

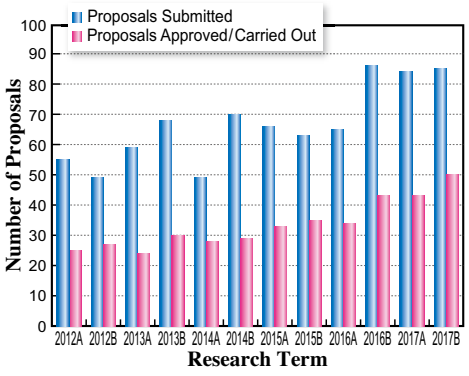

Fig. 1

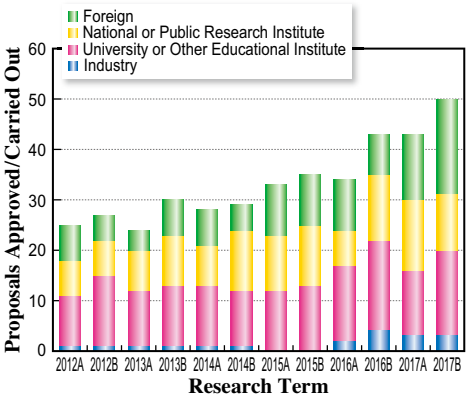

Fig. 2

Table 2. Number of proposals submitted, proposals approved/carried out, cumulative users, and beamtime available by research term

Half-year Research Term	Proposals Submitted	Proposals Approved / Carried Out					Cumulative Users	Beamtime Carried Out (Shifts)
			Priority Strategy Proposals	Non-proprietary	Proprietary			
				General Proposals	General Proposals	Time-Designated Proposals		
2012A	55	25	(12)	(13)	–	–	297	126
2012B	49	27	(19)	(8)	–	–	461	154
2013A	59	24	(15)	(9)	–	–	268	117
2013B	68	30	(19)	(11)	–	–	410	139
2014A	49	28	(20)	(8)	–	–	400	147
2014B	70	29	(17)	(12)	–	–	430	140
2015A	66	33	(23)	(10)	–	–	527	144
2015B	63	35	(23)	(12)	–	–	552	152
2016A	65	34	(21)	(12)	(1)	–	538	158
2016B	86	43	(21)	(20)	(1)	(1)	650	197
2017A	84	43	–	(43)	(0)	(0)	577	210
2017B	85	50	–	(50)	(0)	(0)	642	244

One shift = 12 hours at SACLA beamlines

SPring-8 SACLA
Research Frontiers 2017

Editor
Naoto Yagi
Japan Synchrotron Radiation Research Institute (JASRI)

Editing, Design & Layout
Marcia M. Obuti-Daté
Japan Synchrotron Radiation Research Institute (JASRI)

Printing
Hokuoh Printing Co.

JASRI
Information & Outreach Section
Users Administration Division

1-1-1 Kouto, Sayo-cho, Sayo-gun
Hyogo 679-5198 • JAPAN
Tel. +81-(0)791-58-2785 Fax. +81-(0)791-58-1869

Email: frontiers@spring8.or.jp
http://www.spring8.or.jp/

August 2018

SPring-8 SACLA

http://www.spring8.or.jp

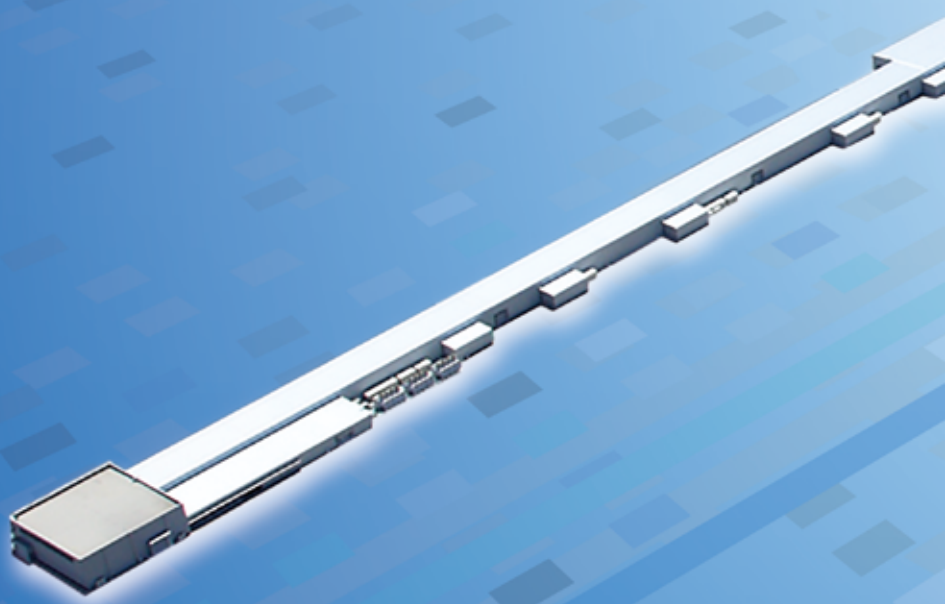

Japan Synchrotron Radiation Research Institute (JASRI)
1-1-1 Kouto, Sayo-cho, Sayo-gun, Hyogo 679-5198, Japan